Modelling early age cracking in blended cement concrete

by

Yingda Zhang

A thesis in fulfilment of the requirements for the degree of Doctor of Philosophy

School of Civil and Environmental Engineering

Faculty of Engineering

The University of New South Wales, Sydney, Australia

October 2022

Thesis submission for the degree of Doctor of Philosophy

Thesis Title and Abstract | Declarations | Inclusion of Publications Statement | Corrected Thesis and Responses

ORIGINALITY STATEMENT

☑ I hereby declare that this submission is my own work and to the best of my knowledge it contains no materials previously published or written by another person, or substantial proportions of material which have been accepted for the award of any other degree or diploma at UNSW or any other educational institution, except where due acknowledgement is made in the thesis. Any contribution made to the research by others, with whom I have worked at UNSW or elsewhere, is explicitly acknowledged in the thesis. I also declare that the intellectual content of this thesis is the product of my own work, except to the extent that assistance from others in the project's design and conception or in style, presentation and linguistic expression is acknowledged.

COPYRIGHT STATEMENT

☑ I hereby grant the University of New South Wales or its agents a non-exclusive licence to archive and to make available (including to members of the public) my thesis or dissertation in whole or part in the University libraries in all forms of media, now or here after known. I acknowledge that I retain all intellectual property rights which subsist in my thesis or dissertation, such as copyright and patent rights, subject to applicable law. I also retain the right to use all or part of my thesis or dissertation in future works (such as articles or books).

For any substantial portions of copyright material used in this thesis, written permission for use has been obtained, or the copyright material is removed from the final public version of the thesis.

AUTHENTICITY STATEMENT

☑ I certify that the Library deposit digital copy is a direct equivalent of the final officially approved version of my thesis.

Thesis submission for the degree of Doctor of Philosophy

Thesis Title and Abstract | Declarations | **Inclusion of Publications Statement** | Corrected Thesis and Responses

UNSW is supportive of candidates publishing their research results during their candidature as detailed in the UNSW Thesis Examination Procedure.

Publications can be used in the candidate's thesis in lieu of a Chapter provided:

- The candidate contributed **greater than 50%** of the content in the publication and are the "primary author", i.e. they were responsible primarily for the planning, execution and preparation of the work for publication.
- The candidate has obtained approval to include the publication in their thesis in lieu of a Chapter from their Supervisor and Postgraduate Coordinator.
- The publication is not subject to any obligations or contractual agreements with a third party that would constrain its inclusion in the thesis.

☑ The candidate has declared that **some of the work described in their thesis has been published and has been documented in the relevant Chapters with acknowledgement**.

A short statement on where this work appears in the thesis and how this work is acknowledged within chapter/s:

> Chapter 3 is a re-written version of an article submitted by the candidate, 'Autogenous shrinkage of High Volume of Fly ash and Ground Granulated Blast Furnace Slag Concrete', in Magazine of Concrete Research. I did more than 50% of the experiments and all of the writing. Some of the materials in this chapter have been expanded from a recent submission.
> Chapter 4 is a re-edited version of an article published by the candidate, 'Analytical Model Predicting the Concrete Tensile Stress Development in the Restrained Shrinkage Ring Test', in Construction and Building Materials. I did more than 50% development and all of the writing. Some of the materials in this chapter have been re-edited from a recent publication.
> Chapter 5 is a re-written version of an article submitted by the candidate, 'Modelling Blended Cement Concrete Tensile Creep for Standard Ring Test Application', in Structural Concrete. I did more than 50% the development and all of the writing. Some of the materials in this chapter have been re-written from a recent submission.
> Chapter 6 is a re-written version of an article submitted by the candidate, ' Tensile creep of Steam-cured UHPC: Linear and Nonlinear Creep', in Cement and Concrete Composites. I did more than 50% experiments and the development as well as the writing. Some of the materials in this chapter have been expanded and re-written from a recent submission.

Candidate's Declaration

I declare that I have complied with the Thesis Examination Procedure.

Acknowledgements

I firstly would like to express my heartfelt thanks to my supervisor, Professor Arnaud Castel, for his invaluable academic advice, consistent encouragement and continuous support of my PhD study. Meanwhile, I would like to deliver the most sincere and lofty gratitude to my joint supervisor, Dr Taehwan Kim, for his meticulous patience and guidance when I was facing a dilemma. He also trained me to be independent and think laterally. The credit also goes to my co-supervisor, Emeritus Professor Raymond Ian Gilbert, for his constructive suggestions. In addition, I would like to thank my external supervisor, Professor Tengfei Xu from Southwest Jiaotong University. His impeccable work ethic and insightful suggestions truly inspired me. His financial support also helped me during the COVID-19 period. It was such a good fortune to work closely with them.

The technical assistance from Paul Gwynne, Willian Terry and Luiz Paulo in preparing and conducting experimental tests at the Valentine Annex Laboratory of UNSW is gratefully acknowledged. Meanwhile, the funded research project (LP170100912) by Cement Concrete and Aggregate Australia (CCAA) and Australia Research Council (ARC), and my financial support from the University International Postgraduate Award (UIPA), are herein acknowledged.

I thank all the help from my research group and fellow PhD candidates. To Dr Quang Dieu Nguyen, Sumaiya Afroz, Zuobang Yao, Jiehong Li, Dr Mohammed Alnahhal, Abdelrahman Hamdan, Yuhan Zhao, Dr Ruizhe Si, Dr Yuan Yuan, A/Prof Kang Gao, Dr Qian Huang, Dr Xi Du, Shukai Ya, Dr Pengjiao Jia, Chen Li, Hao Gao, Xiaoran Zhang, Wanqi Zhang, Hongzhe Chen, Yunxuan Cui, Ziyi Xu, Chenggong Zhao, Yuehan Sun, Wei Huang, Wenfeng Huang, Zhenyu Zhu and Wanli Shi. We shared a wonderful time.

I am grateful to my beloved families, my parents, my first teachers and they always offer me remarkable confidence to overcome any difficulties.

Lastly, I would like to thank myself. I have spent more than 8 years in UNSW, growing from an ignorant undergraduate to a mature doctor, and will become a glorious academic staff of the university in the future. Thanks for never giving up!

Abstract

Concrete is one of the most commonly used building materials in the world because of its excellent versatility. The concrete consumption has increased considerably because of the rapid urbanisation development. Annual cement consumption is expected to increase to 5.2 billion tons by 2050. An average of 850 kg of carbon dioxide can be released into the environment to produce one tone of clinker. To minimise the disadvantages of cement production, one option is to use Supplementary Cementitious Materials (SCMs) such as fly ash and ground granulated blast furnace slag (GGBFS) to partially replace cement in concrete. Accordingly, this thesis extensively focuses on the research of time-dependent behaviour such as shrinkage and creep of blended cement concrete containing high volume of fly ash and GGBFS.

To advance the understanding of volumetric changes in concrete mixes with high volume of fly ash and GGBFS, the presented research focused on five areas: (a) autogenous, drying and total shrinkage of concrete; (b) tensile stress development of concrete in restrained ring test; (c) tensile creep of concrete; (d) nonlinear tensile creep of concrete; and (e) thermal cracking of concrete.

The first part of this dissertation reports the autogenous, drying and total shrinkage results of a total of 21 concrete mixes with a high volume of fly ash and GGBFS using concrete prisms. The experimental results were also compared to the predictions by Australian Standard AS3600 (2009 and 2018 versions) and Eurocode 2. Additional tests on pastes with the same SCM content were conducted to investigate both autogenous and chemical shrinkage in relation to their time-dependent pore structure refinement assessed using the nitrogen adsorption isotherm technique. For concrete with a characteristic compressive strength lower than 50 MPa, the autogenous shrinkage of concretes with 40-60% GGBFS was significantly higher than that of reference concretes mostly due to a later increase in the autogenous shrinkage between 28 and

100 days. No clear difference in autogenous shrinkage was observed for GGBFS concretes with a compressive strength greater than 50 MPa. Autogenous shrinkage of fly ash concretes was overall equivalent to that of reference concretes. However, the drying shrinkage of concrete mixes with SCMs was significantly lower than that of reference concretes, leading to an overall reduction in total shrinkage for most of the concretes with SCMs. Some amendments to the shrinkage model in AS3600 are proposed to improve the estimation of both autogenous shrinkage and drying shrinkage of high-volume fly ash or GGBFS concretes.

The restrained ring test is conducted to determine the early age cracking performance of blended cement concrete with the same SCM content under standard conditions. An analytical model for the analysis of the restrained ring test is proposed, capturing the effect of both restrained shrinkage and tensile creep based on the age-adjusted effective modulus theory. The analytical model allows for accurately predicting the tensile stress of the restrained concrete ring based on the experimental measurements of the time-dependent development of elastic modulus, total free shrinkage, and tensile creep of concrete. A numerical finite element simulation was also successfully carried out to validate the new analytical model.

The dog-bone test was carried out to determine the tensile creep of blended cement concrete with the same SCM content under standard conditions. It was observed that the tensile creep of fly ash concretes was slightly lower than that of the reference mixtures without SCM. For GGBFS concrete, the higher the GGBFS content, the higher the tensile creep. The experimental results were compared with existing creep models and a tensile creep model was then proposed to improve the prediction for concretes with fly ash and GGBFS. The new model was calibrated only for controlled environmental conditions (23 °C and 50% RH) and was validated to analyse the development of concrete tensile stress in the restrained ring test.

The nonlinear tensile creep behaviour of ultra-high performance concrete (UHPC) is further evaluated using dog-bone specimens. The tensile creep test series were subjected to three tensile stress levels (40%, 60% and 75%) and loaded at the age of 2 and 28 days after curing. The experimental results were compared with the values calculated based on various existing prediction models (ACI-209R-92, GL 2000, AS3600-2018, and Eurocode 2). In addition, some simple analytical models from the literature for calculating nonlinear creep coefficient were also compared with the experimental values. A nonlinear tensile creep model was proposed for UHPC allowing a better prediction of the experimental results.

Finally, the thermal cracking resistance of concrete mixes with fly ash and GGBFS is investigated using a rigid cracking frame (RCF) with a computer-controlled temperature profile. RCF was used to evaluate the coupled effects of restrained shrinkage, tensile creep and temperature. The temperature profile is determined using the software ConcreteWorks at the centre point of the concrete specimen. The free shrinkage frame (FSF) and match-curing oven followed the same temperature profile used in RCF test to measure the free total deformation and time-dependent mechanical properties of concrete, respectively. Autogenous shrinkage was measured using concrete prisms. Basic tensile creep was computed according to the modified FIB 2010 model. An analytical model was proposed to calculate the autogenous shrinkage induced and thermal stress separately. The time-dependent ratio and risk coefficient to analyse the early-age cracking of concrete are also performed.

Table of Contents

List of Figures

List of Tables

CHAPTER 1: INTRODUCTION

1.1 Introduction

This chapter presents an overview of the current knowledge and highlights the research gaps in the literature. The background that elaborates on present development and existing problems of current research is introduced. The motivation for the research is discussed. Compared with traditional concrete technology, this dissertation aims to investigate the mechanical properties and time-dependent behaviour of concrete mixes with supplementary cementitious materials (SCMs) and evaluate the cracking risk at an early age. This chapter defines the objectives and scope of the research and provides a brief description of the chapters.

1.2 Background and motivation for research

In recent years, the concept of reducing carbon footprint has been raised and has become a hotspot in construction practices because about 10 billion tons of concrete are produced worldwide and utilised in construction every year [1]. The cement production process leads to the emission of a massive amount of carbon dioxide (CO_2), which contributes to climate change. The cement industry emitted approximately 5-8% of the total CO_2 emission [2]. Therefore, numerous studies have been conducted to mitigate the carbon emission from cement production by finding alternative materials to replace cement.

Supplementary cementitious materials (SCMs) such as fly ash (FA) and ground granulated blast furnace slag (GGBFS) are by-products from coal burnt power plants and iron manufacturing processes, respectively. These SCMs are commonly employed as cement replacement. According to RILEM [3], fly ash and GGBFS react with water to produce C-S-H, which contributes to the strength of concrete due to pozzolanic or hydraulic reactions,

indicating fly ash and GGBFS can be successfully used in concrete to replace cement. SCMs also provide several advantages like improving the durability [4, 5] and decreasing the heat of hydration of concrete [6]. However, the SCMs can change the fresh properties and viscoelastic behaviour of concrete such as shrinkage and creep.

Although the influence of SCMs on concrete shrinkage, creep, and mechanical properties has been investigated, the early age cracking in SCMs based concrete has not been widely evaluated. Early age cracking of concrete is a complex phenomenon governed by the degree of restraint (internal and external), total shrinkage (autogenous shrinkage and drying shrinkage), creep, thermal gradient, and mechanical properties of concrete. This thesis intends to assess the risk of early age cracking in SCMs based concrete by testing and modelling various concrete mixes.

1.3 Objective and scope

The risk of early age cracking poses a significant challenge in concrete structures, and it has rightly attracted quite considerable research. However, there are still some issues that require further attention. Based on the above brief review of the research background, some of these issues have been identified as current research gaps:

- It is known that the introduction of fly ash and GGBFS in the concrete impacts shrinkage. It is questionable whether cement shrinkage prediction models in existing standards are suitable for fly ash and GGBFS based concrete. Therefore, it is important to assess existing models and, if necessary, recalibrate them to predict SCMs concrete shrinkage correctly.
- The restrained ring test is commonly adopted to investigate the risk of early age cracking of concrete. It is known that adding SCMs like fly ash and GGBFS affects

the development of mechanical performance, leading to slow early age development of tensile strength and elastic modulus. Therefore, the cracking time of concrete mixtures with SCMs should be investigated. There is still a lack of research to fully understand the trend of restrained tensile stress development of SCMs blended concrete, the timing of concrete cracking in the restrained ring test, and the best mix design proportions against the early age cracking.

- Regarding the tensile creep behaviour of concrete, dog-bone-shaped specimens are utilised because of the relatively simple procedure required to apply a restrained stress. Unlike compressive creep, tensile creep may occur at a much smaller stress magnitude in uniaxial tension. Most prediction models in standards and specifications are established for compressive creep test. Understanding tensile creep for concrete mixes with SCMs and establishing suitable tensile creep prediction model is crucial.
- UHPC is a relatively new construction material attracting the attention of researchers. UHPC in the negative bending moment region consistently exhibits nonlinear tensile creep behaviour in the field. The nonlinear tensile creep of UHPC is more critical than that of conventional concrete. Therefore, understanding of nonlinear tensile creep behaviour of UHPC is crucial. However, both threshold stress level triggering nonlinear tensile creep and tensile creep coefficient development which depend on the restrained stress level have not been fully understood. The effect of curing age on nonlinear tensile creep also needs to be re-examined.

- The use of SCMs like GGBFS and fly ash allows to reduce the generation of heat of hydration and the low-temperature rise in concrete. However, it has been reported to also lead to a slow strength development. It is unclear how these two opposite consequences of using SCMs can affect the restrained thermal cracking in mass concrete structural element.

As mentioned above, the overall aim is to study the risk of early age cracking of the concrete, with the view of deriving concrete mixes with better resistance to early age cracking through an appropriate choice of materials and proportions. The following objectives have been set:

- Assess the shrinkage of concrete mixtures with fly ash and GGBFS. Suggest empirical models for predicting the concrete shrinkage based on experimental results.
- Use the restrained ring test results to examine the early age cracking resistance of concrete mixes with fly ash and GGBFS. Establish an analytical model capturing the combined effects of restrained shrinkage and tensile creep to predict the tensile stress development in the restrained ring test.
- Evaluate the tensile creep behaviour of SCMs based concrete using dog-bone shaped specimens. Investigate the impact of tensile creep on the risk of early age restrained shrinkage induced cracking. Develop a suitable model to predict tensile creep for SCMs based concrete.
- Investigate the nonlinear tensile creep behaviour of UHPC by conducting the tensile creep tests under different stress to strength levels and examine the effect of curing

ages. Analyse the test results and propose a suitable nonlinear tensile creep model for UHPC.

- The development of restraint thermal stresses was investigated using the rigid cracking frame (RCF). The free deformation including autogenous shrinkage and thermal deformation was measured using the free shrinkage frame (FSF). Match-curing oven was utilised to evaluate the development of mechanical properties of concrete. An analytical model to predict the restrained shrinkage and thermal contraction-induced stress is proposed.

1.4 Outline of thesis

This thesis is organised into eight main chapters. The first and last chapters are INTRODUCTION and CONCLUSIONS respectively. Each chapter starts with an introduction to present a brief overview of the contents and critical conclusions are summarised at the end of that particular chapter.

Chapter 2 presents an overall review of the existing literature. It includes the essential findings based on the experimental and analytical work and the relevant model in the international codes and standards. The literature review typically consists of several sections. The SCMs, including fly ash and GGBFS and UHPC, are first reviewed , followed by the time-dependent behaviour and mechanical properties of SCMs based concrete and UHPC. Then the experimental studies on shrinkage of concrete mixes with SCMs, including autogenous, drying, and total shrinkage, are reviewed. Subsequently, the creep behaviour of concrete is outlined, along with the development of mechanical properties of concrete. The experimental studies on factors affecting concrete cracking due to restrained shrinkage, tensile creep and thermal effects are presented. The final review

describes the test methods for assessing the shrinkage, creep, and thermal cracking of concrete.

Chapter 3 provides the experimental program relating to shrinkage, including autogenous, drying and total shrinkage of concrete mixes with fly ash and GGBFS. Autogenous shrinkage of concrete was measured using a method involving self-adhesive aluminium foil. Total shrinkage was conducted with similar procedures in AS1012.13 [7] but starting measuring shrinkage 24 hours after batching. Drying shrinkage was calculated considering the difference between total and autogenous shrinkage. Experimental results were compared to different international codes and standards, and some amendments to the shrinkage prediction model in AS3600 were proposed to improve shrinkage estimation of SCM concrete.

Chapter 4 develops an analytical model to predict the tensile stress development in concrete due to restrained shrinkage and tensile creep. The proposed analytical model was verified using both a large number of experimental restrained ring test results and finite element modelling. The proposed analytical model can incorporate the degree of restraint, free shrinkage, tensile creep coefficient and time-dependent elastic modulus of concrete to estimate the tensile stress development in the concrete ring.

Chapter 5 compares various existing creep models to the experimental results. Since existing creep models are established based on compressive creep tests, the prediction accuracy needs to be examined for the tensile creep. A tensile creep model was proposed at specific conditions, and the proposed model was validated using the test results and analytical model in Chapter 4.

Chapter 6 shows the experimental results relating to the nonlinear tensile creep behaviour of ultra-high performance concrete. Three different stress levels, including 40%, 60% and 75% applied at two different ages, including 2 days and 28 days, were performed. The test results were compared to existing creep models. A new nonlinear tensile creep model was also introduced.

Chapter 7 is related to the risk of thermal cracking test conducted on concrete mixes with fly ash and GGBFS using the rigid cracking frame. The temperature profile was obtained using the software ConcreteWorks and applied to all relevant tests, including the free shrinkage frame test and mechanical properties determination. Autogenous shrinkage test results were also used as per Chapter 3. An analytical model was also proposed to calculate the restrained thermal stress and restrained autogenous shrinkage induced stress.

Chapter 8 summarises the key findings and conclusions based on the work done in this dissertation, followed by suggestions and recommendations for possible further research related to the scope of this dissertation.

1.5 List of publications

During the four years of my PhD life, the following journal papers have been published. They are direct outputs of my research towards the writing of this thesis. The details of the papers are:

Y. Zhang, S. Afroz, Q.D. Nguyen, T. Kim, J. Eisenträger, A. Castel and T. Xu, "Analytical Model Predicting the Concrete Tensile Stress Development in the Restrained Shrinkage Ring Test", *Construction and Building Materials*, vol. 307, pp124930, 2021.

Y. Zhang, S. Afroz, Q.D. Nguyen, T. Kim, D. Nguyen, A. Castel, J. Nairn and R.I. Gilbert, "Autogenous Shrinkage of Fly Ash and Ground Granulated Blast Furnace Slag Concrete," *Magazine of Concrete Research*, 2022, DOI: 10.1680/jmacr.21.00300.

Y. Zhang, S. Afroz, Q.D. Nguyen, T. Kim, A. Castel and T. Xu, "Modeling Blended Cement Concrete Tensile Creep for Standard Ring Test Application", *Structural Concrete*, 2022, DOI: 10.1002/suco.202200304.

CHAPTER 2: LITERATURE REVIEW

2.1 Introduction

This chapter reviews the existing studies about early age concrete cracking, focusing on finding ways to mitigate cracking and test methods to determine the viscoelastic deformation and restrained shrinkage induced stress and thermal stresses in concrete. Performance of sustainable concrete, including supplementary cementitious materials (SCMs) and ultra-high performance concrete (UHPC), is summarised in Section 2.2. The viscoelastic behaviour of concrete, such as shrinkage, creep and thermal deformation and the development of mechanical properties, are reviewed in Section 2.3. Section 2.4 summarises the past and current studies on factors that affect the risk of cracking. The test methods for determining shrinkage, creep, and thermal cracking of concrete are described in Section 2.5. Section 2.6 provides a summary of the review in this dissertation.

2.2 Sustainable concrete

2.2.1 Supplementary cementitious materials (SCMs)

2.2.1.1 Fly ash

Fly ash is one of the most commonly used SCMs, and it is the industrial by-product of coal burning power plants generated during coal combustion. In the past few decades, fly ash has been re-utilised as raw materials in the construction industry. Fly ash is generally identified into two categories, such as class F (low calcium ashes) and class C (high calcium ashes), based on calcium content. The typical micromorphology observations of fly ash particles are shown in Figure 2-1.

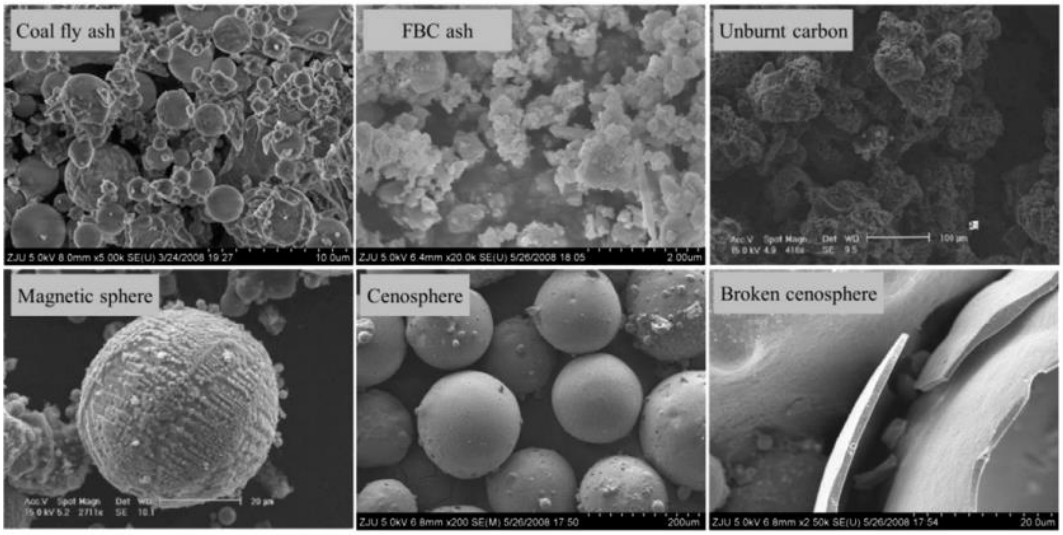

Figure 2 - 1: SEM images of fly ash [8].

It is beneficial to utilise fly ash to achieve economic and environmental objectives. In addition, fly ash has extensively been investigated in concrete [9, 10, 11]. The introduction of fly ash to concrete has several advantages. For instance, the surface area of fly ash is higher than cement which can reduce the bleeding of water and the spherical morphology enhances its workability [12]. Fly ash can significantly reduce the early age heat of hydration compared to cement systems due to the dilution effect, leading to a lower thermal cracking risk [13, 14]. Dockter [15] stated that the expansion caused by the alkali-silica reaction could be mitigated in fly ash concrete. On the other hand, Ling et al. [16] reported that the development of strength for fly ash concrete is slower than that of normal concrete. According to the work done by Naik et al. [17], fly ash can also decrease the permeability and porosity of concrete.

2.2.1.2 Ground granulated blast furnace slag (GGBFS)

Ground granulated blast furnace slag (GGBFS) is a by-product of the iron manufacturing process. It can replace a high cement content as high as 70% in concrete production [18]. GGBFS offers many benefits, such as reducing the heat of hydration, improving long-term

compressive strength and durability, and decreasing the adiabatic temperature rise of concrete [19, 20]. Gao et al. [21] reported that the workability, slump and setting time were increased when GGBFS was introduced. Li and Ding [22] stated that the GGBFS could retard cement hydration because the rate of GGBFS hydration reaction is slower than cement, leading to an extended setting time. Khatib and Hibbert [23] studied that the long-term strength of GGBFS concrete is improved by about 20% compared to that of control concrete.

However, GGBFS can sometimes negatively affect the mechanical properties of concrete at early age. A typical SEM image of GGBFS is shown in Figure 2-2. In work by Oner and Akyuz [24], it is shown that the early strength of GGBFS concrete is lower than that of OPC concrete due to the slow hydraulic reaction.

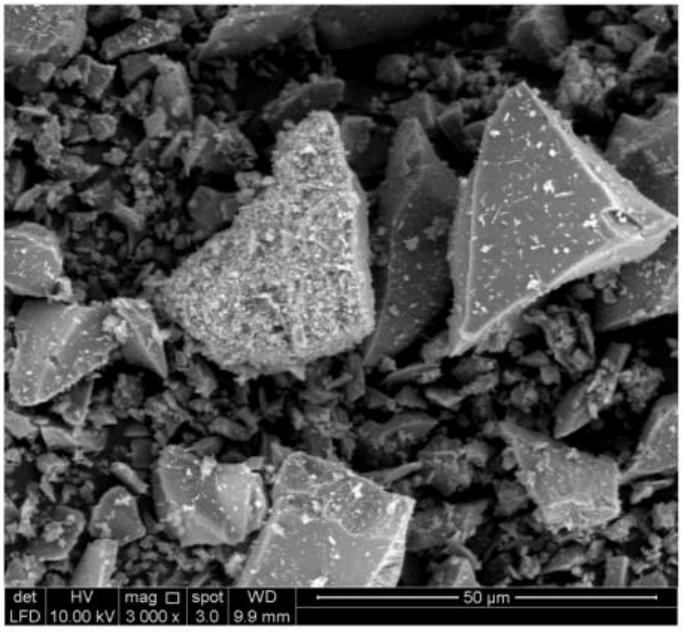

Figure 2 - 2: SEM image of GGBFS [25].

2.2.2 Ultra-high performance concrete (UHPC)

Ultra-high performance concrete (UHPC) is a relatively construction material with excellent mechanical properties compared to conventional concrete. UHPC typically requires a very low water to binder ratio of approximately 0.15-0.25 and a high content of fine particles such as silica fume and finely grounded quartz sand and fibres [26]. A typical image of the microstructure of UHPC is presented in Figure 2-3. A very dense structure in the hardened matrix with only a few pores can be observed. Therefore, UHPC is more durable than traditional concrete. For instance, Li et al. [27] stated that the UHPC matrix is impermeable to CO_2, chloride, sulphate, etc., resulting in excellent durability. Moreover, Wille et al. [28] reported that the compressive strength of UHPC can reach 120 MPa under standard curing, which illustrates a very high mechanical property of UHPC. Granger et al. [29] demonstrated that the self-healing ability of UHPC is superior because of a large amount of unhydrated cement particles.

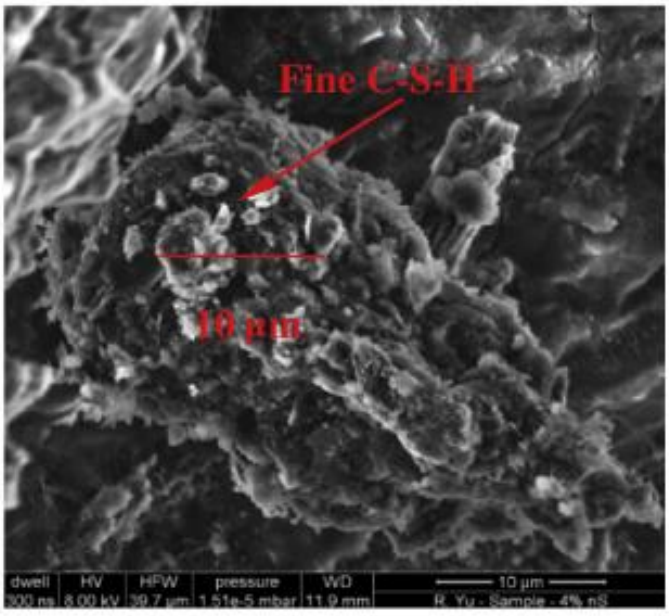

Figure 2 - 3: SEM image of UHPC [30].

However, the materials used in UHPC are much more expensive than conventional concrete. The current application of the UHPC is mostly in connections and joints of bridges. Another drawback of UHPC is that the allowable volume of each batch was restricted. For example, a pan mixer with a maximum capacity of 0.5 m^3, but the allowable batch size was restricted to 0.1 m^3, leading to lower construction efficiency. As such, UHPC has to be used strategically to achieve both economic and engineering objectives.

2.3 Volume changes and restraint stresses in concrete

The total free deformation of concrete that may cause cracking contributes to different deformation components, including autogenous shrinkage, thermal effects (contraction or expansion) and drying shrinkage. This can be expressed as in Eq. (2-1) below:

$$\varepsilon_{tot} = \varepsilon_{au} + \varepsilon_{d} + \varepsilon_{th} \tag{2-1}$$

where ε_{tot} is the total unrestrained strain; ε_{au} is the autogenous shrinkage; ε_{d} is the drying shrinkage strain; and ε_{th} is the thermal strain.

Drying shrinkage is caused by physical loss of moisture from concrete to the surrounding environment, while autogenous shrinkage is a macroscopic volume change occurring after initial setting in cases of restricted supply of outside water. On the other hand, thermal strain results from changes in concrete temperature due to heat from cement hydration and changes in the ambient temperature. If the strain given in Eq. (2-1) is restrained, either fully or partially, tensile creep also occurs because of the sustained tensile stress caused by the degree of restraint. Meanwhile, the tensile stresses would result in cracking once the tensile strength of concrete is reached.

2.3.1 Autogenous shrinkage

Autogenous shrinkage is the time-dependent decrease in the volume of concrete due to internal consumption of moisture by hydration reactions. The main contribution to autogenous shrinkage is self-desiccation, the reduction in internal relative humidity of concrete as a consequence of ongoing hydration reactions [31]. Autogenous shrinkage is considered as a basic component of shrinkage because volume reduction occurs without the loss of moisture in concrete to the environment.

According to Neville & Brooks [32], autogenous shrinkage is relatively low in normal concretes with w/b above 0.4 compared to concretes having w/b lower than 0.4. In normal strength concrete, autogenous shrinkage is in the range of 50 to 150 με, while in high strength concrete, it can be much higher, reaching the same order as drying shrinkage. In work by Kim et al. [33], they studied the relationship between hydration heat and autogenous shrinkage for high-strength mass concrete. In their study, it was found that the autogenous shrinkage of concrete increased with the increase of mass concrete specimen size and decreased when the concrete contains heat-resistant admixtures such as fly ash and GGBFS. Even in samples with the same mixing proportions, it was noted that the autogenous shrinkage became higher with the increasing of specimen inner temperature.

Additionally, Lee et al. [34] reported that fly ash could effectively decrease autogenous shrinkage of high-performance concrete. Figure 2-4 shows that the higher the fly ash replacement level, the lower the autogenous shrinkage. In a work by Termkhajornkit et al. [35], the relationship between the degree of hydration of fly ash and autogenous shrinkage was proposed. It was found that fly ash affects autogenous shrinkage at an early age but only marginally influences the long term autogenous shrinkage.

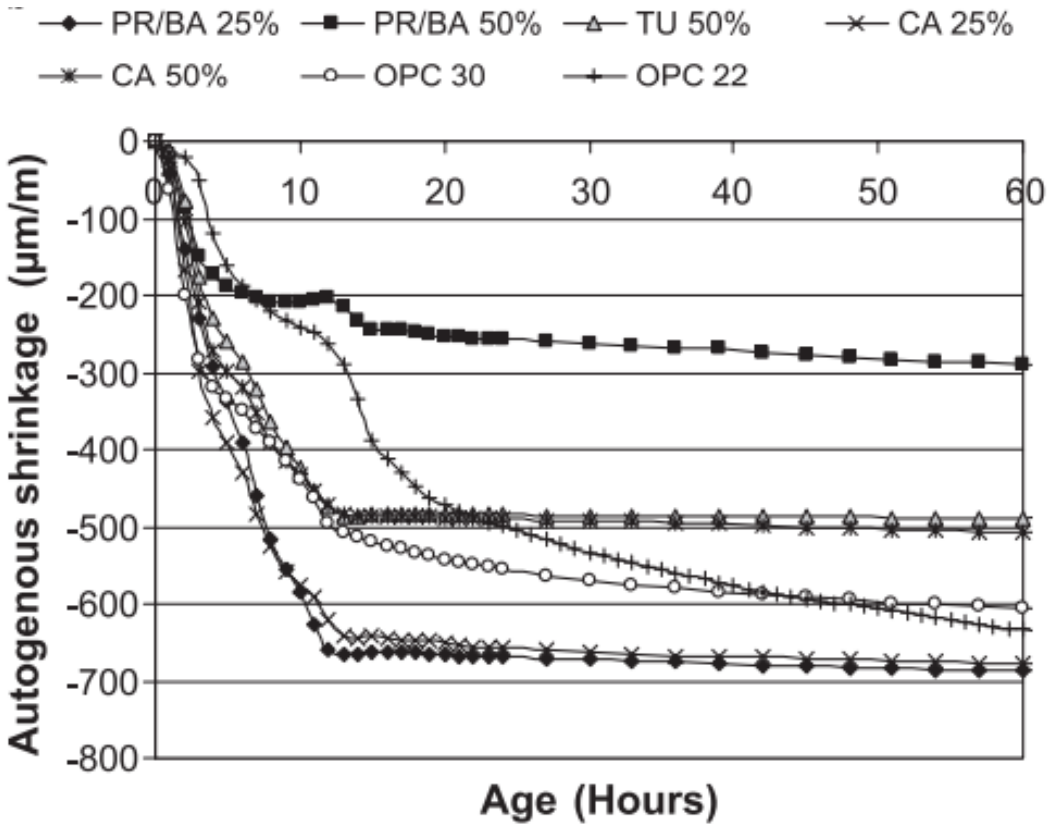

Figure 2 - 4: Effect of fly ash on autogenous shrinkage [35].

By contrast, GGBFS has an opposite effect on autogenous shrinkage. According to Zhao et al. [36], the inclusion of GGBFS in high-performance concrete can lead to a great increase in autogenous shrinkage. A similar observation was reported by Lim and Wee [37], who found that concrete mixes with GGBFS exhibited greater autogenous shrinkage and faster compressive strength development. Wei et al. [38] stated that GGBFS could reduce the early age shrinkage because the cement hydration is faster than its potential hydraulic and pozzolanic reactions, but the long term autogenous shrinkage of GGBFS concrete is greater than that of the control concrete because of the continuous reactions of GGBFS, as presented in Figure 2-5.

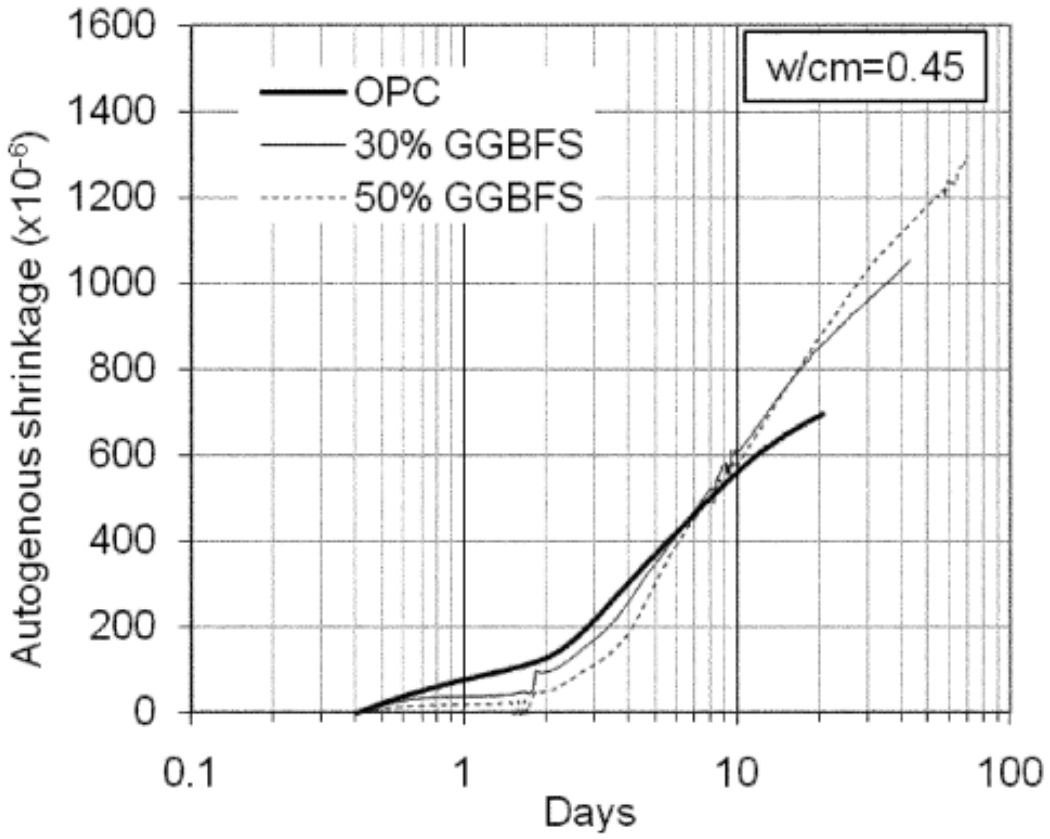

Figure 2 - 5: Effect of GGBFS on autogenous shrinkage [38].

On the other hand, the development of autogenous shrinkage of UHPC leads to a very high values. According to Xie et al. [39], the autogenous shrinkage of UHPC was about 600 με after 90 days, which is very high compared to that of conventional concrete. They also demonstrated that the use of shrinkage reducing admixture and replacing the water with crushed ice could effectively control the autogenous shrinkage, as depicted in Figure 2-6.

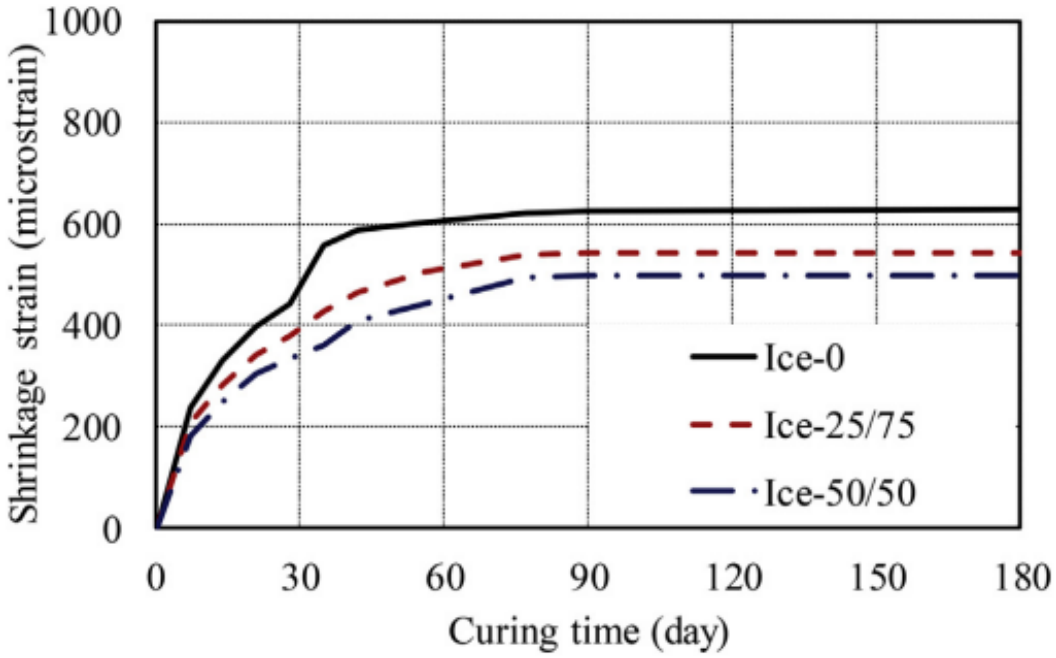

Figure 2 - 6: Effect of crushed ice dosage on autogenous shrinkage of UHPC [39].

2.3.2 Drying shrinkage

Drying shrinkage is important in concrete elements with a large surface-area-to-volume ratio, such as concrete pavements, overlays, and bridge decks. Drying shrinkage occurs when moisture is lost from concrete to the environment. The rate at which moisture is lost is fairly slow, and the strain response is time dependent. There is considerable literature regarding the drying shrinkage of concrete mixes with fly ash and GGBFS. For instance, a high volume of fly ash as a replacement for cement led to lower drying shrinkage [40]. As shown in Figure 2-7, the drying shrinkage of concrete mixes with 40% fly ash was about 20% lower than that of reference concrete after 180 days [40]. Similar results were reported by Seo et al. [41]. They also stated that the decreased drying shrinkage is beneficial in reducing the cracking risk for concrete under restrained conditions.

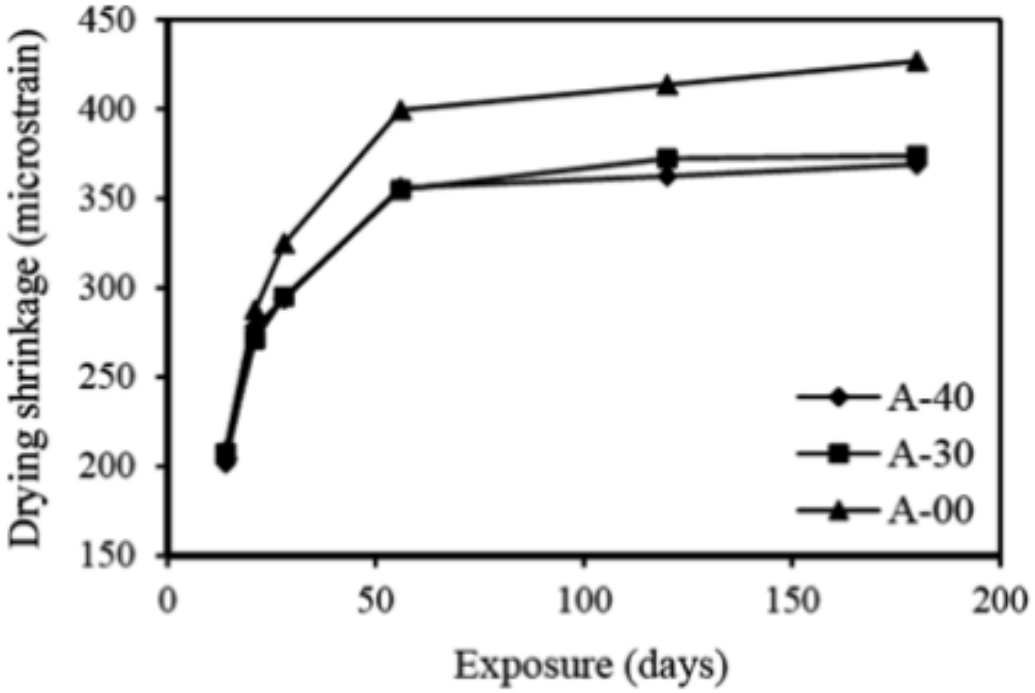

Figure 2 - 7: Effect of fly ash on drying shrinkage [40].

On the other hand, the literature reports contradictory views on the drying shrinkage of concrete mixes with GGBFS. For example, Yuan et al. [42] reported that the drying shrinkage of GGBFS decreased compared to the control system. It was observed that the reduction of drying shrinkage increased as the cement replacement level with GGBFS increased. While Shariq et al. [43] stated that a higher drying shrinkage was found with the incorporation of GGBFS as shown in Figure 2-8. In work by Saluja et al. [44], the drying shrinkage of GGBFS concrete subjected to various temperature exposures was examined. The results showed that drying shrinkage is directly associated with temperature conditions because the temperature has an impact on the loss of water. They also found that the addition of GGBFS led to marginally higher drying shrinkage.

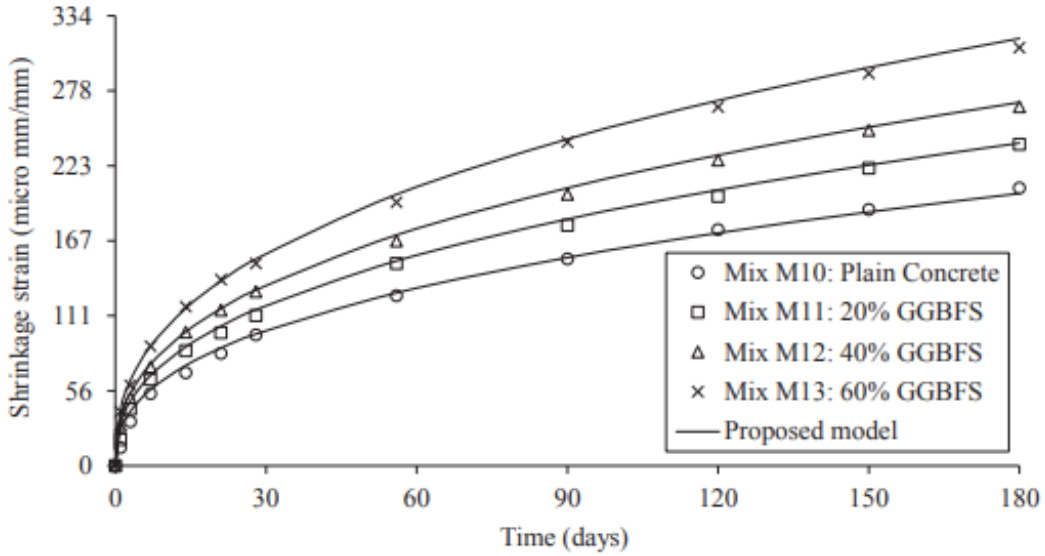

Figure 2 - 8: Effect of GGBFS on drying shrinkage of concrete [43].

In unsealed concrete surfaces, the rate of moisture loss is highly dependent on environmental factors such as wind, relative humidity, solar radiation, and ambient temperature. For mass concrete elements susceptible to early age thermal and autogenous deformations, drying shrinkage strains are usually less significant within the few days following concrete casting. Overall, proper curing and good construction practices are essential to minimize the effects of restrained drying shrinkage.

2.3.3 Creep

Creep is a critical time-dependent behaviour of concrete that can affect the performance of concrete structures. Creep may lead to various effects, for instance, the increase in the long-term deformation of concrete, redistribution of the internal stress, force and bending moment, and even failure of concrete structures [32, 45]. When concrete shrinkage is restrained, tensile creep occurs, leading to tensile stress relaxation, which has to be considered in calculating the tensile stress. Creep effects are more crucial at an early age

because concrete tensile strength is low, which results in a higher risk of concrete cracking [46].

The creep behaviour of fly ash and GGBFS based concrete has been widely investigated. For example, Klausen et al. [47] reported that the specific creep of fly ash concrete increased slightly over time with an increasing amount of fly ash in concrete. They also found that the creep behaviour was similarly in compression and tension. Zhao et al. [48] conducted creep tests on fly ash concrete under different curing temperatures. They found that the quantity and microstructure of C-S-H gel is the main reason contributing to the creep characteristics of fly ash concrete. In work by Wang et al. [49], the creep behaviour of high strength fly ash concrete was studied. The results were also compared to existing model predictions. They proposed an influencing factor for fly ash and recommended using GL 2000 model to predict the tensile creep of fly ash concrete. In addition, Wei and Hansen [50] assessed the effect of curing temperature and GGBFS on the tensile creep of concrete. They stated that the development of strain and stress is faster and greater when subjected to a higher curing temperature. The effect of GGBFS was not significantly for the test duration of 12 days [50]. While Khan et al. [51] revealed that the tensile creep of GGBFS concrete is much higher than that of control concrete at an early age. Similar results were obtained by Shariq et al. [43]. A modification factor was proposed for incorporating the effect of GGBFS in existing models.

Zhu et al. [52] assessed the influence of creep on restrained shrinkage induced stresses in UHPC. They conducted tests under normal curing and high temperature steam curing. They reported that increasing the creep coefficient can decrease the restrained shrinkage induced stresses. Xu et al. [53] also studied the creep of UHPC and found that the steel fibres can

remarkably reduce the creep coefficient compared to those without steel fibres. They stated that the 1% and 2% steel fibres decreased the creep coefficient by 25.4% and 13.4% respectively after 180 days in comparison to control mixes. In the work by Garas et al. [54], the effect of thermal treatment on the creep of UHPC was studied in tension and compression. They reported that the thermal treatment increased the tensile strength, and the tensile creep was found to be decreased. They demonstrated that the phenomenon of tensile creep in UHPC is different from compressive creep according to microstructural refinements.

2.3.4 Thermal effects

In mass concrete elements [55], the heat generated by cement hydration and the relatively poor heat dissipation conditions cause the concrete temperature to rise substantially within a few days after placement. Figure 2-9 shows the typical temperature history from two mass concrete structures, each measuring 2 m × 3 m × 5 m, made with Type IS cement and w/b = 0.385 [56].

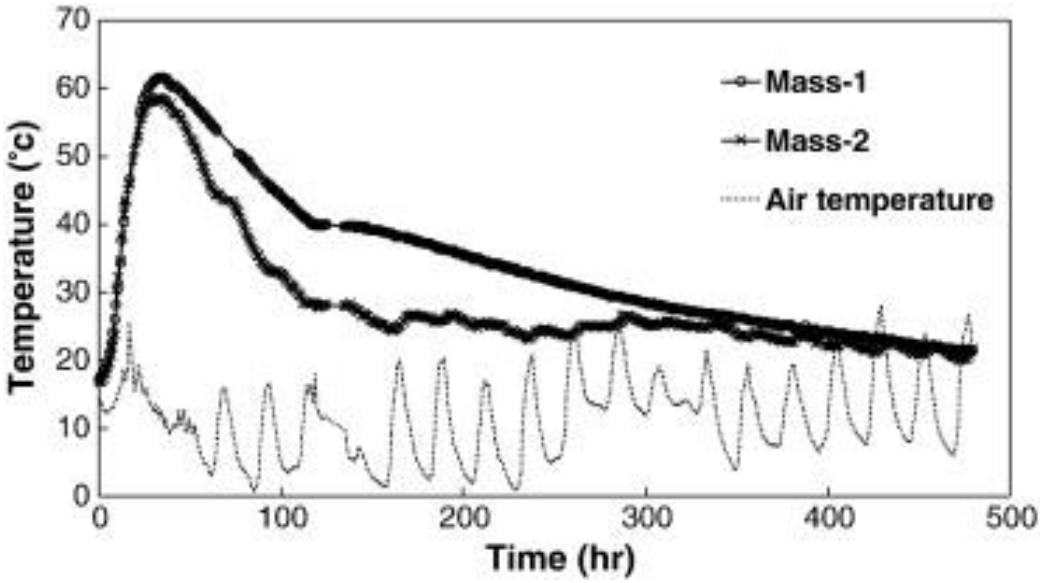

Figure 2 - 9: Typical temperature history in the interior of a mass concrete element [56].

As the hydration of cement proceeds, the heat produced increases the internal temperature of concrete and induces differential thermal gradients between the interior and the surface of the concrete element, owing to the low thermal conductivity of concrete [57]. These thermal gradients generate tensile stress near the surface, which may lead to surface cracking, while the interior of the element will be subjected to compressive stress. During the cooling phase to ambient temperature, the interior will be subjected to tensile stress resulting from both thermal gradients and external restraint. This may lead to the formation of through cracks if the tensile stress exceeds the tensile strength of concrete. Figure 2-10 shows the mechanisms of thermally induced cracking in mass concrete.

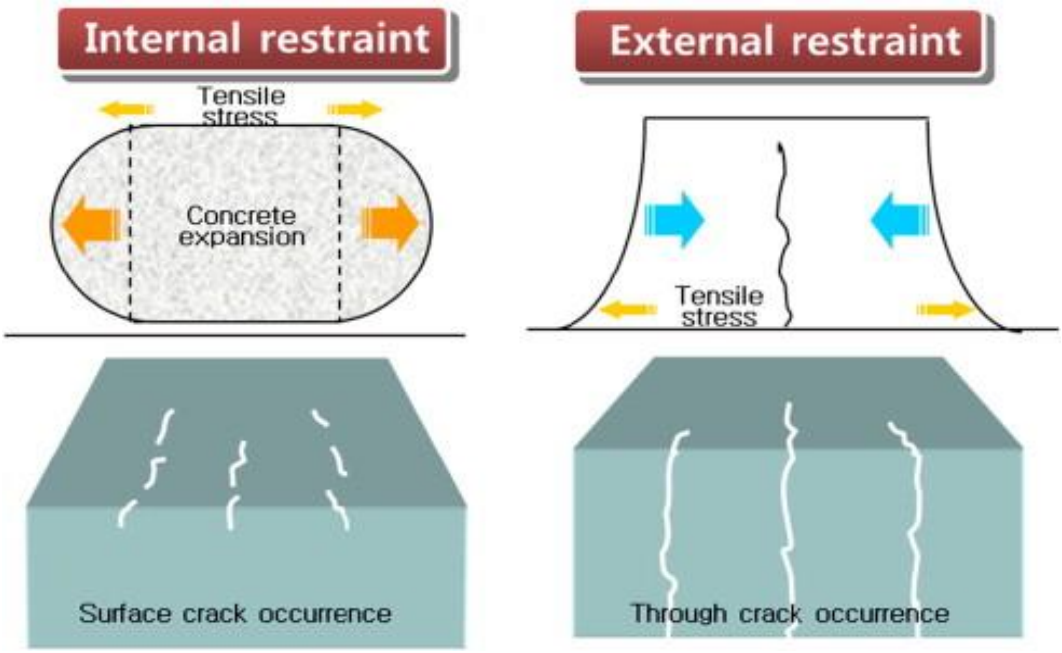

Figure 2 - 10: Schematic showing thermal crack occurrence in mass concrete [56].

The amount of heat generation is determined by the amount and type of cementitious binder used and the water-to-binder ratio (w/b). Thermal strain developed due to the temperature change depends upon the coefficient of thermal expansion (CTE) of concrete. Thus, the

CTE of concrete provides a means of quantifying thermal strain and accurate thermal stress determination.

As a preventative measure, the CTE is used to determine the allowable maximum temperature difference between the interior and the surface of a mass concrete element that can be tolerated without cracking. The lower the CTE of concrete, the higher the allowable temperature difference without cracking. To avoid cracking, the allowable temperature difference can be calculated from Eq. (2-2) [58]:

$$\Delta T_{max} = \frac{\varepsilon_{ctu}}{KR\alpha_c} \tag{2-2}$$

where ΔT_{max} is the maximum temperature change in the concrete (°C); ε_{ctu} is the tensile strain capacity of the concrete under short term loading m/m); K is the modification factor that considers sustained loading and creep (unitless); α_c is the CTE of the concrete (m/m/°C); and R is the restraint factor (unitless). However, it should be noted that Eq. (2-2) is based on several assumptions including zero deformation due to other mechanisms such as autogenous and drying shrinkage.

The CTE of hardening concrete is a function of various factors, including the amount and type of cementitious binder, w/b, the type of aggregate, the age of the concrete, temperature variations and the moisture content [59]. The CTE of concrete can be computed from its components weighted average, and since concrete is made up of up to 60 - 80% aggregates, its CTE is controlled primarily by the CTE of the aggregate used. Assuming a CTE of 12×10^{-6} and ε_{ctu} of 70×10^{-6}, for concrete made with a gravel aggregate, with restraint factor R = 0.36 and creep factor K = 0.8, Eq. (2-2) gives the allowable maximum temperature difference of 20.3 °C. For concrete made with a Limestone aggregate, with $\alpha_c = 8 \times 10^{-6}$, $\varepsilon_{ctu} = 90 \times 10^{-6}$, R = 0.36 and creep factor K = 0.8 [58], Eq. (2-2) gives the allowable

maximum temperature difference of 39.1 °C, which is almost twice that of the concrete made with gravel aggregate.

Kada et al. [60] observed that the CTE of hardening concrete changes substantially during the first few hours following concrete casting (Figure 2-11). Therefore, when evaluating early age thermal stress behaviour in concrete, it is unreasonable to rely on a constant CTE value computed for hardened mature concrete. Failure to account for the changes in CTE at an early age may result in underestimation of the thermal stress development.

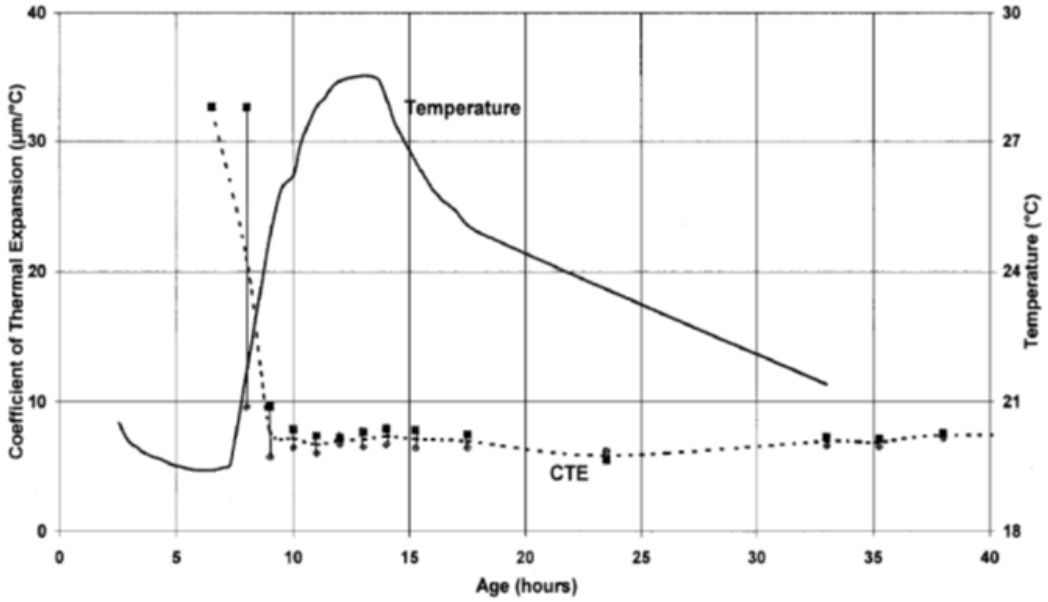

Figure 2 - 11: Evolution of CTE for concrete with w/c = 0.35 and a Limestone aggregate [60].

Li et al. [61] utilised a newly developed temperature stress testing machine (TSTM) to evaluate the early age evolution of CTE of two concrete mixtures with w/b ratios of 0.35 and 0.42. As shown in Figure 2-12, both measured CTE showed a rising trend. The increase in CTE could result from the decrease in moisture content of cement paste induced cement hydration. They also found that the measured CTE of the concrete mixture with a w/b ratio of 0.35 appeared to be slightly higher than that of concrete with a w/b ratio of 0.42.

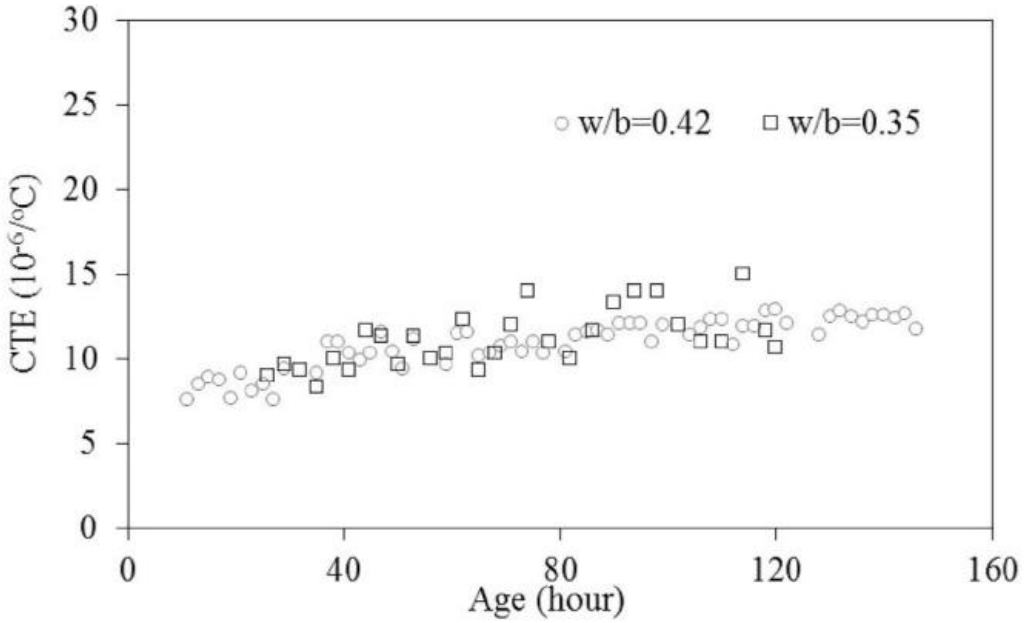

Figure 2 - 12: Evolution of CTE at early ages [61].

2.3.5 Effects of the development of mechanical properties on restrained shrinkage induced stress

The generation of tensile stress due to the restrained shrinkage does not only depend on the deformations given in Eq. (2-1) but also on the development of the mechanical properties, including elastic modulus, tensile relaxation characteristics (creep effects), tensile strength and the degree of restraint. Furthermore, for mass concrete undergoing a considerable rise in temperature due to the heat from cement hydration, the concrete mechanical properties, especially the elastic modulus, develop very fast during the first 24 to 36 hours after concrete placement [62]. In fact, studies [63, 64] have shown that the increase in modulus of elasticity is much quicker than that of tensile strength during this time. This implies that the increase in tensile stress will also be very high.

However, studies of early age stress development in concrete have also shown the significance of concrete viscoelastic behaviour, resulting in considerable stress relaxation.

It has been reported that tensile relaxation can relieve from 50% to 60% of the stress that is supposed to be produced considering only shrinkage without relaxation [64, 65].

The above discussion highlights the need to consider the overall behaviour of concrete when studying the development of restrained shrinkage induced tensile stresses including free shrinkage, tensile creep, temperature rise and cracking sensitivity. In particular, the development of mechanical properties should be done under similar temperature history as that of the core part of the mass concrete element.

2.4 Factors affecting concrete cracking

2.4.1 Degree of restraint

The degree of restraint or restraint factor [55, 66, 67] determines how much of the free deformations (Eq. (2-1)) of hardening concrete are converted into restraint stress. It is expressed as a percentage of full restraint, i.e., 100% indicates that all deformations are suppressed while 0% restraint indicates free uninhibited movement. For example, mass concrete structural elements are subjected to both internal and external restraint. Therefore, the stress that arises is a sum of the individual stress components resulting from internal and external restraint. Internal restraint stress results from non-uniform temperature distribution within the concrete section. External restraint stress is produced when the expansion and contraction of an element are obstructed by adjacent structures, foundations and subsoil. The degree of external restraint depends primarily on the relative dimensions and elastic modulus of the concrete as well as that of the restraining element.

Kawabata et al. [68] evaluated the effect of a degree of restraint on expansive pressure and cracking patterns due to delayed ettringite formation in concrete. They found that expansion behaviour was strongly related to the degree of restraint. Moreover, the

distribution of surface cracks of concrete was significantly affected by the degree of restraint. Zych [69] investigated the degree of external restraint of wall segments in reinforced concrete. He also proposed an analytical model to calculate the distribution of restraint degree of wall segments in rectangular reinforced concrete tanks. Knoppik-Wróbel and Klemczak [70] also researched the early age stresses development due to restrained shrinkage and thermal effects. They proposed a numerical model to take into account casting and interaction between early age structure and founding soil, providing an accurate prediction of the degree of restraint for modelling early age concrete stresses and structural behaviour of concrete walls.

2.4.2 Influence of concrete constituents

SCMs such as fly ash and GGBFS can adversely affect the mechanical properties of concrete. As such, the early age cracking of concrete is significantly affected by the type of binder. Altoubat et al. [71] conducted the restrained shrinkage test to assess the effect of fly ash on early age cracking. The result showed that curing condition (air curing, water curing for 3 days and water curing for 7 days) can influence the cracking potential. Allowing 3 or 7 days of water curing significantly decreased the early age cracking than air curing. Moreover, fly ash improved the cracking resistance and relaxation behaviour compared to the control mix. Zhao et al. [72] used very high fly ash content (80% fly ash) and normal content (35% fly ash) in concrete to evaluate the early age cracking. They found concrete with very high fly ash content had approximately the same restrained stress development as normal content fly ash concrete. For GGBFS concrete, Shen et al. [73] stated that concrete containing 50% GGBFS can reduce the restrained strain leading to higher cracking resistance than the control mix.

The temperature history in mass concrete elements depends upon the type of binder used. Studies [74, 75, 33, 76, 77] have shown that replacing ASTM Type I cement with Type II or Type IV cement, and by partial substitution of Portland cement with pozzolans can significantly reduce the adiabatic temperature rise in concrete (Figure 2-13). Also, increasing the w/b leads to a reduction in the amount of heat of hydration and slows down the kinetics of its release in the early stages of hydration.

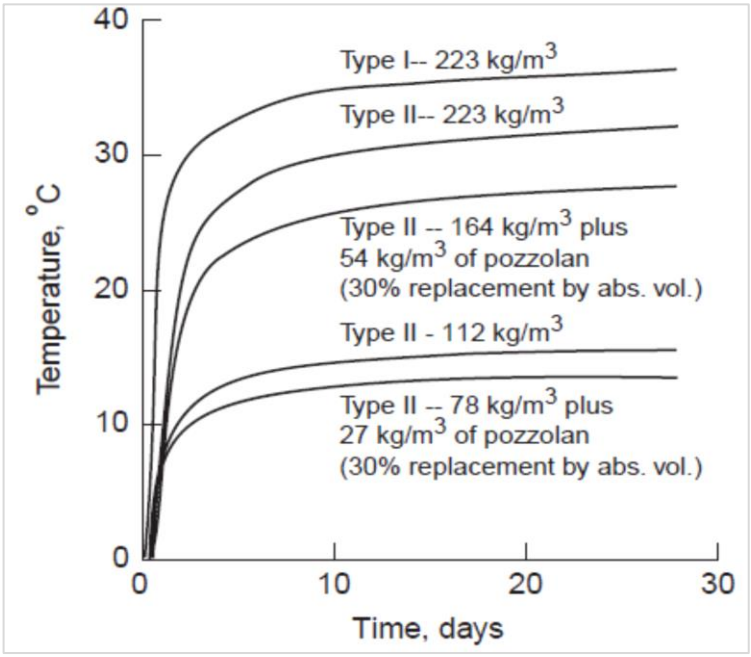

Figure 2 - 13: Effect of cement and pozzolan contents on temperature in concrete [74].

Batog and Giergiczny [76] studied the effect of blending CEM I 42.5R cement with siliceous fly ash and GGBFS on the heat of hydration and concrete hardening temperature. The CEM I cement was replaced in the following ratios: 10%, 30%, 50% and 70% by mass. The results of their study are given in Figure 2-14. It was found that, with the increasing amount of either fly ash or GGBFS in the cement composition, the rate and amount of heat generated decreased, and the effect was most pronounced in mixes made with fly ash. They also found that the maximum temperature of the temperature profile, measured at the centre

of insulated 400 mm × 400 mm × 400 mm concrete blocks, meant to simulate mass concrete, was reduced with the addition of fly ash and GGBFS. Reductions of 11 – 15°C and 15 - 17°C were recorded for fly ash and GGBFS, respectively.

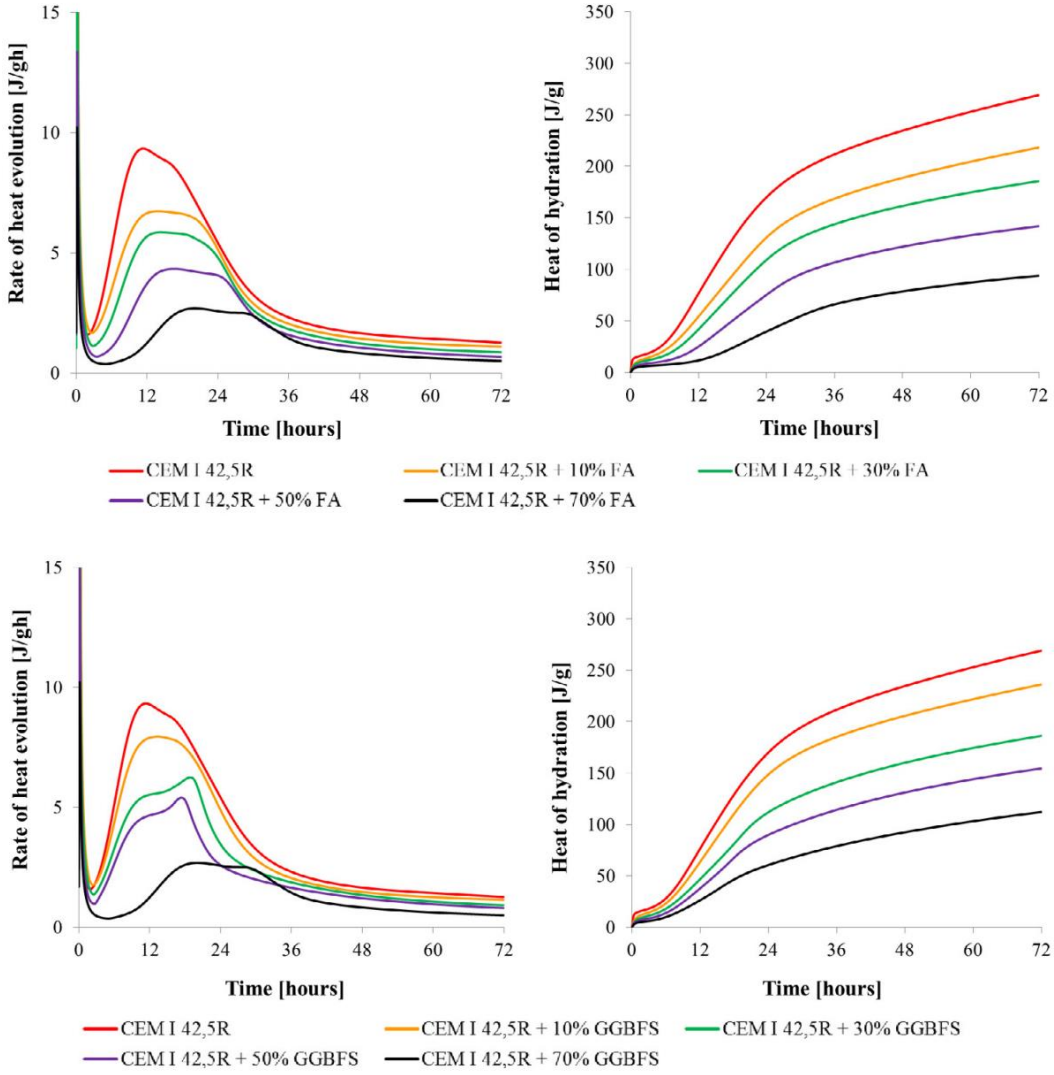

Figure 2 - 14: Effect of siliceous fly ash (FA) and GGBFS on the heat of hydration and the rate of its release under isothermal conditions (20°C, w/c = 0.5) [76].

Although the use of supplementary cementitious materials may lead to a reduction in temperature rise in mass concrete elements, it has to be stated that cracking may still occur. According to Springenschmid and Breitenbücher [62], this is because the elastic modulus

develops too slowly in the early hardening phase, i.e., the first 12 hours. Therefore, no relatively high compressive (pre-) stresses develop during this time to counter the tensile stresses that develop during the cooling phase. In addition, the low rate of hydration means low tensile strength to counter the thermal stresses.

It follows from the above discussion that more research is needed on how the use of pozzolans and other supplementary cementitious materials will affect not just the total shrinkage but also the development of mechanical properties such as elastic modulus, strength, and creep coefficient, and the heat generation for mass concrete.

2.5 Test method for determining viscoelastic deformation and restrained shrinkage induced stress of concrete

2.5.1 Shrinkage test

According to Australian Standard AS1012.13 [78], the concrete specimens are cured under standard curing conditions in lime water and the drying shrinkage measurement starts after 7 days. This concrete shrinkage test method allows for measuring drying shrinkage, but it actually measures the drying shrinkage plus that part of autogenous shrinkage after 7 days. Therefore, alternative test methods are suggested to obtain the drying shrinkage by using the total shrinkage minus the autogenous shrinkage [79]. For this purpose, in this study, total shrinkage is measured after demoulding at day 1 instead of 7-day curing. While autogenous shrinkage is measured at the same time as total shrinkage but wrapped with aluminium foil. These test methods can also be found in published studies [80, 81].

2.5.2 Restrained ring test

The restrained ring test is one of the most commonly used methods to investigate the cracking potential of concrete. The ring test can simulate the restrained condition of

concrete subjected to time-dependent shrinkage. The ring test is composed of an inner ring and a surrounding concrete ring. Thus, the shrinkage of the concrete ring is restrained by the inner steel ring. Hossain and Weiss [152] proposed a method to assess both residual stress development and stress relaxation using the restrained ring test.

Several previous works have studied the effect of tensile creep of concrete on the early age restrained cracking. Khan et al. [66] investigated the effect of the tensile creep on the early age cracking using the restrained ring test. They concluded that the creep behaviour should be considered to properly assess the stress relaxation in the restrained ring test. Liang and Wei [82] investigated the early age basic creep of high strength concrete using the restrained ring test. The restrained ring test was under biaxial tensile-compressive stress condition. They found the stress condition is a key factor that affects the creep properties of high strength concrete. As such, they conducted numerical analysis to calculate the concrete creep and the results were applied to the restrained stress calculation and crack risk assessment of high strength concrete structures. Ozawa et al. [83] conducted the restrained ring test to evaluate the restrained stress of high performance concrete. The stress was calculated based on the thin-wall cylinder model theory. They also determined the spalling initiation point and the spalling depth. More details of the restrained ring test and the analytical calculations of the stresses in the restrained ring test can be found in Chapter 4.

2.5.3 Tensile creep test

A lot of effort has been directed at developing methods for determining the tensile creep of concrete. These test methods include the Temperature Stress Testing Machine (TSTM) [84], dog-bone shaped specimens [85], restrained ring test [73], and direct tensile creep test [86]. Dabarera et al. [84] conducted the tensile creep test at an early age using Temperature

Stress Testing Machine (TSTM). Cheng et al. [85] utilised the dog-bone shaped specimens to determine the tensile creep and ageing coefficient for geopolymer concrete. Shen et al. reported that the GGBFS could increase stress relaxation due to higher tensile creep using the restrained ring test [73]. While Khan et al. used internally restrained specimens to characterise the tensile creep behaviour [87]. Ni et al. adapted the direct tensile creep test to concrete prisms [86].

2.5.4 Thermal cracking test

Due to the complex interaction of the different factors such as thermal strain, elastic modulus, degree of restraint, relaxation, etc., thermal and other restraint stresses in early age hardening concrete cannot be determined by the use of traditional methods based solely on the measurement of concrete deformations. The rigid cracking frame (RCF) test can give a global measure of thermal stresses by inherently considering the influence of many parameters. The RCF is made up of a concrete specimen held by two mild steel crossheads, which are fixed in place by two Invar sidebars, as shown in Figure 2-15.

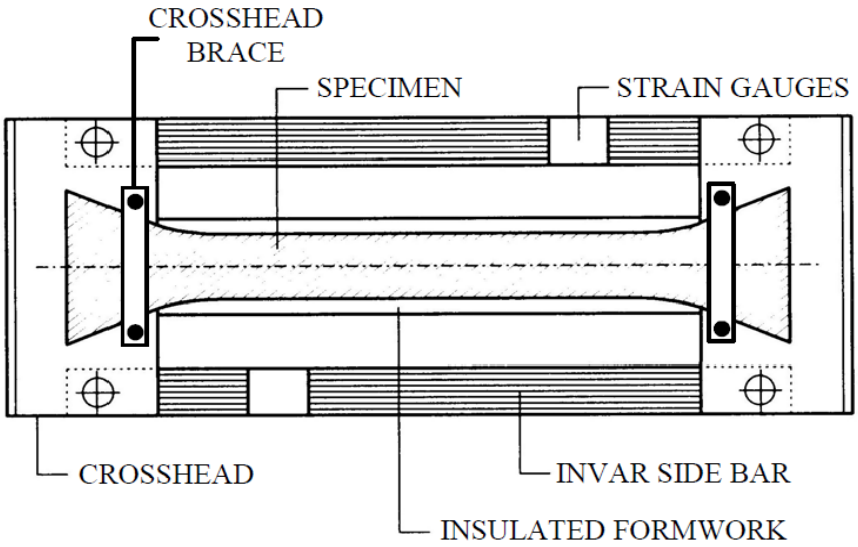

Figure 2 - 15: Schematic of the rigid cracking frame [88].

According to Breitenbücher [88], the behaviour of concrete in the rigid cracking frame can be described in five stages (Figure 2-16). Stage I, during which the temperature of the fresh concrete remains constant, starts immediately after concrete placement. During Stage II, with the onset of hydration and proceeding heat development, the concrete still behaves plastically and thus, there are no compressive stresses. Stage III begins once the final setting has been reached and the concrete is gaining strength. Compressive stresses are generated because of an increase in temperature due to continued hydration. The relatively high degree of relaxation in the young concrete produces maximum compressive stress that occurs a few hours before the concrete reaches its maximum temperature. During Stage IV, the remaining compressive stresses are rapidly reduced as the temperature continues to decrease. This is as a result of an increase in the elastic modulus as well as the high relaxation of the young concrete. The specimen then reaches a stress-free state at a temperature called the zero-stress temperature (T_{zs}), which is above the concrete placement temperature but a few degrees below its maximum. In Stage V, tensile stresses are generated as the concrete temperature decreases further. Eventually, cracking occurs when these stresses exceed the concrete tensile strength at a temperature called the cracking temperature (T_{cr}).

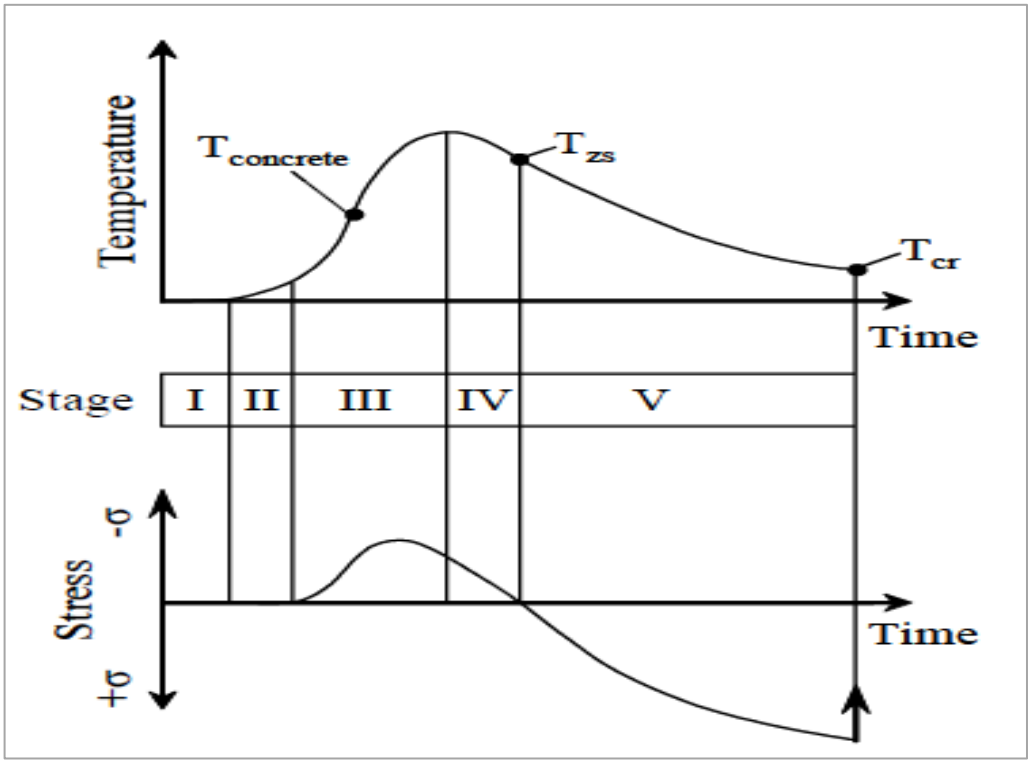

Figure 2 - 16: Behaviour of restrained specimen in RCF [88].

Figure 2-17 shows typical results from an RCF test. The different stages of concrete behaviour in the RCF test, as discussed in the previous section, can be easily identified from the figure. The data in the figure is from Markandeya et al. [77], in which the effects of different types of GGBFS on early-age cracking of concrete were investigated. It can be seen that slag replaces 60% cement can reduce the temperature rise of concrete and improve the cracking resistance of concrete compared with the reference concrete.

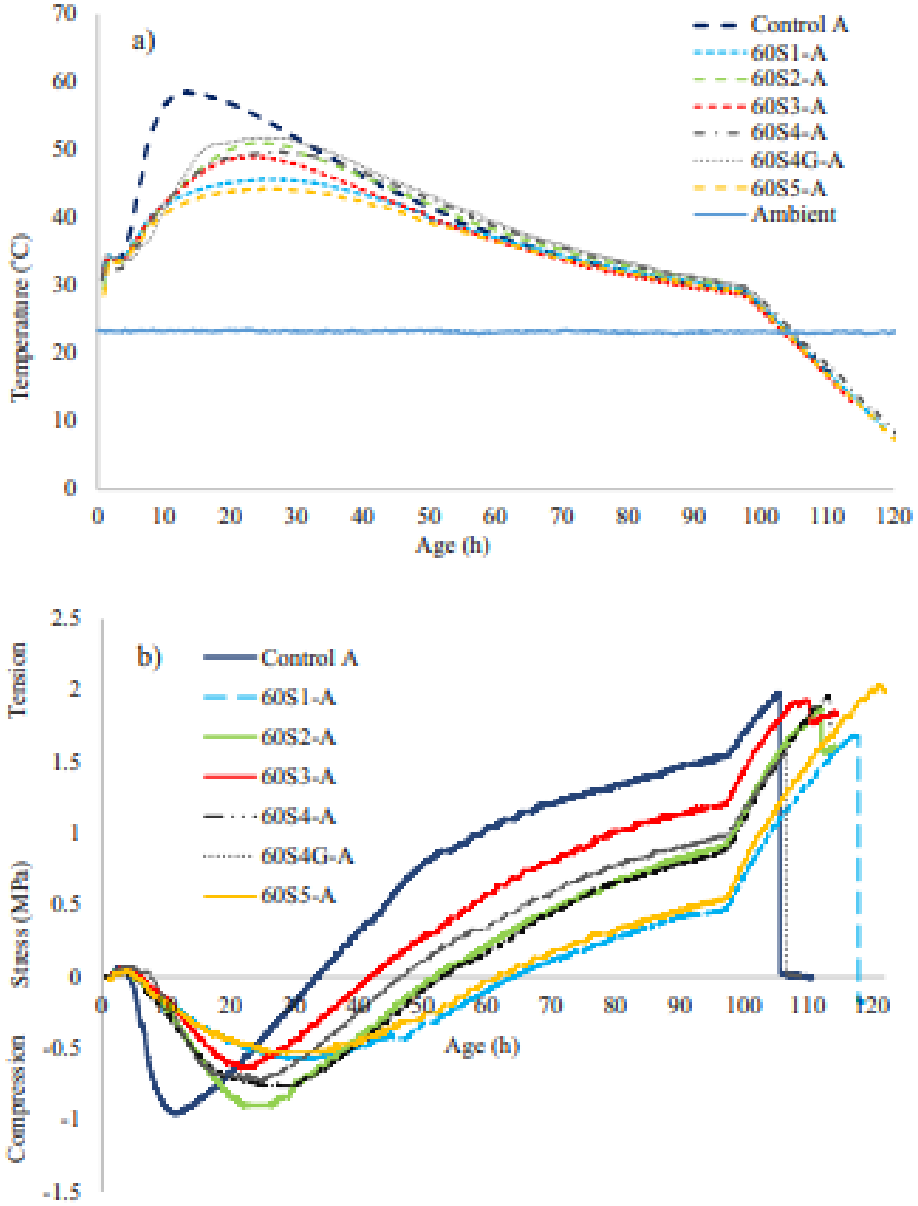

Figure 2 - 17: Mixes with different types of GGBFS in RCF: (a) temperature profile; (b) stress development [77].

2.6 Summary

This chapter has reviewed a wide range of published literature that is closely related to the objectives of the thesis. Past experimental research on early age cracking of conventional concrete has mainly focused on time dependent behaviours such as shrinkage, tensile creep,

temperature and pattern of cracking instead of comprehensively considering the combined effects. Moreover, SCMs such as fly ash and GGBFS have attracted the research interests due to environmental benefits, but the effect of fly ash and GGBFS on the early age concrete cracking has not been widely conducted. In addition, less attention has been received to model the early age concrete cracking by predicting the time dependent behaviours of concrete. As a result, this thesis aims to comprehensively investigate the factors affecting the early age cracking of fly ash and GGBFS concrete by studying the shrinkage, tensile creep, temperature and tensile stress development of concrete. Relevant experimental tests on various concrete mixes with fly ash and GGBFS have been conducted and the time dependent behaviours of fly ash and GGBFS concrete including free shrinkage, tensile creep, restrained tensile stress and thermal cracking have been analytically modelled.

CHAPTER 3: SHRINKAGE OF HIGH VOLUME OF FLY ASH AND GGBFS CONCRETE

Chapter 3 is a re-written version of an article published by the candidate, 'Autogenous shrinkage of High Volume of Fly ash and Ground Granulated Blast Furnace Slag Concrete', in Magazine of Concrete Research. I did more than 50% of the experiments and all of the writing. Some of the materials in this chapter have been expanded from a recent publication, which has been acknowledged and detailed in the 'Inclusion of Publications Statement' for this thesis.

3.1 Introduction

To reduce the environmental impact of cement production, supplementary cementitious materials (SCMs) have gained tremendous popularity in the concrete industry. In existing design codes, predictive models for shrinkage can be used for both Type General Purpose (GP) and blended cement-based concretes without specifically accounting for the binder composition. As a result, the accuracy of standard models to predict shrinkage of concrete with high SCMs content is questionable because these models were not developed and calibrated for these types of concrete.

Two categories including drying shrinkage and autogenous shrinkage can be classified in shrinkage of hardened cementitious materials. Drying shrinkage occurs when the loss of water from the pores to the environment. Autogenous shrinkage is defined as the concrete volume change without any moisture transfer to the environment. Autogenous shrinkage is mainly caused by the capillary pressure induced by self-desiccation resulting from the chemical shrinkage when cementitious materials hydrate and form reaction products [89]. Autogenous shrinkage can be monitored under an isothermal condition where any exchange

of moisture with the surrounding environment is prevented. In structures, autogenous shrinkage of high strength concrete may induce significant stress when shrinkage is restrained, particularly at early age.

The presence of SCMs can affect concrete shrinkage. De Belie et al. [90] reported that GGBFS can lead to an increase in concrete autogenous shrinkage. Li et al. [91] also reported that GGBFS and silica fume can lead to an increase in autogenous shrinkage while using fly ash allows for decreasing the autogenous shrinkage of cement pastes. Li et al. [91] also observed that silica fume and GGBFS led to the overall refinement of the pore structure (decrease in mean pore diameter), including an increase in specific surface area of pores and the volume percentage of small pores within the range from 5 to 50 nm of diameter. They noted an obvious correlation between the increase in autogenous shrinkage and the increase in the volumetric percentage of small pores with size within 5-50 nm highlighting the strong influence of paste pore structure on autogenous shrinkage [91]. Numerous other studies assessing the effect of fly ash and GGBFS on shrinkage are available in the literature but have yet to draw any unanimous conclusion. While some researchers noted an increase in drying and autogenous shrinkage for SCMs based concretes [92, 93], others observed a reduction [94, 95, 96]. It is always difficult to compare shrinkage results from different groups as tests are carried out using different concrete grades, different cement replacement rates, different types of SCMs with different chemical compositions and different aggregates. This chapter intends to address this recurring issue by testing fly ash and GGBFS blended cement-based concretes considering the whole range of standard compressive strengths (25MPa to 100 MPa) using the same materials.

A variety of influencing factors makes the prediction of shrinkage a complex process. Among those factors, curing conditions and the pore structure, in essence, govern shrinkage in hardened concrete. Instead of focusing on the mix design, a strength-based approach can be considered to evaluate the deformation of concrete. This approach narrows down the myriad of parameters that regulate various aspects of concrete shrinkage to just two (i.e., strength and concrete age). This strength-based evaluation approach for shrinkage prediction is adopted by most of the building codes because of its simplicity [97, 98, 99]. The current rise in blended cement usage suggests that the effect of SCMs on shrinkage should be implemented in prediction models of design codes. Therefore, assessing the accuracy of current standard models for predicting shrinkage of blended cement-based concrete is critical.

In this chapter, autogenous, drying and total shrinkage of SCMs based concrete as well as autogenous and chemical shrinkage of blended cement-based paste are investigated. High but practical replacement ratios of Type GP cement by weight were selected based on Australian industry common practice: 30% for fly ash, 40% and 60% for GGBFS. The same percentage of cement replacement by fly ash and GGBFS were applied to paste mixes. In addition, the nitrogen adsorption isotherm technique was used to examine the relationship between pore structure and autogenous shrinkage. Six concrete compressive strengths were tested ranging from 25 MPa to 100 MPa requiring the design of 21 different concrete mixes. Shrinkage results obtained on concrete were compared to existing codes predictions. Some amendments to the Australian code AS3600 model are proposed for autogenous shrinkage of concrete with GGBFS and drying shrinkage of concrete mixes with fly ash and GGBFS.

3.2 Experimental programme

3.2.1 Materials and mix proportion

In this study, blended cement-based concretes and reference Type GP cement-based concretes were tested considering the whole range of standard compressive strengths (25, 32, 40, 50, 80, and 100MPa). A total of 21 concrete mixes were designed. Type GP cement was used for all the concrete mixes, containing up to 7.5% of mineral additions to reduce the clinker content and up to 5% of other constituents in accordance with AS3972 [100]. Two types of SCMs were used, namely, fly ash and GGBFS, complying with Australian Standard AS3582.1 [101] and AS3582.2 [102], respectively. The chemical compositions of cement, fly ash and GGBFS were tested by wavelength-dispersive X-ray Fluorescence (WDXRF) analysis. The results are presented in Table 3-1. A crushed basalt with a maximum aggregate size of 10mm and Sydney fine sand with a maximum nominal grain size of 2.36mm were used as coarse and fine aggregates in concrete, respectively. The particle size distribution curves of coarse and fine aggregates are reported in a previous study of the authors [67]. The mix design proportions are shown in Table 3-2. The particle size distributions of the cement, fly ash and GGBFS are shown in Figure 3-1. 20 μm, 26 μm and 13 μm are the median particle sizes of cement, fly ash and GGBFS, respectively. One control concrete mix without SCM was tested as a reference for each concrete grade. Fly ash is not considered for high strength concretes (i.e., 80 and 100MPa) because designing high strength concrete mix incorporating 30% standard grade fly ash is not practical. In addition, water-reducing admixture and superplasticizer were utilised for some concrete mixes to control workability.

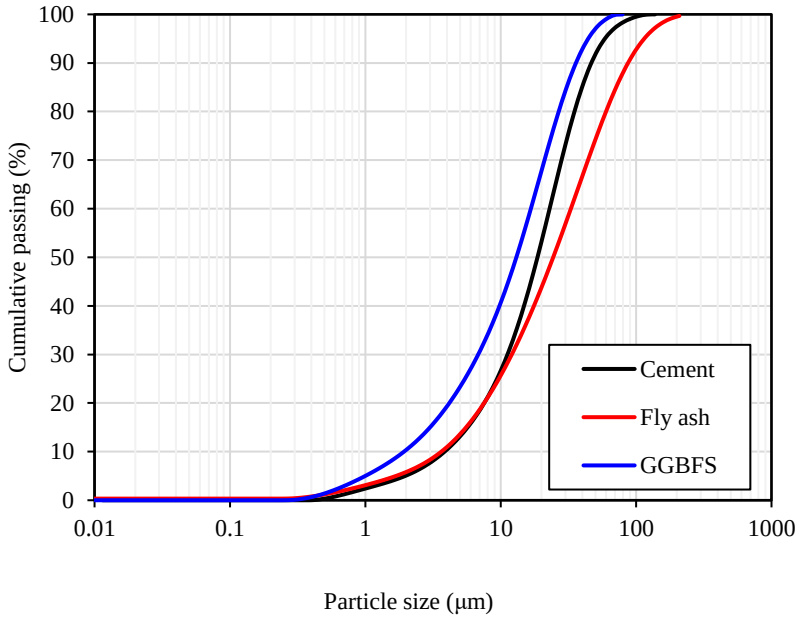

Figure 3 - 1: Particle size distribution of cement, fly ash and GGBFS.

Table 3 - 1: Chemical compositions of cement, fly ash and GGBFS (w.t.%).

Chemical composition	GP cement (wt.%)	Fly ash (wt.%)	GGBFS (wt.%)
SiO_2	18.8	65.9	34.1
Al_2O_3	5	22.1	15.4
Fe_2O_3	2.8	3.4	0.8
CaO	63.8	1.6	36
MgO	1	0.7	6.6
Na_2O	0.3	0.6	0.4
K_2O	0.7	1.8	0.6
TiO_2	0.3	0.9	2.4
SO_3	3	0.1	2.5
Mn_3O_4	-	0.1	1.1

Concrete cylinders with dimensions of 200 mm height by 100 mm diameter were cast to measure the concrete compressive strength. The average 28-day compressive strength (f_{cm}) for three cylinders was measured according to AS1012.9-2014 [103]. The concrete cylinders were cured in standard conditions at a temperature of 23 ± 2 °C and relative

humidity (RH) of 95 ± 5% in accordance with AS1012.8.4-2015 [104]. As mentioned above, the characteristic compressive strength-based approach is used in existing codes. In this chapter, the characteristic compressive strength (f_c') of concrete was determined in accordance with [105]. In AS1379-2007, f_c' can be computed using the measured compressive strength (f_{cm}) and its factored standard deviation, i.e., $f_c' = f_{cm} - k_c \times S$, where k_c is the assessment factor which is equal to 3.2, and S is the standard deviation for the grade being assessed (S_c or S_a), where S_c is the standard deviation for 'controlled grade' and S_a is the standard deviation for 'associated grade', complying with [105]. The lab testing situation is considered similar to the test of the associated grade. As a result, S_a (= S_c × Relative factor) is adapted, in which relative factor is ranging from 1.0 to 1.4 depending on the strength grade of concrete. Slump tests were performed according to AS1012.3.1-2014 to evaluate the workability of each concrete mix [106]. The air content is 2-5% for fresh concrete in accordance with AS1012.4.2-2014 [107]. The unit weight of the concretes was obtained by weighing fresh concrete while casting according to AS1012.5-2014 [108]. Table 3-3 shows the mechanical properties of all concrete mixes including measured and characteristic compressive strength at 28 days, slump, air content, and fresh density.

Table 3 - 2: Mix proportions of concretes.

Sample ID	Mix proportions by weight (kg/m^3)						Designed
	GP Cement	FA	GGBFS	Coarse Agg	Fine Agg	Water	w/b
N25-0	310	0	0	1059	866	174	0.56
N25-FA30	215	95	0	1071	876	143	0.46
N25-G40	185	0	125	1056	864	161	0.52
N25-G60	125	0	185	1056	864	155	0.5
N32-0	360	0	0	1025	839	176	0.49
N32-FA30	250	110	0	1043	853	144	0.4
N32-G40	215	0	145	1033	845	162	0.45
N32-G60	145	0	215	1037	848	155	0.43
N40-0	450	0	0	966	790	194	0.43
N40-FA30	315	135	0	983	804	153	0.34
N40-G40	270	0	180	974	797	184	0.41
N40-G60	180	0	270	981	803	167	0.37
N50-0	510	0	0	927	759	204	0.4
N50-FA30	355	155	0	955	782	153	0.3
N50-G40	305	0	205	930	761	199	0.39
N50-G60	205	0	305	941	770	179	0.35
S80-0	585	0	0	908	743	164	0.28
S80-G40	350	0	235	911	746	158	0.27
S80-G60	235	0	350	915	748	152	0.26
S100-0	650	0	0	880	720	143	0.22
S100-G60	260	0	390	880	720	137	0.21

Table 3 - 3: Fresh properties and 28-day compressive strength of concrete.

Sample ID	Measured compressive strength (MPa)	Characteristic compressive strength (MPa)	Slump (mm)	Air Content (%)	Density(kg/m^3)
N25-0	25.1	23.3	30	3.8	2364
N25-FA30	25.1	22.7	50	4.5	2377
N25-G40	29.1	27.8	45	4.3	2380
N25-G60	27.2	22.0	60	4.8	2386
N32-0	32.5	29.7	60	4.8	2300
N32-FA30	33.5	29.8	85	4.0	2307
N32-G40	39	36.6	35	3.7	2414
N32-G60	32.9	28.3	60	1.5	2481
N40-0	46.2	41.7	60	2.6	2411
N40-FA30	41.3	36.5	35	4.8	2391
N40-G40	48.7	41.6	70	4.5	2421
N40-G60	44.8	32.6	70	5.5	2366
N50-0	51.2	44.3	80	2.8	2433
N50-FA30	61.8	53.2	75	2.6	2411
N50-G40	54.4	47.5	70	3.7	2414
N50-G60	56	49.7	60	3.1	2414
S80-0	82.1	78.0	100	3.1	2425
S80-G40	83.3	78.1	70	2.6	2414
S80-G60	80.2	75.3	250	2.3	2443
S100-0	101.2	97.0	50	3.2	2457
S100-G60	100.5	91.9	200	2.8	2440

3.2.2 Autogenous shrinkage of concrete

Drying shrinkage measurement according to AS1012.13-2015 starts after 7 days of standard water curing [78]. Although this standard test method aims to measure drying shrinkage, it actually measures the drying shrinkage plus that part of the autogenous shrinkage that occurs after 7 days because autogenous shrinkage continues due to hydration and self-desiccation. Moreover, numerous experimental studies can be found in the literature considering the autogenous shrinkage of concrete at a very early age [109, 110, 111].

In these studies, the effect of the first measurement time on the autogenous shrinkage was first studied. The 'time zero' of autogenous shrinkage measurement was determined as the final setting time because the autogenous shrinkage evolution of cementitious materials is closely related to the time when the paste becomes a solid skeleton to transfer tensile stress. Three concrete mixes were selected, one low strength grade (N25-FA30), one middle strength grade (N40-G40) and one high strength grade (S100-G60) to examine the effect of different grades and percentages replacement of SCMs on setting time and early age autogenous shrinkage. Two different autogenous shrinkage tests were conducted using the three concrete mixtures by examining the development of autogenous shrinkage i) from 'time-zero' and ii) from 24 hours after casting. According to AS2350.4-2006 [112] and previously reported studies [109, 113, 114, 115], the final setting time was obtained from the Vicat needle test.

To measure autogenous shrinkage, standard shrinkage prisms were cast in steel moulds and demoulded at the final setting (for N25-FA30, N40-G40 and S100-G60) and 24 hours after casting for all 21 concrete mixes. Immediately after demoulding, all faces of autogenous

shrinkage specimens were well-wrapped using a self-adhesive water-proof aluminium foil to avoid any loss of moisture to the environment [80]. The digital shrinkage gauge meter used for measuring autogenous shrinkage is shown in Figure 3-2.

To compare and minimise systematic and random errors, two or three shrinkage prisms were tested in parallel for each concrete mix. The typical size of the shrinkage prisms in Australia is 280 mm × 75 mm × 75 mm [104]. After demoulding, the autogenous shrinkage specimens were kept in an environmentally controlled room at a temperature of 23°C ± 2 °C and RH of 50 ± 3%. It should be noted that the actual temperature in the test specimens might be higher than 23°C at an early age due to the hydration and varied across the cross-section of test specimens. However, since the autogenous shrinkage is measured after 24 hours from casting, and the size of the specimen is relatively small, as such, the temperature variation along the cross-section is assumed to be uniformly distributed and equal to the temperature in the environmental chamber (23°C). Benchmark readings were recorded when the specimens were demoulded. Measurements were carried out once a day for the first week and then once a week after the first week until 100 days.

Figure 3 - 2: Autogenous shrinkage specimens.

3.2.3 Total and drying shrinkage of concrete

As mentioned in Section 3.2.2, drying shrinkage of concrete is determined according to Australian Standard AS1012.13-2015 [78]. However, the development of autogenous shrinkage SCMs based concrete after 7 days can be significant due to the pozzolanic reactions [116]. Therefore, an alternative approach was carried out to evaluate concrete shrinkage. After 1 day, total shrinkage test was carried out using unsealed concrete prisms that were fully exposed to the air (23 ˚C and 50% relative humidity), as depicted in Figure 3-3. Consequently, the drying shrinkage is simply obtained from the difference between the total shrinkage measured on the unsealed specimens and the autogenous shrinkage measured on the sealed specimens. However, it should be noted that the drying shrinkage may not be simply computed by subtracting the autogenous shrinkage from the total shrinkage due to the non-uniform hydration reaction in the drying condition.

Figure 3 - 3: Total shrinkage specimens.

3.2.4 Autogenous shrinkage of paste

The autogenous shrinkage of pastes was assessed in accordance with ASTM C1698 [117]. This method uses corrugated tubes for the determination of autogenous shrinkage in cement paste. In this chapter, 4 mixes with identical water to binder ratio of 0.4 were tested. The cementitious materials replacements percentage was the same as for concrete mixes. To distinguish the paste samples from concrete, the label 'FA30', 'G40', or 'G60' stands for the 30% fly ash, 40% and 60% GGBFS replacement of Type GP cement by weight respectively. The details of the paste mix proportions are presented in Table 3-4. The autogenous shrinkage measurements of pastes started at the final setting time. The final setting time of cement pastes was determined by the isothermal calorimetry. The precision of the measurement is ± 10 min. The deformation of each specimen was continuously monitored until 100 days.

Table 3 - 4: Mix proportions of paste.

Sample	binders		w/b ratio
	GP cement	SCMs	
Control	1	0	0.4
FA30	0.7	0.3	0.4
G40	0.6	0.4	0.4
G60	0.4	0.6	0.4

3.2.5 Chemical shrinkage of paste

Chemical shrinkage of cementitious materials has a significant contribution to the early volume change of concrete. ASTM C1608 is one of the popular test methods to determine chemical shrinkage [118]. However, many factors affect the accuracy and repeatability of the test results including the shape and size of the glass vial, w/c ratio, thickness of the

cement paste. Zhang et al. [119] reported the modified test method with superior precision and repeatability than ASTM C1608. An Erlenmeyer flask was used instead of vials to prevent the formation of the skeleton structure in cement paste. Precision was increased by maintaining the thickness of the paste at about 7.5 mm. Therefore, in this chapter, chemical shrinkage was measured by a modified version of ASTM C1608 as described by Zhang et al. [119]. Note that paste mixes have the same binder mix proportion as for autogenous shrinkage specimens shown in Table 3-4. Chemical shrinkage was monitored for 100 days.

3.2.6 Pore structure analysis of paste

The pore structure of the pastes was determined by the nitrogen sorption test. The w/b ratio for the paste used in pore structure analysis is the same as the paste mixes in the autogenous and chemical shrinkage tests. The specific surface area was evaluated by Brunauer–Emmett–Teller (BET) method with an accelerated surface area and porosimetry system: Novatouch LX4 from Quantachrome Instrument. The gas used is nitrogen (N_2) with a liquefaction temperature of -195.87 °C. The paste samples were sealed until the testing date. Hydration of paste samples was prevented by a modified RILEM method [120]. IPA exchange for 1 hour, drying at 40 °C for 0.5 hours. Prior to this, the paste sample was ball-milled and screened at a size of 850 μm. To remove the adsorbed water from the fine pores, the degassing process was carried out using 40 °C under the vacuum condition for 16 hours [121]. To evaluate the pore size distribution, the adsorption branches of isotherm curves were analysed using the Barrett-Joyner-Halenda (BJH) method [122]. Each specimen was tested at the age of 28 days and 90 days.

3.3 Results and analysis

3.3.1 Autogenous shrinkage of concrete tested immediately after final setting

The Vicat needle test results show that the final setting time of N25-FA30, N40-G40 and S100-G60 were 10 hours, 8 hours, and 15 hours, respectively. Figure 3-4 presents the comparisons between the autogenous shrinkage of concrete mixes measured from 24 hours and immediately after the final setting. It should be noted that the purpose of this section is to compare the absolute shrinkage value between the measurement after 24 hours and the measurement after final setting. By doing that more conservative (higher autogenous shrinkage) could be identified.

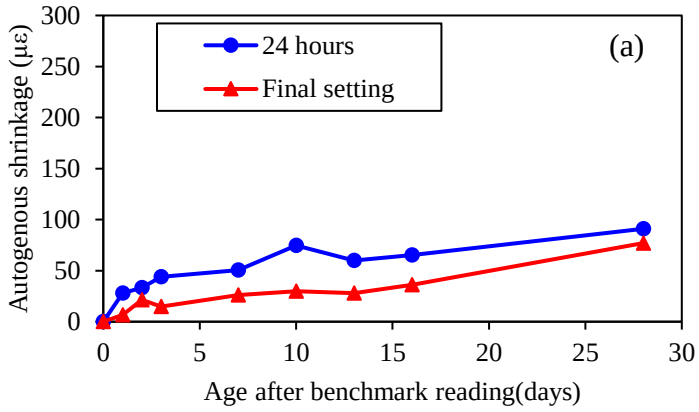

Figure 3 - 4: Autogenous shrinkage measured after 24 hours or final setting: (a) N25-FA30; (b) N40-G40; (c) S100-G60.

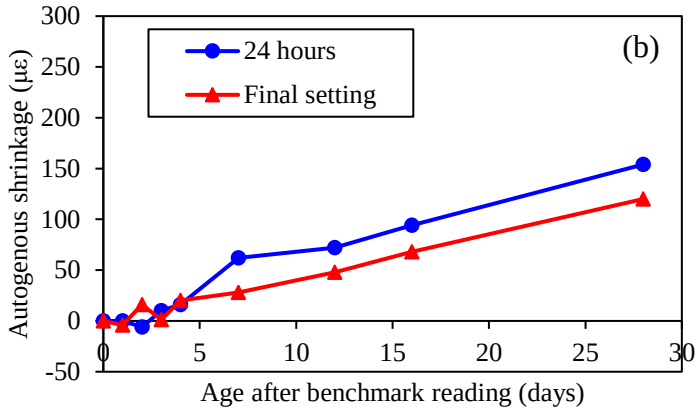

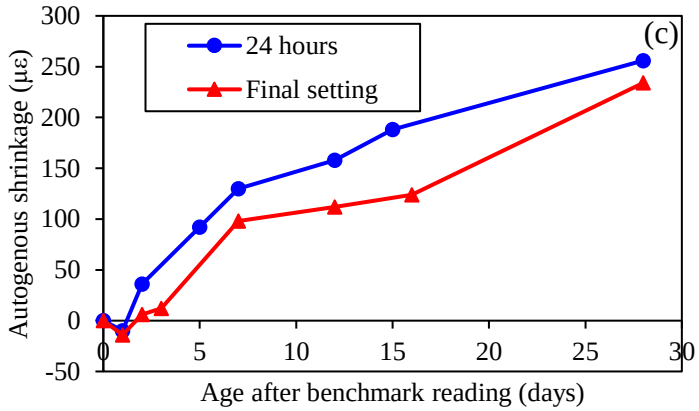

Figure 3 – 4: (continued)

As depicted in Figure 3-4, although the measurement starts at different time, the age is adjusted as age after the benchmark reading until 28 days. The results show that the autogenous shrinkage measured by starting immediately after the final setting was always lower than when starting after 24 hours. The maximum difference at 28 days is 30 με. This could be attributed to a not fully recovered concrete expansion rather than shrinkage that can occur after the final setting and before 24 hours. This phenomenon occurring at a very early age was also reported by several authors [123, 124, 125]. This can be attributed to a thermal expansion due to the heat of hydration, absorption of bleeding water [126], water adsorption by filler [127], and CH growth and primary ettringite formation [128].

Nevertheless, the measurement of autogenous shrinkage starting after 24 hours appears to be more conservative compared to the immediate measurement after the final setting. In this comparison, starting to measure autogenous shrinkage after 24 hours seems to be justified, avoiding interferences with complex phenomena leading to concrete expansion.

3.3.2 Autogenous shrinkage of concrete tested from 24 hours

The autogenous shrinkage strains are presented in Figure 3-5 for all concrete mixes at 3, 7, 14, 28, 56 and 100 days. The displayed points represent the average value of two or three measured strains. Figure 3-6 provides typical autogenous shrinkage results for three replicate samples, indicating good repeatability of the test method. As expected, autogenous shrinkage increased with the increase in characteristic compressive strength. This is due to the autogenous shrinkage is predominant in lower water/binder ratio mixtures [80, 81].

At 28 days (Figure 3-5 (d)), it was observed that for fly ash mixes, regardless of the strength, the autogenous shrinkage was similar to that of the reference concretes. For GGBFS mixes with compressive strength less than 50 MPa, autogenous shrinkage appears to be similar to that of the control mixes. However, for concrete strengths greater than 50 MPa, the autogenous shrinkage of GGBFS concretes was about 10% lower than that of the reference concretes. Concrete mixes with 30% fly ash at about 20 MPa shows a statistically higher and 60 MPa shows a significantly lower autogenous shrinkage.

The autogenous shrinkage test results at 56 days (one of the key age in Australia to report shrinkage results [78]) are shown in Figure 3-5 (e). For concrete mixes with 30% fly ash, the results at about 20 MPa shows a statistically higher and 60 MPa shows a significantly lower autogenous shrinkage. For GGBFS concretes, except for N25-G60, the autogenous shrinkage was about 30% higher on average than that of the control mixes for compressive

strength below 50 MPa. N25-G60 concrete did not show the same trend due to an initial swelling. GGBFS concrete with strength range 35-50 MPa shows a significantly higher autogenous shrinkage. The autogenous shrinkage of GGBFS concretes with strengths greater than 50 MPa remained about 10% lower than reference concretes.

Figure 3-5 (f) shows the long-term autogenous shrinkage test results at 100 days. Fly ash concretes still perform similarly to control concretes. For GGBFS concretes with strength range 35-50 MPa, the autogenous shrinkage is about 50% higher in average than that of the reference concretes. It was also seen that autogenous shrinkage is increasing with the GGBFS content from 40% to 60%. For strength higher than 50 MPa, autogenous shrinkage of GGBFS concretes was equal to control mixes autogenous shrinkage. After 100 days, autogenous shrinkage of N25-G60 also became superior to that of N25-0 despite its initial swelling.

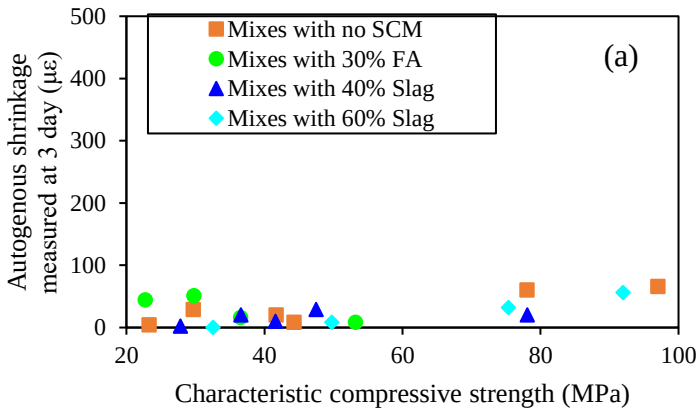

Figure 3 - 5: Autogenous shrinkage of concretes mixes with FA and GGBFS measured: (a) at 3 days; (b) at 7 days; (c) at 14 days; (d) at 28 days; (e) at 56 days; (f) at 100 days.

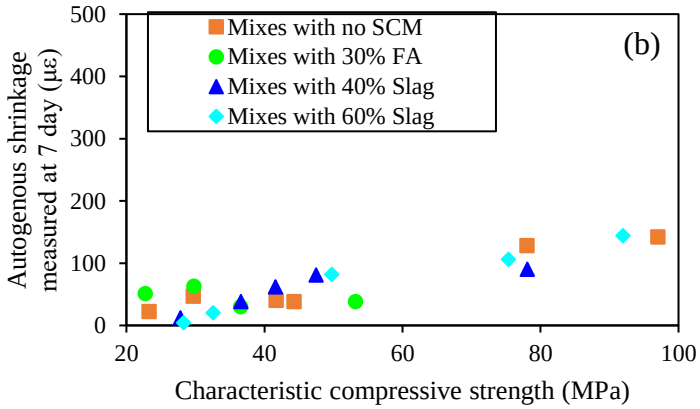

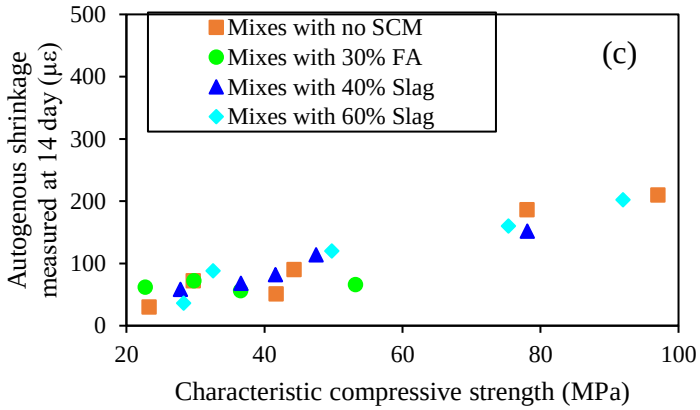

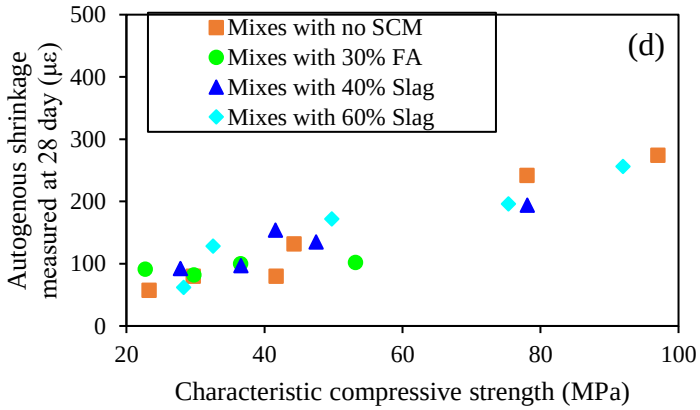

Figure 3 – 5: (continued)

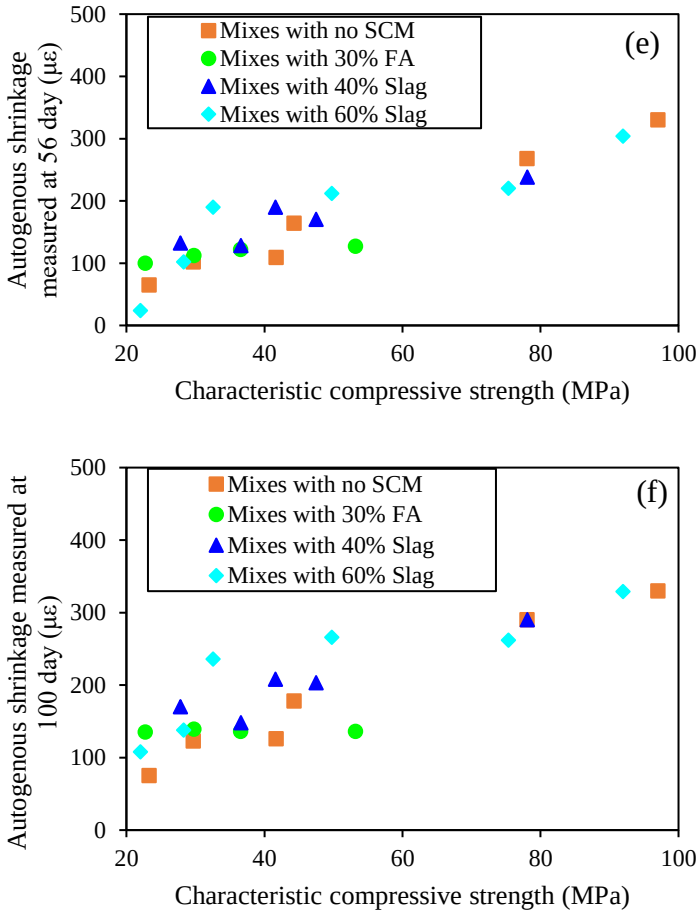

Figure 3 – 5: (continued)

Experimental results consistently showed significantly higher autogenous shrinkage for GGBFS concretes compared to reference concretes for concrete grades below 50 MPa. Excluding N25-G60, the autogenous shrinkage of GGBFS concretes was on average 20% higher than reference concretes at 28 days, increasing up to 30% and 50% after a test period of 56 and 100 days, respectively. For reference concretes, hydration reactions after 28 days seemed to be almost complete and the autogenous shrinkage due to the self-desiccation appeared to be negligible. By contrast, GGBFS concretes showed a continuous autogenous shrinkage development due to late hydration reactions [129], leading to a higher

autogenous shrinkage at a later stage. The results of increased autogenous shrinkage were in agreement with those reported in the literature [123, 130, 131].

The introduction of GGBFS led to a refinement of the pore structure in cement paste. It was reported that pores less than 50 nm increase the self-desiccation which contributes to higher autogenous shrinkage [132]. This pore refinement happened over a large period and will be discussed in Section 3.3.6. However, autogenous shrinkage of GGBFS high strength concretes is about 10% lower than reference concretes at 28 and 56 days. At 100 days, autogenous shrinkage of GGBFS concretes was almost the same as the control mixtures for high strength concretes. Based on these test results, it can be concluded that the autogenous shrinkage of GGBFS blended high strength concretes with a low water/binder ratio (less than 0.3) exhibited a slow development compared to reference concretes. The possible explanation is that the low water to binder ratio affects the hydration as cement cannot be fully hydrated and the final degree of hydration is limited, compensating for some late pozzolanic reactions and resulting in a low self-desiccation and autogenous shrinkage [133]. Such behaviour was also noted by Lee et al. [134].

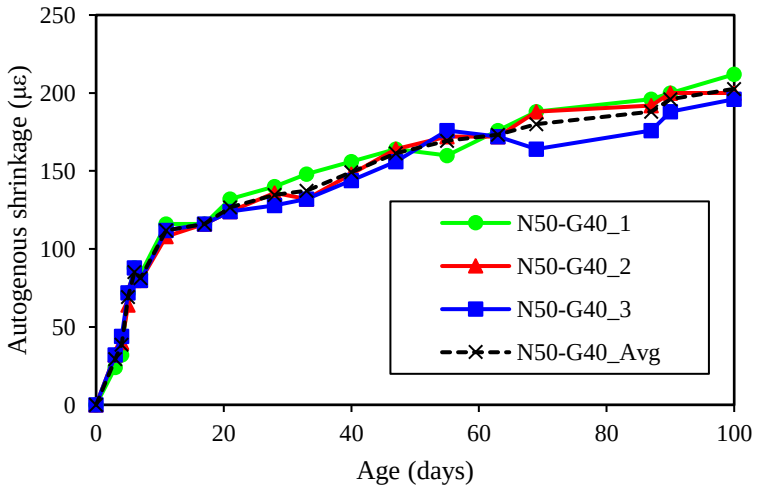

Figure 3 - 6: Autogenous shrinkage results of three N50-G40 concrete samples.

For concretes with fly ash, autogenous shrinkage seemed to be only marginally affected by the decrease in water to binder ratio or increase in strength. In addition, the autogenous shrinkage development of fly ash concretes was overall similar to that of control concretes. Like reference concretes, only a marginal increase in fly ash concretes autogenous shrinkage was observed from 28 days to 100 days. Fly ash concretes autogenous shrinkage was significantly lower than that of GGBFS concretes. This can be attributed to the dilution effect of fly ash and the slow reaction rate in comparison with reference concretes. The hydration products are reduced because of the lower cement content [135]. Yet, the dilution effect of GGBFS is compensated by the hydraulic nature of GGBFS. After being in contact with water, GGBFS reacts faster than fly ash [136, 137].

3.3.3 Total and drying shrinkage of concrete

According to AS3600-2018 [98], the drying shrinkage at 100 days could be ideally identified as basic drying shrinkage. Based on this principle, Figure 3-7 shows the basic drying shrinkage of all concretes which is the difference between total and autogenous shrinkage after 100 days.

The basic drying shrinkage for the reference concretes appeared to be marginally dependent on the compressive strength. Concretes with strength less than 50 MPa showed slightly higher drying shrinkage values than concrete strength grades higher than 50 MPa. Moreover, based on the results in Figure 3-7, the basic drying shrinkage of concrete mixes with SCMs appeared not to be affected significantly by compressive strength.

Basic drying shrinkage for concrete mixtures with SCMs was significantly lower than that of reference concretes for all grades. The average shrinkage reduction for mixtures with 30% fly ash was about 29%, while for mixtures with 40-60% slag, the reduction was about

32% compared to the reference concretes. Similar results were also reported by Güneyisi et al. [138].

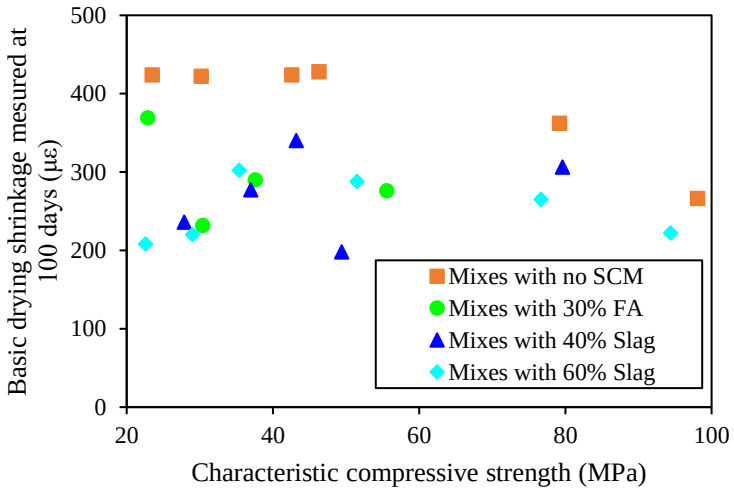

Figure 3 - 7: Basic drying shrinkage of concretes mixes with FA and GGBFS calculated at 100 days.

Figures 3-8 presents the results of total shrinkage of concrete mixes with SCMs at 100 days. Total shrinkage for all concrete mixes without SCMs from 25 to 100MPa is almost constant or slightly increasing versus concrete grade increases. GGBFS at 40-60% has less reduction of total shrinkage from control mixes compared to drying shrinkage at high concrete grades. The average decrease of total shrinkage of GGBFS concrete was about 10% for concrete grades more than 40-50MPa and for low strength, concrete was about 26%, which was a distinct drop. It is also observed that the total shrinkage for GGBFS concrete exhibited a similar trend to control mixes which total shrinkage slightly increased as strength increased. While fly ash at 30% shows a different performance, the total shrinkage could be effectively controlled but experienced large variation. Total shrinkage for concrete mixes with SCMs was overall lower than without SCMs because a huge reduction in drying

shrinkage and a slight increase in autogenous shrinkage resulted in the deceases in total shrinkage.

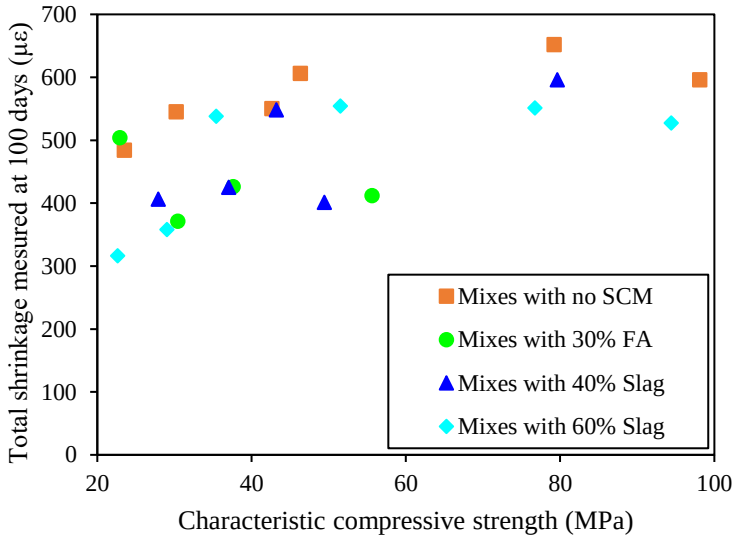

Figure 3 - 8: Total shrinkage of concretes mixes with FA and GGBFS measured at 100 days.

3.3.4 Autogenous shrinkage of paste

Autogenous shrinkage is macroscopic volume change in external dimensions without moisture transferred to an external environment. This shrinkage considers a subset of chemical shrinkage and it is closely related to the hydration reaction. The reduction of relative humidity in the capillary pores results in self-desiccation during the hydration process. As a result, self-desiccation is the driving force of autogenous shrinkage [139].

In this study, the autogenous shrinkage of paste was monitored using the plastic corrugated tube test (ASTM C1698). The length change of corrugated tubes after the final setting was monitored. The chemical shrinkage test (explained in Section 3.4) carried out in this study was in a fully saturated condition allowing for eliminating the effects of self-desiccation.

The simultaneous analysis of the results from both tests will help in understanding the late autogenous shrinkage observed on GGBFS concretes in relation to the pore structure refinement.

Figure 3-9 shows the autogenous shrinkage of pastes with fly ash and GGBFS compared to reference paste. It can be observed that the development of autogenous shrinkage of the pastes follows a similar trend to that of corresponding concretes but with different rates of development depending on the pastes. It can also be observed that the trends in Figure 3-9 and Figure 3-5 are consistent, indicating that the increase of autogenous shrinkage of GGBFS and fly ash systems from 28 to 100 days is significantly higher than that of reference mixes. The shrinkage of the control sample reached a plateau but the SCMs blended samples kept shrinking after 28 days. The autogenous shrinkage of the control mix was recorded as 730 με after 100 days. The autogenous shrinkage of GGBFS pastes was lower than the control mix at an early age but overtook the control mix after 80 days. The rate of shrinkage for slag blends (both 40% and 60% slag replacements) was steeper at later ages. These results were consistent with the higher autogenous shrinkage development observed for GGBFS concrete after 28 days. Similar results were also noted by Wei et al. [38]. According to previous research, due to the difference in the chemical composition of cement and slag, the introduction of slag in the paste mixes seemed to develop denser hydration products [140]. Densification of microstructures may increase the capillary pressure, thereby increasing the autogenous shrinkage [140].

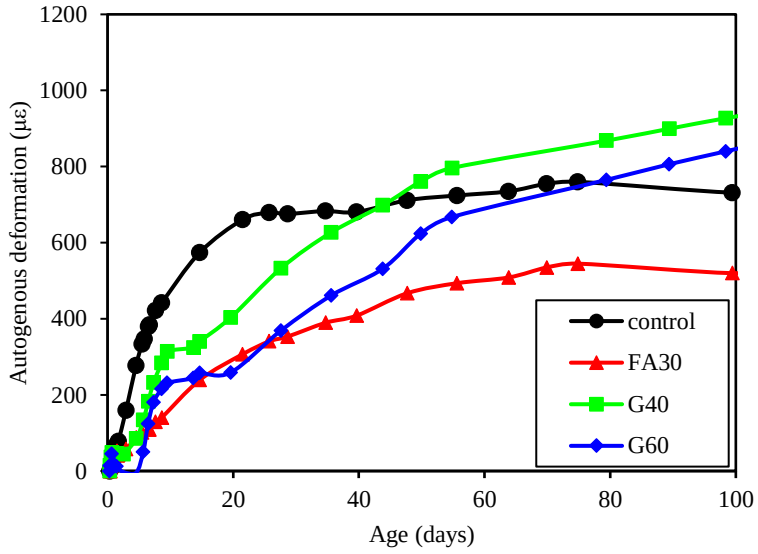

Figure 3 - 9: Autogenous shrinkage of pastes mixes with FA and GGBFS.

The autogenous shrinkage of paste mix with fly ash was overall lower than that of reference paste, which agreed with the experimental findings of Talcinkaya and Yazici [141] and most of the results obtained on fly ash concretes in this study (Figure 3-5). Some increase in autogenous shrinkage was observed on fly ash paste from 28 days to 100 days due to pozzolanic reactions. However, the extent of this increase was only small compared to GGBFS pastes. Indeed, both fly ash and 40% GGBFS pastes achieved similar autogenous shrinkage at 28 days, just over 300 με. But at 100 days, while the autogenous shrinkage of the fly ash paste reached about 500 με, 40% GGBFS paste achieved about 850 με. This increase observed on fly ash paste autogenous shrinkage from 28 days to 100 days seems too small to be observed on fly ash concretes due to the influence of aggregates (Figure 3-6).

3.3.5 Chemical shrinkage of paste

Chemical shrinkage is the reduction in absolute volume of paste due to hydration because the volume of the products forming is less than that of the reactants. In addition, when the cement paste has hardened and is unable to freely reduce its macroscopic volume due to the hydration reactions, capillary pores form internally to accommodate the volume reduction.

Figure 3-10 displays the evolution of chemical shrinkage of pastes with fly ash and GGBFS in comparison with reference paste. It can be observed that the chemical shrinkage slightly decreases with the increase in slag content compared to the control mix. As the slag content increased from 40% to 60%, the ultimate chemical shrinkage decreased from 6.8 mL/100g of binder to 6.3 mL/100g of binder. Such behaviour was also noted by Merzouki et al. [142]. However, these results were not consistent with the autogenous shrinkage test results discussed in the previous sections. In addition, it is also found that the chemical shrinkage of paste with fly ash was slightly lower than reference paste before 56 days but became equal to 100 days. The ultimate chemical shrinkage was 7.2 ml/100g of binder for both reference paste and fly ash paste. The lower chemical shrinkage may be explained by the dilution effect of the SCMs and the lower heat released in fly ash and slag pastes compared to Type GP cement paste as the heat of hydration and the resulting increase in concrete temperature contributes to accelerating hydration reactions.

The chemical shrinkage test measures the volume reduction associated with the hydration reactions of cementitious materials in a fully saturated condition, eliminating the effect of self-desiccation. While autogenous shrinkage measured using the corrugated tubes in this chapter is a length reduction caused by the measurable portion of hydration reactions and self-desiccation. After the pore structure is built, the consumption of water during hydration

reaction results in voids formations and relative humidity reduction within the pore structure. Then, capillary pores become unsaturated leading to meniscus formation, which causes self-desiccation induced autogenous shrinkage [143]. Therefore, the chemical shrinkage measured in this chapter is mainly due to the difference in sizes between the products before and after hydration. Based on these test results, one may conclude that considering the similar chemical shrinkage between GGBFS and control pastes, the higher long term autogenous shrinkage of GGBFS pastes is caused by the self-desiccation due to the sequences of pore structure refinement of GGBFS pastes. The effect of the time-dependent pore structure refinement will be discussed in Section 3.3.6.

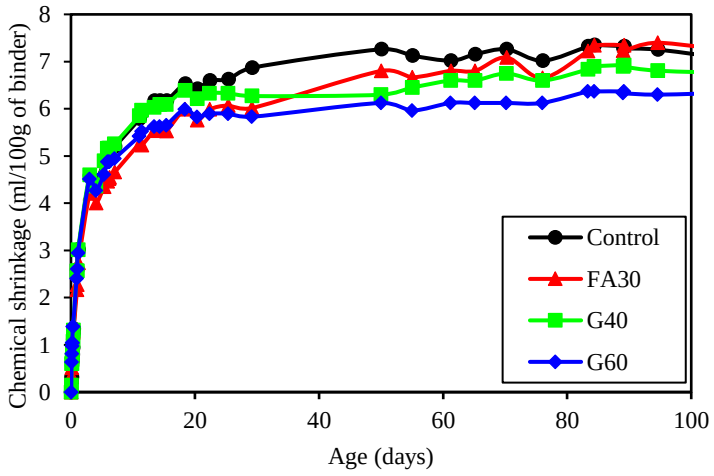

Figure 3 - 10: Chemical shrinkage of pastes mixes with FA and GGBFS.

3.3.6 Pore structure analysis of paste

The shrinkage stress induced by capillary pressure mainly depends on the size and volume fraction of pores less than 25 nm in radius according to Young et al. [144]. The relationship between the autogenous shrinkage and the time-dependent variation of small pores by the nitrogen adsorption technique is assessed in this chapter. Figure 3-11 shows the differential

pore size distribution curves of pastes with fly ash and GGBFS at 28 and 90 days in comparison with the reference paste. Though the differential pore volume was acquired up to about 67 nm radius as shown in Figure 3-11, the pore volume relevant to autogenous shrinkage was considered up to 25 nm.

In this chapter, GGBFS seems to have a more obvious impact on the time-dependent change of pore structure (in the range 2.5 to 5 nm) as manifested by the considerable shift of the differential pore size distribution curve towards left from 28 days to 90 days (Figure 3-11) compared to the other two mixes. As shown in Figure 3-11, the increase in pores with size ranging from 2.5 to 5nm was the highest for GGBFS system. The reasons can be attributed to their different physical characteristics and hydration process. GGBFS is a fine mineral powder with high hydration activity and specific surface area. The radius of GGBFS grains is smaller than fly ash and cement as presented in Figure 3-1. The gaps formed between cement particles can be filled by the finer GGBFS grains. Then, the generated hydration products continually fill the pores, splitting the original large pores into several micro-pores [91]. The average pore size is approximated from the total volume to nitrogen absorbed assuming the pores are filled with liquid nitrogen under pressure and BET surface area. The average pore radius of control, fly ash and GGBFS pastes were 13.1 nm, 11.2 nm and 11.3 nm at 28 days, respectively, while the average pore radius decreased to 8.7 nm, 9.0 nm and 8.3 nm at 90 days, respectively. This reduction in average pore radius is attributed to the continuing hydration of pastes. Pores are further filled by hydration products [91].

To better investigate the relationship between autogenous shrinkage and the pore structure of cement pastes with fly ash and GGBFS, test results including the autogenous shrinkage

of N40 concrete mixes (Figure 3-12), autogenous shrinkage of pastes (Figure 3-9) and the pore structure of pastes (Figure 3-11) were selected and compared (summarized in Table 3-5) because they have very similar w/b ratio for further analysis. It can also be observed that the trends in Figure 3-9 and Figure 3-12 are quite consistent, showing that GGBFS can lead to a higher autogenous shrinkage while fly ash exhibits similar or smaller autogenous shrinkage compared to reference mixes. The underlying logic that links all these test series together is that the state of pore structure at each specific time and the change in microstructures between 28 days and 90 days should correlate with the evolution of autogenous shrinkage within this period, which should be observed on both paste and concrete systems.

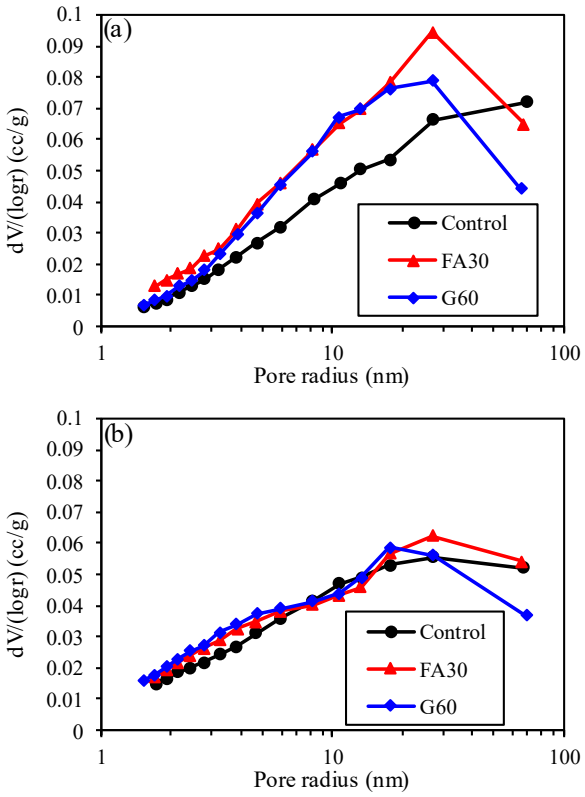

Figure 3 - 11: Pore size distribution curves of pastes mixes with FA and GGBFS: (a) at 28 days; (b) at 90 days.

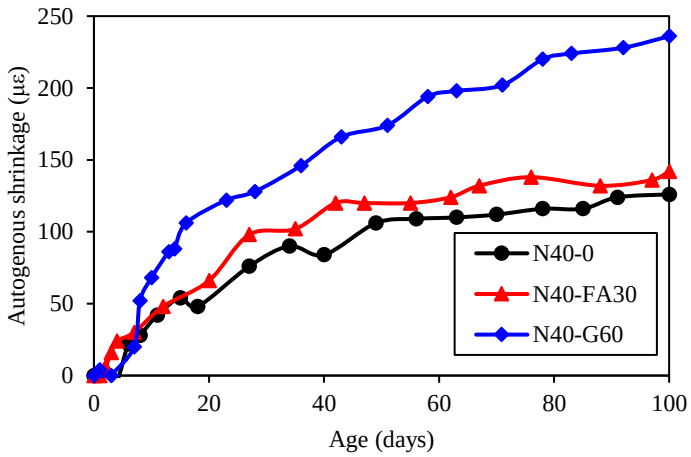

Figure 3 - 12: Autogenous shrinkage of N40 concretes mixes.

Table 3-5 summarises the pore volume fractions obtained within the pore size range 2.5-25 nm radius for control paste, FA30, and G60 and autogenous shrinkage values at 28 and 90 days. It can be seen from Table 3-5 that the pore volume fraction within 2.5-25 nm radius for FA30 and G60 mixes were 14% and 5% higher than that of control paste at 28 days, respectively. Then, this same pore volume fraction of FA30 and G60 pastes became 1% and 8% lower than that of the control system at 90 days, respectively due to the pore structure refinement. These results were strongly correlated with the much greater increase in autogenous shrinkage from 28 to 90 days of GGBFS materials compared to other pastes and concretes (see Table 3-5). Fly ash paste showed a larger increase in autogenous shrinkage than reference materials from 28 to 90 days but to a much smaller extent compared to GGBFS paste and concretes. This can be attributed to the less replacement ratio of fly ash mix. The autogenous shrinkage after 28 days was governed by the decrease in RH due to late pozzolanic reaction in addition to the pore refinement. For fly ash concrete, only a marginal increase in autogenous shrinkage was observed between 28 and 100 days, similar to that observed on reference concretes.

Table 3 - 5: Parameters of control paste, FA30 and G60 for autogenous shrinkage analysis.

Parameters	Control	FA30	G60
1. Total pores (2.5-25 nm radius) at 28 days	100%	114%	105%
2. Total pores (2.5-25 nm radius) at 90 days	78%	77%	70%
3. Change in total pores (2.5-25 nm radius) from 28 days to 90 days	22%	37%	35%
4. Change in autogenous shrinkage (GP paste, w/b = 0.4) from 28 days to 90 days, με	56	179	517
5. Change in autogenous shrinkage (Concrete N40, w/b = 0.34-0.43) from 28 days to 90 days, με	28	36	100

Notes: Parameters 1, 2 and 3 are the relative percentages of the total pores (2.5-25 nm radius) compared to that of the control paste at 28 days.

3.4 Shrinkage models

In this section, analytical models including Australian Standard AS3600 [97, 98] and European Standard Eurocode 2 [99] are discussed and their predictions are compared to the test results shown in Figure 3-6 to Figure 3-8.

3.4.1 AS3600-2018 [98]

In the recently published Australian Standard AS3600-2018, the development of autogenous shrinkage ε_{cse} is modelled versus time t (in days) and the characteristic compressive strength of concrete f_c' as follows:

$$\varepsilon_{\mathrm{cse}} = \varepsilon^{*}_{\mathrm{cse}} \times (1.0 - \mathrm{e}^{-0.07\mathrm{t}}) \quad (3\text{-}1)$$

$$\varepsilon^{*}_{\mathrm{cse}} = (0.07 f_c' - 0.5) \times 50 \times 10^{-6} \quad \text{for } f_c' \leq 50 \text{ MPa} \quad (3\text{-}2)$$

$$\varepsilon^{*}_{\mathrm{cse}} = (0.08 f_c' - 1) \times 50 \times 10^{-6} \quad \text{for } f_c' > 50 \text{ MPa} \quad (3\text{-}3)$$

The drying shrinkage ε_{csd} is calculated as follows:

$$\varepsilon_{\mathrm{csd}} = k_1 \times k_4 \times \varepsilon_{\mathrm{csd.b}} \tag{3-4}$$

where k_1 is obtained based on the hypothetical thickness and time using Eq. (3-5); k_4 is equal to 0.7 for an arid environment, 0.65 for an interior environment, 0.6 for a temperate inland environment and 0.5 for a tropical or near-coastal or coastal environment; $\varepsilon_{\mathrm{csd.b}}$ is the basic drying shrinkage strain which is calculated based on the characteristic compressive strength of concrete using Eq. (3-7).

$$k_1 = \frac{(0.8 + 1.2e^{-0.005t_h})t^{0.8}}{t^{0.8} + 0.15t_h} \tag{3-5}$$

where t_h is the hypothetical thickness which can be calculated based on the gross cross-sectional area (A_g) and the exposed perimeter of a member cross-section (u_e), as shown in Eq. (3-6):

$$t_h = \frac{2A_g}{u_e} \tag{3-6}$$

$$\varepsilon_{\mathrm{csd.b}} = (0.9 - 0.005f_c') \times \varepsilon^*_{\mathrm{csd.b}} \tag{3-7}$$

where $\varepsilon^*_{\mathrm{csd.b}}$ is the final basic drying shrinkage and is equal to 800×10^{-6}.

3.4.2 AS3600-2009 [97]

In AS3600-2009, the development of autogenous shrinkage ε_{cse} is depicted depending on the time t (in days) and the characteristic compressive strength of concrete f_c' as follows:

$$\varepsilon_{\mathrm{cse}} = \varepsilon^*_{\mathrm{cse}} \times (1.0 - \mathrm{e}^{-0.1\mathrm{t}}) \tag{3-8}$$

$$\varepsilon^*_{\mathrm{cse}} = (0.06f_c' - 1) \times 50 \times 10^{-6} \tag{3-9}$$

The drying shrinkage model in AS3600-2009 is the same as Eq. (3-4), but the calculation of basic drying shrinkage is different, as shown in Eq. (3-10):

$$\varepsilon_{\mathrm{csd.b}} = (1 - 0.008 f_c') \times \varepsilon^*_{\mathrm{csd.b}} \quad (3\text{-}10)$$

where the final basic drying shrinkage ($\varepsilon^*_{\mathrm{csd.b}}$) is taken as 800×10^{-6} for Sydney and Brisbane, 900×10^{-6} for Melbourne and 1000×10^{-6} elsewhere.

3.4.3 Eurocode 2 [99]

In the standard EN 1992-1-1, which is also called Eurocode 2, the development of autogenous shrinkage $\varepsilon_{\mathrm{cse}}$ is represented relying on the age of concrete t (in days) and the characteristic compressive strength of concrete f_c' as follows:

$$\varepsilon_{\mathrm{cse}} = \beta_{as}(t) \times \varepsilon^*_{\mathrm{cse}} \quad (3\text{-}11)$$

$$\beta_{as}(t) = 1 - e^{-0.2t^{0.5}} \quad (3\text{-}12)$$

$$\varepsilon^*_{\mathrm{cse}} = 2.5 \times (f_c' - 10) \times 10^{-6} \quad (3\text{-}13)$$

The drying shrinkage in Eurocode 2 is calculated as follows:

$$\varepsilon_{\mathrm{csd}} = \beta_{ds}(t, t_0) \times k_h \times \varepsilon^*_{\mathrm{cse}} \quad (3\text{-}14)$$

where $\beta_{ds}(t, t_0)$ is a time development function as per Eq. (3-15); k_h is a coefficient depending on the hypothetical thickness (t_h), which equals to 1.0, 0.85, 0.75 and 0.7 for t_h is equal to 100, 200, 300 and greater than or equal to 500, respectively; $\varepsilon^*_{\mathrm{cse}}$ is the final drying shrinkage value as per Eq. (3-16).

$$\beta_{ds}(t, t_0) = \frac{t - t_0}{(t - t_0) + 0.04\sqrt{t_h^3}} \quad (3\text{-}15)$$

$$\varepsilon^*_{\mathrm{csd.b}} = 0.85[(220 + 110\alpha_{ds1}) \times exp\left(-\alpha_{ds2} \times \frac{f_c'}{f_{cmo}}\right)] \times 10^{-6} \times \beta_{RH} \quad (3\text{-}16)$$

where f_{cmo} is equal to 10 MPa; α_{ds1} and α_{ds2} are equal to 3, 4, 6 and 0.13, 0.12, 0.11 for cement class S, N, R, respectively. β_{RH} is a relative humidity-dependent factor which can be calculated using Eq. (3-17).

$$\beta_{RH} = 1.55[(1 - \left(\frac{RH}{RH_0}\right)^3] \quad (3\text{-}17)$$

where RH is the ambient relative humidity in percentage; RH_0 is 100%.

3.4.4 Performance of existing models to predict autogenous shrinkage

Figure 3-13 shows a comparison between measured autogenous shrinkage and the predicted values based on the different models at 28 days, 56 days and 100 days. It can be seen that the observed autogenous shrinkage strains for the control concrete mixtures complied well with the predictions of AS3600-2018 for all concrete grades. AS3600-2018 autogenous shrinkage model was more accurate and conservative than the models in AS3600-2009 and Eurocode 2 for these concrete mixes. The high autogenous shrinkage of GGBFS concretes with strength below 50 MPa was not well captured by existing models. All of the codes appear to underestimated the autogenous shrinkage of GGBFS concretes for compressive strength less than 50 MPa. Even though AS3600-2018 performs better than AS3600-2009 and Eurocode 2, a recalibration of the models for concrete mixes with GGBFS for characteristic compressive strengths less than 50 MPa should be considered. For fly ash concretes, overall, no significant difference in autogenous shrinkage was observed compared to reference concretes. As a result, no recalibration of AS3600 needs to be considered for fly ash concretes based on the test results of this chapter. Notwithstanding, AS3600-2018 model predictions are accurate for all high strength concretes at all ages.

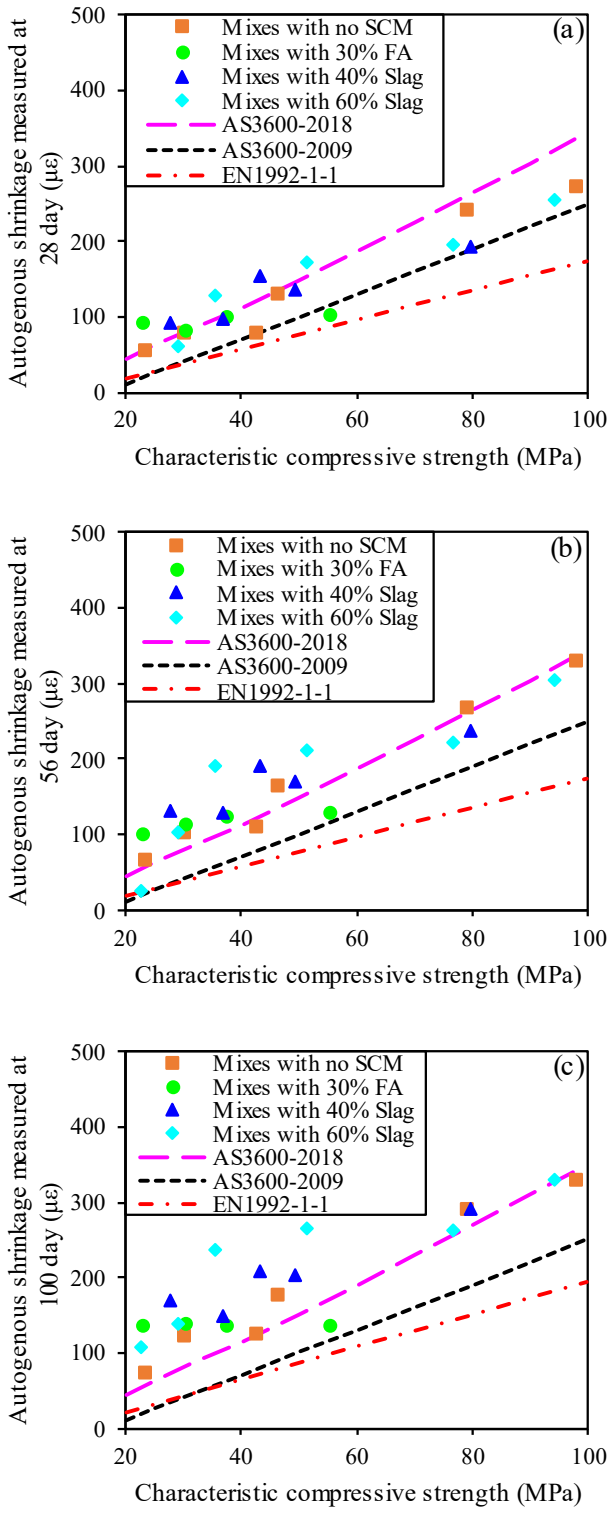

Figure 3 - 13: Autogenous shrinkage measurements against models: (a) at 28 days; (b) at 56 days; (c) at 100 days.

Figure 3-14 shows a comparison between calculated basic drying shrinkage and the predicted values based on the different models at 100 days. AS3600-2018 provided an acceptable estimation of basic drying shrinkage for reference concretes with strength greater than about 50 MPa and was more conservative than AS3600-2009 and Eurocode 2. However, AS3600-2018 is over-conservative for concrete grades less than 50 MPa. The average difference between AS3600-2018 and the experimental results for reference concretes was about 22%. AS3600-2018 failed to predict basic drying shrinkage of concretes with SCMs for all grades and requires recalibration.

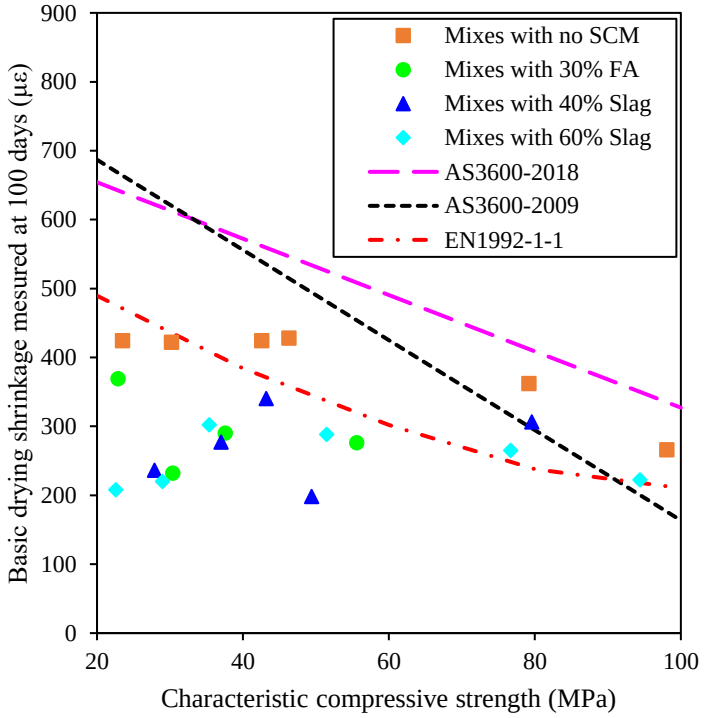

Figure 3 - 14: Basic drying shrinkage against models at 100 days.

Figure 3-15 shows a comparison between measured total shrinkage and the predicted values based on the different models at 100 days. Total shrinkage for all concrete mixtures without SCMs remained almost constant as concrete compressive strength increased which was consistent with the AS3600-2018 trend. The AS3600-2018 predictions were acceptable and

conservative for the reference concretes. The average difference between AS3600-2018 model and experimental results for the concrete mixtures without SCMs was about 18% higher, although prediction is better for higher strength grade concretes. The two other models provided poor predictions compared to AS3600-2018.

For 40-60% GGBFS concretes, the higher autogenous shrinkage observed seems to compensate for the lower drying shrinkage for some of the concrete grades less than 50 MPa. However, in most cases, the total shrinkage of GGBFS concretes was overestimated by AS3600-2018. Similarly, the total shrinkage of fly ash concretes in most of the cases was much lower than the total shrinkage of the reference concretes. The average errors obtained from AS3600-2018 model for concretes mixes with fly ash was about 38% higher, while for concrete mixes with GGBFS was about 31% higher.

Total shrinkage of 40-60% GGBFS low grade concretes was the most overestimated by AS3600-2018. Total shrinkage of concrete mixes with SCMs was lower than without SCMs because of the large reduction in drying shrinkage observed, except for some mixes with GGBFS experiencing an increase in autogenous shrinkage compensating for their low drying shrinkage.

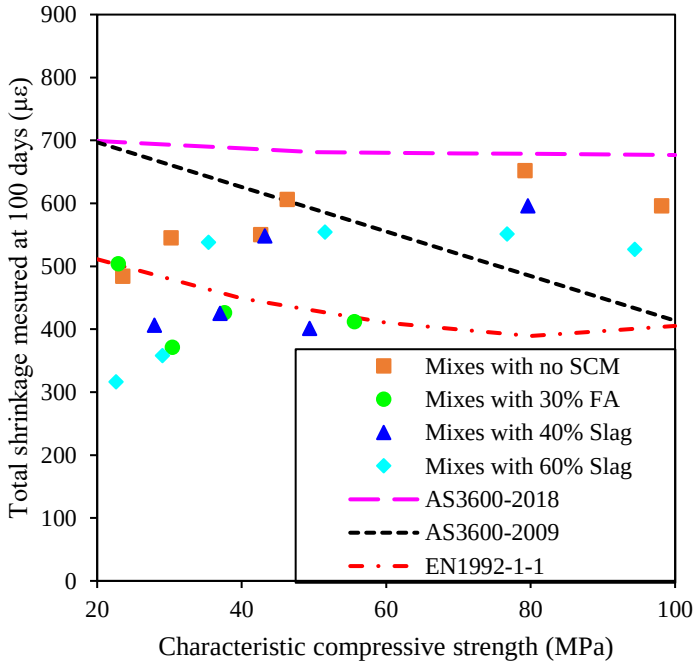

Figure 3 - 15: Total shrinkage measurement against models at 100 days.

3.5 Model recalibration for SCMs

3.5.1 Autogenous shrinkage model recalibration

GGBFS concretes with compressive strength less than 50 MPa consistently showed a higher long-term autogenous shrinkage than that of the reference concretes. As a result, modifications to AS3600-2018 are proposed below to account for the effect of GGBFS. Moreover, for concrete strengths greater than 50 MPa, AS3600-2018 model is also revised to ensure continuity in the model at a characteristic compressive strength of 50 MPa.

The following modifications are implemented into the existing model. The new autogenous shrinkage model applies to concrete mixtures with GGBFS content superior or equal to 40%.

$$\varepsilon_{cse} = \varepsilon^{*}_{cse} \times (1.0 - e^{-0.05t}) \quad (3\text{-}18)$$

$$\varepsilon^{*}_{cse} = (0.07 f'_c + 2.25) \times 50 \times 10^{-6} \quad \text{for } f'_c \leq 50 \text{ MPa} \quad (3\text{-}19)$$

$$\varepsilon^{*}_{cse} = (0.025 f'_c + 4.5) \times 50 \times 10^{-6} \quad \text{for } f'_c > 50 \text{ MPa} \quad (3\text{-}20)$$

In Eq. (3-18), the power -0.07 in the time function is adjusted to -0.05 to account for the late reactions of GGBFS concretes [129]. Indeed, the experimental results showed that autogenous shrinkage of control concrete mixes without SCMs stabilized much earlier than for concrete with GGBFS. The other coefficients have been calibrated firstly based on the least square method to fit GGBFS concretes data. Secondly, the model has been shifted up by 50%, keeping the same trend, in order to conservatively predict all autogenous shrinkage values.

3.5.2 Drying shrinkage model recalibration

Similar to the autogenous shrinkage model, a new drying shrinkage model is introduced for fly ash and GGBFS concretes based on drying shrinkage test results. The existing model in AS3600-2018 is revised as follows:

$$\varepsilon_{csd.b} = (0.5 - 0.0015 f'_c) \times \varepsilon^{*}_{csd.b} \quad (3\text{-}21)$$

In Eq. (3-21), the coefficients have been calibrated firstly based on the least square method to fit SCMs concrete data. Secondly, the model has been shifted up, keeping the same trend, to conservatively predict all drying shrinkage values. It should be noted that this drying shrinkage model is valid for a minimum content of 30% fly ash and 40% slag.

3.5.3 Comparing experimental results with recalibrated model for SCMs

Figure 3-16 presents the comparison between the current and the proposed new autogenous shrinkage model for the GGBFS concretes experimental results at 100 days. For

compressive strength inferior to or equal to 50 MPa, the current AS3600-2018 model underestimates the experimental results of concrete mixes with GGBFS by an average difference of 59% after a test period of 100 days. The modified autogenous shrinkage model was calibrated to provide conservative estimates of the experimental results, focusing on predicting accurately the long-term design autogenous shrinkage value, often called the final shrinkage value.

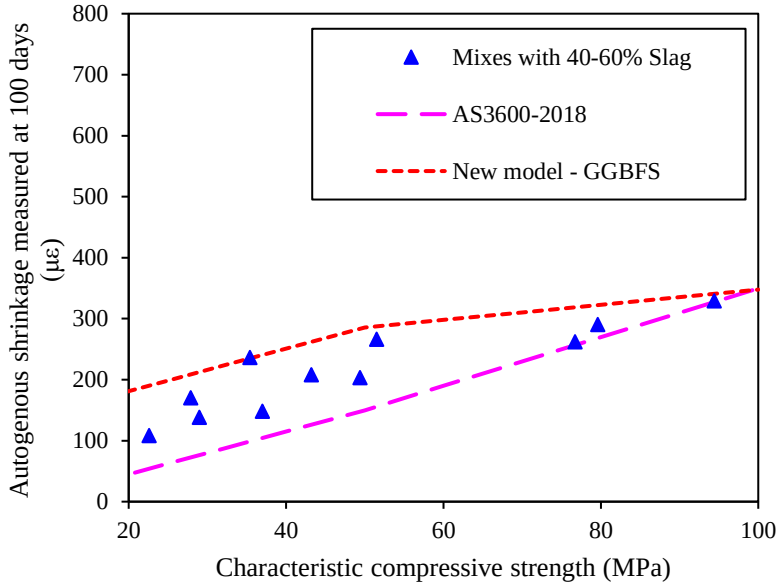

Figure 3 - 16: Comparison between current and modified autogenous shrinkage model and experimental results at 100 days.

Figure 3-17 presents the comparison between the revised model and the current AS3600-2018 model with the experimental results for concrete mixes with SCMs at 100 days. While AS3600-2018 is overestimating the drying shrinkage by about 50% at 100 days, the recalibrated model for fly ash and GGBFS is conservatively complying with experimental results. The average error at 100 days is reduced to 22%.

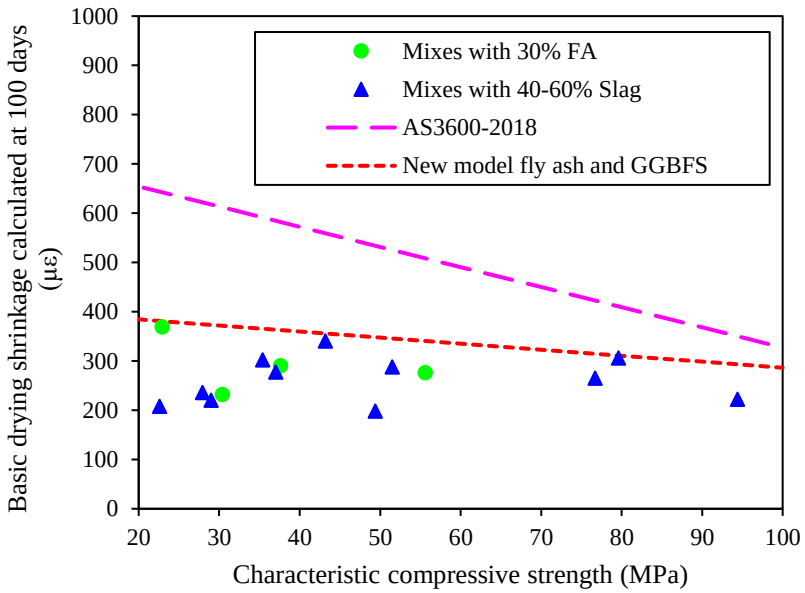

Figure 3 - 17: Comparison between current and modified drying shrinkage model and experimental results at 100 days.

Figure 3-18 shows the comparison between the AS3600-2018 model and the recalibrated model for concrete mixes with fly ash and GGBFS against measured total shrinkage experimental results at 100 days. For concrete strengths less than 50 MPa, AS3600-2018 overestimates the experimental results observed on SCMs concretes on average by about 41% at 100 days. While the overestimation is reduced to about 27% for the model after recalibration. On the other hand, for concrete strength greater than 50 MPa, the revised model for concretes mixtures with fly ash and GGBFS provides a better prediction than AS3600-2018. The average overestimation by AS3600-2018 is about 18% at 100 days. While the overestimation by the revised model is 12% in average at 100 days.

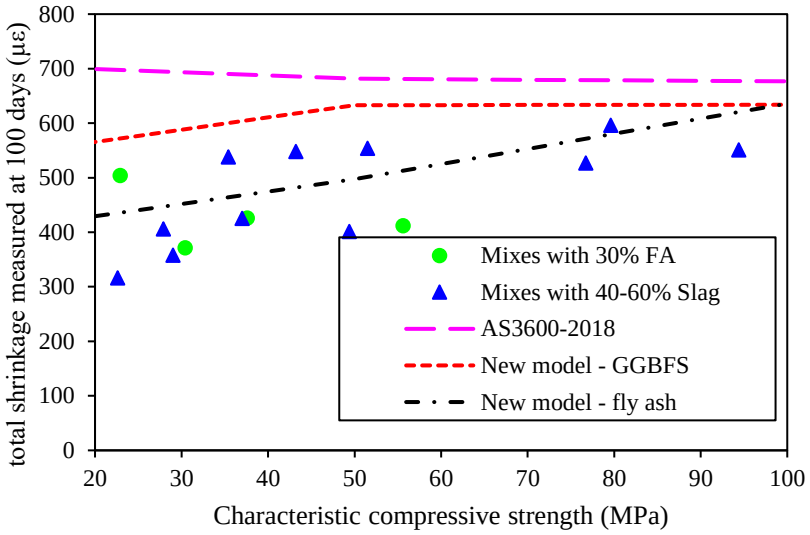

Figure 3 - 18: Comparison between current and modified total shrinkage model and experimental results at 100 days.

3.6 Conclusions

This chapter presents an experimental investigation aiming to assess autogenous shrinkage of concrete with fly ash or GGBFS. The conclusions of this work are as follows:

1. Autogenous shrinkage of concretes with GGBFS is greater than that of the reference concretes for characteristic compressive strengths ranging from 35 to 50 MPa. Autogenous shrinkage also increases with an increasing GGBFS content from 40% to 60%. No significant difference could be observed for 80 MPa and 100 MPa concretes.
2. Autogenous shrinkage of concretes with fly ash is overall equivalent to that of reference concretes. Only fly ash concrete with 55 MPa compressive strength shows a significantly lower autogenous shrinkage.
3. Starting to measure autogenous shrinkage 24 hours after batching appears to be more conservative than starting the measurements earlier, following the final setting.

4. The development of autogenous shrinkage depends on the variation of the pore structure. For GGBFS system, analysis of the pore size distribution of GGBFS paste confirmed a significant refinement of the pore structure from 28 to 90 days.
5. No difference could be noted between the chemical shrinkage of GGBFS paste and reference paste. Despite a similar chemical shrinkage, the long-term refinement of the pore structure of GGBFS pastes compared to reference pastes led to greater self-desiccation and higher autogenous shrinkage. The chemical shrinkage of the fly ash paste was significantly lower than the chemical shrinkage observed on other pastes at any age.
6. The existing AS3600-2018 model performed well to predict and better than the models in AS3600-2009 and Eurocode 2 for predicting both autogenous and drying shrinkage of concrete mixtures without SCMs. For concretes with SCMs, AS3600-2018 was not accurate and a recalibration of the model for both autogenous shrinkage and drying shrinkage was proposed.

CHAPTER 4: ANALYTICAL MODEL PREDICTING THE CONCRETE TENSILE STRESS DEVELOPMENT IN THE RESTRAINED SHRINKAGE RING TEST

Chapter 4 is a re-edited version of an article published by the candidate, 'Analytical Model Predicting the Concrete Tensile Stress Development in the Restrained Shrinkage Ring Test', in Construction and Building Materials. I did more than 50% development and all of the writing. Some of the materials in this chapter have been re-edited from a recent publication, which has been acknowledged and detailed in the 'Inclusion of Publications Statement' for this thesis.

4.1 Introduction

The risk of early-age cracking is a critical indicator of the performance of concrete structures [145, 146, 147, 148]. Concrete structures may experience unexpected cracking at an early age when the tensile stress arisen in the concrete reaches the tensile strength of concrete [149, 150]. The tensile stress induced by restraint in concrete is governed by restrained shrinkage and tensile creep [151]. To increase the safety and serviceability of concrete structures, it is essential to understand their performance over time and to develop suitable and reliable theoretical models for their analysis and safety assessment.

Numerous researchers have been investigating restrained shrinkage induced cracking of concrete [152, 66, 85, 153, 154]. Traditionally, three types of approaches have been used to investigate early age cracking of concrete caused by restrained shrinkage, such as one-dimensional restrained shrinkage analysis [155, 156], two-dimensional restrained shrinkage analysis [157, 158] and restrained ring test [159, 160]. The restrained ring test is the most

popular experimental method to determine the cracking potential of concrete subjected to restrained shrinkage because it is simple to implement compared to the one-dimensional and the two-dimensional restrained shrinkage tests [152, 161, 162].

Hossain and Weiss [152] proposed a method allowing to assess both residual stress development and stress relaxation using the restrained ring test. They also provided quantitative information to estimate the theoretical elastic stress and actual residual stress in a restrained ring specimen. Khan et al. [66] conducted an experimental study using both restrained ring tests and tensile creep tests to examine the effect of early age tensile creep on early-age cracking. Results showed that the tensile creep coefficients measured using tensile creep tests could be used to assess the stress relaxation induced by tensile creep in the restrained ring test. In another study, Khan et al. [149], carried out internally restrained shrinkage tests using reinforced concrete specimens including the effect of tensile creep. The degree of restraint and ageing coefficient were calibrated [149].

As mentioned above, the restrained ring test is the most popular method to investigate the risk of early-age cracking and evaluate tensile stress development. The tensile stress development in concrete can be computed by measuring the strain of the steel ring [152]. As such, this approach is not suitable for predicting the tensile stress development in concrete but only for the analysis of ring test results. Meanwhile, the theoretical elastic stress model proposed by Hossain and Weiss [152] allows for calculating the tensile stress in concrete from free shrinkage, elastic modulus, and degree of restraint. The effect of tensile creep is not considered. Thus, this model needs to be improved to account for the effect of tensile creep and correctly predict the tensile stress development in concrete.

Supplementary cementitious materials (SCMs) and new construction materials have been widely used in concrete due to numerous beneficial effects, including i) improving the sustainability of concrete by reducing the usage of Portland cement, ii) lowering the heat of hydration by decreasing the content of cement, and iii) improving the durability of concrete [163, 164, 1, 2, 165, 166]. However, it is still difficult to accurately predict the performance of these blended cement-based concretes because of the inconsistent physical and chemical properties of SCMs used in concrete [167, 168]. There are also controversial results on their shrinkage and early-age cracking behaviour [169, 51, 71]. Several experimental studies can be found in the literature regarding the effects of fly ash and slag on the risk of early-age cracking. Khan et al. [170] concluded that the strength development of fly ash-blended concrete is lower than OPC concrete and the cracking time is reduced. Nguyen et al. [171] summarized that ferronickel slag decreases the risk of early-age cracking because of a significantly higher tensile creep.

In this chapter, an analytical model is proposed to accurately predict the tensile stress in the restrained concrete ring test and capture the effect of both restrained shrinkage and tensile creep. The risk of early-age cracking of concrete is significantly influenced by the compressive strength and the incorporation of either fly ash or GGBFS. As a result, the analytical model presented in this chapter is validated considering a total of 21 concretes consisting of 6 strength grades (25 MPa to 100 MPa), one fly ash blend (30%), and 2 different GGBFS blends (40% and 60%). However, the purpose of this chapter is not to discuss the influence of the concrete mix design parameters such as fly ash or GGBFS content on early-age cracking.

4.2 Prediction of concrete tensile stress in the restrained ring test

The shrinkage of the concrete ring in the radial direction can induce a uniform external pressure to the steel ring. The schematic diagram of the pressure and stress obtained in the ring specimen is shown in Figure 4-1. The steel ring is pressurised at the outer surface, and the strain developing in the steel ring is equivalent to the measured strain at the corresponding time [152]. The tensile stress of concrete specimens (σ_{act}) can be expressed as a function of the measured steel strain, steel properties, and dimensions of the ring as shown in Eq. (4-1) [152]:

$$\sigma_{act} = -\varepsilon_{st} \cdot E_s \cdot \frac{R_{OS}^2 - R_{IS}^2}{2R_{OS}^2} \frac{R_{OC}^2 + R_{OS}^2}{R_{OC}^2 - R_{OS}^2} \quad (4\text{-}1)$$

where ε_{st} is the measured steel strain; E_s is the elastic modulus of steel; R_{OS} and R_{IS} are the outer and inner radius of the steel ring; and R_{OC} is the outer radius of the concrete ring.

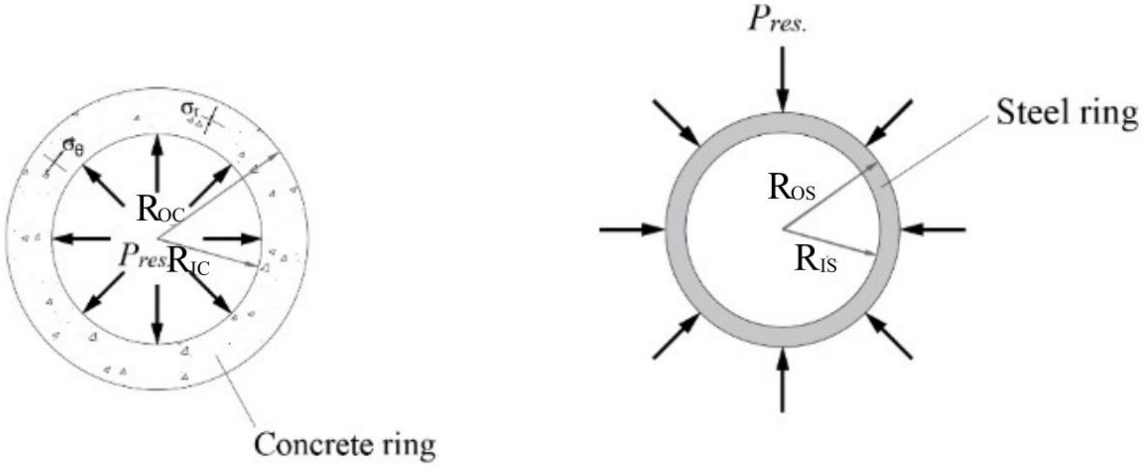

Figure 4 - 1: Concrete and steel ring under surface pressure.

The model shown in Eq. (4-1) provides an accurate estimation of the development of tensile stress in the concrete ring caused by restrained shrinkage. However, this model requires measuring the steel strain. In this context, Eq. (4-1) can only be used to analyse the

results of the restrained ring test instead of predicting the tensile stress development in concrete. For the sake of prediction, the development of the concrete tensile stress should be deduced from the concrete free total shrinkage and the creep coefficient, which can be provided through material testing or from creep and shrinkage models. Thus, it is critical to establish an analytical model to predict the concrete tensile stress development capturing the effects of restrained shrinkage and tensile creep.

As mentioned in Figure 4-1, it is assumed that a fictitious pressurising force is applied to the interface between steel and concrete rings. Hence, the fictitious pressurising force can be expressed from the perspectives of steel and concrete rings respectively by considering the new and original area of steel and concrete rings as shown in Eq. (4-2):

$$P_{el} = -\sigma_{el} \cdot \frac{(R_{OS}^2 - R_{IS}^2)}{(1+\nu_s)R_{IS}^2 + (1-\nu_s)R_{OS}^2} \tag{4-2a}$$

$$P_{el} = \sigma_{el} \cdot \frac{(R_{OC}^2 - R_{IC}^2)}{(1+\nu_c)R_{OC}^2 + (1-\nu_c)R_{IC}^2} \tag{4-2b}$$

where ν_s and ν_c are the Poisson's ratio of steel and concrete respectively; σ_{el} is the pressurising stress; P_{el} is the pressurising force.

The deformation of the outer surface of the steel ring under fictitious force can be expressed using Eq. (4-3a), while the displacement of the inner surface of the concrete ring is provided in Eq. (4-3b).

$$U_s = -R_{OS} \cdot \varepsilon_s \tag{4-3a}$$

$$U_c = R_{IC} \cdot \varepsilon_c \tag{4-3b}$$

where U_s and U_c are the displacement at the outer surface of the steel ring and the inner surface of the concrete ring, respectively; ε_s and ε_c are the total strain of steel and concrete, respectively. In Eq. (4-3b), since concrete is a viscoelastic material that undergoes creep

over time under sustained loading [66, 172, 173], stress relaxation occurs. As a result, tensile stress redistribution occurs in the concrete ring over time which changes the time-dependent deformations. The total strain of concrete ε_c is considered the sum of the elastic strain ε_{el}, the creep strain ε_{cr}, and the free shrinkage strain ε_{sh}.

$$\varepsilon_c = \varepsilon_{el} + \varepsilon_{cr} + \varepsilon_{sh} \tag{4-4}$$

In Eq. (4-4), the creep strain ε_{cr} can be rewritten in terms of ageing coefficient and creep coefficient as follows:

$$\varepsilon_{cr} = \chi(t,\tau)\ \varphi(t,\tau)\ \varepsilon_{el} \tag{4-5}$$

where $\varphi(t,\tau)$ is the tensile creep coefficient which is defined as the ratio between tensile creep strain and instantaneous elastic strain; and $\chi(t,\tau)$ is the ageing coefficient of concrete. The recommended value of the ageing coefficient is 0.80 for relaxation problems [174].

By substituting Eqs. (4-4) and (4-5) into Eq. (4-3b), the displacement of the inner surface of the concrete ring can be calculated as presented in Eq. (4-6):

$$U_c = R_{IC} \cdot \left[\left(1 + \chi(t,\tau)\ \varphi(t,\tau)\right)\varepsilon_{el} + \varepsilon_{sh}\right] \tag{4-6}$$

Hence, the deformation of the steel and concrete ring in Eqs. (4-3) and (4-6) can be rewritten as follows:

$$U_s = -R_{OS} \cdot \frac{\sigma_{el}}{E_s} \tag{4-7a}$$

$$U_c = R_{IC} \cdot \frac{\sigma_{el}}{\bar{E}_e} + R_{IC} \cdot \varepsilon_{sh} \tag{4-7b}$$

where $\bar{E}_e(t,\tau)$ is the age-adjusted effective modulus, and this is the so-called age-adjusted effective modulus method.

Conventionally, the age-adjusted effective modulus was adopted to consider the reduction in creep coefficient caused by the ageing of concrete [175]. Torst [175] proposed the age-

adjusted effective modulus method for creep analysis. This method was then fully demonstrated by Dilger and Neville [176], Bazant [177], and Gilbert and Ranzi [174]. Hence, the age-adjusted effective modulus $\bar{E}_e$ is applied in Eq. (4-7b) to account for the effects of concrete ageing and tensile creep in the calculation of the tensile stress in concrete.

Considering the displacement compatibility, the deformation of the outer radius of the steel ring (R_{OS}) should be equivalent to the inner radius of the concrete ring (R_{IC}). The fictitious interface pressure compresses the steel ring and expands the concrete ring until displacement compatibility is accomplished ($R_{OS} = R_{IC}$).

After displacement compatibility is satisfied due to the fictitious interface force, the difference between the two deformations should be equivalent to the amount of radial deformation as shown in Eq. (4-8).

$$U_c = U_s \tag{4-8}$$

By substituting Eqs. (4-2), (4-3) and (4-7) into Eq. (4-8), the fictitious interface pressure can be expressed as follows:

$$P_{el} = -\frac{\varepsilon_{sh}\bar{E}_e}{\frac{\bar{E}_e}{E_s}\cdot\frac{[(1+\nu_s)R_{IS}^2+(1-\nu_s)R_{OS}^2]}{(R_{OS}^2-R_{IS}^2)}+\frac{[(1+\nu_c)R_{OC}^2+(1-\nu_c)R_{OS}^2]}{(R_{OC}^2-R_{OS}^2)}} \tag{4-9}$$

Once the fictitious interface force is determined from Eq. (4-9), the tensile stress in concrete σ_{cs} can be expressed as follows:

$$\sigma_{cs} = -\frac{\varepsilon_{sh}\bar{E}_e}{\frac{\bar{E}_e}{E_s}\cdot\frac{[(1+\nu_s)R_{IS}^2+(1-\nu_s)R_{OS}^2]}{(R_{OS}^2-R_{IS}^2)}+\frac{[(1+\nu_c)R_{OC}^2+(1-\nu_c)R_{OS}^2]}{(R_{OC}^2-R_{OS}^2)}}\cdot\frac{R_{OC}^2+R_{OS}^2}{R_{OC}^2-R_{OS}^2} \tag{4-10}$$

In the literature, Hossain and Weiss also revealed the theoretical elastic stress model by neglecting the effect of tensile creep. The theoretical maximum tensile stress in concrete is expressed as follows [152]:

$$\sigma_{max} = -\frac{\varepsilon_{sh} E_c}{\frac{E_c}{E_s} \cdot \frac{[(1+\nu_s)R_{IS}^2 + (1-\nu_s)R_{OS}^2]}{(R_{OS}^2 - R_{IS}^2)} + \frac{[(1+\nu_c)R_{OC}^2 + (1-\nu_c)R_{OS}^2]}{(R_{OC}^2 - R_{OS}^2)} \frac{R_{OC}^2 + R_{OS}^2}{R_{OC}^2 - R_{OS}^2}} \quad (4\text{-}11)$$

where σ_{max} is the theoretical elastic stress that would develop if tensile creep did not occur. Therefore, Eq. (4-11) always overestimates the tensile stress in concrete, and this is the so-called theoretical maximum tensile stress model.

According to ACI 207.2 [178], the tensile stress due to restraint can be determined as per Eq. (4-12):

$$\sigma_{cs} = D_R \, \varepsilon_{sh} \, E_c \quad (4\text{-}12)$$

where D_R is the degree of restraint. It is defined as the ratio of the actual stress caused by the volume change to the stress produced in a fully restrained condition. Numerically speaking, the strain is equal to the product of the degree of restraint and the change in unit length when the concrete is not restrained [178].

Note that the elastic modulus of concrete in Eq. (4-12) should be changed to the age-adjusted effective modulus as explained above. Thus, the tensile stress development can be rewritten as shown in Eq. (4-13):

$$\sigma_{cs} = D_R \, \varepsilon_{sh} \, \bar{E}_e \quad (4\text{-}13)$$

Considering the form of Eqs. (4-10) and (4-13), the degree of restraint D_R can be written as shown in Eq. (4-14a). The degree of restraint is also suggested in ACI 207.2 [178], and it is taken as the ratio of the stiffness of the steel ring to the sum of the steel ring and concrete ring. Khan et al. [66] proposed an alternative degree of restraint based on ACI 207.2 [178] by implementing the age-adjusted effective modulus method. Both the degree of restraint suggested by ACI 207.2 [178] and Khan et al. [66] are defined herein as shown in Eqs. (4-14b) and (4-14c), respectively:

$$D_R = \frac{\frac{R_{OC}^2 + R_{OS}^2}{R_{OC}^2 - R_{OS}^2}}{\frac{\bar{E}_e}{E_s} \cdot \frac{[(1+\nu_s)R_{IS}^2 + (1-\nu_s)R_{OS}^2]}{(R_{OS}^2 - R_{IS}^2)} + \frac{[(1+\nu_c)R_{OC}^2 + (1-\nu_c)R_{OS}^2]}{(R_{OC}^2 - R_{OS}^2)}} \quad (4\text{-}14a)$$

$$D_R = \frac{1}{1 + \frac{A_c E_c}{A_s E_s}} \quad (4\text{-}14b)$$

$$D_R = \frac{1}{1 + \frac{A_c \bar{E}_e}{A_s E_s}} \quad (4\text{-}14c)$$

where A_c and A_s are the cross-sectional area of concrete and steel ring, respectively. By using the D_R proposed by ACI 207.2 [178] or Khan et al. [66] in Eq. (4-12), the model of tensile stress σ_{cs} can be considered as a simplified model. In this chapter, the analytical model in Eq. (4-13) is used, providing a better estimation of concrete tensile stress. The proposed analytical model will be verified by considering a large number of concrete mixes as well as numerical simulations (Section 4.5).

4.3 Experimental program

4.3.1 Materials and mixture proportions

General Purpose (GP) cement was used to prepare all concrete mixtures, complying with Australian Standard AS3972 type GP [100]. The compressive strength of GP cement is higher than 45 MPa at 28 days. It contains up to 7.5% of mineral additions such as limestone to reduce the clinker content and up to 5% of additional mineral constituents such as cement kiln dust [100]. Two typical SCMs, such as fly ash and GGBFS, were used in this chapter, complying with Australian Standard AS3582.1 [101] and AS3582.2 [102], respectively. Table 4-1 shows the chemical oxide compositions of GP cement, fly ash, and GGBFS measured by X-ray fluorescence (XRF) analysis. All concrete mixes were prepared using a crushed basalt coarse aggregate with a maximum size of 10 mm and Sydney fine

sand with a maximum nominal grade size of 2.36 mm. The particle size distribution of both coarse and fine aggregates was assessed by sieving analysis as shown in Figure 4-2. To control workability, a superplasticizer (Master Glenium SKY 8100) was utilised for some concrete mixtures.

Table 4 - 1: Chemical oxide compositions of GP cement, fly ash and GGBFS.

Chemical composition	GP cement (wt.%)	Fly ash (wt.%)	GGBFS (wt.%)
SiO_2	18.8	65.9	36.6
Al_2O_3	5.0	22.1	10.2
Fe_2O_3	2.8	3.4	0.4
CaO	63.8	1.6	42.9
MgO	1.0	0.7	6.7
Na_2O	0.3	0.6	0.3
K_2O	0.7	1.8	0.4
TiO_2	0.3	0.9	0.5
SO_3	3.0	0.1	1.3
Mn_3O_4	-	0.1	0.3

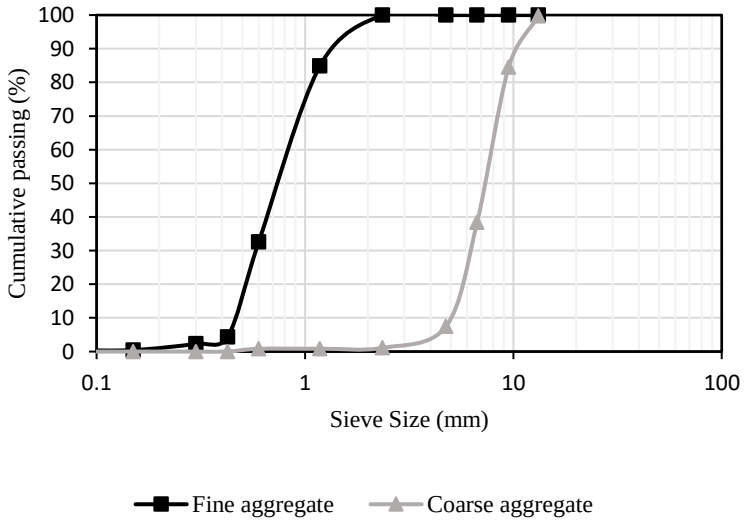

Figure 4 - 2: Gradation of coarse and fine aggregates.

Six different concrete grades targeted at 25, 32, 40, 50, 80, and 100 MPa were prepared to consider a wide range of strengths of concrete. The mixtures were designated as ‘N25’, ‘N32’, ‘N40’, ‘N50’, ‘S80’, and ‘S100’, respectively, as shown in Table 4-2. Mixture ‘0’ was the reference mixture without any SCMs, while mixtures ‘FA30’, ‘G40’, and ‘G60’ represented the cement replacement by 30% fly ash, 40% GGBFS and 60% GGBFS, respectively. Fly ash was not considered for the high strength concretes (i.e., 80 and 100 MPa) because high strength concrete mixes with fly ash require a water-to-binder ratio (w/b) lower than 0.2, resulting in an excessive dosage of superplasticizer. Such mix negatively affects the practical application of the concrete mix and causes the problem of bleeding and increased setting time [179, 180]. For each strength grade of concrete mix, the w/b was adjusted based on the w/b of the control mixture for each strength grade to achieve a suitable compressive strength with SCMs. This is attributed to late strength development due to the slower reactivity of fly ash and GGBFS than the reactivity of GP cement [181, 182].

4.3.2 Mechanical properties of concrete

Concrete cylinders with dimensions of 200 mm in height by 100 mm in diameter were cast and cured in an environmentally controlled condition with a temperature at 23 °C and relative humidity of 50% to meet the same exposure condition of the restrained ring test. The accuracy of a static hydraulic machine is 0.1 MPa for measuring the mechanical properties of concrete mixes, including compressive strength, indirect tensile strength, and elastic modulus. The results were the average of three concrete cylinders tested at the age of 1, 2, 3, 7, and 28 days. The time-dependent compressive strength of all mixtures was conducted in accordance with AS1012.9 [183]. The indirect tensile strength of each

concrete mixture was assessed through a splitting test according to AS1012.10 [184]. The elastic modulus of all the concrete mixes was obtained in accordance with AS1012.17 [185].

Table 4 - 2: Mixture proportions of concrete.

Sample ID	Mix proportions by weight (kg/m^3)						w/b
	GP Cement	FA	GGBFS	Coarse Agg	Fine Agg	Superplasticizer (ml/m^3)	
N25-0	310	0	0	1059	866	400	0.56
N25-FA30	215	95	0	1071	876	400	0.46
N25-G40	185	0	125	1056	864	400	0.52
N25-G60	125	0	185	1056	864	400	0.5
N32-0	360	0	0	1025	839	500	0.49
N32-FA30	250	110	0	1043	853	500	0.4
N32-G40	215	0	145	1033	845	500	0.45
N32-G60	145	0	215	1037	848	500	0.43
N40-0	450	0	0	966	790	600	0.43
N40-FA30	315	135	0	983	804	600	0.34
N40-G40	270	0	180	974	797	600	0.41
N40-G60	180	0	270	981	803	600	0.37
N50-0	510	0	0	927	759	700	0.4
N50-FA30	355	155	0	955	782	700	0.3
N50-G40	305	0	205	930	761	700	0.39
N50-G60	205	0	305	941	770	700	0.35
S80-0	585	0	0	908	743	1000	0.28
S80-G40	350	0	235	911	746	1000	0.27
S80-G60	235	0	350	915	748	1000	0.26
S100-0	650	0	0	880	720	1200	0.22
S100-G60	260	0	390	880	720	1200	0.21

4.3.3 Restrained ring test

Figure 4-3 shows the dimension of the mould for the restrained ring test and the ring specimen used in this chapter. The presented restrained ring test is in accordance with modified ASTM C1581 [66, 170, 149, 186]. The dimensions of the inner and the outer radii

of the steel ring were R_{IS} = 130 mm and R_{OS} = 135 mm, respectively. The inner radius of the concrete ring is equivalent to the outer radius of the steel ring (i.e., $R_{IC} = R_{OS}$), and the outer radius of the concrete ring was R_{OC} = 170 mm, and the system was 70 mm in height. Two restrained ring tests were conducted in parallel. The outer surface of the inner steel ring was oiled to minimise the effect of friction between the steel and concrete rings. Three strain gauges with an accuracy of 1 με were placed on the inner steel surface at mid-height at equal distances (angle of 120°). Immediately after casting, the fresh concrete in the restrained ring mould was covered by wet cloth to minimise moisture loss. After 24 hours, the mould of the outer steel ring was removed, and the specimens were moved to the environmentally controlled room at a temperature of 23 °C and relative humidity (RH) of 50%. In the present chapter, the top, bottom, and outer surfaces of the concrete ring were exposed to drying, as reported by previous studies [160, 187, 188]. The steel strains were monitored over time from 1 day after casting to the time of cracking. In general, a sudden drop in steel strain was observed when cracking occurred.

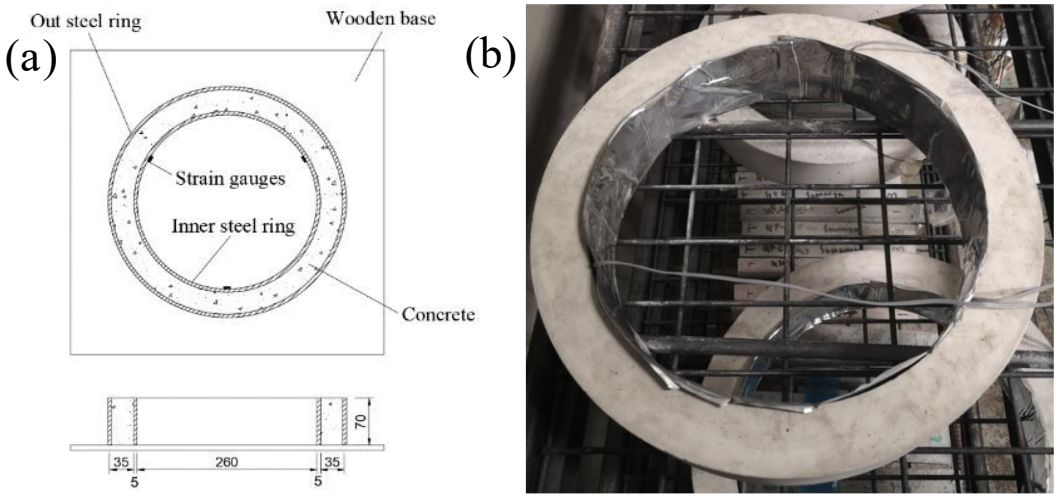

Figure 4 - 3: Restrained ring test: (a) dimension; (b) ring specimen.

4.3.4 Free shrinkage test

In this chapter, free shrinkage is defined as the total shrinkage of specimens without external restraint [189]. The free shrinkage tests were performed using prismatic specimens with the size of 280 mm × 75 mm × 75 mm, as shown in Figure 4-4. Three free shrinkage samples were prepared for each concrete mix, as shown in Table 4-2. All concrete prismatic specimens were prepared in accordance with the provision of AS1012.13 [7]. The moulds containing fresh concrete were covered by wet cloth to avoid any moisture loss. After 24 h of curing, the concrete prisms were removed from the moulds, and the specimens were stored in the environmentally controlled room (23°C and RH = 50%) where the ring tests were conducted. The free shrinkage was measured from 1 day after the casting until 28 days by the digital shrinkage gauge meter with an accuracy of 1 με. The dimensions of the prismatic concrete specimens and the concrete ring specimens were different. However, the free shrinkage in the concrete ring (ε_{sh}) in Eq. (4-4) can be assumed to be equal to the free shrinkage measured from the prismatic specimens because of their similar volume-to-surface area ratio (37.5 mm for the prismatic specimen and 35 mm for the concrete ring).

Figure 4 - 4: Total shrinkage specimens.

4.3.5 Tensile creep test

Tensile creep tests were performed using dog-bone-shaped specimens. The method for the tensile creep test was designed by the authors and used in the previous works [66, 51, 149, 171]. The dimensions and loading configuration of the dog-bone-shaped specimens are shown in Figure 4-5. In this design, the specimens have an equal cross-section part with a length of 50 mm at mid-height. The stress distribution in this part is assumed to be even. The strain gauges were attached to each 35-mm-thick face of this part, where the width of the specimen is 70 mm. The curing procedure for dog-bone specimens was the same as the restrained ring and the prism tests. All specimens were covered with a wet cloth during the 24 hours period after casting. After 24 hours, the specimens were demoulded and moved to the environmentally controlled room (23°C and RH = 50%). The dog-bone specimen was fixed into the creep rig by tightening the nut on the top of the frame. Steel plates with two threaded bolts were cast in the specimen and they were glued to both ends of the specimen to ensure an even stress distribution from the applied tensile load. Two dog-bone specimens were loaded under a sustained stress level of 50% of the tensile strength measured at the age of 2 days for each mix. Strain gauges with an accuracy of 1 με were attached to the faces of the dog-bone specimens to measure the total deformation, including elastic, creep, and shrinkage strains, as shown in Eq. (4-15):

$$\varepsilon_{tot} = \varepsilon_{el} + \varepsilon_{cr} + \varepsilon_{sh} \quad (4\text{-}15)$$

In the tensile creep test, two loaded dog-bone specimens were also accompanied by two unloaded dog-bone specimens to assess the free shrinkage in the same control room. The elastic strain can be easily calculated based on the constant tensile stress and elastic

modulus. Then the creep strain can be calculated by using the total strain minus the shrinkage strain minus the elastic strain, as shown in Eq. (4-16).

$$\varepsilon_{cr} = \varepsilon_{tot} - \varepsilon_{el} - \varepsilon_{sh} \quad (4\text{-}16)$$

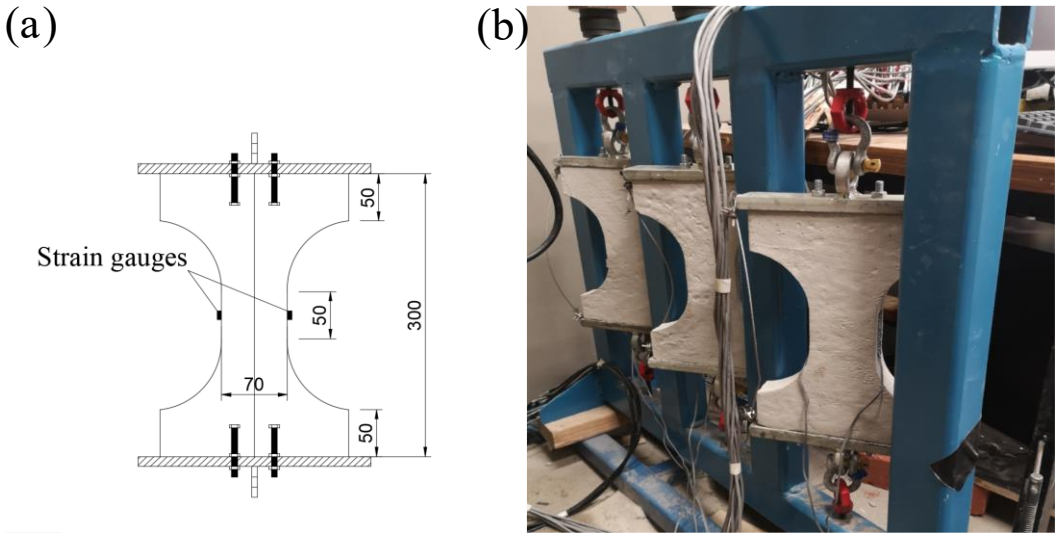

Figure 4 - 5: Tensile creep test using dog-bone-shaped specimens: (a) dog-bone-shaped specimen; and (b) loading of dog-bone-shaped specimen.

4.4 Finite element modelling

Finite element modelling of restrained ring specimens was performed using the commercial finite element (FE) code ABAQUS, to simulate the time-dependent tensile stress development. For the FE modelling, due to the symmetry of the restrained ring specimens and the uniform free shrinkage, a two-dimensional (2-D) axisymmetric model was used for simulating the steel and concrete ring. An axisymmetric quadrilateral element with eight nodes and quadratic shape functions (CAX8) was used. The generated mesh for steel and concrete parts contains 2 × 28 and 14 × 28 elements in radial (r) and vertical (z) direction, respectively. The geometry and finite element mesh of the axisymmetric model are presented in Figure 4-6. The boundary condition of the axisymmetric model is assumed that the vertical displacement of the bottom edge is zero. The contact layer is the interface

between steel and concrete parts where is located at the right edge of steel and left edge of concrete in the axisymmetric model. The friction coefficient of tangential direction is taken as zero because the effect of friction is eliminated by applying the mould releasing agent in the experimental restrained ring test. The hard contact is taken in the normal direction.

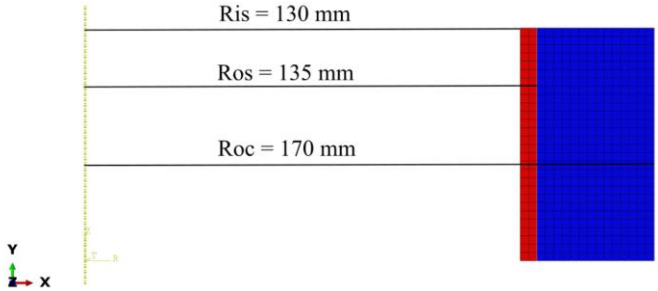

Figure 4 - 6: Geometry and finite element mesh of the axisymmetric model.

Since the shrinkage behaviour of concrete cannot be implemented as a direct entry in FE codes, a fictitious temperature drop approach was adopted to represent the shrinkage behaviour in this chapter because this approach has been successfully used in the literature [190, 191]. This approach mimics the shrinkage of concrete by applying a fictitious temperature field that causes a length change identical to the free shrinkage. To simplify the calculation, the coefficient of thermal expansion is taken as $\alpha = 10 \times 10^{-6}\ \mathrm{K}^{-1}$. Thus, the fictitious temperature drop at different ages can be calculated by using the free shrinkage strain divided by the coefficient of thermal expansion of concrete.

$$T(t) = \frac{\varepsilon_{sh}(t)}{\alpha} \tag{4-17}$$

where $T(t)$ is the time-dependent fictitious temperature and α is the coefficient of thermal expansion of concrete, $\varepsilon_{sh}(t)$ is the experimentally measured free shrinkage strain of concrete as explained in Section 4.3.3.

In addition, the elastic modulus of steel is taken as 210 GPa. The Poisson's ratio is assumed to be 0.3 and 0.18 for steel and concrete, respectively. Isotropic elasticity is used as constitutive models for steel and concrete. The age-adjusted effective modulus of concrete was used as a direct entry for concrete material properties. According to Eq. (4-7b), the age-adjusted effective modulus is calculated based on the tensile creep coefficient. However, since the geometry and concrete age when the test started were different for the restrained ring and the dog-bone tensile creep tests, the measured tensile creep coefficients from dog-bone specimens were modified as follows [192]:

$$\varphi(t,\tau)_r = \varphi(t,\tau)_d \times \frac{(k_2 k_3)_r}{(k_2 k_3)_d} \tag{4-18}$$

where $\varphi(t,\tau)_r$ and $\varphi(t,\tau)_d$ represent tensile creep coefficient of ring specimen and dog-bone specimen, respectively. According to Australian Standard AS3600 [192], k_2 is the factor depending on the hypothetical thickness and age of concrete which is calculated in Eq. (19a), k_3 is the factor depending on the age of concrete τ at the time of loading which is calculated in Eq. (4-19b) [192].

$$k_2 = \frac{\alpha_2 t^{0.8}}{t^{0.8} + 0.15 t_h} \tag{4-19a}$$

$$k_3 = \frac{2.7}{1 + \log(\tau)} \tag{4-19b}$$

where α_2 is calculated as $1.0 + 1.12e^{-0.008 t_h}$ and t_h is the hypothetical thickness of the specimens as shown in Eq. (4-19c) [192].

$$t_h = \frac{2A_g}{u_e} \tag{4-19c}$$

where A_g is the gross cross-sectional area and u_e is the exposed perimeter of a member cross-section.

4.5 Validation and discussion

4.5.1 Test results

The time-dependent mechanical properties including compressive strength, indirect tensile strength, and elastic modulus are provided in Table 4-3. As shown in Table 4-3, the mechanical properties test failed for N25-G40 and N25-G60 at the age of 1 day due to their very low compressive and tensile strength at that time. It can be seen that the incorporation of SCMs delays the development of compressive strength, indirect tensile strength, and elastic modulus. For the concrete mixes with 30% fly ash, the average compressive, indirect tensile strengths, and elastic modulus were 98%, 97% and 92% to that of control mixtures at the age of 28 days. While the average 28-day compressive, indirect tensile strengths and elastic modulus were 91%, 92%, 92% and 83%, 85%, 92% to that of control mixtures for the GGBFS content increased from 40% to 60%, respectively.

Figure 4-7 shows the free total shrinkage development measured on prismatic specimens. The measured free shrinkage of GGBFS concrete was higher than that of reference concrete for low-strength concrete. The free shrinkage of G40 and G60 concrete was on average 7% and 23% higher than that of reference mixtures at 28 days, respectively. However, for high-strength GGBFS concrete, a slight increase in free shrinkage was observed compared to that of reference concrete. For concretes mixes with fly ash, the absolute value of free shrinkage strain of fly ash concretes decreased by on average 25% compared to that of control concretes.

Table 4 - 3: Mechanical properties of concrete.

Sample ID	Measured compressive strength (MPa)					Splitting Tensile strength (MPa)					Elastic modulus (GPa)				
	1d	2d	3d	7d	28 d	1d	2d	3d	7d	28d	1d	2d	3d	7d	28d
N25-0	9	14.5	16	22.5	27.5	1.1	1.8	2.2	2.7	2.8	22.3	24	24.3	27.5	28.4
N25-FA30	6	11	14	18.5	24.5	1	1.6	1.7	2.5	2.7	20.7	20.8	22.6	25.3	24.8
N25-G40	N/A	9.2	11.5	17.5	21.5	N/A	1.2	1.5	2.1	2.4	N/A	16.2	21.3	24.4	27.4
N25-G60	N/A	5.8	10.5	15	17	0.4	0.9	1.1	1.8	1.9	N/A	20.6	23.6	20.8	23.1
N32-0	12	17	24	29	32.5	1.8	2.3	2.7	3.7	3.8	21.3	27.1	29.2	33.5	37
N32-FA30	13	18	21	26	32.5	1.8	2.2	2.6	3.1	3.3	26.3	27.2	28.2	29.2	35
N32-G40	8.7	14.5	18.5	24.5	29	1.2	1.9	2.5	2.8	3.1	20	23.8	28.8	28.9	31
N32-G60	5.5	9.3	14.5	23.5	27.5	0.8	1.2	1.8	2.7	3.1	17.7	21.6	24.1	26.4	29.3
N40-0	17	30.5	32.2	34.7	40.7	2.4	3.2	3.4	3.6	3.8	22.7	24.9	27.8	33.1	36.3
N40-FA30	18.2	24.4	30.9	35.3	42.1	2.1	2.8	3.2	3.3	3.9	25.7	27.1	30.6	32.8	34.7
N40-G40	11.6	20.5	26.4	33.9	42.4	1.5	2.1	2.8	3.4	3.9	20.6	22.4	25.5	30.9	33.1
N40-G60	8.5	15.6	21.6	29.3	37.7	1	1.8	2.3	3	3.5	18.3	22.7	25.3	28.6	31.7
N50-0	18	28	34.5	40.5	50.5	2.2	3.2	3.2	3.6	4.6	24	29.5	31.9	35.1	36.7
N50-FA30	19	27	33.5	41	50	2.3	2.9	3.5	3.9	4.6	28.2	30.8	31.8	33	33.7
N50-G40	14.9	22.7	29.2	40.1	47.2	1.7	2.3	3.1	4.1	4.4	21.4	23.9	26.8	28.0	30.7
N50-G60	8.4	16.5	21.7	34.3	44.7	1.1	2.0	2.9	3.0	3.6	25.6	27.5	29.2	32.7	34.2
S80-0	49.1	61.4	67.6	77.1	85.7	4.7	5.1	5.3	6.0	6.2	33.2	36.2	37.2	38.4	38.6
S80-G40	30.8	45.8	54.9	67.8	77.5	3.3	4.1	4.7	5.0	5.7	31.4	35.6	37.8	39.5	40.4
S80-G60	21.8	38.8	45.9	60.7	73.6	2.4	3.3	4.2	4.9	5.9	28.1	32.7	34.6	38.0	39.3
S100-0	63.1	73.5	85.1	90.0	99.0	5.8	6.2	6.5	6.6	6.9	36.2	37.1	37.8	38.1	39.0
S100-G60	28.2	44.1	54.0	70.1	85.4	2.7	3.9	4.5	5.3	6.5	31.5	34.4	37.3	39.4	40.9

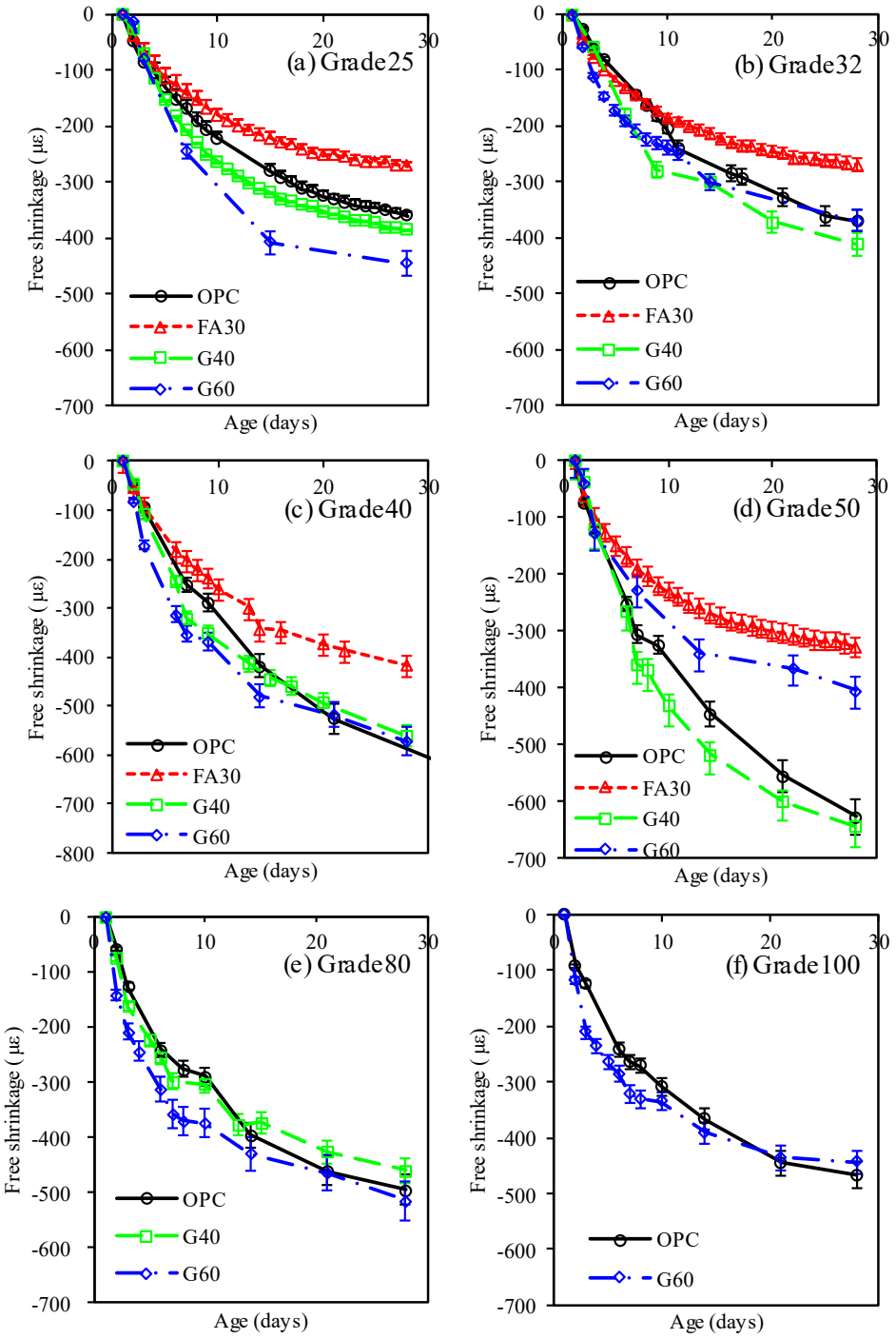

Figure 4 - 7: Time-dependent free shrinkage of: (a) Grade 25; (b) Grade 32; (c) Grade 40; (d) Grade 50; (e) Grade 80; and (f) Grade 100.

Figure 4-8 presents the tensile creep coefficients measured on dog-bone specimens. Some tensile creep tests were stopped for some of the grade 32 and 40 mixes when cracking was observed on the rings. The tensile creep coefficient of concrete mixes with 30% fly ash concrete was slightly reduced compared to that of OPC concrete. This was consistent with results reported by Wang et al. [193]. For GGBFS mixes with compressive strength less than or equal to 50 MPa (excluding the N32 group because the tensile creep coefficient at 28 days is unknown), experimental results consistently showed that the concrete with higher GGBFS content in its binder was found to have higher tensile creep coefficient, which is also in agreement with those reported by Khatri et al. [194].

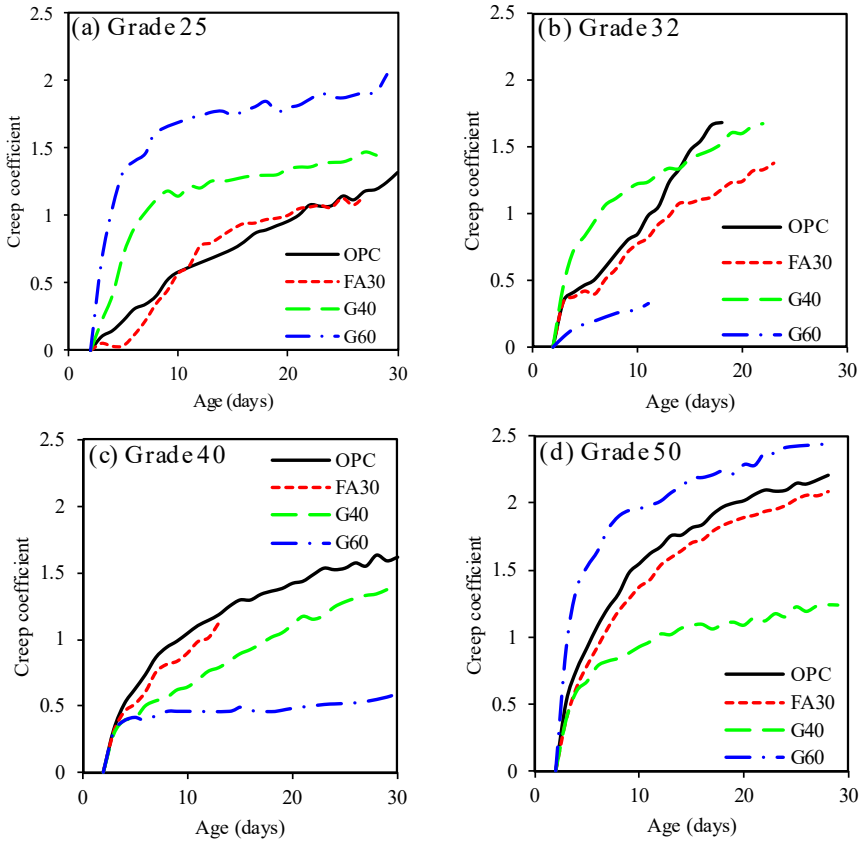

Figure 4 - 8: Time-dependent tensile creep coefficient of: (a) Grade 25; (b) Grade 32; (c) Grade 40; (d) Grade 50; (e) Grade 80; and (f) Grade 100.

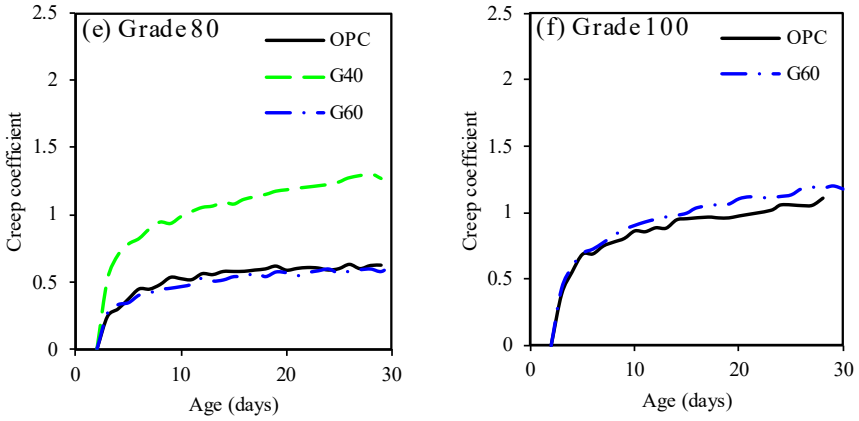

Figure 4 – 8: (continued)

4.5.2 Comparison of experimental, numerical and analytical tensile stress of concrete

Figure 4-9 presents the tensile stresses of grade N25 and N32 mixes calculated by using i) the measured steel strains (experimental) (Eq. (4-1)), ii) the analytical model (Eq. (4-13)), and iii) the numerical simulation. The theoretical elastic stresses (Eq. (4-11)) are also included to illustrate the significance of tensile creep. The accuracy of the tensile stress by analytical model depends on the elastic modulus and free shrinkage, as mentioned above, the accuracy is 0.1 MPa for elastic modulus, leading to an accuracy of the tensile stress by analytical model is 0.1 MPa. As shown in Figure 4-9, the tensile stress analytically calculated using Eq. (4-13) agrees well with both experimentally assessed tensile stress and numerical simulation, indicating the accurate prediction of the time-dependent development of concrete stress. It can also be seen that the theoretical elastic stress always greatly overestimates the tensile stress because the stress relaxation due to creep is ignored. The results confirmed that neglecting tensile creep would result in underestimating the age of cracking. Therefore, it can be concluded that the benefit of the modified model is to account for the stress relaxation effect due to tensile creep. Moreover, the modified tensile

creep coefficients measured on the dog-bone specimens have been successfully used in the analysis of the restrained ring tests.

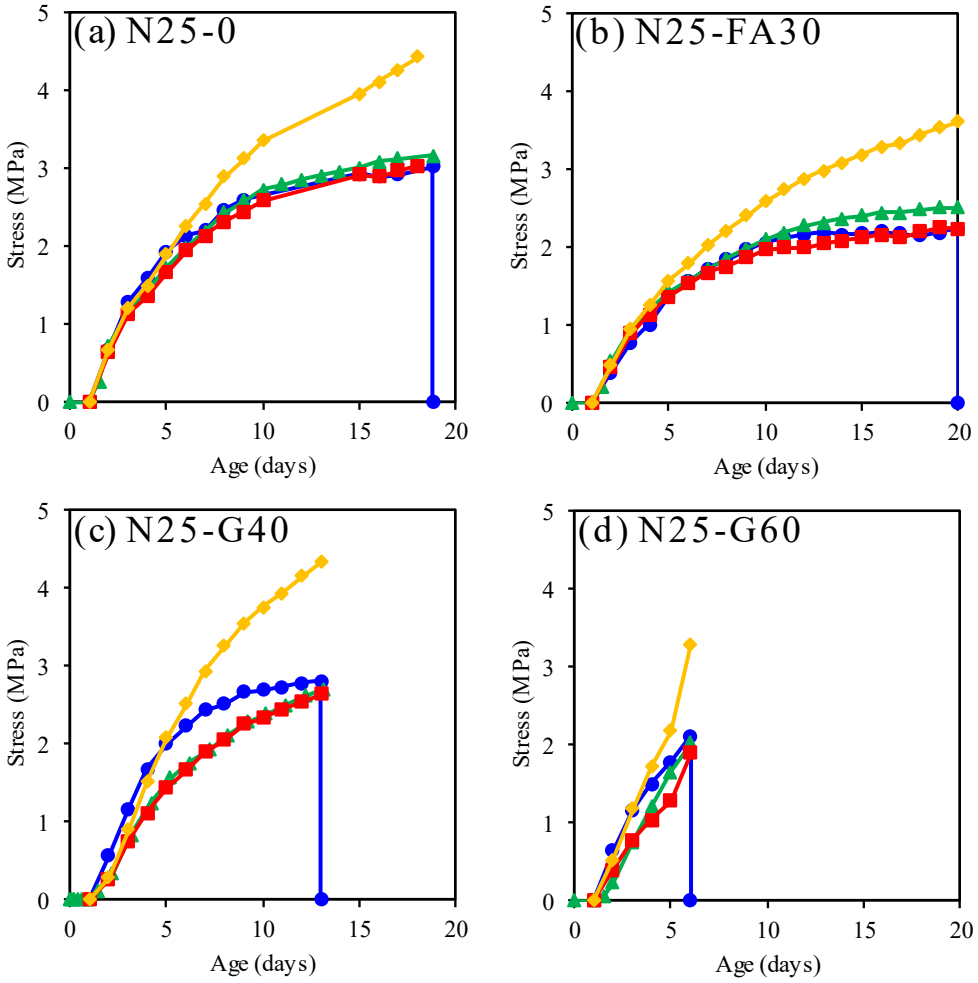

Figure 4 - 9: Stress comparison (a) N25-0; (b) N25-FA30; (c) N25-G40; (d) N25-G60; (e) N32-0; (f) N32-FA30; (g) N32-G40; (h) N32-G60.

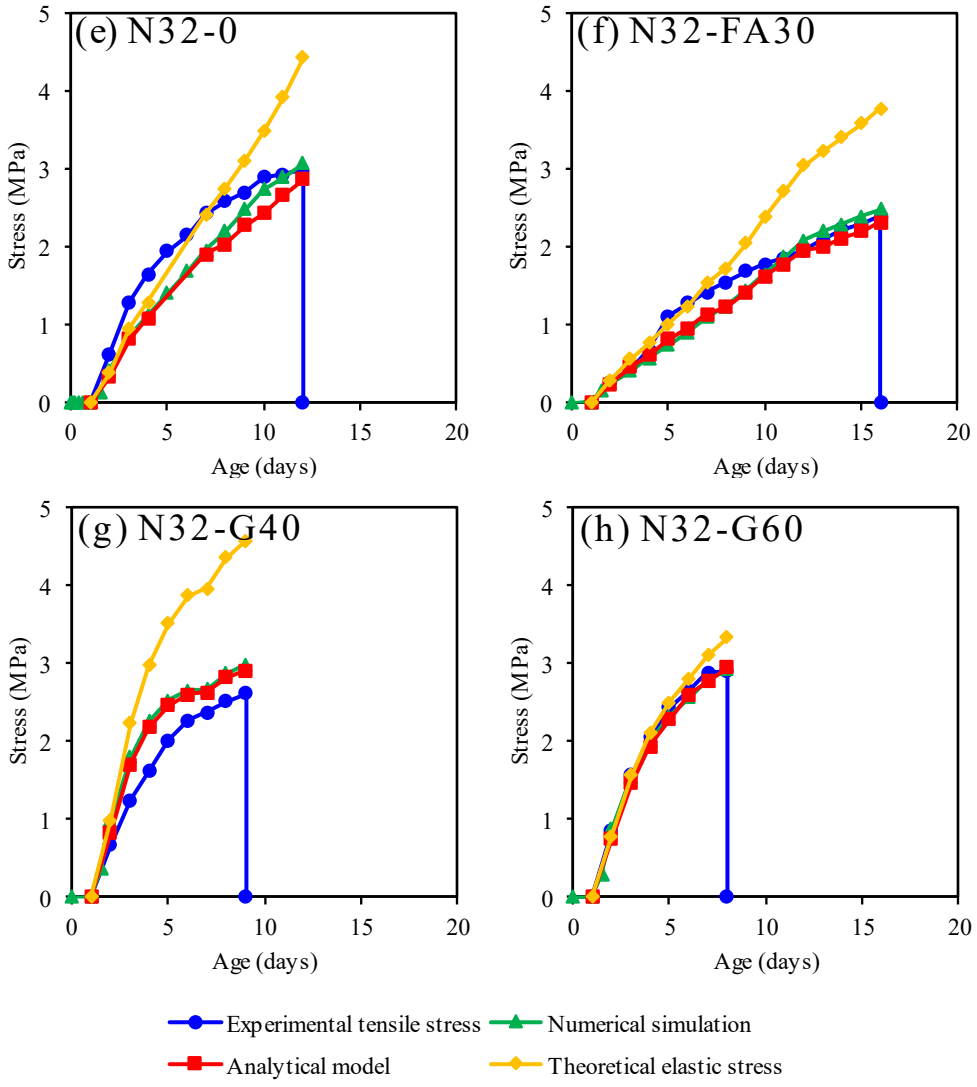

Figure 4 – 9: (continued)

To better demonstrate the reliability of the proposed analytical model for various concrete mixes, the tensile stress at the time of concrete cracking (observed experimentally) obtained from both simulation and analytical model are plotted against experimental values calculated from the maximum steel strain measured just before concrete cracking (see Figure 4-10a). A good agreement among calculated and simulated as well as measured stresses can be observed. The comparison between analytically calculated, numerical simulated and experimental stresses at the experimental cracking time is also provided for

all concretes in Figure 4-10b. The mean value and the coefficient of variation (CoV) of the ratio by analytical and experimental results are 0.97 and 0.05, respectively. Meanwhile, the mean value and the CoV of the ratio by numerical simulation and experimental results are 0.99 and 0.06, respectively. This shows that the proposed analytical model is accurate for all concrete mixes, and predictions are validated by the restrained ring test. The proposed analytical model can be used as a predictive tool to study the effect of different parameters such as the steel ring thickness to examine the effect of the degree of restraint on cracking time. This will be discussed in Section 4.5.4.

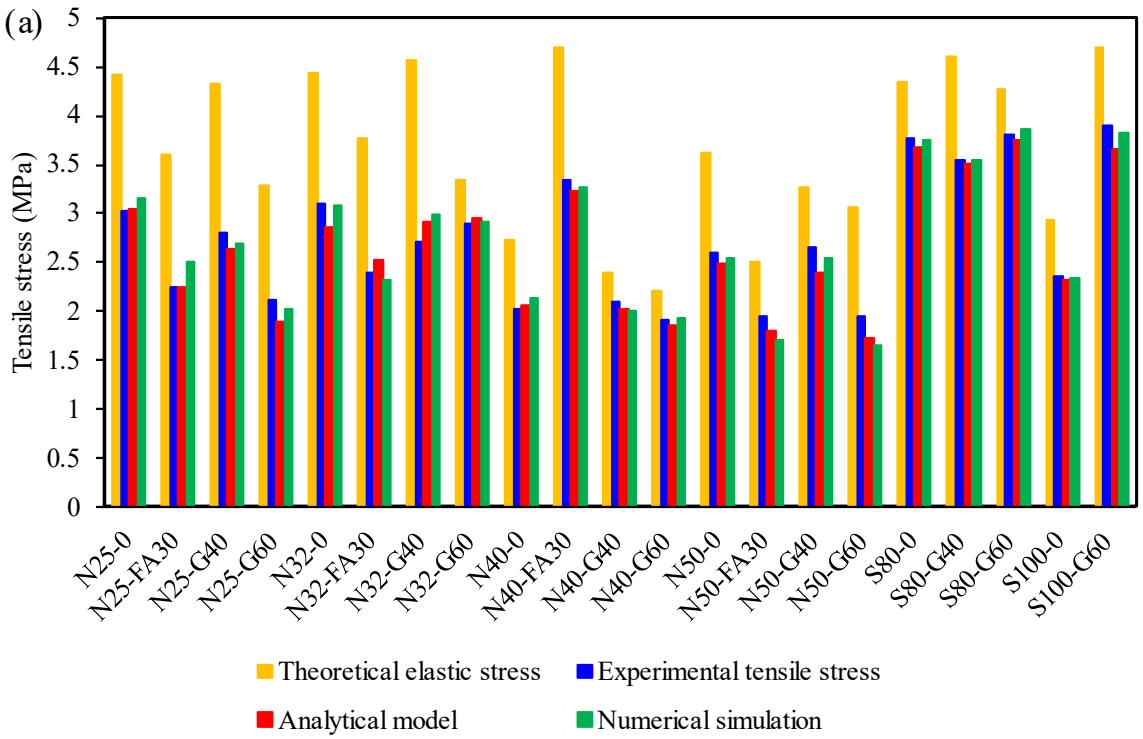

Figure 4 - 10: (a) Comparison between calculated and experimental tensile stress at cracking time for all the concrete mixes; (b) statistical analysis for all concrete mixes.

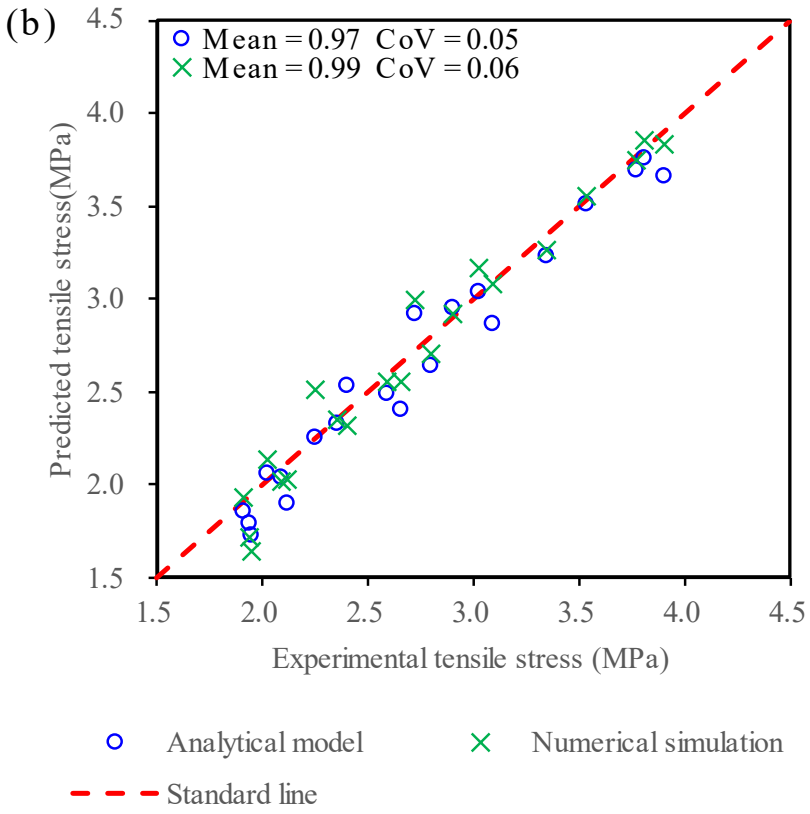

Figure 4 – 10: (continued)

4.5.3 Discussion on the degree of restraint

The significance of the degree of restraint on the risk of cracking has been widely investigated [195, 70, 196]. Experimentally speaking, it is defined as the ratio of the strain of the steel ring to the free shrinkage strain of concrete ring which can be calculated as follows:

$$D_R = 1 - \frac{\varepsilon_{st}(t)}{\varepsilon_{sh}(t)} \tag{4-20}$$

To investigate the reliability of the proposed analytical model, the degree of restraint is calculated based on five methods: i) based on experimentally measured steel strain and free shrinkage of concrete (Eq. (4-20)), ii) based on numerically simulated steel strain and free

shrinkage of concrete (Eq. (4-20)), iii) the new analytical model (Eq. (4-14a)), iv) the ACI207.2 code (Eq. (4-14b)) [178], and v) the simplified model (Eq. (4-14c)). The results are shown in Table 4-4. It can be seen that the degree of restraint calculated by the analytical model provides the best results. The degree of restraint suggested by the ACI code is significantly lower than other methods because tensile creep is neglected. This indicates that the time-dependent analysis by implementing the age-adjusted effective modulus is essential. Meanwhile, the degree of restraint calculated based on the simplified model provides comparable results to the analytical model. The statistical analysis of the error and robustness of the different models is shown in Figure 4-11. The mean value and CoV of the ratio between the proposed analytical model and the experimental degree of restraint are 1.00 and 0.025, respectively, which are closer than the ones obtained by numerical simulation with 1.00 and 0.032, respectively. The mean value and CoV of the ratio between D_R by simplified model and the experimental degree of restraint are 0.97 and 0.027. As a result, it can be concluded that the simplified model also performs well. Therefore, the degree of restraint model can be presented in an accurate or simplified form as follows:

$$\sigma_{cs} = D_R \, \varepsilon_{sh} \, \bar{E}_e \tag{4-21a}$$

$$D_R = \begin{cases} \dfrac{R_{OC}^2 + R_{OS}^2}{R_{OC}^2 - R_{OS}^2} \\ \dfrac{\bar{E}_e}{E_s} \cdot \dfrac{[(1+\nu_s)R_{IS}^2 + (1-\nu_s)R_{OS}^2]}{(R_{OS}^2 - R_{IS}^2)} + \dfrac{[(1+\nu_c)R_{OC}^2 + (1-\nu_c)R_{OS}^2]}{(R_{OC}^2 - R_{OS}^2)} \end{cases} \quad \text{(Accurate)}$$

$$\dfrac{1}{1 + \dfrac{A_c \bar{E}_e}{A_s E_s}} \quad \text{(Simplified)} \tag{4-21b}$$

Table 4 - 4: Comparison between experimental and predicted values of D_R.

Sample ID	DOR (i)	DOR (ii)	DOR (iii)	DOR (iv)	DOR (v)	Ratio (ii/i)	Ratio (iii/i)	Ratio (iv/i)	Ratio (v/i)
N25-0	0.690	0.666	0.676	0.517	0.659	0.965	0.980	0.750	0.955
N25-FA30	0.736	0.705	0.719	0.546	0.708	0.958	0.977	0.741	0.962
N25-G40	0.724	0.734	0.722	0.543	0.711	1.014	0.998	0.750	0.983
N25-G60	0.744	0.755	0.750	0.571	0.744	1.015	1.009	0.768	1.001
N32-0	0.647	0.649	0.662	0.466	0.643	1.003	1.023	0.721	0.994
N32-FA30	0.693	0.681	0.688	0.486	0.673	0.984	0.993	0.702	0.971
N32-G40	0.725	0.697	0.691	0.508	0.676	0.962	0.953	0.701	0.933
N32-G60	0.618	0.615	0.605	0.531	0.580	0.996	0.979	0.859	0.940
N40-0	0.647	0.628	0.632	0.496	0.610	0.970	0.976	0.767	0.942
N40-FA30	0.645	0.654	0.648	0.475	0.628	1.014	1.004	0.736	0.973
N40-G40	0.615	0.629	0.618	0.528	0.595	1.023	1.005	0.858	0.967
N40-G60	0.623	0.618	0.626	0.535	0.604	0.993	1.006	0.859	0.970
N50-0	0.641	0.648	0.646	0.472	0.626	1.010	1.007	0.737	0.975
N50-FA30	0.619	0.663	0.638	0.481	0.617	1.072	1.032	0.777	0.998
N50-G40	0.634	0.650	0.659	0.523	0.641	1.025	1.040	0.824	1.010
N50-G60	0.728	0.771	0.741	0.543	0.733	1.060	1.018	0.746	1.007
S80-0	0.535	0.539	0.546	0.441	0.517	1.007	1.020	0.823	0.967
S80-G40	0.587	0.585	0.588	0.437	0.562	0.998	1.002	0.745	0.959
S80-G60	0.574	0.535	0.546	0.458	0.518	0.933	0.952	0.799	0.903
S100-0	0.567	0.575	0.576	0.442	0.549	1.014	1.015	0.779	0.969
S100-G60	0.555	0.563	0.579	0.439	0.553	1.015	1.044	0.791	0.997
Mean						1.002	1.002	0.773	0.970
CoV						0.032	0.025	0.049	0.027

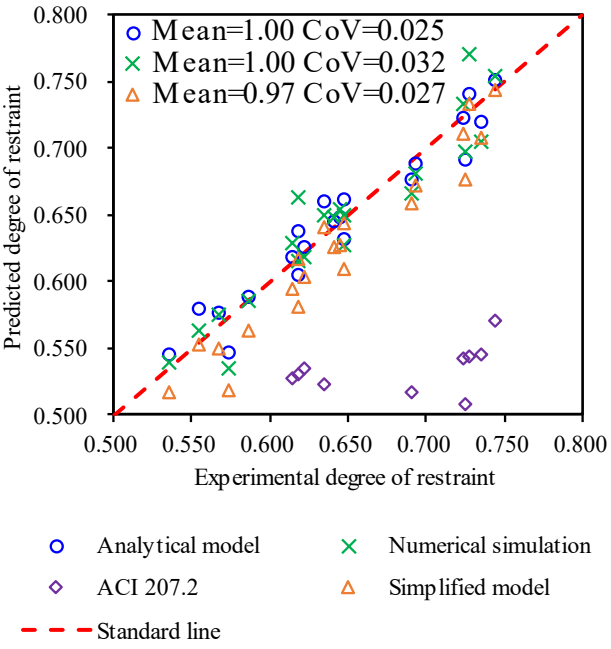

Figure 4 - 11: Comparison between different models of D_R.

4.5.4 Effect of steel ring thickness

As mentioned in the previous section, the ring specimens are further simulated by using i) the analytical model and ii) the simplified model to investigate the effect of the steel ring thicknesses on the tensile stress development and the degree of restraint. N25-0 was selected as the representative study. All other parameters were kept constant, only the thickness of the steel ring was ranging from 2.1 mm to 10.5 mm. Different thicknesses of the steel ring including 2.1 mm, 3.5 mm, 7 mm, 10.5 mm, and 17.5 mm were analysed. As shown in Figure 4-12, the thinner the steel ring, the lower the tensile stress due to a lower degree of restraint, delaying cracking age. For 2.1 mm thickness, the tensile stress developing according to the simulation is too low to result in any cracking even after 18 days.

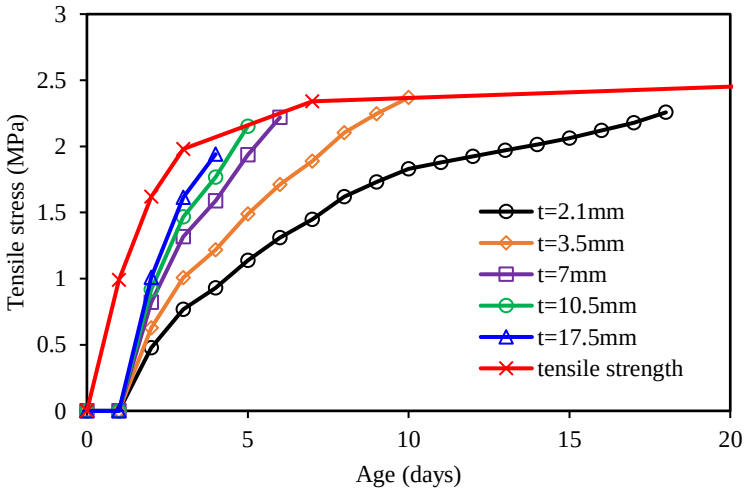

Figure 4 - 12: Numerically simulated tensile stress development in restrained ring tests with different steel ring thickness.

Table 4-5 shows the degree of restraint and tensile stress calculated based on the analytical model and the simplified model. The ratio of the result of the simplified model to the outcome of the analytical model is also provided in Table 4-5. The mean value and CoV are 0.97 and 0.025, respectively, showing that the simplified model can also be used to analyse the restrained ring test with different steel ring thicknesses. The new analytical model proposed in this chapter provides the most accurate predictions for the restrained shrinkage ring test and can be used for any steel-concrete ring geometry. However, this analytical model, specifically developed to account for the restrained ring test parameters, cannot be used to analyse concrete structures subjected to different restraint conditions. In this case, the simplified model by Khan et al. [66] (Eq. 4-14c) is recommended due to its better adaptability.

Table 4 - 5: Comparison between calculated D_R and tensile stress by the analytical model (i) and the simplified model (ii).

Concrete ring thickness (mm)	Steel ring thickness (mm)	D_R (i)	D_R (ii)	Tensile stress (i) (MPa)	Tensile stress (ii) (MPa)	Ratio
35	2.1	0.45	0.42	2.01	1.89	0.94
35	3.5	0.58	0.55	2.56	2.45	0.96
35	5	0.66	0.64	2.92	2.83	0.97
35	7	0.72	0.71	3.22	3.16	0.98
35	10.5	0.79	0.79	3.52	3.50	0.99
35	17.5	0.86	0.86	3.80	3.82	1.01
Mean						0.97
CoV						0.025

4.6 Conclusions

In this chapter, an analytical model of the restrained ring test is proposed by capturing the effect of both restrained shrinkage and tensile creep based on the age-adjusted effective modulus theory. The main conclusions can be drawn as follows:

1. Free shrinkage and tensile creep, measured on prismatic and dog-bone-shaped concrete specimens, were successfully used to determine the age-adjusted effective modulus.
2. Importantly, the model was validated considering a total of 21 concretes consisting of 6 strength grades ranging from 25 MPa to 100 MPa. For each grade, one fly ash blend (30%), two GGBFS blends (40% and 60%), and a reference mix without supplementary cementitious materials were tested.
3. The analytical model allows for accurately predicting the tensile stress of the restrained

concrete ring based on the time-dependent development of elastic modulus, total free shrinkage, and tensile creep of concrete, measured experimentally. The mean value and the CoV of the ratio by analytical and experimental results are 0.97 and 0.05, respectively. A numerical finite element simulation was also successfully carried out to validate the new analytical model. The mean value and the CoV of the ratio by numerical simulation and experimental results are 0.99 and 0.06, respectively.

4. The new analytical model also provides a very accurate estimation of the degree of restraint for the restrained ring test. The mean value and CoV of the ratio between the proposed analytical model and the experimental degree of restraint are 1.00 and 0.025, respectively, which is better than numerical simulation, ACI207.2 code, and simplified model.
5. A parametric study to investigate the effect of the steel ring thickness on the degree of restraint is also discussed. The mean value and the CoV of the ratio by the analytical and simplified model are 0.97 and 0.05, respectively, indicating the analytical model can be used to analyse the restrained ring test with different steel ring thicknesses.

CHAPTER 5: MODELLING BLENDED CEMENT CONCRETE TENSILE CREEP FOR STANDARD RING TEST APPLICATION

Chapter 5 is a re-written version of an article published by the candidate, 'Modelling Blended Cement Concrete Tensile Creep for Standard Ring Test Application', in Structural Concrete. I did more than 50% the development and all of the writing. Some of the materials in this chapter have been re-written from a recent publication, which has been acknowledged and detailed in the 'Inclusion of Publications Statement' for this thesis.

5.1 Introduction

Creep is one of the most critical properties for assessing the risk of early age cracking of concrete. Generally, tensile creep relaxes the restrained strain caused by shrinkage and thermal effects, thereby reducing the tensile stress in concrete. However, in the case of restrained shrinkage of massive structures, compressive stresses are firstly generated. Creep in this case will reduce these compressive stresses and tensile stresses could be generated at early age when concrete tensile strength is low [197], potentially leading to cracking. However, cracking of massive structural concrete members is out of the scope of the experiments carried out in the study. In the past few decades, although the compressive creep behaviour of concrete has been extensively investigated [198, 199, 200, 174], less attention has been paid to tensile creep behaviour [87, 85, 66, 51]. Numerous other studies assessing compressive creep and tensile creep of concrete are available in the literature and conclude that concrete compressive creep and tensile creep are different [201, 202, 203]. As such, tensile creep cannot be estimated by the compressive creep. This is because the

mechanisms of creep in tension are different from those in compression [174]. Rossi et al. [204] investigated the mechanisms of tensile creep and concluded that the microcrack initiation and propagation of tensile creep are different from that of compressive creep.

Hossain and Weiss [152] confirmed that tensile creep plays an important role in relaxing the tensile stress in concrete. Khan et al. [87] conducted an early age tensile creep test on internally restrained members, observing that lower humidity leads to higher tensile creep, thereby increasing the relaxation of tensile stress. In another study, Khan et al. [205] studied the tensile creep and shrinkage behaviour of geopolymer concrete under heat curing conditions, showing that the risk of early age cracking can be mitigated. The Chapter 4 in this thesis proposed an analytical model allowing for predicting the tensile stress development in the restrained ring test. This analytical model involves a tensile creep coefficient at early age, which can be determined by either the tensile creep experiments or the appropriate tensile creep models. However, the tensile creep experiments require extensive testing, resulting in large costs and not all laboratories are capable of doing this test. In addition, all creep models in current codes are calibrated from creep experiments under compression [206, 207, 208, 209].

A few studies can be found in the literature relating to prediction models of concrete tensile creep [84, 210, 211, 212, 213]. Dabarera et al. [84] proved that the FIB 2010 model failed to predict the early age basic tensile creep. The authors also proposed a modified model based on FIB 2010 model to predict the early age basic tensile creep of high performance concrete. Wei et al. [210] developed a tensile creep model based on the theory of micro-prestress solidification by considering the effects of temperature and relative humidity. Zhao et al. [211] also established a tensile creep model of concrete slab utilising the micro-

prestress solidification theory. Forth [212] collected tensile creep data over four years and provided a second-order polynomial as a recommended prediction formula based on the least square method. Brugger et al. [213] utilised multiphase modelling to simulate the tensile creep of concrete by introducing a load-dependent desorption isotherm. However, owing to the requirements of other experimental data such as the degree of hydration, temperature and relative humidity variations, these models are not suitable for implementation in standard codes. In addition, the applicability of these tensile creep models [19, 20] does not distinguish between conventional concrete and SCMs based concrete. It is known that the tensile creep behaviour of concrete mixes with SCMs is considerably different from that of conventional concrete [51, 170, 171, 214].

SCMs have been widely used in concrete to reduce cement content (consequently decreasing CO_2 emission) and improve the mechanical and durability performance of concrete. In addition, SCMs are mainly industrial by-products, so more economical than cement. However, SCMs also have drawbacks, such as decreasing the early age strength development and impacting the viscoelastic properties like tensile creep [215, 79, 216]. For instance, Khan et al. reported that incorporating GGBFS can significantly increase tensile creep [51], while the performance of fly ash concrete is similar to that of reference concrete [170]. Nguyen et al. [171] pointed out that the introduction of Ferronickel Slag (FNS) can also increase tensile creep. Pane and Hansen [214] reported that the risk of early age cracking of GGBFS concrete is reduced due to increased tensile creep. Therefore, it is essential to understand the influence of SCMs on the tensile creep of concrete mixes with SCMs such as fly ash and GGBFS, and it is necessary to develop a reliable tensile creep model to capture the effect of fly ash and GGBFS in concrete.

In this work, a tensile creep experimental database is used. The database consisted of test results used in Chapter 4 and a collection from other sources [87, 212, 217, 218, 219, 220, 221, 222]. The tensile creep results are then compared with four existing creep models used in standards and specifications, including ACI-209R-02 model [206], FIB 2010 model [207], GL2000 model [208], and Eurocode 2 model [209]. These models have been used to predict the compressive creep but the application of these models to tensile creep should be investigated. A modified model valid for specific environmental conditions (23 °C, 50% of RH) is proposed to predict the tensile creep of fly ash and GGBFS based concrete. The proposed model can be also used for analysing the concrete tensile stress development in the restrained ring test under the same specific environmental conditions and thus this model can replace the tensile creep test which is quite complex and expensive for this purpose.

5.2 Existing creep models

Several models in the existing codes available for the prediction of creep of plain concrete are presented in this section [206, 207, 208, 209]. These models were successfully used to predict the compressive creep of concrete [223, 43, 224]. However, their application to tensile creep is questionable requiring further investigation, which will be carried out in section 5.4.

5.2.1 ACI-209R-92 model [206]

The American Concrete Institute (ACI) recommended expressions for the compliance function prediction. The model applies to normal and lightweight (using both moist and steam curing; types I and III cement) under standard conditions, as shown in Eq. (5-1):

$$J(t,t_0) = \frac{1+\varphi(t,t_0)}{E_{cmt0}} \tag{5-1}$$

where E_{cmto} is the modulus of elasticity at the time of loading t_0; $\varphi(t,t_0)$ is the creep coefficient which depends on the types of curing, the age of loading, the relative humidity, the volume-surface ratio, the slump, the fine aggregate content, and the air content, as shown in Eq. (5-2).

$$\varphi(t,t_0) = \frac{(t-t_0)^{0.6}}{10+(t-t_0)^{0.6}} \times 2.35 \times \gamma_{c,t0}\gamma_{c,RH}\gamma_{c,vs}\gamma_{c,s}\gamma_{c,\psi}\gamma_{c,\alpha} \tag{5-2}$$

the remaining ACI-209-R92 expressions in Eq. (5-2) are provided in Table 5-1.

Table 5 - 1: ACI-209-R92 creep prediction expressions [206].

Factors	Conditions	ACI-209-R92 expressions
Age of concrete at loading factor, $\gamma_{c,t0}$	Moist curing	$1.25t_0^{-0.118}$
	Steam curing	$1.13t_0^{-0.094}$
Ambient relative humidity factor, $\gamma_{c,RH}$	Relative humidity ≥ 0.40	$1.27-0.67RH$
	Relative humidity < 0.40	1.0
Volume-surface ratio factor, $\gamma_{c,vs}$	Volume-surface ratio ≥ 38 mm	$\frac{2}{3}(1+1.13e^{\{-0.0213(V/S)\}})$
Slump factor, $\gamma_{c,s}$	Slump of fresh concrete	$0.82+0.00264s$
Fine aggregate factor, $\gamma_{c,\psi}$	Ratio of the fine aggregate to total aggregate by weight	$0.88+0.0024\psi$
Air content factor, $\gamma_{c,\alpha}$	Air content in percent	$0.46+0.09\alpha \geq 1$

where RH is the relative humidity; V and S are the specimen volume and surface area, respectively; s is the slump of fresh concrete; ψ is the ratio of fine aggregate to total aggregate by weight; and α is the air content in percent.

5.2.2 FIB 2010 model [207]

The FIB 2010 model is valid for ordinary structural concrete with compressive strength in the range of 12 and 80 MPa. The mean ambient relative humidity should be in the range of 40% to 100%. The mean ambient temperatures should be between 5 to 30 °C. The maximum sustained stress should not exceed 40% of the compressive strength. For this model, the expression for compliance function is shown as follows:

$$J(t,t_0) = \frac{1}{E_{cmt0}} + \frac{\varphi(t,t_0)}{E_{cm28}} \tag{5-3}$$

where E_{cm28} is the mean elastic modulus at 28 days; $\varphi(t,t_0)$ is the creep coefficient which is defined as the sum of its basic and drying components, as shown in Eq. (5-4).

$$\varphi(t,t_0) = \varphi_{bc}(t,t_0) + \varphi_{dc}(t,t_0) \tag{5-4}$$

where the basic and drying creep are the product function of a 'final' creep coefficient depends on parameters such as the compressive strength, notional size, relative humidity and time development function, as shown in Eqs. (5-5a) and (5-5b), respectively.

$$\varphi_{bc}(t,t_0) = \beta_{bc}(f_{cm})\beta_{bc}(t,t_0) \tag{5-5a}$$

$$\varphi_{dc}(t,t_0) = \beta_{dc}(f_{cm})\beta(RH)\beta_{dc}(t_0)\beta_c(t,t_0) \tag{5-5b}$$

the remaining FIB 2010 model expressions in Eq. (5-5) are provided in Table 5-2.

Table 5 - 2: FIB 2010 creep prediction expressions [207].

Factors	FIB 2010 expressions
Compressive strength factor, $\beta_{bc}(f_{cm})$	$\frac{1.8}{(f_{cm})^{0.7}}$
Time development function, $\beta_{bc}(t,t_0)$	$\ln\left\{\left(\frac{30}{t_{0,adj}} + 0.035\right)^2 \times (t-t_0) + 1\right\}$
Compressive strength factor, $\beta_{dc}(f_{cm})$	$\frac{412}{(f_{cm})^{1.4}}$

Table 5 – 2: (continued)

Relative humidity factor, $\beta(RH)$	$\frac{1-\frac{RH}{100}}{\sqrt[3]{0.1\cdot\frac{h}{100}}}$
where h is the hypothetical thickness	$\frac{2A_g}{u_e}$
Age of initial loading factor, $\beta_{dc}(t_0)$	$\frac{1}{0.1+t_0^{0.2}}$
where t_0 is the age of concrete at loading;	$t_{0,T}[\frac{9}{2+t_{0,T}^{1.2}}+1]^{\beta}$
where $t_{0,T}$ is the age of concrete at loading adjusted to the concrete temperature; β is a power depends on the types of cement, which equals to 0 for normal or rapid hardening cement	$\sum_{i=1}^{n}\Delta t_i \exp\left[13.65-\frac{4000}{273+T(\Delta t_i)}\right]$
Time development function, $\beta_{dc}(t-t_0)$	$[\frac{(t-t_0)}{\beta_H+(t-t_0)}]^{\gamma(t_0)}$
where $\gamma(t_0)$ is the function depends on the adjusted age at loading	$\frac{1}{2.3+\frac{3.5}{\sqrt{t_0}}}$
where β_H is the coefficient depends on notional size and mean compressive strength	$1.5h+250(\frac{35}{f_{cm}})^{0.5}$

5.2.3 GL 2000 model [208]

The GL 2000 model was developed for the prediction of creep of normal-strength plain concrete with a mean compressive strength less than 82 MPa and a w/c ratio of 0.4 to 0.6. The relative humidity is in the range of 20% to 100%. The expression of the compliance function in this model is the same as Eq. (5-3), and $\varphi(t,t_0)$ is the creep coefficient which includes three terms, considering the relative humidity, volume-surface ratio, and time development function, as shown in Eq. (5-6).

$$\varphi(t,t_0) = \frac{2(t-t_0)^{0.3}}{(t-t_0)^{0.3}+14} + (\frac{7}{t_0})^{0.5}(\frac{(t-t_0)}{(t-t_0)+7})^{0.5} + 2.5(1-1.086RH^2)(\frac{(t-t_0)}{(t-t_0)+0.12(v/s)^2})^{0.5} \quad (5\text{-}6)$$

5.2.4 Eurocode 2 model [209]

The Eurocode 2 model is valid for ambient temperatures varying between -40 and 40°C, and a mean relative humidity ranging between 40% to 100%. The model adopted for the compliance function is the same as Eq. (5-3), and $\varphi(t,t_0)$ is computed based on the relative humidity, mean compressive strength of concrete at 28 days, the age of concrete at loading, and time development function, as shown in Eq. (5-7):

$$\varphi(t,t_0) = \beta(RH)\beta(f_{cm})\beta(t_0)\beta_c(t,t_0)\varphi_{nl} \quad (5\text{-}7)$$

the remaining Eurocode 2 model expressions in Eq. (5-7) are provided in Table 5-3.

Table 5 - 3: Eurocode 2 creep prediction expressions [209].

Factors	Eurocode 2 expressions
Relative humidity factor, $\beta(RH)$ where h is the hypothetical thickness	$\begin{cases} 1+\frac{1-RH/100}{0.1\sqrt[3]{h}} & for\ f_{cm} \le 35 \\ \left[1+\frac{1-RH/100}{0.1\sqrt[3]{h}}(\frac{35}{f_{cm}})^{0.7}\right](\frac{35}{f_{cm}})^{0.2} & for\ f_{cm} \ge 35 \end{cases}$ $\frac{2A_g}{u_e}$
Strength-dependent factor, $\beta(f_{cm})$	$\frac{16.8}{\sqrt{f_{cm}}}$
Age of loading factor, $\beta(t_0)$	$\frac{1}{0.1+t_0^{0.2}}$
Time development function, $\beta_c(t,t_0)$	$\left[\frac{t-t_0}{\beta_H+t-t_0}\right]^{0.3}$

Table 5 – 3: (continued)

where β_H is the factor depending on relative humidity and compressive strength	$\begin{cases} 1.5[1+(1+0.012RH)^{18}]h_0+250 \le 1500 & for\ f_{cm} \le 35 \\ 1.5[1+(1+0.012RH)^{18}]h_0+250(\frac{35}{f_{cm}})^{0.5} \le 1500(\frac{35}{f_{cm}})^{0.5} & for\ f_m \ge 35 \end{cases}$
Nonlinear creep factor for sustained stress levels in excess of $0.45f_{cmi}$, φ_{nl}	$e^{1.5(\frac{\sigma_0}{f_{cmi}}-0.45)}$

5.2.5 Comparison of various creep models

The required factors for the prediction of creep from these four analytical models are tabulated in Table 5-4. It can be seen that GL 2000 model requires the minimum number of parameters while the ACI-209R-92 model requires the maximum number of parameters for predicting the concrete creep. However, all models do not consider fly ash or GGBFS effect in predicting the tensile creep of concrete.

To compare the various prediction models and investigate the modelling of early age tensile creep of fly ash or GGBFS concrete, the model results are compared with the experimental results of the 21 concrete mixes with fly ash or GGBFS considered in this chapter. A new model is then proposed to better reflect the early age tensile creep of concrete mixes with fly ash or GGBFS.

Table 5 - 4: Factors required for the prediction models for creep of concrete.

Factors	ACI-209R	FIB 2010	GL 2000	Eurocode 2
Mean compressive strength at 28 days	Yes	Yes	Yes	Yes
Elastic modulus at the time of loading	Yes	Yes	Yes	Yes
Type of cement	Yes	Yes		Yes
Type of curing	Yes			
Age of concrete at loading	Yes	Yes	Yes	Yes
Relative humidity	Yes	Yes	Yes	Yes
Volume-surface ratio	Yes	Yes	Yes	
Slump	Yes			
Fine aggregate content	Yes			
Air content	Yes			
Hypothetical thickness				Yes
Nonlinear creep factor		Yes		Yes

5.3 Experimental database on tensile creep

The database includes test results performed at specific conditions (23 °C, 50% of RH, and loading at 2 days after casting) from Chapter 4 and a collection of published literature [87, 212, 217, 218, 219, 220, 221, 222]. The tensile creep test in Chapter 4 was initiating initiated at 2 days after casting because, after 1 day, the concrete tensile strength was too low to be able to apply the sustained loading without breaking the dog bone specimens.

The creep data in Chapter 4 were used to assess the flexibility of existing creep models to predict tensile creep. Then the creep data from Chapter 4 and other sources in Ref. [87, 212, 217, 218, 219, 220, 221, 222] were utilised to study the effects of compressive strength (w/b ratio), paste content and SCMs on concrete tensile creep. The creep data in Chapter 4 were then used to develop the tensile creep model for concrete mixes with SCMs. In

addition, the tensile stress model and the results of restrained ring test and free shrinkage test in Chapter 3 are also adopted to examine the applicability of the new tensile creep model.

In Chapter 4, Six different concrete grades ranging from 25 MPa to 100 MPa were tested. Based on the nominated compressive strength, the concrete was designated as ‘N25’, ‘N32’, ‘N40’, ‘N50’, ‘S80’, and ‘S100’, respectively. Two types of SCMs, namely Fly ash and GGBFS, were used to replace cement by weight. According to the cement replacement level, the fly ash and GGBFS mixtures were designated as ‘FA30’, ‘G40’, and ‘G60’, respectively. The tensile compliance values of 21 concrete mixes were computed using experimental results obtained in Chapter 4 and summarized in Table 5-5. The tensile creep data of fly ash and GGBFS based concrete are newly analysed using the data in Chapter 4 and considered in the present chapter.

Table 5 - 5: Measured compliance of concrete mixes with SCMs.

Mix ID	Compliance at different ages (days)					
	2	3	7	14	21	28
N25-0	41.7	46.0	56.0	73.1	83.6	91.5
N32-0	36.9	49.7	58.3	86.4	N/A	N/A
N40-0	40.1	53.1	74.8	90.2	97.8	105.7
N50-0	33.9	51.4	75.1	93.6	103.9	108.7
S80-0	27.6	34.4	40.0	43.6	44.2	44.8
S100-0	27.0	37.4	47.2	52.5	54.9	56.9
N25-FA30	48.1	50.7	58.7	89.0	98.7	103.1
N32-FA30	36.8	49.4	55.6	76.4	85.4	N/A
N40-FA30	36.9	48.2	64.7	78.6	N/A	N/A
N50-FA30	32.5	44.9	67.2	85.8	94.4	100.1
N25-G40	61.7	75.0	124.8	138.8	145.3	150.7
N32-G40	42.1	61.5	86.8	98.2	111.6	N/A
N40-G40	44.5	55.8	63.8	73.8	86.2	92.6

Table 5 – 5: (continued)

N50-G40	41.8	58.0	76.3	86.6	90.0	94.0
S80-G40	28.1	42.7	53.2	58.8	61.7	64.6
N25-G60	48.5	80.5	119.4	134.6	136.7	141.3
N32-G60	46.3	49.9	53.7	N/A	N/A	N/A
N40-G60	44.1	63.1	82.7	85.2	89.3	90.7
N50-G60	36.4	69.7	102.1	113.7	119.4	125.2
S80-G60	30.6	38.8	43.3	46.3	47.2	48.8
S100-G60	29.0	41.5	51.6	57.6	61.6	63.5

The details relating to tensile creep tests of conventional concrete from the literature are summarised in Table 5 - 6. It can be seen that different researchers used different test methods. According to the test specimens and methods, investigations can be divided into five types: dog-bone [87, 217, 67], cylinder [212, 222], prism [219, 220], restrained ring test [218] and temperature stress testing machine (TSTM) [221]. Although the test specimens and methods are different, the tensile creep characteristic can still be explored from similar test conditions.

Table 5 - 6: Summary of tensile creep tests reported in the literature.

Authors	Test specimen	Expressions	Paste content	w/b ratio	Temp	RH	Test duration	Results	Age at loading
Khan et al. [87]	Dog-bone specimen	Tensile creep coefficient	23%	0.55	23 °C	50%	22d	1.67	2d
			24%	0.45				1.07	
Forth [212]	Prism and cylinder	Tensile creep strain	N/A	0.65	20 °C	60%	100d	175	28d
				0.45				125	
Liu et al. [217]	Dog-bone Specimen	Tensile creep coefficient	23%	0.37	20 °C	60%	54d	1.65	7d
			25%	0.33				1.25	
			28%	0.29				1.05	
Hwang and Khayat [218]	Restrained ring	Tensile creep coefficient	26%	0.35	23 °C	50%	7d	0.18	3d
			27%	0.42				0.32	

Table 5 – 6: (continued)

Bissonnette et al. [219]	Prism	Specific creep	32%	0.4	23 °C	50%	175d	100	7d
			27%	0.4				115	
			22%	0.4				180	
Hashida and Yamazaki [220]	Prism	Tensile creep coefficient	24%	0.4	20 °C	80%	20d	1.7	0.7d
			31%	0.27				2.8	
Shen et al. [221]	TSTM	Tensile creep strain	24%	0.5	N/A	100%	4.6d	45	2d
			25%	0.4				103	
			27%	0.33				161	
Wei et al. [222]	Cylinder	Specific creep	42%	0.3	23 °C	50%	20d	60	7d
			38%	0.4				70	
			37%	0.5				72	
Zhang et al. [67]	Dog-bone specimen	Tensile compliance function	20%	0.56	23 °C	50%	28d	91.5	2d
			22%	0.49				N/A	
			27%	0.43				105.7	
			30%	0.4				108.7	
			31%	0.28				44.8	
			33%	0.22				56.9	

5.4 Comparison between experimental results and predictions

As mentioned in the previous section, existing creep models [206, 207, 208, 209] are predominately suitable for compressive creep. It should be noted that these models are developed mainly based on test data collected using mature concrete rather than at early age. Moreover, the accuracy of the models for predicting the tensile creep of concrete with high SCMs content is still questionable. As such, the comparison in this section is divided into two parts: firstly, the prediction of the existing models is compared to tensile creep results of reference concretes in Table 5; then existing models are compared to the tensile creep of SCMs based concrete.

Figure 5-1 presents the comparison for reference concretes. Table 7 lists the comparison at 7 days (early age) and at 28 days (later age) to evaluate the accuracy of the existing model. As shown in Figure 5-1, any existing model could not predict well all tensile compliances obtained from five different strength grades of reference OPC concretes (N25, N32, N40, N50, S80, and S100). Each model only worked for some of the grades. For example, the ACI209R-92 model performed well in the low and high strength groups (N25-0, N32-0 (early age), S80-0, S100-0), whereas it showed a large deviation in the middle strength groups (N40-0, N50-0). As shown in Figure 5-1 and Table 5-7, FIB 2010 and Eurocode 2 models provided good predictions only for the middle to high strength groups (N40-0, N50-0 and S100-0). GL 2000 model could also effectively predict the middle strength groups (N40-0 and N50-0) but overestimated the low and high strength grades (N25-0, S80-0 and S100-0).

The concrete grade is determined by the compressive strength (or w/b ratio). As mentioned in Section 5.2, most models consider the influence of compressive strength and an increase in compressive strength leads to a decrease in the tensile compliance. However, as shown in Figure 5-1, the values of tensile compliance and compressive strength are not monotonically related. Therefore, the relationship between tensile creep and compressive strength (or w/b ratio) will be reconsidered in the next section.

Regarding the accuracy of the predictions, ACI209R-92 model had the lowest mean value and coefficient of variation (CoV) of the ratio between prediction and experimental results, with mean value and CoV being 0.81 and 0.20, respectively (see Table 7). This means that the ACI209R-92 model underestimated the tensile creep and was conservative for the relaxation problem [85]. The prediction of Eurocode 2 model was slightly higher than the

experimental results, with the mean value and CoV being 1.20 and 0.32, respectively. FIB 2010 and GL 2000 models mostly overestimated the tensile creep of concrete as shown in Table 5-7.

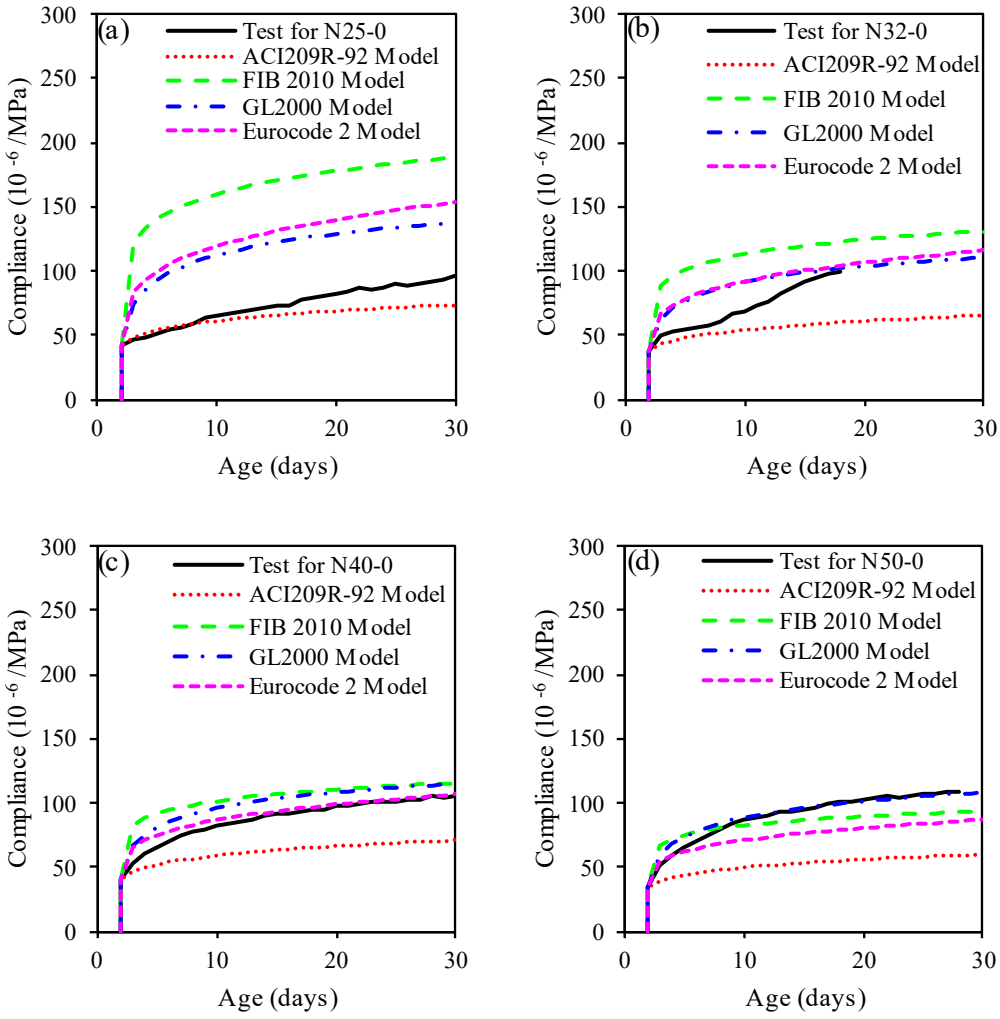

Figure 5 - 1: Experimental results of compliance function against models for: (a) N25-0; (b) N32-0; (c) N40-0; (d) N50-0; (e) S80-0; and (f) S100-0.

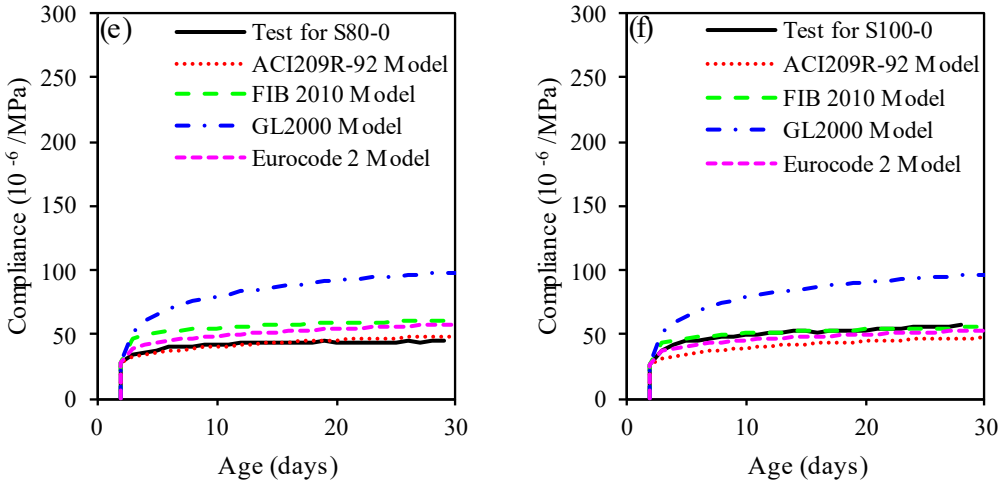

Figure 5 – 1: (continued)

To better evaluate the performance of the 4 creep prediction models for various concrete mixes including SCMs, Table 5-7 shows the experimental compliances and model predictions of creep compliances obtained from all mixes at the age of 7 and 28 days. The ratio of predicted creep compliances to corresponding experimental results is also provided in Table 5-7. Moreover, Figure 5-2 presents a box plot to illustrate the 4 models performance by using the ratio of model prediction to experimental results for conventional and concrete mixes with SCMs. It can be seen that ACI 209R model has the lower scatters, while FIB 2010 model has the higher scatters. ACI 209R and GL 2000 models also have less outliers than FIB 2010 and Eurocode 2 models, indicating the lower CoV and prediction variations. Generally, it can be seen from both Table 5-7 and Figure 5-2 that both OPC mixes and SCM mixes cannot be well predicted using the current models, indicating the need for a better model to predict the tensile creep of concrete. This will be further discussed in the next sections.

Table 5 - 7: Comparison of predicted compliance with the experimental results.

Mix ID	Concrete age (days)	Compliance (10^{-6} /MPa)	ACI209R		FIB 2010		GL2000		Eurocode 2	
			value	ratio	value	ratio	value	ratio	value	ratio
N25-0	7	56.0	57.4	1.03	158.1	2.82	103.1	1.84	111.7	2.00
	28	91.5	73.0	0.80	196.5	2.15	136.2	1.49	154.7	1.69
N32-0	7	58.3	50.8	0.87	107.1	1.84	84.1	1.44	84.9	1.46
N40-0	7	74.8	55.3	0.74	96.8	1.29	88.3	1.18	80.5	1.08
	28	105.7	70.3	0.67	114.8	1.09	114.2	1.08	105.2	1.00
N50-0	7	75.1	46.7	0.62	79.0	1.05	81.5	1.08	66.2	0.88
	28	108.7	59.4	0.55	93.0	0.86	107.1	0.98	85.8	0.79
S80-0	7	40.0	38.1	0.95	53.2	1.33	72.9	1.82	46.2	1.15
	28	44.8	48.4	1.08	60.7	1.35	97.2	2.17	57.3	1.28
S100-0	7	47.2	37.2	0.79	49.0	1.04	71.7	1.52	43.0	0.91
	28	56.9	47.2	0.83	55.4	0.97	95.8	1.68	52.7	0.93
Mean (OPC mixes only)			0.81		1.44		1.48		1.20	
CoV (OPC mixes only)			0.20		0.42		0.25		0.32	
N25-FA30	7	58.7	66.2	1.13	189.2	3.22	118.5	2.02	130.5	2.22
	28	103.1	84.2	0.82	236.0	2.29	156.4	1.52	181.0	1.76
N32-FA30	7	55.6	50.7	0.91	111.0	2.00	86.6	1.56	87.5	1.57
N40-FA30	7	64.7	50.8	0.78	94.2	1.45	87.1	1.35	77.7	1.20
N50-FA30	7	67.2	44.7	0.67	84.5	1.26	84.3	1.25	69.7	1.04
	28	100.1	56.9	0.57	100.8	1.01	112.2	1.12	92.4	0.92
N25-G40	7	124.8	85.0	0.68	208.7	1.67	125.4	1.01	141.3	1.13
	28	150.7	108.1	0.72	257.9	1.71	159.8	1.06	190.1	1.26
N32-G40	7	86.8	58.0	0.67	136.5	1.57	98.4	1.13	102.7	1.18
N40-G40	7	63.8	61.4	0.96	104.2	1.63	97.2	1.52	87.1	1.36
	28	92.6	78.0	0.84	123.0	1.33	125.6	1.36	113.1	1.22
N50-G40	7	76.3	57.6	0.76	99.6	1.30	98.7	1.29	83.1	1.09
	28	94.0	73.3	0.78	117.6	1.25	129.4	1.38	108.3	1.15

Table 5 – 7: (continued)

S80-G40	7	53.2	38.7	0.73	54.9	1.03	71.3	1.34	47.5	0.89
	28	64.6	49.2	0.76	62.9	0.97	94.5	1.46	59.2	0.92
N25-G60	7	119.4	66.9	0.56	268.8	2.25	122.5	1.03	152.5	1.28
	28	141.3	85.0	0.60	344.0	2.43	162.4	1.15	216.2	1.53
N32-G60	7	53.7	63.8	1.19	151.9	2.83	105.9	1.97	112.1	2.09
N40-G60	7	82.7	60.7	0.73	114.4	1.38	99.2	1.20	94.2	1.14
	28	90.7	77.2	0.85	136.9	1.51	128.9	1.42	124.8	1.38
N50-G60	7	102.1	50.1	0.49	91.1	0.89	87.5	0.86	75.5	0.74
	28	125.2	63.7	0.51	108.3	0.87	115.0	0.92	99.3	0.79
S80-G60	7	43.3	42.2	0.97	59.7	1.38	75.0	1.73	51.6	1.19
	28	48.8	53.6	1.10	68.4	1.40	98.9	2.03	64.3	1.32
S100-G60	7	51.6	40.0	0.78	53.2	1.03	71.7	1.39	46.6	0.90
	28	63.5	50.9	0.80	60.4	0.95	94.7	1.49	57.2	0.90
Mean (all mixes)			0.79		1.53		1.40		1.23	
CoV (all mixes)			0.22		0.39		0.24		0.30	

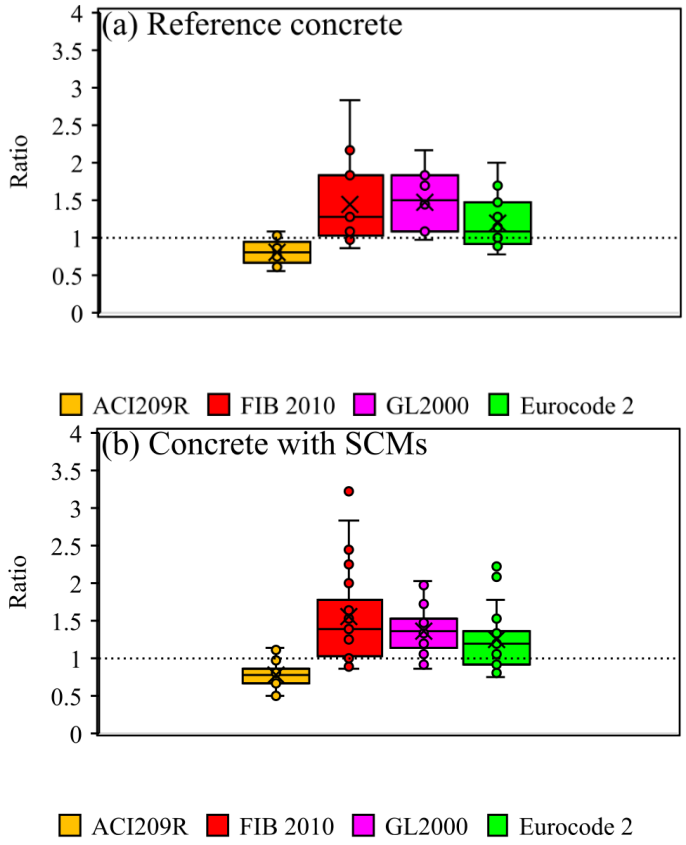

Figure 5 - 2: Statistical analysis of ratios of predicted creep compliances to corresponding experimental results obtained from concrete mixes with SCMs: (a) reference concrete; (b) concrete with SCMs.

5.5 Factors influencing tensile creep

5.5.1 Influence of compressive strength or w/b ratio

Figure 5-3 presents the tensile compliances of reference concretes without SCMs. Two groups of tensile compliances are observed in Figure 5-3. The compressive strength of concrete in the first group was equal or less than 50 MPa (w/b > 0.4), having higher values of compliances than those from S80 and S100. The tensile compliance increased with the increase in compressive strength in the first group (the compressive strength ≤ 50 MPa). This was consistent with a previous study reporting that creep increased with increasing of

w/c ratio and increasing paste content in the case of compressive creep [225]. It suggests that apart from compressive strength (w/b ratio), the paste content also affects the tensile creep [32]. This will be discussed in Section 5.5.2.

The compressive strength of concrete in the second group is equal or higher than 80 MPa (w/b < 0.28), with lower values of compliances. The compliance increased with the increase in compressive strength in this second group, which was similar to the first group. The compliance of group 1 was higher than that of group 2. This can be attributed to the w/b ratio in group 1 (normal strength concrete) which was overall higher than that of group 2 (high strength concrete), indicating more available water in concrete which could increase the flowability and shear stress [226]. Therefore, more available water results in a higher viscous shear between paste and aggregates, leading to a higher tensile creep.

Figure 5-3 confirmed that the tensile compliance is not a monotonic function of compressive strength or w/b ratio. As a result, existing creep models for compressive creep are not suitable for tensile creep. To better support this assumption, the tensile creep results from other sources are summarised in Table 6 (see w/b ratio and the creep results), showing controversial results as tensile creep increases with the w/b ratio in [87, 212, 217, 218, 222] but decreases in [220, 221].

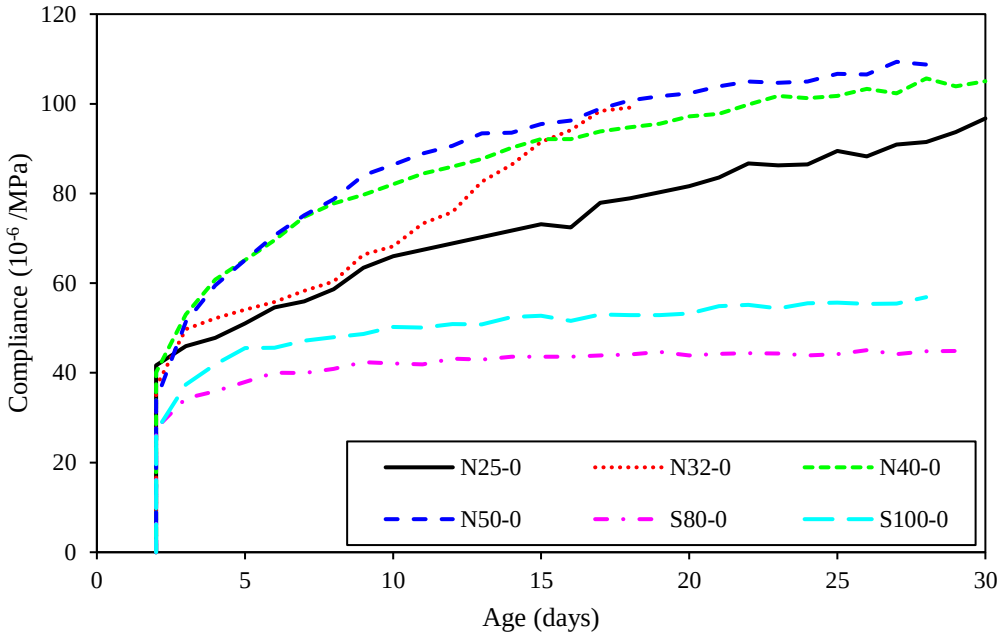

Figure 5 - 3: Time-dependent tensile compliance function of reference concrete.

5.5.2 Influence of paste content

Figure 5-4 displays the compliance of reference concrete without SCMs as a function of paste content to facilitate the understanding of the effect of the paste content on the tensile creep. Similar to Figure 5-3, two groups of concrete are also observed. The first group includes concretes with a compressive strength equal to or lower than 50 MPa (N25-0, N32-0, N40-0 and N50-0) and the second group includes the concretes with compressive strength equal or superior to 80 MPa (S80-0 and S100-0). The paste content in the first group was less than or equal to 30%, while the paste content in the second group was higher than 30%. In each group, the tensile compliance of the reference concrete increased with the increase in the paste content at different ages. However, between the two groups, the tensile creep of group 2 was lower than that of group 1. The overall trend of these test data was consistent with published results [218, 221]. This can be attributed to the

aggregates in concrete that can be regarded as an inert material, allowing only elastic deformation under sustained stress rather than creep. Therefore, the aggregates play an inhibitory role in the creep process of concrete, and the higher the aggregate content, the less the creep. In contrast, the higher the paste content in concrete, the greater the creep [227].

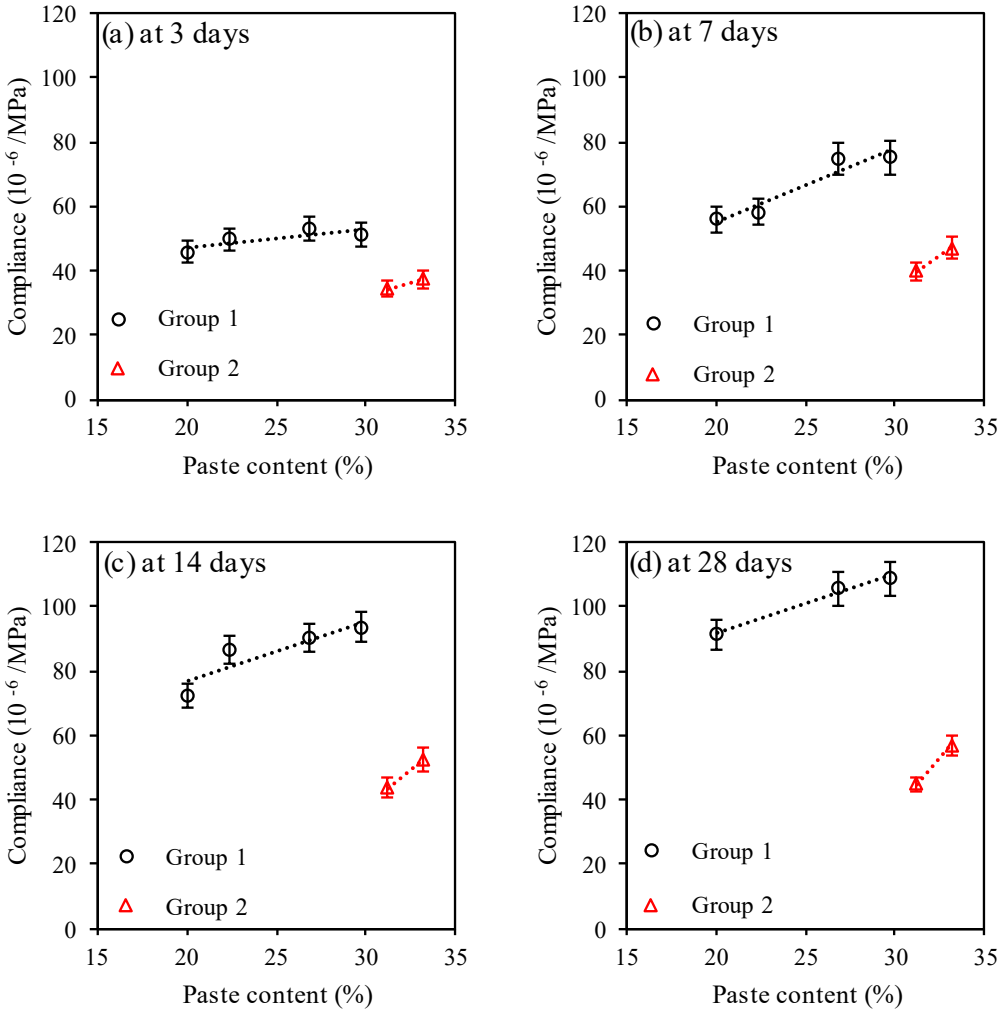

Figure 5 - 4: Tensile creep compliance of reference concrete against paste content at the age of: (a) 3 days; (b) 7 days; (c) 14 days; (d) 28 days.

5.5.3 Influence of SCMs

Figure 5-5 presents the tensile compliance of concrete mixes with fly ash and GGBFS in comparison with reference concretes. The tensile creep of concrete mixes with 30% fly ash concrete is slightly lower than that of reference concrete mixes except for Grade 25. This is consistent with the results reported by Wang et al. [193]. GGBFS concrete generally shows the higher compliance than the reference concrete. The experimental results also show that, excluding N32 group, the tensile compliance of concretes with 60% GGBFS content is higher than that of 40% GGBFS. The impact of GGBFS on concrete creep observed in this study is also in agreement with results reported by Khatri et al. [194]. However, for high strength GGBFS concrete, the tensile compliance is only slightly increased compared to the reference concrete.

Overall, the tensile creep results seem to be well aligned with the seepage theory [201, 228, 229, 230]. This theory describes that the diffusion of water molecules from layers of free absorbed water to free zones is leading to a deformation of solid skeleton. In other words, the higher the free water content, the higher the creep.

For fly ash concretes, to achieve a similar compressive strength to reference concretes, the water-to-binder ratio was significantly reduced (See Table 2 in Ref. [67]). Based on Powers hydration model [231], assuming a degree of hydration of 60% and that fly ash does not react with water at early age, it can be predicted that the free water content in concretes with 30% fly ash is 6% to18% lower than that of reference concretes, which can explain the lower creep compliance of fly ash concretes according to the seepage theory.

On the other hand, for a compressive strength less than or equal to 50 MPa, the free water in GGBFS concretes is higher than in reference concretes. Firstly, because the water-to-

binder ratio of GGBFS concretes was not significantly reduced as it is for fly ash concretes. Secondly, because the water requirement for GGBFS hydration is smaller than for Portland cement hydration [43]. As a result, an excess of free water can be expected in GGBFS concretes compared to reference concrete that can explain the higher creep compliance measured for GGBFS concretes according to the seepage theory. However, for high strength concretes (Grade 80 and Grade 100), the water to binder ratio is so drastically reduced that the difference in free water content seems to have only a marginal influence on the creep compliance of GGBFS concretes.

To conclude, results indicate that besides the w/b ratio and the paste content of concrete, the type and the properties of SCM can also greatly affect the tensile creep behaviour of concrete.

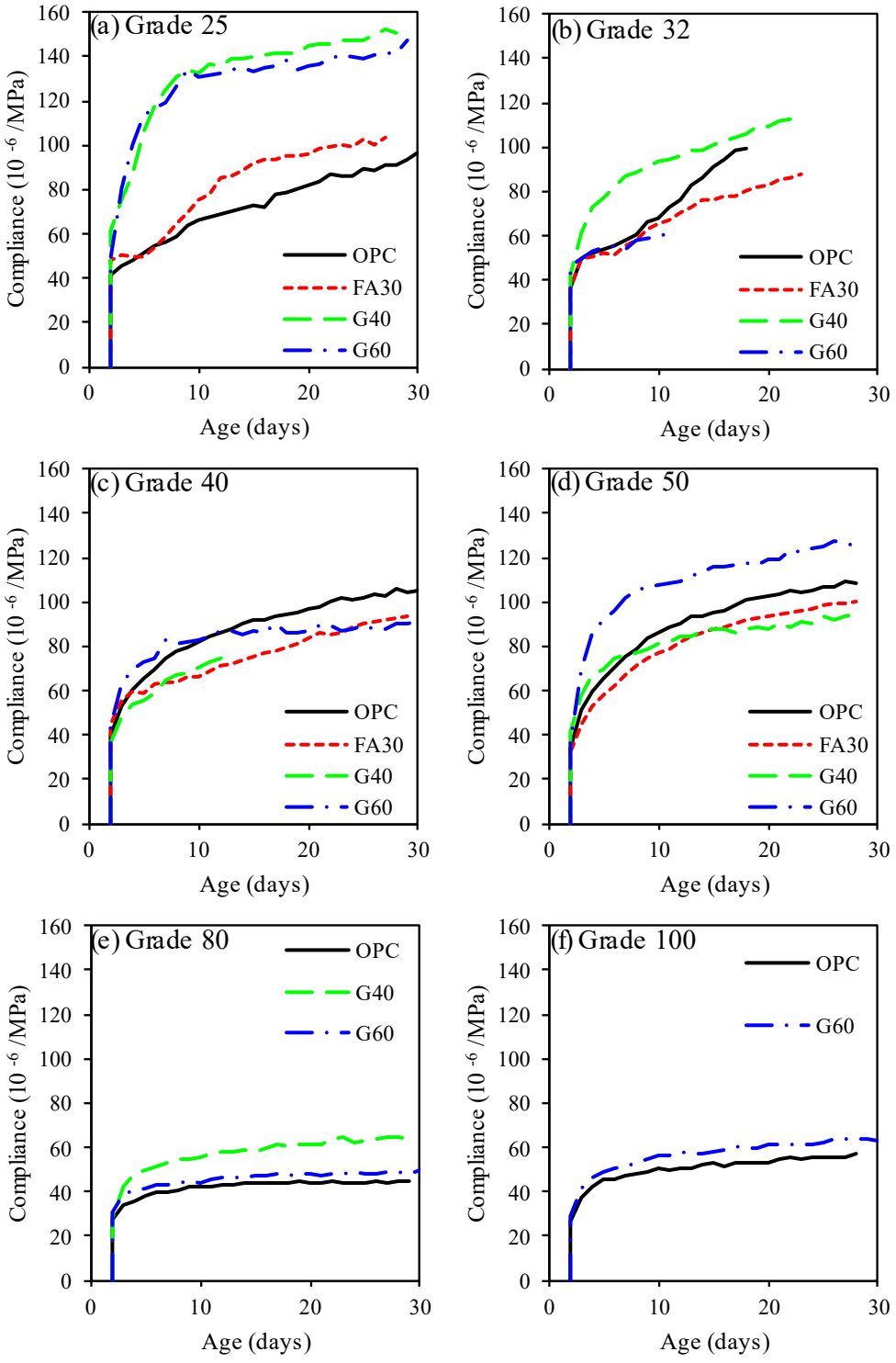

Figure 5 - 5: Time-dependent tensile compliance of: (a) Grade 25; (b) Grade 32; (c) Grade 40; (d) Grade 50; (e) Grade 80; and (f) Grade 100.

5.6 Modelling of tensile creep for SCMs concrete

This chapter proposed a model to improve the prediction of tensile creep of the concretes including with fly ash and GGBFS. Despite the relatively large number of concrete mixes used, the tensile creep tests were carried out using a specific condition (23 °C, 50% of RH, and loading at 2 days after casting). Therefore, the proposed model in this chapter aims to study the effects of compressive strength, paste content and the type of SCM under the specific test condition mentioned above, rather than proposing a new model with a general length form. These environmental conditions are suitable for early age concrete cracking investigations typically using the restrained ring test. It should be noted that the tensile compliance function depends on the creep coefficient and can be calculated using Eq. (5-3) as shown in Section 5.2. Therefore, a tensile creep coefficient model is proposed as follows:

$$\varphi(t, t_0) = \varphi_{fc} \times \varphi_{a/b} \times \varphi_t \quad (5\text{-}8)$$

These functions in Eq. (5-8) are provided in Table 5-8.

Table 5 - 8: Factors of the proposed tensile creep coefficient prediction model.

Factors	Proposed model expressions
Strength-dependent factor, φ_{fc}	$\frac{\alpha}{(f_{cm})^{0.7}}$
Aggregate-binder ratio factor, $\varphi_{a/b}$	$(\frac{a/b}{6})^{\beta}$
Time development function, φ_t	$\ln[\gamma(t - t_0) + 1]$

In Table 5-8, the formats of strength-dependent factor (φ_{fc}) and time development function (φ_t) are similar to the FIB 2010 model because of their simplicity and wide applicability. These formats were also adopted in tensile creep model proposed by Dabarera et al. [84]. Note that the time development function (φ_t) in FIB 2010 model considers the temperature

effect. However, due to the absence of realistically measured activation energy values, the influence of temperature variation on tensile creep is not considered in the proposed model. As a result, the format of φ_t is similar to that of FIB 2010 model but the temperature part in FIB 2010 model is reconsidered by introducing a new parameter γ to account for the effect of fly ash and GGBFS. Moreover, to account for the effect of paste content on creep, Bazant et al. [232] adopted an alternative method considering the aggregate to binder ratio factor ($\varphi_{a/b}$). However, the B4 model is complex as the value of $\varphi_{a/b}$ can vary according to the types of creep compliance: instantaneous compliance, ageing viscoelastic compliance, non-ageing viscoelastic compliance, flow compliance, and drying creep compliance. In Eq. (5-8), the format of $\varphi_{a/b}$ is the same as those in B4 model, but $\varphi_{a/b}$ is simplified by using a constant β which depends only on the binder compositions. In Table 5-8, α, β and γ are constants, depending on the type of SCM and the percentage of cement replacement. α, β and γ values were determined by fitting the test data of each concrete type (no SCMs, 30% fly ash, 40% and 60% GGBFS) separately. Levenberg–Marquardt least square regression analysis method was used to determine these as shown in Table 5-9. Initially, the parameter α fitting was carried out using the experimental data on each concrete type separately. It is observed that the constants obtained based on each type of concrete were consistent with each other. As a results, for simplicity, a single value was defined for parameter α, and the constant value was 4. β and γ values of reference concrete were higher than those of fly ash concrete. This was consistent with the observation that using fly ash can slightly reduce the tensile creep coefficient. However, β and γ values were higher for GGBFS concretes and increased with the increase in GGBFS content, this was also consistent with the creep

results showing that GGBFS leads to an increase in concrete creep. At this stage, the parameters α, β and γ are fitting parameters without a more precise physical explanation.

Table 5 - 9: Parameters of the tensile creep model.

Parameters	No SCMs	30% fly ash	40% GGBFS	60% GGBFS
α	4	4	4	4
β	-1	-1.5	-0.8	-0.7
γ	1	0.9	1.2	1.3

An interesting linear relationship between β and γ values and the percentage of SCM is observed in Table 5-9. As a result, β and γ functions are developed as a function of two variables (percentage of GGBFS and fly ash) to preserve the simplicity of the proposed prediction formula. The functions are as shown in Eqs. (5-9a) and (5-9b):

$$\beta(p,q) = \frac{p}{2} - \frac{5q}{3} - 1 \quad (5\text{-}9a)$$

$$\gamma(p,q) = \frac{p}{2} - \frac{q}{3} + 1 \quad (5\text{-}9b)$$

where p and q are the percentage of GGBFS and fly ash, respectively.

The above β and γ functions can also be applied to ternary blends. For example, for concrete mix containing 15% fly ash and 20% GGBFS, the values of β and γ can be calculated as -1.15 and 1.05 as per Eq. (5-9), respectively. This is consistent with a previous paper reporting that the properties of fly ash and GGBFS ternary blends-based concrete lied between the fly ash concrete and GGBFS concrete [233]. The concrete tensile creep coefficient then can be determined using Eq. (5-8). Although further research should be required, the influence of fly ash and GGBFS on tensile creep and the applicability of the model is extended to a wide range of concrete mixes with fly ash or GGBFS and ternary

blends. It should also be noted that the proposed model is valid for concrete mixtures with fly ash content up to 30% and with GGBFS content up to 60%.

To demonstrate the reliability of the proposed tensile creep models for various concrete mixes, Figure 5-6 summarises the 7- and 28-day tensile compliances. For the sake of comparison, the values of ACI209R-92, FIB 2010, GL 2000 and Eurocode 2 models are also included in Figure 5-6. The proposed model exhibited a better agreement between the predicted and experimental compliances than the compliances obtained from other models. Statistical analysis showed that the mean value and CoV of the ratio of the proposed model to the experimental results are 0.95, 0.19 and 0.96, 0.18 at 7 and 28 days, respectively. Secondly, the mean value of the proposed model is 0.95, indicating that it can provide conservative results, which is beneficial in estimating the development of tensile stress and reducing the risk of early age cracking.

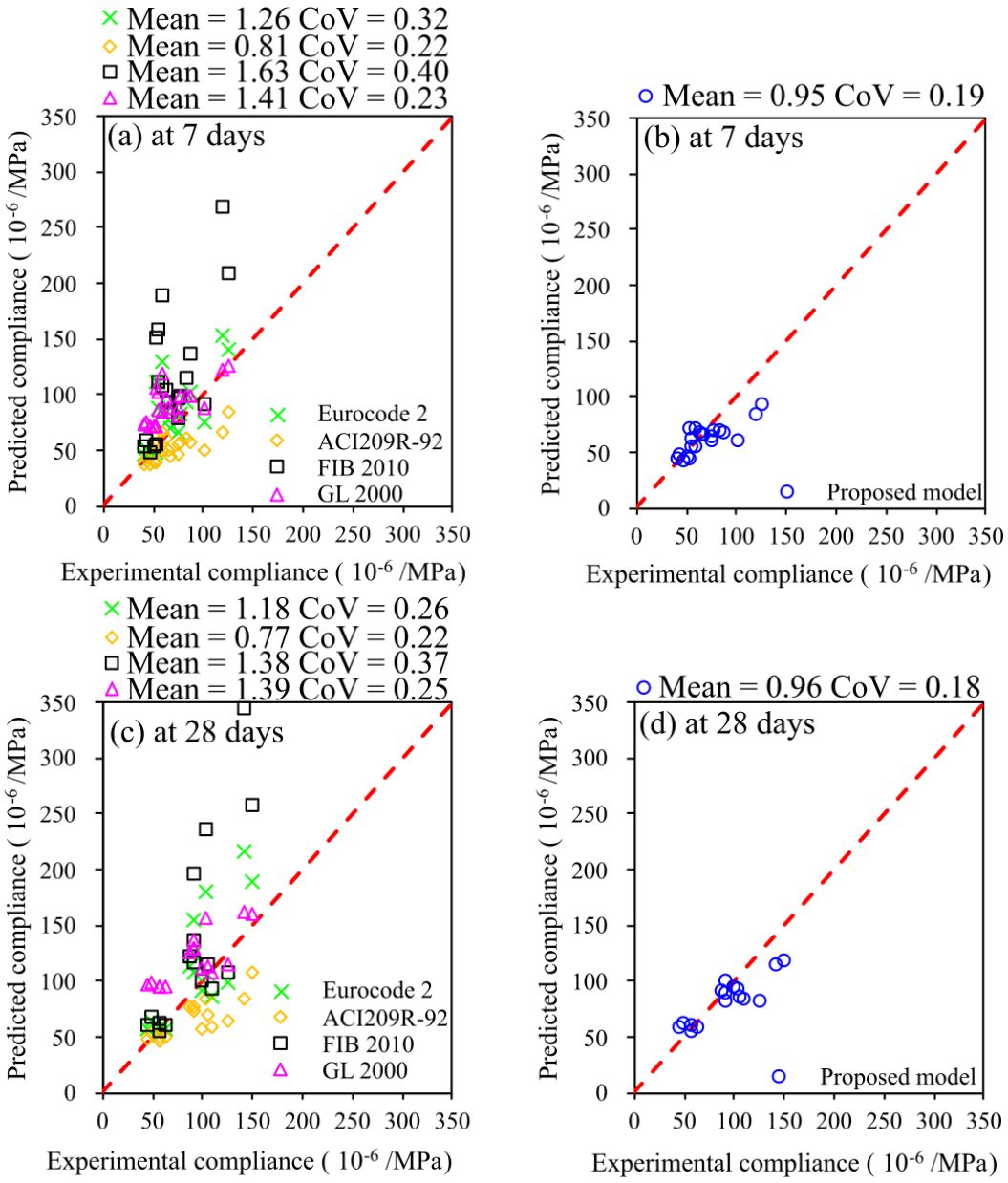

Figure 5 - 6: Statistical analysis between predicted and experimental compliance for all concrete mixes: (a) existing models at 7 days; (b) proposed model at 7 days; (c) existing models at 28 days; (d) proposed model at 28 days.

5.7 Applications: analysis of early age tensile stress development in the restrained shrinkage ring test

Chapter 4 proposed an analytical model to predict the development of concrete tensile stress in the restrained shrinkage ring test based on the age-adjusted effective modulus method. The tensile creep coefficient is an input parameter of the model, which was determined experimentally. To improve the adaptability of the analytical model and to avoid time-depending experiments, the authors propose to implement the new tensile creep model. The predicted results are compared to the experimental results shown in Chapter 4, in terms of tensile stress development. The concrete mixes used in the restrained ring test and the environmental conditions were identical to the ones used for the tensile creep test. As shown in Figure 5-7, the dimensions of the inner and outer radii of the steel ring are 130 mm and 135 mm, respectively. The outer radius of the concrete ring is 170 mm. The height of concrete ring is 70 mm, and the thickness is 35 mm. The analytical model is shown in Chapter 4. On the other hand, by measuring the strain of steel, the tensile stress in concrete can be obtained from Eq. (4-1) [152].

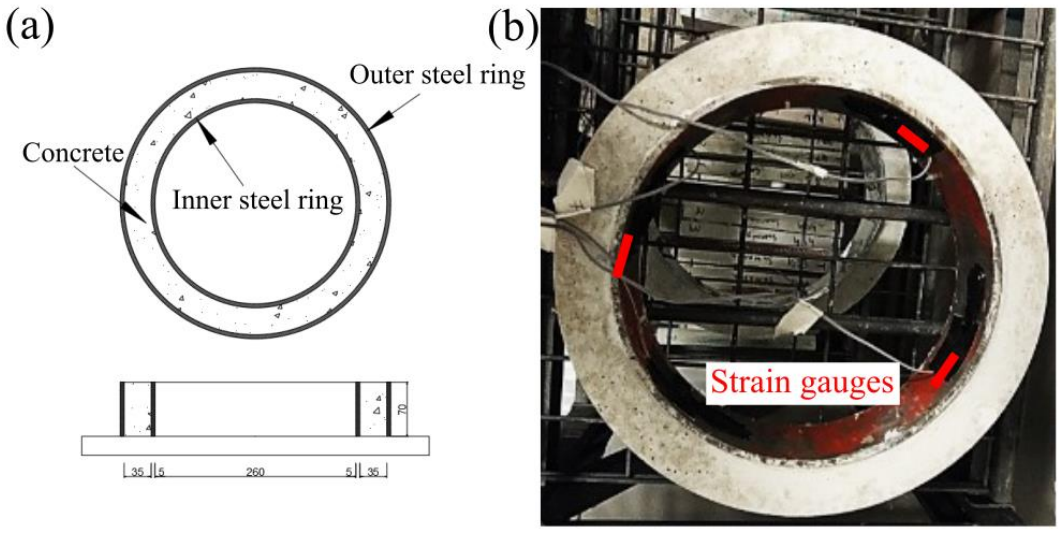

Figure 5 - 7: Restrained ring test: (a) dimension; (b) ring specimen.

Figure 5-8 shows the tensile stress at the time of concrete cracking (observed experimentally) using three approaches: (i) denoted as 'Measured stress' which was calculated using the measured steel strain and Eq. (5-10); (ii) is denoted as 'Tensile stress – creep results', where the experimental tensile creep strains are used to calculate the tensile creep coefficient and Eq. (5-10); and (iii) is denoted as 'Tensile stress – creep model, where the tensile creep model prediction in Eq. (5-8) are used to calculate the tensile stress (Eq. (5-10)). A good agreement between experimentally measured and analytically calculated tensile stress is obtained. The mean value and CoV of the ratio of analytical and experimental values are 1.00 and 0.08, respectively. This indicates that the proposed tensile creep model can be used to analyse the development of concrete tensile stress in the restrained ring test, allowing to avoid experimentations related to tensile creep which are not straightforward tests and testing rigs unlikely to be available in the industry.

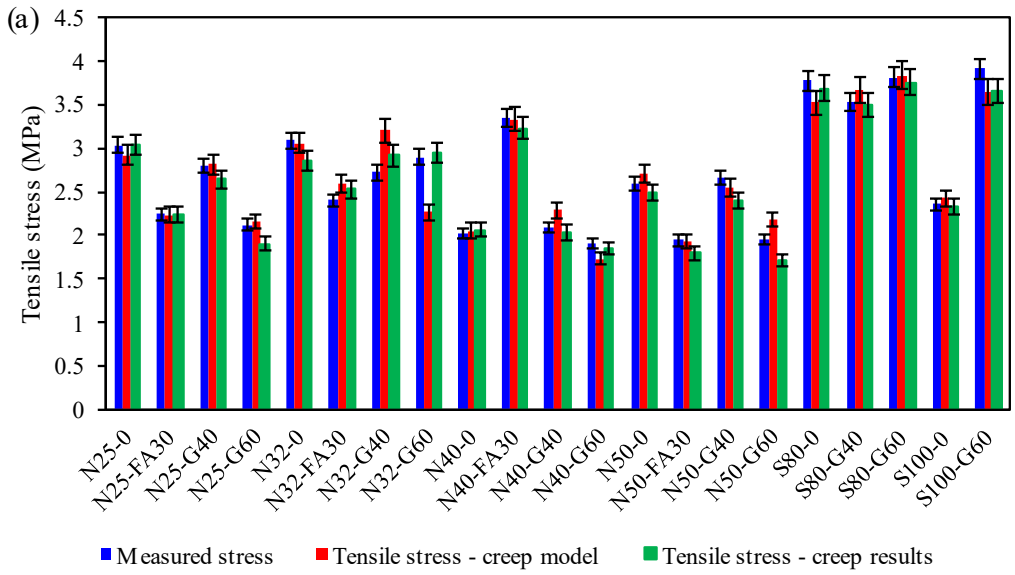

Figure 5 - 8: (a) Comparison between calculated stress using the proposed creep model and experimentally determined stress at cracking time for all mixes; (b) statistical analysis for all mixes.

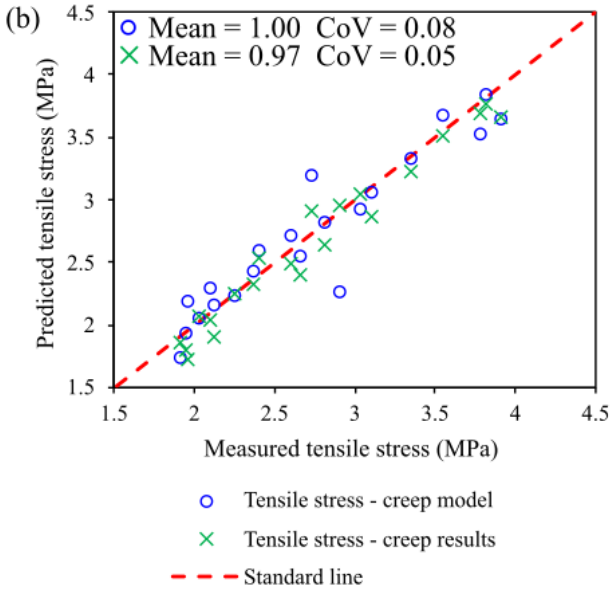

Figure 5 – 8: (continued)

5.8 Conclusions

In this chapter, the tensile creep of concrete mixes with a high volume of fly ash and GGBFS were investigated. The main observations are outlined as follows:

1. The tensile creep of concrete depends on various factors, such as compressive strength or w/b ratio, the paste content, and the type of SCM. The addition of fly ash slightly reduces the tensile creep coefficient of concrete. For GGBFS concrete, the tensile creep is higher. Moreover, the higher the GGBFS content, the higher the observed tensile creep.
2. On the basis of the newly collected test data in this chapter, existing models including ACI-209R-92, FIB 2010, GL2000, and Eurocode 2 are used to predict the compliance. None of the models initially developed for compressive creep are suitable to predict tensile creep.
3. A new model is proposed to predict of the tensile creep of concrete mixes including or not fly ash and GGBFS at a specific environmental condition of 23 °C and 50% of RH.

The model is developed based on each type of concrete (Control, 30% fly ash, 40% and 60% GGBFS) but can be extended to a wide range of concrete mixes with fly ash and GGBFS and ternary blends.

4. The proposed model can conservatively reflect the development of the early age tensile creep. The proposed model can be used to predict the tensile stress development in the restrained ring test, allowing for avoiding experimentations related to tensile creep which are not straightforward tests. The tensile creep model proposed requires further validation using different sources of binders and the governing parameters may need to be further calibrated. In addition, a more general form of the tensile creep model could be developed considering the effect of temperature, relative humidity, and loading age in order to expand its applicability. This research can also contribute to developing a performance-based specification based on the ring test, allowing to reduce the risk of concrete early age cracking due to restrained shrinkage.

CHAPTER 6: EXPERIMENTAL STUDY ON NONLINEAR TENSILE CREEP BEHAVIOUR OF ULTRA-HIGH PERFORMANCE CONCRETE (UHPC)

Chapter 6 is a re-written version of an article submitted by the candidate, 'Tensile Creep of Steam-cured UHPC: Linear and Nonlinear Creep', in Cement and Concrete Composite. I did more than 50% the experiments and development. Some of the materials in this chapter have been re-written from a recent submission, which has been acknowledged and detailed in the 'Inclusion of Publications Statement' for this thesis.

6.1 Introduction

Ultra-high performance concrete (UHPC) has been widely utilised in engineering fields such as buildings, bridges, dams, and reinforced concrete (RC) structures due to its high strength, and improved durability [234, 235, 236]. For instance, UHPC can be used in RC structures by replacing fully or partially the traditional concrete to enhance the resistance to cracking, especially in the negative bending moment zone. It is because the tensile strength of UHPC is significantly higher than that of conventional concrete. In the negative bending moment zone of traditional RC structures, the risk of early age cracking is very high due to the significantly low tensile strength [237]. However, in the case of UHPC structures, due to their high tensile load-bearing capacity, the structures can resist large deflection, including tensile creep deformation. In contrast, the system remains uncracked for a long time. Therefore, it is crucial to understand the time-dependent behaviour, such as the tensile creep of UHPC.

Similar to compressive creep, tensile creep increases the curvature of the cross-section, leading to an underestimation of the long-term deformation of the structure. It may put the structure out of service or reduce the service life of the structure. It is worth noting that the level of sustained stresses can exceed the linear limit for UHPC materials. For instance, the tensile creep becomes nonlinear with respect to the high stress level [238].

There is considerable literature on the nonlinear viscoelastic behaviour of concrete but have yet to draw any unanimous conclusions [219, 204, 239, 54, 240, 241]. As shown in Bissonnette et al. [219], the tensile elastic strain of concrete is proportional to tensile stress under a stress level of 50%. In contrast, Rossi et al. [204] demonstrated that the linear viscoelastic behaviour could exhibit up to a loading level of more than 70% in a basic tensile creep test. However, Bazant and Jirasek [239] stated that the nonlinearity in tensile creep might occur at a lower stress level than compressive creep (40%-50%). In work by Garas et al. [240], it was observed that the tensile creep coefficients increased 44% when the stress to tensile strength ratios increased from 40% to 60%, which increases the nonlinearity of tensile creep occurs at a stress level of 40%. In another paper, Garas et al. [54] showed that the tensile creep coefficient was decreased due to the presence of steel fibre. On the other hand, according to Wei et al. [241], the tensile creep coefficient was found to decrease when the stress levels increased from 40% to 70%. Thus, it is critical to understand the behaviour of nonlinear tensile creep of concrete.

In most existing codes, various prediction models, such as ACI-209R-92 [206], GL 2000 [208], AS3600-2018 [192] and Eurocode 2 [209], are predominately proposed to predict the creep coefficient of traditional concrete. However, the accuracy of these models for modern UHPC materials has not been widely investigated. In addition, many theoretical and

experimental studies regarding the nonlinear creep coefficient of plain concrete can be found in the literature [200, 242]. Nevertheless, the theoretical calculations of the nonlinear tensile creep coefficient for UHPC have not been examined. Thus, assessing the accuracy of these prediction models and the analytical models of nonlinear creep coefficient is significant.

This chapter presents the tensile creep test series of UHPC under three different stresses to tensile strength ratios (40%, 60% and 75%) and two different ages of UHPC at loading (2 and 28 days) conducted. A comparison of the tensile creep behaviour including the nonlinear tensile creep coefficient between the experimental results and various model predictions was performed.

6.2 Experimental program

6.2.1 Materials and mix design

In this experiment, UHPC mixes with water to binder ratio of 0.15 were used. Three types of binder, Ordinary Portland cement (OPC), silica fume (SF) and ground granulated blast furnace slag (GGBFS) were, utilised in accordance with Chinese Standard GB 175 [243], GB/T27690 [244], and GB/T18046 [245], respectively. Crushed quartz sand with a maximum size of 1.25 mm was used as aggregate. Steel fibre with a 12-16 mm length and a diameter of 0.18-0.22 mm was utilised to mix the UHPC. In addition, a superplasticiser with high-concentration viscosity was used to improve the workability of UHPC. Table 6 - 1 shows the mix design of the commercial UHPC concrete used in this study.

Table 6 - 1: Mix design of the commercial UHPC concrete.

Materials	UHPC (kg/m^3)
OPC	551
SF	114
GGBFS	285
Aggregate	1560
Steel fibres	0
Water	142
Superplasticizer	9.5

6.2.2 Mechanical properties test

The mechanical properties tests, including compressive strength, splitting tensile strength, and elastic modulus, were conducted on cylinders with a diameter of 100 mm by 200 mm height. The flexural strength of concrete was determined using prismatic specimens. The typical size of the prisms is 400 mm × 100 mm × 100 mm. The mechanical properties tests were carried out at the age of 3, 7, 14, and 28 days and cured in standard conditions (20°C ± 1 °C and relative humidity of 95 ± 5%) in accordance with Chinese Standard GB/T 50081 [246]. In addition, the authors developed the dog-bone specimens to determine the direct tensile strength of UHPC, and the specimens were also used in the tensile creep test, as shown in Figure 6-1. The direct tensile strength was tested at 2, 3, 7, 14 and 28 days.

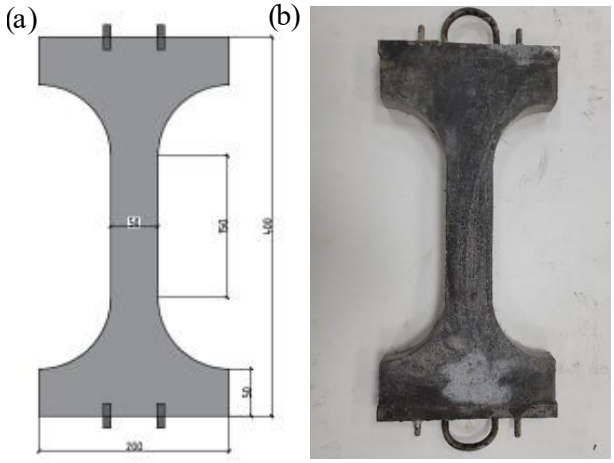

Figure 6 - 1: Dog-bone specimens: (a) dimension; (b) actual specimen.

6.2.3 Tensile creep test

As mentioned above, the tensile creep tests were conducted using dog-bone specimens, as shown in Figure 6-2. This method for the tensile creep test was developed by in the previous works [66, 51, 171, 87, 67]. The dog-bone specimen had an equal cross-section part with a length of 150 mm at mid-height. Two strain gauges were attached on two sides of the specimens to check the deformation. The steel plates were connected to the specimens by two threaded bolts, which were cast into the specimens at each end. Hence, it was assumed that an even stress distribution can be obtained in this design. A total of five tensile creep test series were uniaxially loaded to a tensile stress level of 40%, 60% and 75% of the tensile strength of concrete at the concrete age of 2 and 28 days, respectively, as outlined in Table 6-2. According to different stress levels and initiated loading age, the test series was designated as U2-40, U2-60, U2-75, U28-40, and U28-60, respectively. The stress level of 40% was chosen to examine the linear case, while 60% and 75% were selected to investigate the difference in the nonlinear case. The tensile stress level of 75% for UHPC at the age of 28 days has not been included because of the unexpected failure

during the assembly of the test. Three dog-bone specimens were used for each series, and the constant designated stress levels were maintained for 28 days. All the dog-bone specimens were demoulded after 24 hours and then cured in standard conditions at a temperature of 20 ℃ ± 1 ℃ and a relative humidity of 90% in accordance with GB/T50081-2019 [246]. On the day of testing, the specimens were moved to an environmentally controlled room with a temperature of 20 ℃ ± 1 ℃ and relative humidity of 50 ± 3%. The measurements were continuously recorded until 28 days. For the loaded dog-bone specimens, the total deformation, including elastic, creep, and shrinkage strains, can be represented in Eq. (6-1):

$$\varepsilon_{tot} = \varepsilon_{el} + \varepsilon_{cr} + \varepsilon_{sh} \tag{6-1}$$

In addition, the accompanied free shrinkage test was performed on three unloaded dog-bone specimens in the same environmentally controlled room. Hence, the creep strain can be deduced based on the total strain and shrinkage strain measured on loaded and unloaded dog-bone specimens, respectively, as shown in Eq. (6-2):

$$\varepsilon_{cr} = \varepsilon_{tot} - \varepsilon_{el} - \varepsilon_{sh} \tag{6-2}$$

Figure 6 - 2: Tensile creep tests of UHPC.

Table 6 - 2: Description of test series.

Sample ID	Stress/strength ratio (%)	Loading age (days)
U2-40	40	2
U2-60	60	2
U2-75	75	2
U28-40	40	28
U28-60	60	28

6.3 Test results and discussions

6.3.1 Mechanical properties of UHPC

The mechanical properties, including compressive, splitting tensile and flexural strengths, elastic modulus and the direct tensile strength of UHPC, are provided in Table 6-3. Each result was obtained based on the average of three tested samples. It can be seen that after 3 days, the development of compressive strength rapidly reached 57% of 28-day compressive strength, while the flexural strength and direct tensile strength developed slower than that of compressive strength. The 3-day flexural strength and direct tensile strengths were only 38% and 46% at 28 days. After 14 days, except for flexural strength, all the mechanical properties reached more than 90% of those at the age of 28 days.

Table 6 - 3: Mechanical properties of UHPC.

Age (days)	Compressive strength (MPa)	Splitting tensile strength (MPa)	Flexural strength (MPa)	Elastic modulus (GPa)	Direct tensile strength (MPa)
2	N/A	N/A	N/A	N/A	3.4
3	55.9	5.8	9.2	23.4	4.2
7	71.2	8.8	15.5	32.1	7.1
14	88.9	9.9	20.3	38.7	8.6
28	97.5	10.8	24.1	41.6	9.1

6.3.2 Influence of age at loading on tensile creep

Figures 6-3 and 6-4 show the tensile creep strain and tensile creep coefficient performed for UHPC loaded at 2 and 28 days, respectively. The creep coefficient is one of the most commonly used approaches to illustrate the creep behaviour of concrete, and it is defined as the ratio of the creep strain to the elastic strain, as shown in Eq. (6-3):

$$\varphi_{cr} = \frac{\varepsilon_{cr}}{\varepsilon_{el}} \tag{6-3}$$

where ε_{cr} is the creep strain; ε_{el} is the elastic strain measured immediately after applying the tension to the dog-bone specimen.

It can be seen that allowing for the 26 days curing period, the tensile creep strains of UHPC can be effectively reduced. In other words, more curing before applying the load allowed the reduction of creep strain. After a 28-day test period, the tensile creep strains of U28-40 and U28-60 were reduced by 18.9% and 19.9% to that of U2-40 and U2-60, respectively. While the tensile creep coefficients of U28-40 and U28-60 were reduced by 39.4% and

40.1% compared to their corresponding U2-40 and U2-60, respectively. This is attributed that the bond between the steel fibre and the cement hydration products was significantly increased from 2 to 28 days, reducing the creep strain due to the maturity of UHPC [219, 247]. Such behaviour was also noted by Garas et al. [240].

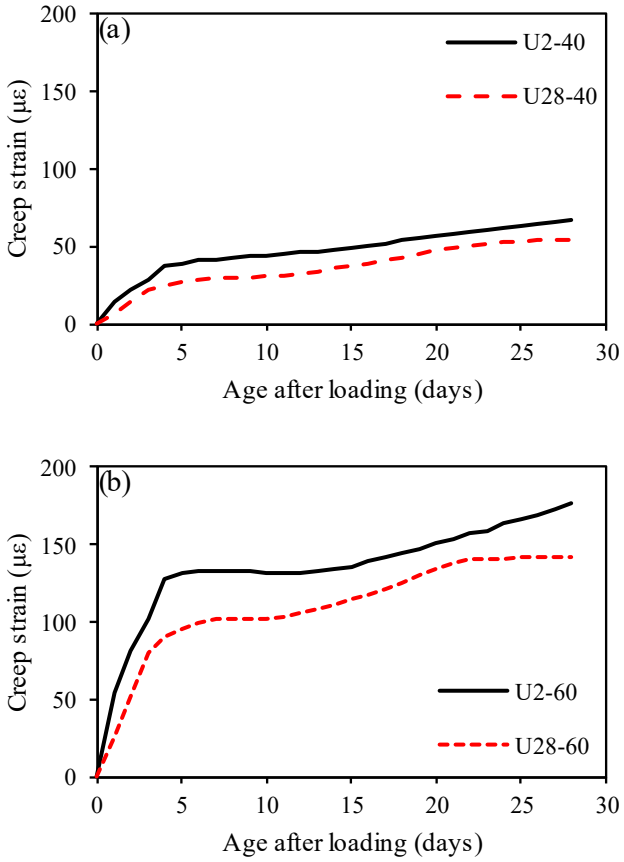

Figure 6 - 3: Tensile creep strain comparison for UHPC loaded at 2 and 28 days: (a) stress to strength ratio = 0.4; (b) stress to strength ratio = 0.6.

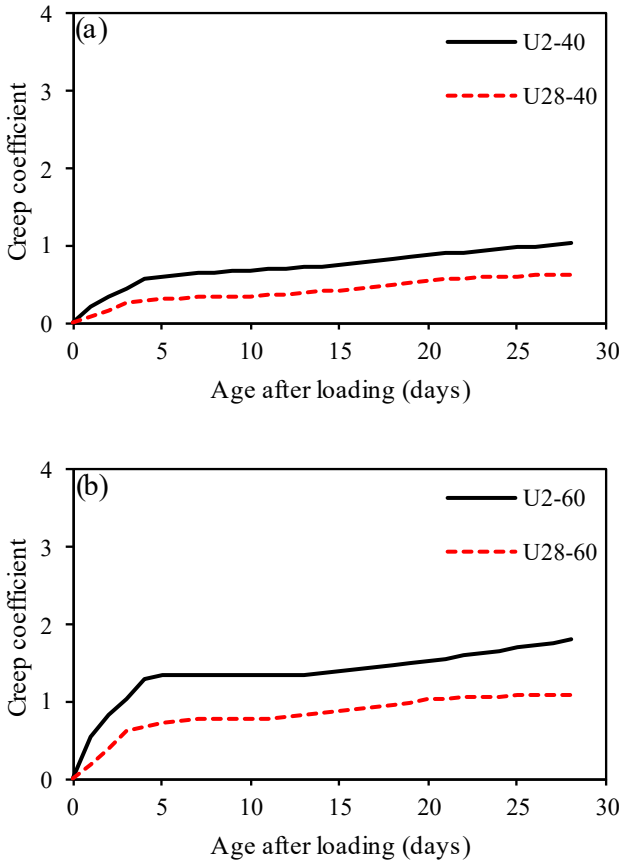

Figure 6 - 4: Tensile creep coefficient comparison for UHPC loaded at 2 and 28 days: (a) stress to strength ratio = 0.4; (b) stress to strength ratio = 0.6.

6.3.3 Influence of stress levels on tensile creep

The tensile creep strain and tensile creep coefficient performed under different stress to strength ratios are shown in Figures 6-5 and 6-6, respectively. Similarly to the previously published findings [219], and as expected, the tensile creep strain and tensile creep coefficient were higher with the higher applied stress levels. It can be seen that the tensile creep strains of U2-60 and U2-75 were about 2.64 and 4.61 times higher than that of U2-40. This relationship was also observed for UHPC loaded at 28 days, i.e., the tensile creep strains of U28-60 were about 2.61 times higher than that of U28-40. In the tensile creep

coefficient of U2-60 and U2-75, the values were 1.24 times and 2.46 times higher than that of U2-40, respectively. While the tensile creep coefficient of U28-60 was about 1.26 times greater than U28-40. It is worth mentioning that the measured elastic strain under a sustained stress level of 40% was approximately equal to that calculated using the applied stress divided by the measured elastic modulus. However, this correlation is not valid for the 60% and 75% of stress levels due to the nonlinearity of materials. Similar results were also noted by Hamed [248]. As a result, experimentally measured ε_{el} will be used in this chapter instead of the calculated value of ε_{el}. The nonlinear tensile creep behaviour of UHPC will be discussed in Section 6.3.4.

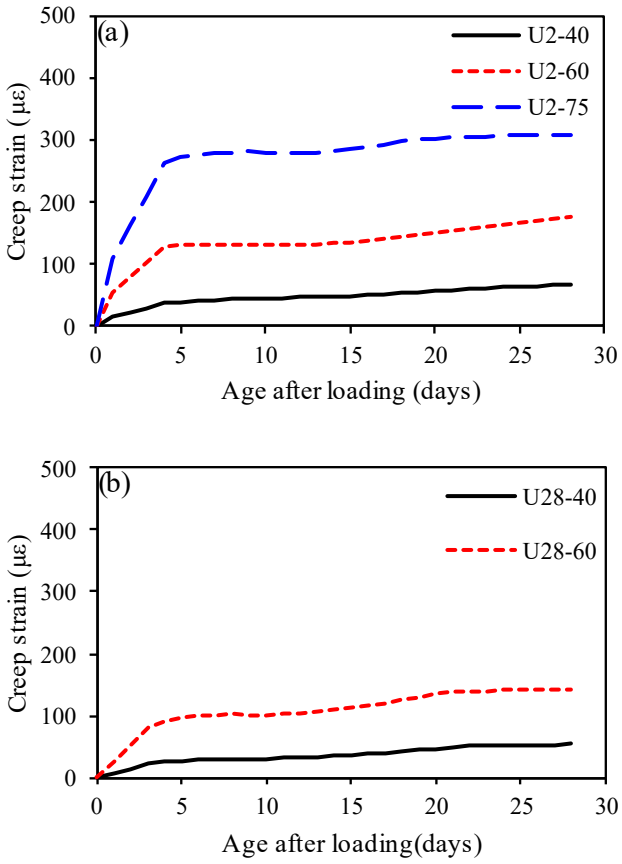

Figure 6 - 5: Tensile creep strain comparison for UHPC: (a) loaded at 2 days; (b) loaded at 28 days.

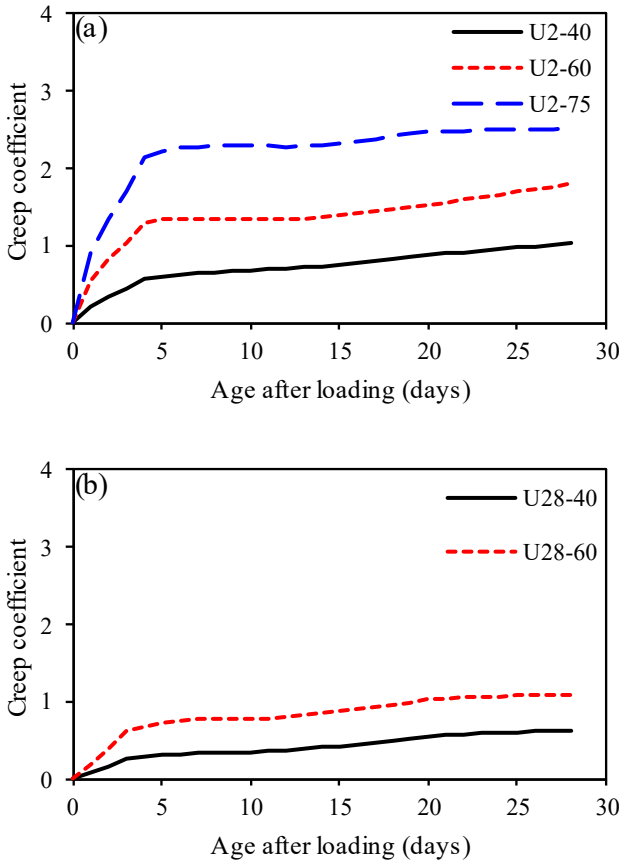

Figure 6 - 6: Tensile creep coefficient comparison for UHPC: (a) loaded at 2 days; (b) loaded at 28 days.

6.3.4 Influence of nonlinear tensile creep

The nonlinear creep effect of concrete is usually described as follows:

$$\varepsilon_{cr} = \varepsilon_{cr}^{L} \cdot \varphi_{nl} \tag{6-4}$$

where ε_{cr}^{L} is the linear creep strain component calculated according to the linear creep theory; φ_{nl} is the nonlinear creep factor.

This chapter adopts the creep strains of U2-40 and U28-40 as the baseline. According to the linear creep theory, the linear creep strain can be calculated as follows:

$$\varepsilon_{cr}^{L} = \varepsilon_{cr}^{40} \cdot \frac{\sigma_t}{0.4 f_{ct}} \tag{6-5}$$

where ε_{cr}^{40} is the tensile creep strain subjected to a stress level of 40%; σ_t is the applied tensile stress.

Substituting Eq. (6-5) into Eq. (6-4), the nonlinear tensile creep factor φ_{nl} can be calibrated as follows:

$$\varphi_{nl} = \frac{\varepsilon_{cr}}{\varepsilon_{cr}^{L}} = \frac{\varepsilon_{cr}}{\sigma_c} \cdot \frac{0.4 f_{ct}}{\varepsilon_{cr}^{40}} \tag{6-6}$$

In addition, the nonlinear tensile creep factor can also be expressed in terms of the tensile creep coefficient as follows:

$$\varphi_{nl} = \frac{\varphi_{cr}}{\varphi_{cr}^{L}} \tag{6-7}$$

where φ_{cr}^{L} is the linear creep coefficient.

Conventionally, the nonlinearity in compressive creep occurs when the stresses are at about 40%-50% of compressive strength [249, 250]. However, according to Bazant and Jirasek [239], the nonlinearity in tension may develop much lower stress than in compression. Therefore, as mentioned earlier, the tensile creep strain under a stress level of 40% was assumed to be the linear case. In comparison, the tensile creep strains corresponded to the 60% and 75% stress levels and were assumed to be nonlinear cases. Figure 6-7 shows the non-linearity of experimental creep strain by comparing experimental creep strains with the computed creep strain assuming that the linear creep strain ($\varphi_{nl} = 1.0$) for U2-60, U2-75, and U28-60, respectively. Note that the linear creep strain values at high stress levels were calculated based on the experimental results of a 40% stress level scaled by the ratio between the corresponding stress level and 40%. For example, the assumed values of U2-60 were calculated by U2-40 experimental results scaled by 60% and 40% ratios. It can be

seen that after a 28-day test period, the experimental tensile creep strains for U2-60 and U2-75 were 43.2% and 59.3% higher than the computed values assuming the linear creep strain, this indicates that the higher stress levels resulted in the higher nonlinearity and the higher tensile creep strains. A similar result can be found in Ref. [251]. When it comes to U28-40 and U28-60, the differences in nonlinear tensile creep strains were similar to that of U2-40 and U2-60, and U28-60 is 42.5% higher than U28-40, indicating the nonlinearity of UHPC material is only marginally affected by the curing age. However, the results are contrary to published reports [241]. The study in [241] shows that the tensile creep coefficient at a stress level of 70% was slightly lower than that of a 40% stress level. The possible reason could be attributed to the tensile creep nonlinearity depending on the stress levels, concrete composition, and exposure conditions.

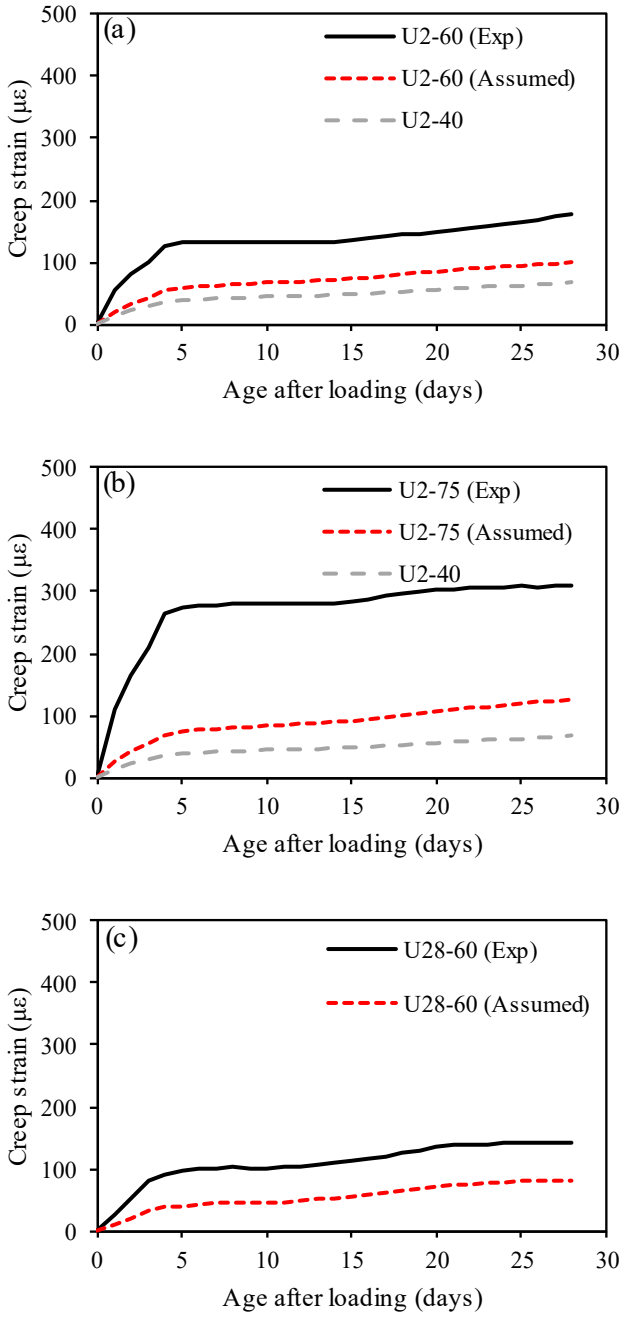

Figure 6 - 7: Nonlinear time-dependent tensile creep comparison for: (a) loaded at 2 days, stress to strength ratio = 0.75; (b) loaded at 2 days, stress to strength ratio = 0.6; (c) loaded at 28 days, stress to strength ratio = 0.6.

The development of the nonlinear tensile creep factor of two groups of UHPC is presented in Figure 6-8. Generally, the nonlinearity decreased with the increasing duration of loading of UHPC. As mentioned above, a stress level of 40% is adopted as a baseline. Moreover, the nonlinear tensile creep factor increased with the stress to strength ratio increment. For a stress level of 60%, the nonlinear creep effect is 1.94 and 2.06 times on average that of baseline for the U2 and U28 groups, respectively. In comparison, the average nonlinear creep factor value is 3.14 for the stress-strength ratio of 75% in the U2 group.

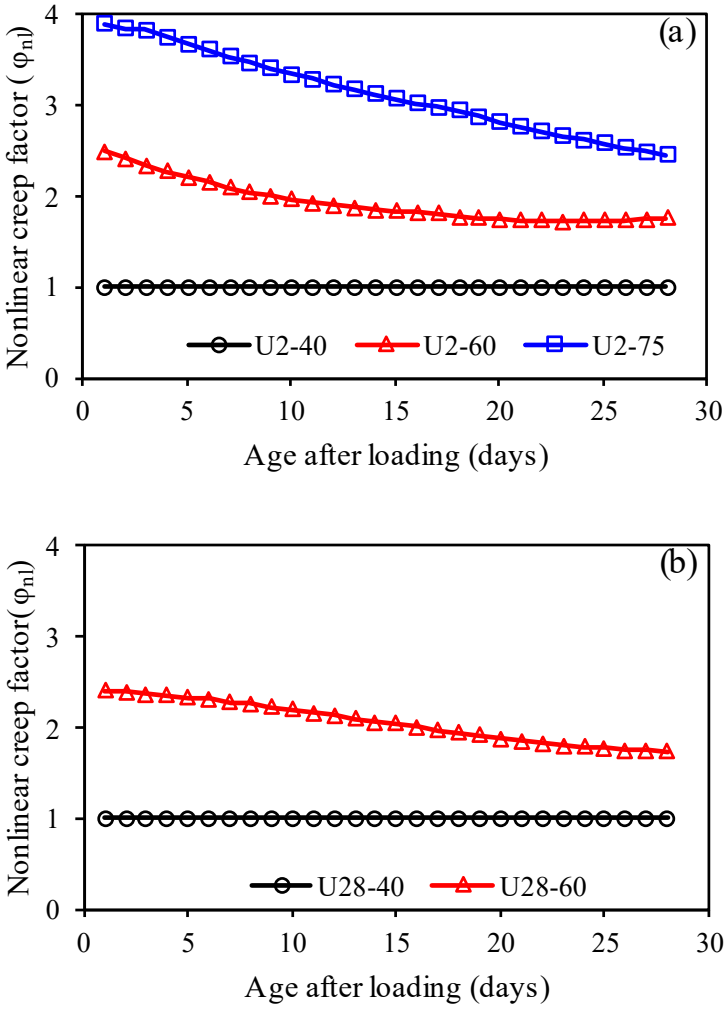

Figure 6 - 8: Time development of nonlinear tensile creep factor: (a) U2; (b) U28.

6.4 Comparison to existing prediction models

6.4.1 Prediction of tensile creep coefficient

As discussed above, the prediction of tensile creep coefficient for UHPC is influenced by numerous factors such as stress to strength ratio, curing age, steel fibre, etc. The available models [206, 208, 209, 192] in existing codes and literature for predicting the tensile creep coefficient are presented, and the comparison of experimental results to those predictions is assessed in this section.

6.4.1.1 ACI209R-92 model [206]

The American Concrete Institute (ACI) 209 proposed the ACI209-92 model in 1992 and confirmed and adopted it again in 2008. The model uses a hyperbolic function to calculate the ultimate creep value. The expression is evaluated as a function of time to reach the final value. The model predicts creep for lightweight concrete with cement types I and III, ambient relative humidity between 40% and 100%, standard curing or steam curing. The shape and the limits of the curve depend on several factors, including curing conditions, age of concrete at loading (in days), mix design, specimen size, ambient temperature, relative humidity, the ratio of fine aggregate to total aggregate, etc. The model is shown in Eq. (6-8):

$$\varphi(t,t_0) = \frac{(t-t_0)^{0.6}}{10+(t-t_0)^{0.6}} \times 2.35 \times \gamma_{c,t0}\gamma_{c,RH}\gamma_{c,vs}\gamma_{c,s}\gamma_{c,\psi}\gamma_{c,\alpha} \qquad (6\text{-}8)$$

where $\gamma_{c,t0}$ is the age at loading factor depends on moist or steam curing; $\gamma_{c,RH}$ is relative humidity factor; $\gamma_{c,vs}$ is the volume-surface ratio factor; $\gamma_{c,s}$ is the slump factor; $\gamma_{c,\psi}$ is the fine aggregate factor; and $\gamma_{c,\alpha}$ is the air content factor, and the expressions to those factors are presented as follows:

$$\gamma_{c,t0} = \begin{cases} 1.25t_0^{-0.118} & \text{for moist curing} \\ 1.13t_0^{-0.094} & \text{for steam curing} \end{cases} \quad (6\text{-}9a)$$

$$\gamma_{c,RH} = \begin{cases} 1.27 - 0.67RH & \text{for RH} \geq 0.40 \\ 1.0 & \text{for RH} < 0.40 \end{cases} \quad (6\text{-}9b)$$

$$\gamma_{c,vs} = \frac{2}{3}(1 + 1.13e^{\{-0.0213(V/S)\}}) \quad (6\text{-}9c)$$

$$\gamma_{c,s} = 0.82 + 0.00264s \quad (6\text{-}9d)$$

$$\gamma_{c,\psi} = 0.88 + 0.0024\psi \quad (6\text{-}9e)$$

$$\gamma_{c,\alpha} = 0.46 + 0.09\alpha \geq 1 \quad (6\text{-}9f)$$

where t_0 is the age of concrete at loading; RH is the relative humidity; V/S is the volume-to-surface ratio; s is the slump of concrete; ψ is the ratio of fine aggregate to total aggregate; and α is the air content of concrete.

6.4.1.2 GL 2000 model [208]

In 1993, Gardner and Zhao analysed a large number of long-term creep test results and proposed the GZ 1993 model, and then Gardner and Lockman improved the GZ 1993 model with the GL 2000 model [208]. The model considers the initial loading age of concrete, loading time, concrete drying age and water curing period, volume to surface ratio, ambient relative humidity, etc. The model is more convenient to calculate because basic creep and drying creep are not distinguished in GL 2000 model. The GL 2000 model also has good calculation accuracy. The model is shown in Eq. (6-10):

$$\varphi(t, t_0) = \frac{2(t - t_0)^{0.3}}{(t - t_0)^{0.3} + 14} + (\frac{7}{t_0})^{0.5}(\frac{(t - t_0)}{(t - t_0) + 7})^{0.5} + 2.5(1 - 1.086RH^2)(\frac{(t - t_0)}{(t - t_0) + 0.12(V/S)^2})^{0.5} \quad (6\text{-}10)$$

In this model, the age of concrete at loading (in days), volume-to-surface ratio, and time development is required to calculate the creep coefficient. In addition, the creep coefficient

can be expressed in three terms. The first two terms are used to calculate basic creep, while the third term calculates the drying creep.

6.4.1.3 Eurocode 2 model [209]

The creep prediction model proposed in the Eurocode 2 model considers the ambient temperatures between -40 and 40 °C and relative humidity between 40% and 100%. The model also takes into account compressive strength, relative humidity, loading age of concrete, time development function and nonlinear creep factor. The prediction model is presented in Eq. (6-11):

$$\varphi(t,t_0) = \varphi_{RH}\beta(f_{cm})\beta(t_0)\beta_c(t,t_0)\varphi_{nl} \tag{6-11}$$

where φ_{RH} is the relative humidity factor which depends on the hypothetical thickness h_0; $\beta(f_{cm})$ is the strength-dependent factor; $\beta(t_0)$ is the age of loading factor; $\beta_c(t,t_0)$ is the time development function; and φ_{nl} is the nonlinear creep factor. The expressions of above factors are provided as follows:

$$\varphi_{RH} = \begin{cases} 1 + \dfrac{1 - RH/100}{0.1\sqrt[3]{h_0}} & \text{for } f_{cm} \le 35 \text{ MPa} \\ \left[1 + \dfrac{1 - RH/100}{0.1\sqrt[3]{t_h}}\left(\dfrac{35}{f_{cm}}\right)^{0.7}\right]\left(\dfrac{35}{f_{cm}}\right)^{0.2} & \text{for } f_{cm} \ge 35 \text{ MPa} \end{cases} \tag{6-12a}$$

$$t_h = \frac{2A_g}{u_e} \tag{6-12b}$$

$$\beta(f_{cm}) = \frac{16.8}{\sqrt{f_{cm}}} \tag{6-12c}$$

$$\beta(t_0) = \frac{1}{0.1 + t_0^{0.2}} \tag{6-12d}$$

$$\beta_c(t,t_0) = \left[\frac{t - t_0}{\beta_H + t - t_0}\right]^{0.3} \tag{6-12e}$$

$$\beta_H = \begin{cases} 1.5[1 + (1 + 0.012RH)^{18}]h_0 + 250 \leq 1500 & \text{for } f_{cm} \leq 35 \text{ MPa} \\ 1.5[1 + (1 + 0.012RH)^{18}]h_0 + 250(\frac{35}{f_{cm}})^{0.5} \leq 1500(\frac{35}{f_{cm}})^{0.5} & \text{for } f_{cm} \geq 35 \text{ MPa} \end{cases} \quad (6\text{-}12f)$$

$$\varphi_{nl} = e^{1.5(\frac{\sigma_0}{f_{cm}} - 0.45)} \quad (6\text{-}12g)$$

6.4.1.4 AS3600-2018 model [192]

The Australian Concrete Association AS3600 proposed a model for predicting concrete creep in 2018. The model also considers the total concrete creep instead of calculating the basic and drying creep separately. The model takes into account time development function, reduced thickness, loading age, location such as arid environment, interior environment, temperate environment, tropical or near-coastal environment, high strength factor and nonlinear creep factors, etc. The model is shown in Eq. (6-13):

$$\varphi(t, t_0) = k_2 k_3 k_4 k_5 k_6 \varphi_{cc,b} \quad (6\text{-}13)$$

where k_2 is the time-dependent factor and it depends on hypothetical thickness t_h; k_3 is the age of loading factor; k_4 is the location-dependent factor, and the values are equal to 0.7, 0.65, 0.6, and 0.5 for the arid environment, the interior environment, the temperate inland environment, and the tropical or near coastal or coastal environment, respectively; k_5 is the modification factor for concrete strength within 50 to 100 MPa; k_6 is the nonlinear creep factor; and $\varphi_{cc,b}$ is the basic creep coefficient which depends on the characteristic strength of concrete. The remaining expressions are presented as follows:

$$k_2 = \frac{\alpha_2}{t^{0.8} + t_h} \quad (6\text{-}14a)$$

$$t_h = \frac{2A_g}{u_e} \quad (6\text{-}14b)$$

$$\alpha_2 = 1.0 + 1.12e^{-0.008t_h} \quad (6\text{-}14c)$$

$$k_3 = \frac{2.7}{1 + \log(\tau)} \quad \text{(6-14d)}$$

$$k_5 = (2 - \alpha_3) - 0.02(1 - \alpha_3) f_c' \quad \text{(6-14e)}$$

$$\alpha_3 = \frac{0.7}{k_4 \alpha_2} \quad \text{(6-14f)}$$

$$k_6 = e^{1.5(\frac{\sigma_0}{f_{cm}} - 0.45)} \quad \text{(6-14g)}$$

6.4.1.5 Comparison to existing predictions

To investigate the accuracy of various prediction models, the experimental results are to be compared with existing model predictions. It should be noted that the ACI-209R-92 model requires the maximum number of parameters and GL 2000 model requires the minimum number of parameters. However, the effect of creep nonlinearity is not considered in both models. By contrast, AS3600-2018 and Eurocode 2 models introduced a nonlinear creep factor to improve the accuracy of estimation of creep coefficient.

Figure 6-9 shows the time-dependent tensile creep coefficient of UHPC at different stress levels and curing age compared to the prediction models. It can be seen that the ACI-209R-92 model showed the lowest prediction values for tensile creep coefficient, while the GL 2000 model provides the highest estimation. The experimental values of tensile creep coefficient of UHPC mix lied between the lower and upper bounds of prediction by existing models, which indicates the correctness of experimental values can be validated. In addition, each model only worked for some of the grades. For example, the prediction by the AS3600-2018 model exhibited overestimations in most cases except U28-60. ACI209R-92 model performed well in U2-60. GL 2000 model showed the highest prediction errors. On the other hand, Eurocode 2 can successfully estimate the tensile creep coefficient developments in U2-40 and U2-60.

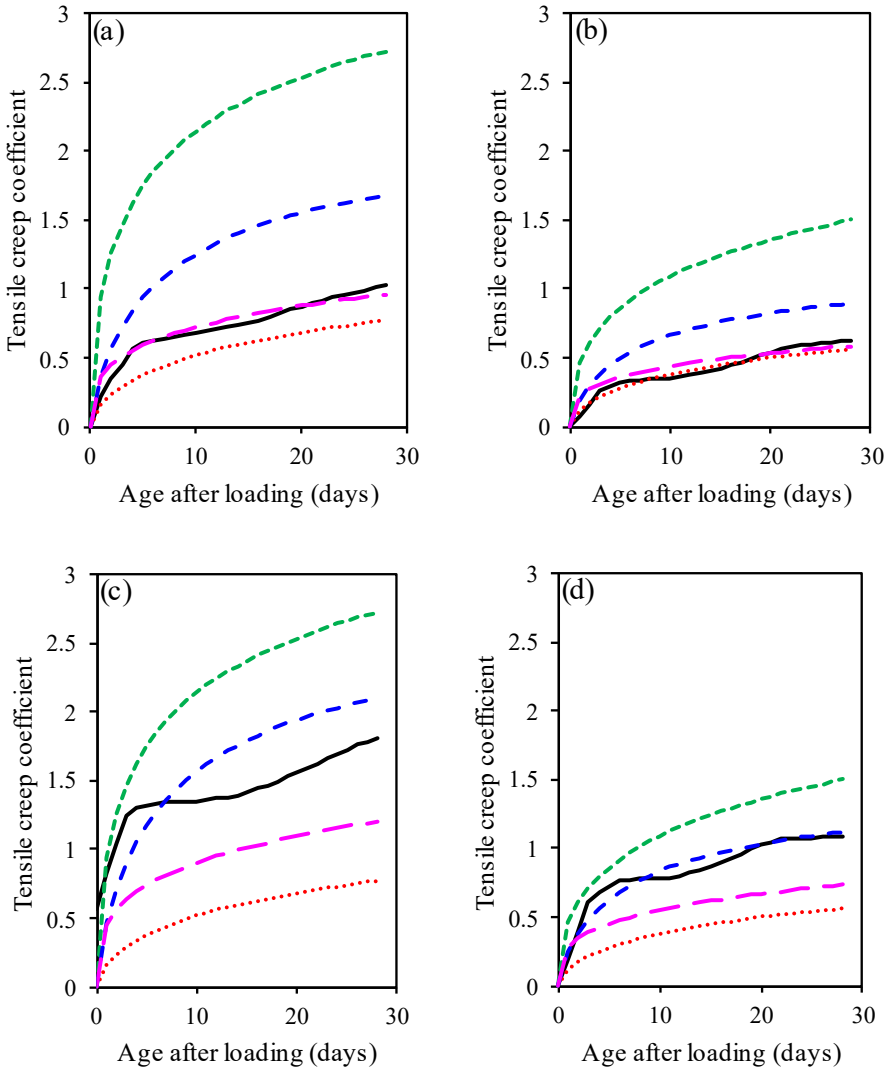

Figure 6 - 9: Comparisons between experimental tensile creep coefficient and model predictions for: (a) U2-40; (b) U28-40; (c) U2-60; (d) U28-60; (e) U2-75.

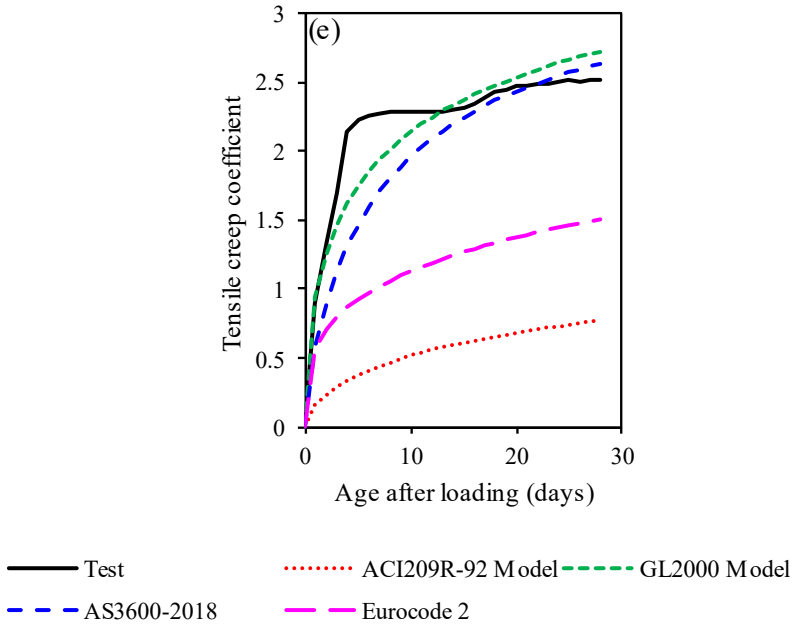

Figure 6 – 9: (continued)

6.4.2 Nonlinear tensile creep coefficient

The nonlinear creep function $f(\varphi_{nl})$ is commonly used in the design of concrete structures. It can be computed based on the linear creep coefficient and the nonlinear creep coefficient, as shown in Eq. (11). In this section, three different expressions of nonlinear creep coefficient from four codes or literature [192, 209, 242, 200] are discussed and compared to the experimental results. The nonlinear creep function is computed as follows:

$$f(\varphi_{nl}) = \varphi_{cr} \cdot \varphi_{nl} \tag{6-15}$$

6.4.2.1 AS3600-2018 and Eurocode 2 models [192, 209]

The AS3600-2018 and Eurocode 2 models [192, 209] provide the same representation for the nonlinear creep coefficient. The model recommends that the nonlinear creep develops at a higher than 45% stress-strength ratio. The expression is shown in Eq. (6-16):

$$\varphi_{nl} = e^{1.5(\frac{\sigma_0}{f_{cm}} - 0.45)} \tag{6-16}$$

6.4.2.2 Model by Ruiz et al. [242]

Ruiz et al. [242] suggested an expression of the nonlinear creep coefficient for both creep and relaxation. They recommended that nonlinear creep occurs at a stress level above 40%. The expression is shown as follows:

$$\varphi_{nl} = 1 + 2(\frac{\sigma_0}{f_{cm}})^4 \quad (6\text{-}17)$$

6.4.2.3 Model by Bazant and Kim [200]

Bazant and Kim [200] proposed an expression for the nonlinear creep coefficient. They recommended that a nonlinear creep appears at a stress level above 30%. The expression is shown as follows:

$$\varphi_{nl} = \frac{1 + 3(\frac{\sigma_0}{f_{cm}})^5}{1 - (\frac{\sigma_0}{f_{cm}})^{10}} \quad (6\text{-}18)$$

6.4.2.4 FIB 2010 Model [207]

FIB 2010 model suggested a model allowing for calculate the increase of the magnitude of creep due to nonlinearity when the stress to strength ratio is in the range from 40% to 60% as follows:

$$\varphi_{nl} = e^{1.5(\frac{\sigma_0}{f_{cm}} - 0.4)} \quad (6\text{-}19)$$

6.4.2.5 Comparison to existing analytical models

In view of the above models, The AS3600-2018 and Eurocode 2 models [192, 209] recommended that the nonlinear creep develops at a stress to strength ratio higher than 45%. While Ruiz et al. [242] recommended that nonlinear creep occurs at stress levels above 40%. In the model developed by Bazant and Kim [200], they illustrated that the

nonlinearity of creep might appear from 30% up to a stress level of 60% in compression. FIB 2010 model suggested that nonlinearity occurs from 40% stress level until 60%.

Figure 6-10 shows the comparison between the measured nonlinear tensile creep factor and the calculated values based on the different analytical models. It can be seen that the differences between the various models are relatively small until the stress to strength ratio is 60%, but all models underestimated the experimental nonlinear creep factor. Note that all these models were built based on the concrete creep tests performed under compression and could be used only for the concrete under compressive.

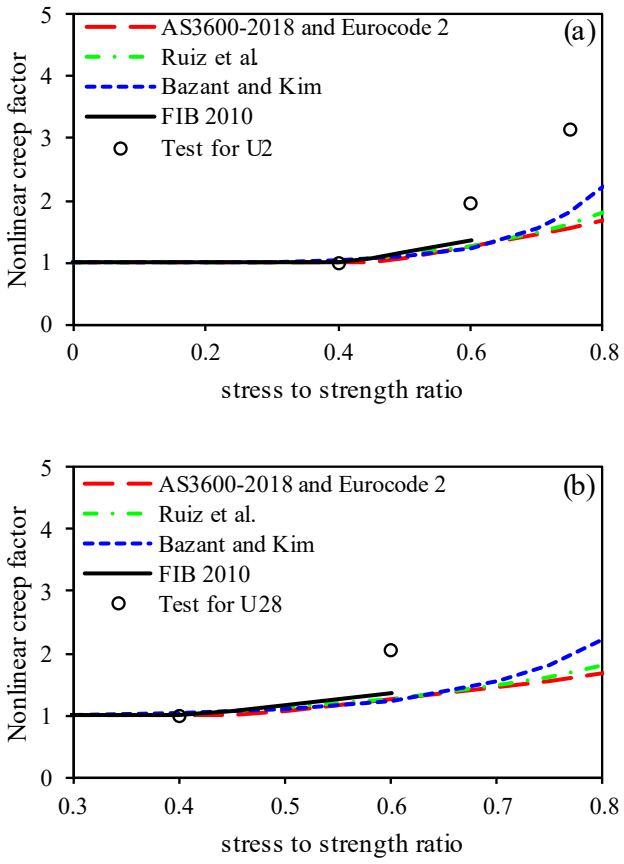

Figure 6 - 10: Comparisons of tensile creep coefficient obtained from experimental results and nonlinear tensile creep coefficient models for: (a) U2; (b) U28.

6.4.3 Analytical model for nonlinear creep factor

According to the experimental results for UHPC under tension, a good linear relationship (shown in Figure 6 – 10) can be observed. However, it should be noted that more tests should be conducted to examine the threshold of nonlinear creep. Because of the limited creep test and stress levels, a stress level of 40% was adopted as a baseline in this chapter. According to the linear creep theory, the nonlinear tensile creep model for UHPC can be obtained using the least square method as follows:

$$\varphi(t) = \varphi_{nl} \times \varphi_{EC}(t) \tag{6-20a}$$

$$\varphi_{nl} = \begin{cases} 5\left(\frac{\sigma_0}{f_{ct}}\right) - 1 & \sigma_0 > 0.4 f_{ct} \\ 1 & \sigma_0 \leq 0.4 f_{ct} \end{cases} \tag{6-20b}$$

where $\varphi_{EC}(t)$ is the tensile creep coefficient at a stress level of 40% using Eurocode 2 model.

Figure 6-11 shows the comparison between the tested tensile creep coefficient under varying stress levels and calculated results by using the proposed model. The calculations are in good agreement with the measured results. The average relative residual errors for U2-60, U2-75 and U28-60 are 11.6%, 12.8%, and 7.2% respectively. It should be noted that the early age (5-10 days) creep coefficient of U2-60 and U2-75 was underestimated by the proposed model, but from engineering point of view, it can provide a more conservative result to reduce the risk of early age cracking. As a result, the proposed model can be accepted to predict the nonlinear tensile creep of UHPC.

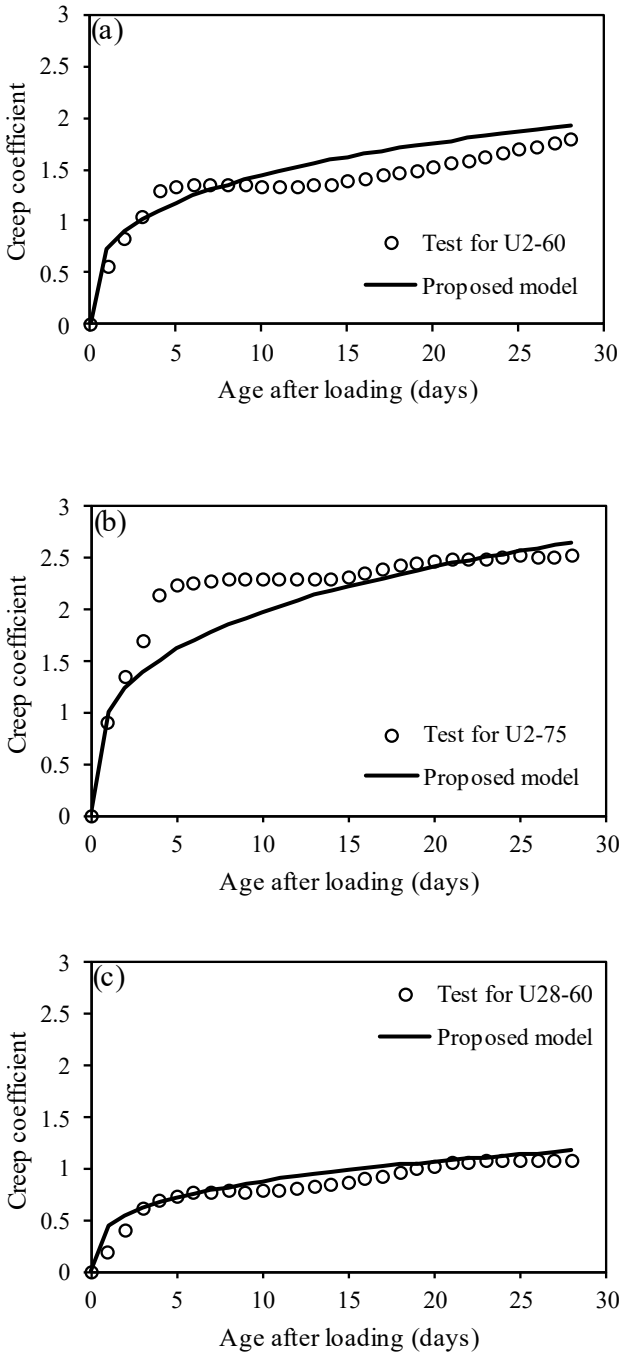

Figure 6 - 11: Comparison of tensile creep coefficient and calculated results by proposed model incorporating nonlinear creep effect: (a) U2-60; (b) U2-75; (c) U28-60.

6.5 Conclusions

This chapter presents an experimental study to assess the nonlinear tensile creep of UHPC using the dog-bone specimens. The tensile creep test was conducted under different levels of uniaxial tensile stresses (40%, 60% and 75%) and curing age (2 and 28 days). The main conclusions can be drawn as follows:

1. Curing can effectively reduce the tensile creep strain and tensile creep coefficient of UHPC. After 28-day loading, the tensile creep strain and tensile creep coefficient of UHPC loaded at 2 days were about 20% and 40% higher than 28 days, respectively.
2. Stress levels significantly influenced the tensile creep strain and tensile creep coefficient. The higher the applied stresses, the larger the tensile creep strain and the tensile creep coefficient. After 28-day testing, the tensile creep strain and tensile creep coefficient of UHPC loaded at 2 days under the stress levels of 60% and 75% were 1.64 and 3.61 times the corresponding values obtained from the stress level of 40%, respectively.
3. The creep nonlinearity of UHPC occurred at a stress to strength ratio of at least 60%. The higher the applied stresses, the larger the nonlinear tensile creep behaviour. Curing age seems to be only marginally affected the nonlinear tensile creep behaviour of UHPC.
4. Based on the test data collected in this chapter, four existing prediction models, including ACI-209R-92, GL 2000, AS3600-2018 and Eurocode 2 models, were compared to the development of tensile creep coefficient. These models only worked for some grades and were unsuitable for all cases.
5. Four analytical models from four available codes or literature, such as Bazant and Kim,

Ruiz et al. and AS3600-2018/Eurocode 2, FIB 2010 models, were compared to the experimental nonlinear tensile creep coefficient of UHPC. All of the models underestimated the nonlinear creep coefficient, and therefore they were not suitable for predicting the nonlinear creep effect.

6. A new model was proposed to predict the nonlinear tensile creep coefficient for UHPC. The tensile creep model for UHPC was considered the Eurocode 2 model and nonlinear creep coefficient model. The proposed tensile creep model was also verified using the experimental results of UHPC.

CHAPTER 7: THERMAL CRACKING IN HIGH VOLUME OF FLY ASH AND GGBFS CONCRETE

7.1 Introduction

Due to restraint stresses caused by volume changes, the risk of early age cracking is exceptionally high in concrete structures such as dams, larger bridge piers, retaining walls, and foundations. The early age of total deformation contributes to different deformation components, including autogenous shrinkage, drying shrinkage and thermal effects (contraction or expansion). When the total deformation is restrained, it leads to a significant tensile stress development which may cause cracking if it exceeds the tensile strength of concrete.

According to ACI 207.1 [55], the combined effect of heat produced by the cement hydration and relatively poor heat dissipation conditions leads to a considerable rise in temperature within a few days after mass concrete placement. As the cement hydration continues, the heat generated increases the internal temperature of concrete and produces the differential thermal gradients between the internal and the surface of concrete structures because of the low thermal conductivity of concrete [57]. The thermal gradients produce tensile stress near the surface, leading to surface cracking. Meanwhile, the interior of the structure is subjected to compressive stress. When the ambient temperature drops, the interior will be subjected to tensile stress resulting from thermal gradients and external restraint.

Tensile stress caused by restrained autogenous shrinkage is critical in early age mass concrete. Autogenous shrinkage is the time-dependent reduction in the volume of concrete due to internal consumption of moisture due to the hydration process. Self-desiccation, the

driving force and one of the primary underlying mechanisms of autogenous shrinkage, is the removal of moisture in the internal relative humidity of concrete due to ongoing hydration reactions [31]. Autogenous shrinkage is considered as a fundamental component of shrinkage because the volume reduction of concrete occurs without loss of moisture to the environment. According to Neville and Aitcin [252], the autogenous shrinkage is relatively low in normal strength concrete with w/b exceeding 0.42 compared to concrete with w/b below 0.42. In high strength concrete, autogenous shrinkage can be the same amount as drying shrinkage.

Drying shrinkage is critical in concrete elements with a large surface area to volume ratios, such as pavements, overlays, and bridge decks. It happens when the physical loss of moisture from concrete to the environment. In unsealed concrete surfaces, the evaporation rate of moisture is dependent on environmental factors, including wind, relative humidity, solar radiation and ambient temperature [253, 254, 255]. Compared to thermal and autogenous shrinkage, mass concrete structures susceptible to drying shrinkage are less significant within the few days after casting concrete. To some extent, proper curing is essential to minimise the impacts of the restrained drying shrinkage.

The early age tensile stress depends not only on the early age deformation, as mentioned above, but also on the development of mechanical properties such as tensile strength, elastic modulus, and viscoelastic properties such as stress relaxation due to tensile creep. Springenschmid and Breitenbucher [62] reported that the elastic modulus of concrete develops very fast in the first 24 to 36 hours after placement. Many studies have shown that the gain in elastic modulus is faster than that of tensile strength during this time [63, 64], which means the development of tensile stress is high. The viscoelastic behaviour such as

stress relaxation due to tensile creep is also significant in contributing to the early age of stress development in concrete. It has been reported that the tensile creep releases 50% - 60% of the stress than that stress developed without relaxation [64, 256, 257, 67]. However, the above discussion resulted from the investigation of the mechanical properties under either standard curing or ambient curing conditions. Therefore, evaluating the development of mechanical properties under the same temperature history as the mass concrete structures should be considered.

Numerous researchers have investigated ways to mitigate the risk of early age thermal cracking. Batog and Giergiczny [76] reported that reducing the amount of heat released is mainly achieved through changes in mix design parameters such as w/b ratio, cement content and use of supplementary cementitious materials (SCMs), including fly ash and ground granulated blast furnace slag (GGBFS). Ballim and Graham [75] showed that the increasing amount of fly ash or GGBFS in the cement composition decreased the rate and amount of heat produced. Mehta and Monteiro [258] revealed that replacing ASTM Type I cement with Type II or Type IV cement, and pozzolans partially substituting Portland cement significantly decreased the adiabatic temperature in concrete. They also stated that the increasing w/b ratio reduces the heat of hydration and slows down the heat kinetics at an early age of hydration. ACI207.2 [259] suggested alternative curing methods to reduce the heat produced by cement hydration, which reduces the risk of early age thermal cracking. However, for some of the above studies, such as Batog and Giergiczny [76], there is no restrained thermal cracking test or thermal stress test, so it is difficult to determine if their mixtures crack.

A lot of effort has been directed at devising test methods to determine the restraint stresses. Conventionally, the two most common test methods, such as rigid cracking frame (RCF) [260] and temperature stress testing machine (TSTM) [261], are used to determine the restraint stress at an early age. Test methods such as the RCF can provide the measure of thermal stress considering various factors such as thermal strain, elastic modulus, degree of restraint and stress relaxation [260]. According to Mangold [262], the RCF provides a 100% degree of restraint for fresh concrete and approximately 80% for hardened concrete. On the other hand, the TSTM achieves 100% restraint by compensating for any length change in the specimen by adjusting a movable crosshead with a computer-controlled system [261]. TSTM can completely suppress the deformation against the combined effects of thermal strain and autogenous shrinkage. Both test methods can reproduce in-site restraint stress in the laboratory. This chapter adopted the RCF test which is available in the UNSW laboratory in accordance with [263].

This chapter presents the results of investigating the tensile stress development and cracking for three concrete mixes with SCMs such as fly ash and GGBFS using RCF. The temperature profile was simulated at the centre point of the mass concrete element using the software ConcreteWorks and applied to all relevant tests. Free shrinkage frame (FSF) and match-curing oven were utilised to determine the free total deformation and mechanical properties of concrete. The basic tensile creep coefficient of concrete mixes subjected to different temperature profiles was predicted using the modified FIB 2010 model. An analytical model was put forward to calculate the autogenous shrinkage and thermal contraction induced stress separately. The risk of early age concrete cracking was also examined.

7.2 Experimental program

7.2.1 Materials and mix proportion

The concrete mixes were produced with General Purpose (GP) cement, fly ash and GGBFS. Table 7-1 summarises the chemical composition of the GP cement, fly ash and GGBFS by X-ray Fluorescence (XRF) analysis. The coarse aggregate is basalt with a maximum nominal size of 10 mm, and local Sydney sand with a maximum nominal size of 2.36 mm is used as fine aggregate. The coefficient of thermal expansion (CTE) of basalt is determined as 6.8×10^{-6}/°C. The water absorption and specific gravities are 1.08% and 2.8 for coarse aggregate and 3.5% and 2.65 for fine aggregate, respectively. The particle size distribution (PSD) for coarse and fine aggregates is shown in Figure 7-1.

Three concrete mixes were prepared to investigate the effect of fly ash and GGBFS on the concrete properties, including the time-dependent mechanical properties, autogenous shrinkage development, thermal stress and the risk of early age cracking potential. ‘N50’ was designated for the concrete mixes because the nominated compressive strength for all mixes was 50 MPa. Mixture ‘0’ was the reference concrete mixes without fly ash or GGBFS. Fly ash and GGBFS replace 30% and 60% of GP cement by weight. Hence, ‘FA30’ and ‘G60’ were designated for fly ash and GGBFS concretes. The water to binder ratio of concrete mixes with fly ash and GGBFS was lower than that of control mixes to achieve the targeted compressive strength. Moreover, a competitive market superplasticizer was utilised to improve the workability of the concrete mixes. The mix design proportions are presented in Table 7-2.

Table 7 - 1: Chemical composition of GP cement, fly ash and GGBFS.

Chemical composition	GP cement (wt.%)	Fly ash (wt.%)	GGBFS (wt.%)
SiO_2	18.8	65.9	34.1
Al_2O_3	5	22.1	15.4
Fe_2O_3	2.8	3.4	0.8
CaO	63.8	1.6	36
MgO	1	0.7	6.6
Na_2O	0.3	0.6	0.4
K_2O	0.7	1.8	0.6
TiO_2	0.3	0.9	2.4
SO_3	3	0.1	2.5
Mn_3O_4	-	0.1	1.1

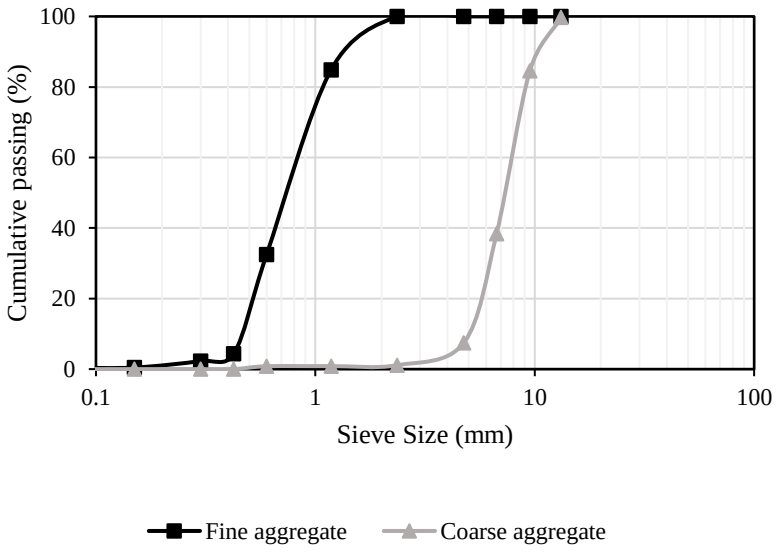

Figure 7 - 1: Particle size distribution of coarse and fine aggregates.

Table 7 - 2: Mix proportions of concrete.

Sample ID	Mix proportions by weight (kg/m^3)					w/b ratio
	GP Cement	FA	GGBFS	Coarse Agg	Fine Agg	
N50-0	510	0	0	927	759	0.4
N50-FA30	355	155	0	955	782	0.3
N50-G60	205	0	305	941	770	0.35

7.2.2 Temperature profile simulation

The temperature profile was simulated using the software ConcreteWorks. ConcreteWorks has been developed to predict the temperature profile of mass concrete, and it has been successfully used in previous research [264, 265, 266]. The simulated temperature profile was applied to the RCF, FSF and match-curing oven. ConcreteWorks provides the concrete temperature history of each concrete mixture based on the geometry of the element, mix design proportions, chemical composition of the cementitious materials, thermal coefficient of expansion of aggregates, and the environmental effects. In addition, the temperature profile was assumed at the centre point of the mass concrete element. Although ConcreteWorks considers the mixture designs assuming the statistically representative properties of Portland cement, fly ash and GGBFS, it cannot specifically consider the effect of fly ash and GGBFS used in this particular study. The effects of fly ash and GGBFS on heat generation and hydration may significantly vary depending on their chemical compositions of them. Thus, it should be noted that the heat profile simulated from ConcreteWorks might not be identical to the actual heat profile for the particular mixture. However, this study assumed that the simulated profile was reasonably correct.

7.2.3 Mechanical and fresh properties test

Mechanical properties of concrete, including the compressive strength, tensile strength and elastic modulus, were tested at the ages of 1, 3, 7, and 28 days based on the Australian Standard AS1012.9 [103], AS1012.10 [184] and AS1012.17 [185], respectively. Note that the 1- and 3-day cylinders were cured in a match-curing oven. While the 7- and 28-day cylinders were moved to a standard curing condition (the temperature at 23 ± 2 °C and relative humidity of 95 ± 5%) after the RCF specimen had cracked (≈ 5 days). The dimension of the cylindrical specimen was 100 mm in diameter by 200 mm in height. The slump test evaluates the workability of concrete in accordance with AS1012.3.2 [106]. The air content of concrete was tested according to AS1012.4.2 [107]. The fresh density of concrete was obtained by weighing the concrete during pouring according to AS1012.5[17], which could eliminate the influence of hydration reaction.

7.2.4 Match-curing oven

Figure 7-2 presents the match-curing oven used to cure the concrete cylinders. To determine the development of mechanical properties of concrete placed in the RCF, tested cylinders are cured under the same temperature profile as the specimen in the RCF and FSF. As mentioned in the previous section, the match-curing oven was used to test the mechanical properties of concrete at the age of 1 and 3 days. The relative humidity in the match-curing oven was controlled at 95% ± 5% to avoid any moisture loss.

Figure 7 - 2: Match-curing oven.

7.2.5 Rigid cracking frame (RCF) test

Due to the complex interaction of different factors such as thermal strain, elastic modulus, degree of restraint, and stress relaxation, traditional methods solely based on the measurement of concrete deformation (ex. restrained ring test) cannot determine the thermal and other restraining stresses in young hardening concrete. The RCF test can give a measurement of thermal stress by inherently considering the influence of elastic modulus, autogenous shrinkage, tensile creep, etc. The RCF is made up of a concrete specimen held by two mild steel crossheads, which are fixed in place by two Invar sidebars, the dimension

of the RCF cross-section is 150 mm × 150 mm, as shown in Figure 7-3. The temperature within test specimens was monitored at three different locations (See Figure 7-3). Two thermal couples were located at two ends of RCF, and one thermal couple was located at the middle of RCF. All thermal couples were inserted into the centre of concrete to measure the internal temperature of concrete. The temperature data from three locations are identical, showing a uniform temperature distribution in the test specimen. Figure 2-15 also showed the schematic illustration to indicate the components of the rigid cracking frame.

For the rigid sidebars to provide the proper restraint, the concrete specimen must be fixed at both ends. Therefore, the steel crossheads are constructed in such a way that they contain dovetails lined with teeth for gripping concrete. Crosshead braces are bolted to the top and bottom of each crosshead to prevent the slip of the concrete sample, and these restrain expansion as the concrete goes into tension (see Figure 2-15). The RCF is made with a thermally insulated formwork that enables measurements to begin immediately after fresh concrete has been placed and helps control the temperature of the sample.

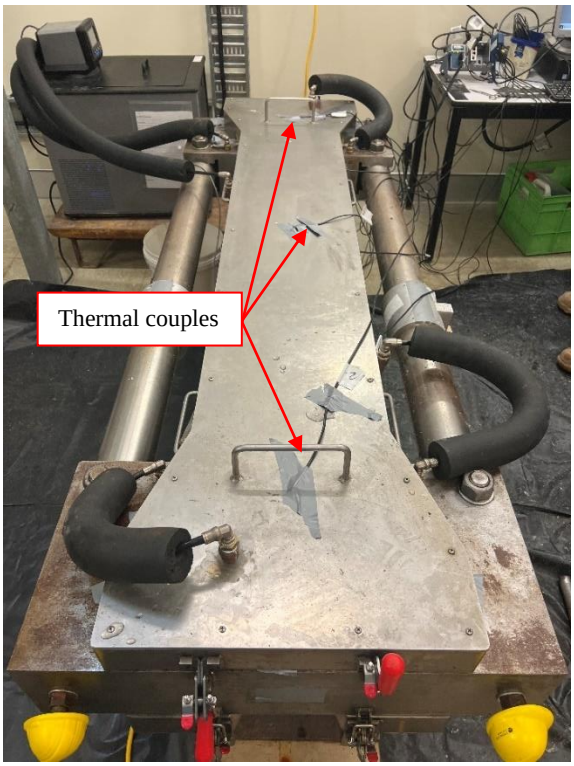

Figure 7 - 3: Test of rigid cracking frame.

To minimize the effect of temperature change on the length of the side bars, Invar steel is used to make the sidebars. Each bar was fitted with strain gauges capable of measuring the small axial strains produced by the combined effects of thermal and autogenous shrinkage in the concrete. In the central portion of the specimen, the stresses were uniaxial, and hence, a uniform stress distribution was assumed. The measured strains in the Invar sidebars could thus be used to compute the corresponding stress development in the restrained concrete specimen. The RCF test was set to follow the temperature profile simulated by ConcreteWorks within the first 96 hours. If the specimen is not cracked during the test period, then it is artificially cooled at a rate of 1 °C/hour to induce cracking. The temperature and stress of the specimen were continuously monitored until the specimen was cracked.

7.2.6 Free shrinkage frame (FSF) test

The FSF test was used to evaluate the free total deformation including the thermal and autogenous shrinkage. As shown in Figure 7-4, the FSF is the framework that is thermally controlled by copper tubing and a supporting Invar steel frame. Thus, the fresh concrete used in this study was allowed to be placed in FSF to cure at the same temperature profile as RCF. Two end steel plates measured the free total deformation with an Invar rod to a linear variable displacement transducer (LVDT). The dimension of the FSF was 150 mm × 150 mm × 600 mm. The FSF maintained the specimen under a sealed condition so that neither moisture loss during the test nor, thus, drying shrinkage occurred in the FSF test.

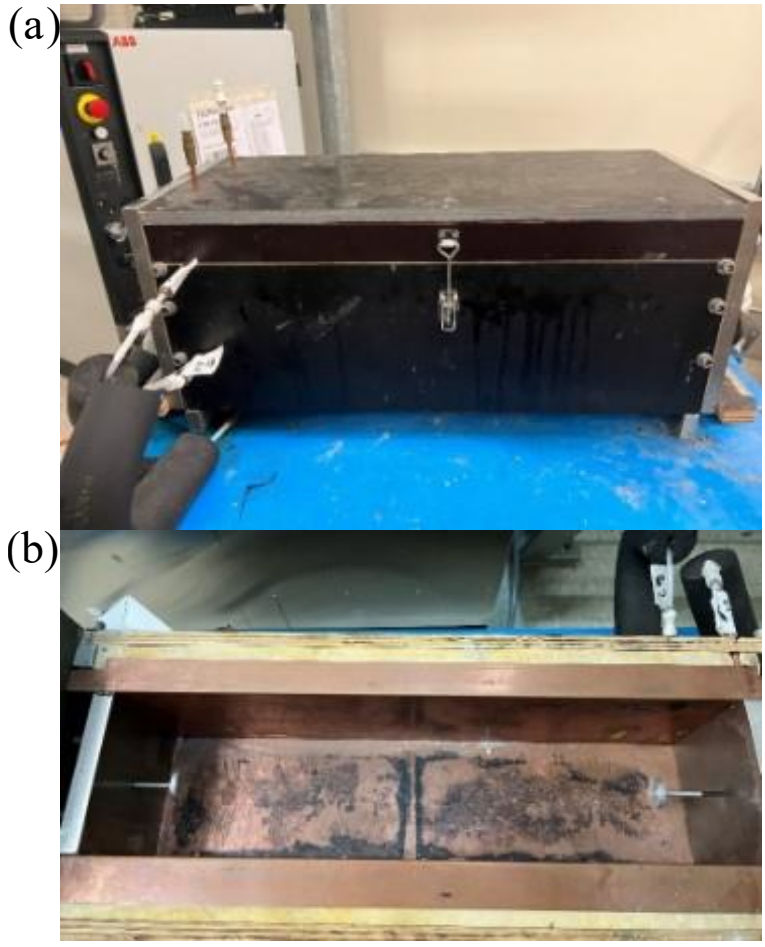

Figure 7 - 4: Test of free shrinkage frame: (a) actual frame; (b) inside of the frame.

7.2.7 Autogenous shrinkage test

As mentioned in Section 7.2.6, the FSF can measure the total deformation including the autogenous shrinkage and thermal deformation (expansion and contraction) but it cannot separately measure these two deformations. Therefore, this section aims to measure the autogenous shrinkage on concrete prisms at the constant temperature of 23 °C, assuming that the autogenous shrinkage is not affected by temperature induced strain. It should be noted that the autogenous shrinkage of concrete prism might not be identical to the autogenous shrinkage of mass concrete because of the difference in dimension and hydration degree at an early age. The measurement of autogenous shrinkage is from an early age is very challenging because autogenous shrinkage is affected by temperature variation. This is a limitation of test method and will be improved in future by considering the temperature effect on autogenous shrinkage measurement in FSF test. However, this method still provides some indications in separating the autogenous shrinkage and thermal strain. As a result, thermal deformation can be deduced from the difference between total deformation measured from FSF and autogenous shrinkage measured from prisms. The autogenous shrinkage specimen is shown in Figure 7-5. The size of the shrinkage prisms in Australia is 280 mm × 75 mm × 75 mm [104]. After demoulding, all faces of autogenous shrinkage specimens were well-wrapped using a self-adhesive water-proof aluminium foil to avoid any moisture loss to the environment [80]. Measurements were carried out once a day for 5 days (120 hours).

Figure 7 - 5: Autogenous shrinkage specimens.

7.3 Test results and discussions

7.3.1 Temperature profile

Figure 7-6 shows the temperature profile data obtained from ConcreteWorks. The peak temperature of the control mixture was higher than those of fly ash and GGBFS mixtures. The time for the maximum temperature was also delayed when the addition of fly ash and GGBFS. The peak temperature for the control mixture was 64.2 °C, and it occurred at 20 hours after pouring concrete, which was higher and earlier than 51.4 °C, 26 hours for FA30 concrete and 49.4 °C, 28 hours for G60 concrete, respectively, which indicates that the fly ash and GGBFS could effectively reduce the heat of hydration and resultant thermal cracking in concrete structures. Similar results were noted in the literature [62, 267]. Springenschmid and Breitenbücher [62] found that GGBFS reduced temperature rises and tensile stresses. Breitenbücher and Mangold [267] reported that fly ash could also decrease the peak temperature. After 72 hours, it is observed that all three temperature profiles were

confronted until 96 hours. Then the concrete was artificially cooled at a rate of 1 °C/hour until the specimen cracked.

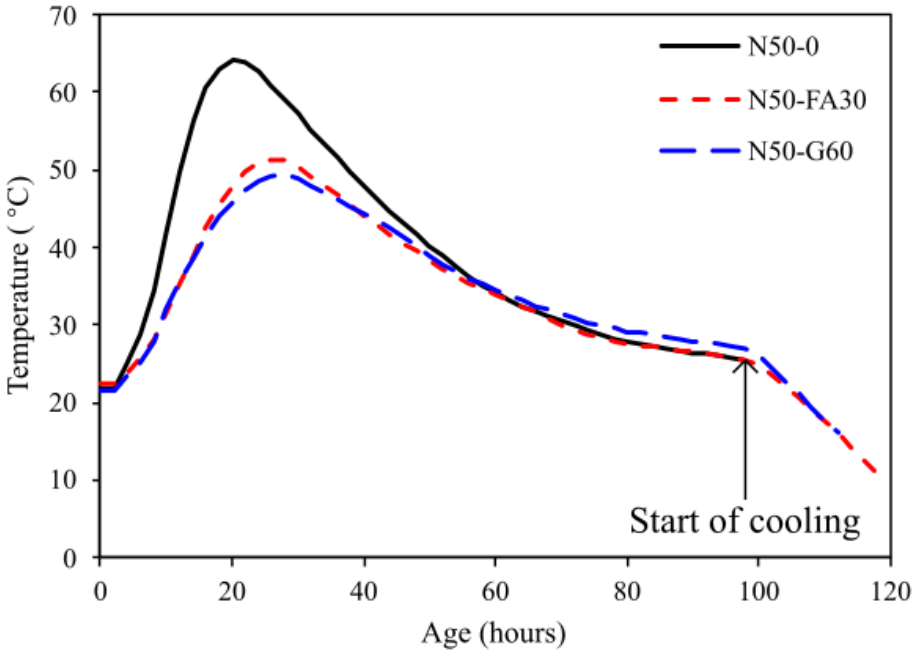

Figure 7 - 6: Simulated temperature profile of concrete.

7.3.2 Mechanical and fresh properties of concrete

Tables 7-3 and 7-4 show the mechanical properties of concrete, including the compressive strength, splitting tensile strength, elastic modulus and fresh properties such as slump, air content and fresh density for each concrete mix. It can be seen that the incorporation of fly ash and GGBFS decreased the compressive strength, tensile strength and elastic modulus compared to that of reference concrete, especially at an early age. This is attributed to the low activity of fly ash and GGBFS, which slows down the hydration process [268]. Another explanation for this phenomenon is that the match-cured cylinders for fly ash and GGBFS mixes experienced a lower temperature rise than that of control samples, contributing to a lower hydration process. Similar results were reported by Byard et al. [264]. The reduced elastic modulus development due to the lower hydration degree caused

a higher tensile creep development when fly ash and GGBFS were incorporated, leading to higher stress relaxation and reduced growth of tensile stress. In addition, the results were similar to that under standard curing or ambient curing conditions according to Chapter 4.

Table 7 - 3: Mechanical properties of concrete.

Sample ID	Compressive strength (MPa)				Splitting tensile strength (MPa)				Elastic modulus (GPa)			
	1d	3d	7d	28d	1d	3d	7d	28d	1d	3d	7d	28d
N50-0	25.5	36.3	43.6	56.9	2.7	3.7	4	4.6	31.2	36.8	37.8	39
N50-FA30	20.3	33.7	42.6	55.2	2.2	3.1	3.9	4.5	24.3	28.7	33.2	37
N50-G60	22.1	35.9	43.1	55.4	2.2	3.6	3.8	4.4	22.6	25.2	31.2	33.2

Table 7 - 4: Fresh properties of concrete.

Sample ID	Slump (mm)	Air content (%)	Density (kg/m^3)
N50-0	75	2.5	2441
N50-FA30	30	4.8	2383
N50-G60	65	4	2445

7.3.3 Rigid cracking frame and free shrinkage frame results

Figure 7-7 presents the stress development obtained from the RCF test and the free deformation development of reference and SCM concretes. It can be seen that all three mixtures exhibited swelling behaviour at a very early age. Previous studies also reported this phenomenon [50, 77, 65]. This could be attributed to thermal dilation due to the heat of hydration, absorption of bleeding water, water adsorption by filler, CH growth and primary

ettringite formation [126, 127, 269]. Three thermal couples were inserted in the centre of concrete as shown in Figure 7-3. The obtained temperature in the concrete was consistent and identical for three measured points. Reference concrete had the highest swelling deformation, which was also attributed to the higher temperature rise shown in Figure 7–6 in addition to the possible reasons mentioned above. This also explained the highest compressive stress development for the reference concrete as determined by the RCF test (see Figure 7-7 (a)). In other words, under the restrained condition, the higher expansion of the reference mixture corresponded to a higher initial precompression. The concrete began to gain strength and compressive stresses were developed due to the increased temperature associated with the continued hydration of the concrete after about 3 to 6 h, but these stresses were still reduced by the relative high relaxation. Thus, maximum in compressive stress was obtained a few hours earlier than the maximum temperature [260]. According to Wei and Hansen [50], the strain for free shrinkage fame at the zero-stress temperature (T_{zs}) (see Figure 7-7 (a)) is called zero-stress strain (ε_{zs}), and it is referred to as the starting point of contraction for comparison (see Figure 7-7 (b)). Note that the ε_{zs} is not necessarily zero because the compressive stress of young concrete is relaxed. Thus, by setting the value of ε_{zs} is numerically equal to zero, then the increase of free deformation after ε_{zs} is denoted as "absolute free total contraction" (see Figure 7-7 (c)). As such, the absolute free total contractions were compared for assessing the cracking risk.

Figure 7-7 (c) shows the measured stress and absolute free total contraction of three concrete mixes. The absolute free total contraction of the control mixture was 295 με at 96 hours, which was higher than that of N50-F30 and N50-G60 concretes with 160 and 241 με, respectively. After 96 hours, the artificial cool process produced a high rate of contraction

development. When the fly ash and GGBFS were incorporated into the concrete mixes, the significant reduction of the absolute free total deformation resulted in reduced tensile stress development This will be discussed in Section 7.3.5.

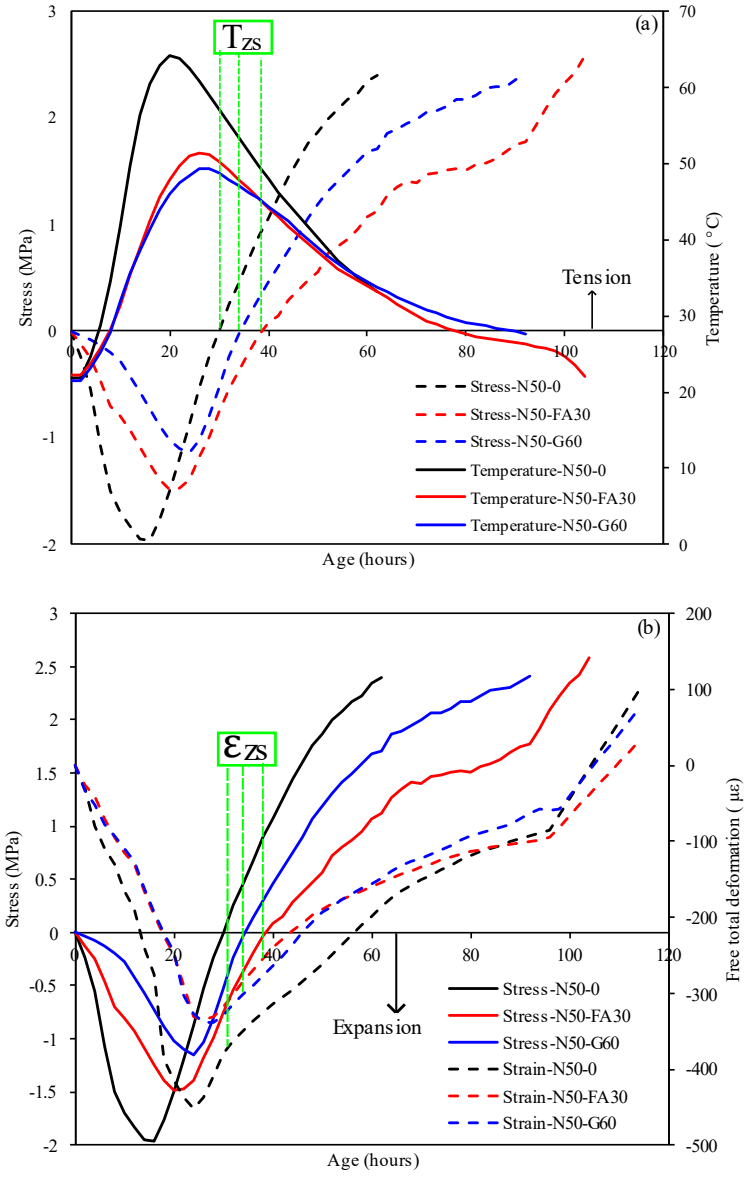

Figure 7 - 7: Measured stress of concrete from RCF test and strains of concrete from FSF test: (a) temperature and stress; (b) stress and free total deformation; (c) stress and absolute free total contraction.

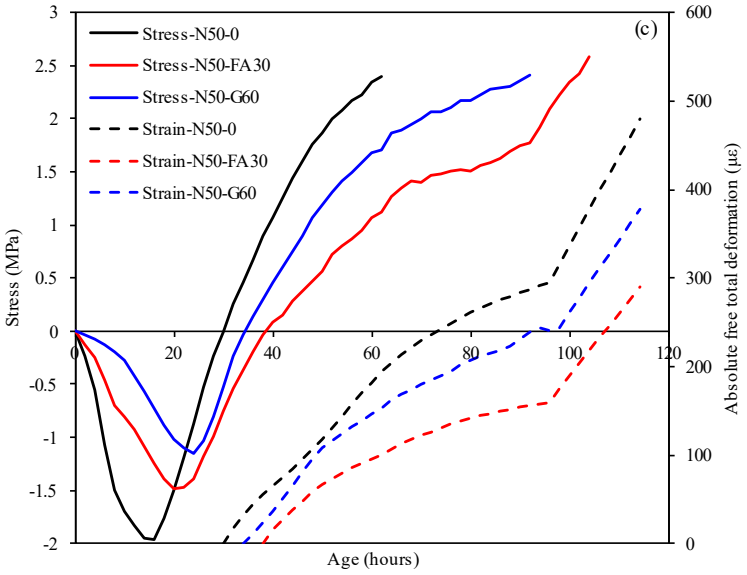

Figure 7-7: (continued)

7.3.4 Autogenous shrinkage of concrete

Figure 7-8 presents the mean value of the experimentally measured autogenous shrinkage for each concrete mixture. The measurement of autogenous shrinkage started 24 hours after casting. The absolute value of autogenous shrinkage strain at 5 days (120 hours) was 90 με, 56 με and 102 με, which decreased by 38% and increased by 13% for concrete mixes from 0% SCM to 30% fly ash and 60% GGBFS, respectively. Similar results can be found in [270, 134]. It can also be observed that the trends in Figure 7-8 and Figure 3-12 are consistent, showing GGBFS can lead to a higher autogenous shrinkage while fly ash exhibits a lower autogenous shrinkage compared to reference mixes at early age. Gao et al. [270] demonstrated that the autogenous shrinkage for concrete mixes with 30% fly ash was approximately 30% lower than reference concrete at an early age. The results can be explained by fly ash as a filling powder material that does not take part in early hydration. Hence, the autogenous shrinkage is effectively decreased [270]. Lee et al. [134] showed

that the early age of autogenous shrinkage increased with GGBFS content. This is attributed to the incorporation of GGBFS leads to a finer pore structure, contributing to lower relative humidity, thus increasing the self-desiccation and autogenous shrinkage. The underlying logic of conducting the autogenous shrinkage test is that the absolute free deformation measured from FSF consists of thermal strain and autogenous shrinkage. After measuring autogenous shrinkage, the thermal strain can be simply deduced. Then the autogenous shrinkage induced stress and thermal stress can be calculated separately. This will be discussed in Section 7.4.

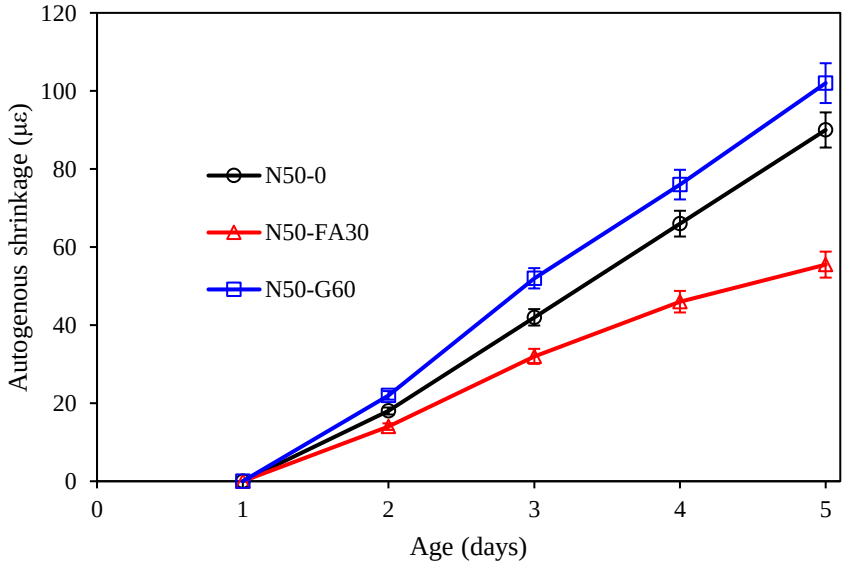

Figure 7 - 8: Measured autogenous shrinkage of concrete from prism test.

7.3.5 Tensile stress development

The behaviour of concrete in the RCF can be described in five stages [260] and explained in Section 2.5.3. The RCF test results of stress development for all concrete mixtures are presented in Figure 7-9. The concrete specimen cracked at 62 hours for the control mixture, and cracking stress was 2.4 MPa. The cracking stress can be calculated using the product of

the degree of restraint which depends on cross-sectional areas of Invar bars and of RCF concrete specimens, Invar strain and its elastic modulus. However, N50-FA30 did not fail in the first 96 hours. It cracked after 8 hours of artificial cooling, which indicated the decreased cracking potential of the mixture. While for the GGBFS mixture, the cracking time was 92 hours which was also significantly delayed compared to that of the reference mixture. In view of these results, the addition of SCMs lowered the early age cracking risk. This was attributed to the significant reduction in the free total deformation that will be discussed in Section 7.3.4 and Figure 7-8 and the elastic modulus development (Table 7-3). Secondly, as shown in Figure 7-6, the temperature rise decreased compared to that of the control mixture. Fly ash was more effective in reducing the cracking risk than GGBFS because: (i) time-dependent tensile capacity of fly ash concrete is higher than GGBFS, and (ii) absolute free total contraction of GGBFS was higher than that of fly ash mixture, leading to a higher tensile stress development as mentioned in Section 7.3.3. Although the tensile strength of SCMs concrete decreased, the combined effect of temperature rises and elastic modulus compensated for the negative impact of tensile strength, resulting in an overall enhancement in performance of resistance to cracking.

Table 7-5 summarises the time and temperature at a zero-stress state and the time and temperature at cracking. The incorporation of fly ash and GGBFS reduced the zero-stress temperature and the zero-stress time because of the lower peak temperature in the applied temperature profile. The addition of SCMs also decreased the cracking temperature and delays the time to cracking, and the lower cracking temperature indicated the better the resistance to early age cracking of the mixes. This is attributed to the decreased rate of temperature development and elastic modulus development [264]. Moreover, Wei and

Hansen [50] reported that the replacement of cement by GGBFS can effectively resist concrete cracking. Markandeya et al. [77] conducted the RCF tests using different types of GGBFS with the same percentage of replacement. They found that the temperature risk and cracking potential decreased compared to that of the control mixture regardless of the slag types. Riding et al. [271] reported that the introduction of fly ash in concrete delayed the tensile stress development, leading to a low-level tendency to crack. Therefore, the results that concrete cracking time is delayed with an increasing proportion of fly ash or GGBFS in this research are rational.

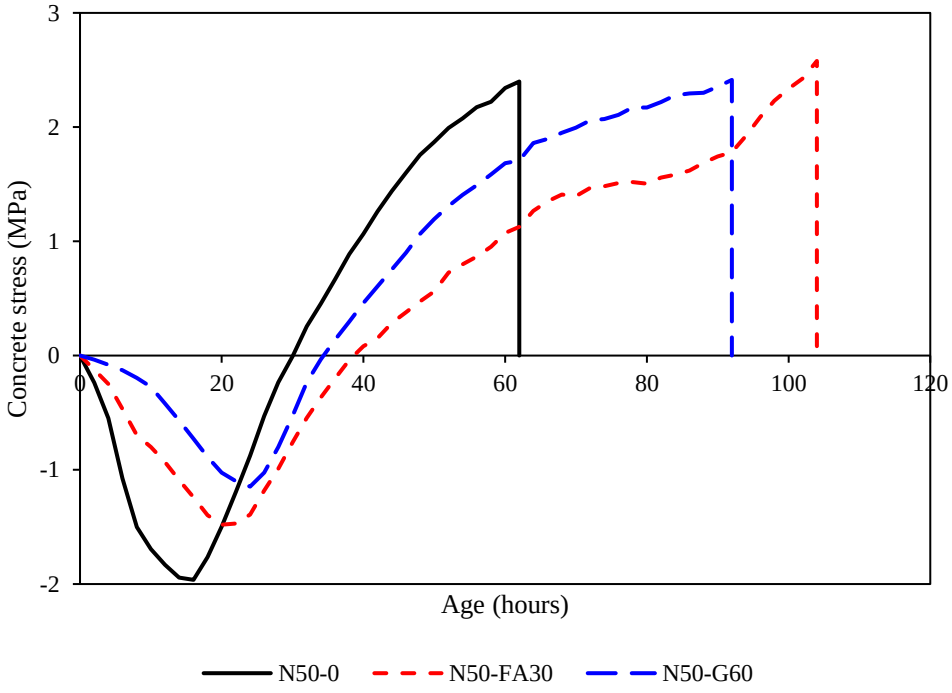

Figure 7 - 9: Comparison of thermal stress development of different concrete mixes.

Table 7 - 5: Cracking indices from RCF tests.

Mix	Zero stress		Cracking	
	Time (h)	Temperature (°C)	Time (h)	Temperature (°C)
N50-0	30	57.2	62	33.2
N50-FA30	38	45.5	104	19.3
N50-G60	34	47.0	92	27.5

7.4 Analytical modelling for tensile stress development in RCF

7.4.1 Analytical solution for tensile stress development

According to ACI 207.2 [259], the tensile stress due to restraint can be calculated using Eq. (7-1):

$$\sigma_t = D_R \varepsilon_t E_c \tag{7-1}$$

where D_R is the degree of restraint which can be computed based on the rigidity of restraining element and concrete, as shown in Eq. (7-2); ε_t is the total contraction due to shrinkage and thermal deformation caused by heat dissipation; E_c is the elastic modulus of concrete.

$$D_R = \frac{1}{1 + \frac{A_c E_c}{A_I E_I}} \tag{7-2}$$

where A_c is the cross-section area of concrete which is equal to 22500 mm^2 in the RCF test; A_s is the cross-section area of Invar side restraining bars in the RCF test, which is equal to 15710 mm^2; E_I is the elastic modulus of Invar side bar which is equal to 137 GPa.

As mentioned in Chapters 4 and 5, stress relaxation due to tensile creep is critical. Hence, in some existing codes, such as JCI guidelines [272], the effective elastic modulus method is utilised to take into account the creep effect [273]. Although this approach captures the

order of magnitude of stress relaxation that occurs in concrete, it might be a bit conservative because the creep increases more slowly under gradually increasing stress than under constant stress [274]. Thus, a reduced creep coefficient by implementing an ageing coefficient was adopted according to Gilbert and Ranzi [275]. The expression of age-adjusted effective modulus is shown as follows:

$$\bar{E}_e = \frac{E_c}{1 + \chi(t,\tau)\varphi(t,\tau)} \tag{7-3}$$

where $\varphi(t,\tau)$ is the tensile creep coefficient which can be obtained from the tensile creep model in Section 7.4.3; $\chi(t,\tau)$ is the ageing coefficient and the recommended value of the ageing coefficient is 0.80 for relaxation problems [275, 85].

Hence, the elastic modulus of concrete in Eqs. (7-1) and (7-2) should be changed to the age-adjusted effective modulus. The tensile stress and degree of restraint can be rewritten as shown in Eqs. (7-4) and (7-5):

$$\sigma_t = D_R \varepsilon_t \bar{E}_e \tag{7-4}$$

$$D_R = \frac{1}{1 + \frac{A_c \bar{E}_e}{A_I E_I}} \tag{7-5}$$

The total contraction of concrete in Eq. (7-4) is considered as the sum of the autogenous shrinkage and thermal contraction due to heat dissipation, as shown in Eq. (7-6):

$$\varepsilon_t = \varepsilon_{au} + \varepsilon_T \tag{7-6}$$

where ε_{au} is the autogenous shrinkage measured from concrete prism; ε_T is the thermal contraction using the measured free deformation strain obtained from FSF minus the autogenous shrinkage or using the CTE multiples with temperature changes, as shown in Eq. (7-7):

$$\varepsilon_T = \alpha \Delta T \tag{7-7}$$

By substituting Eqs. (7-5), (7-6) and (7-7) into Eq. (7-4), the total tensile stress of concrete can be expressed in terms of autogenous shrinkage induced stress and thermal stress, as shown in Eq. (7-8):

$$\sigma_t = \sigma_{au} + \sigma_T \tag{7-8}$$

where σ_{au} and σ_T are the autogenous shrinkage induced stress and thermal stress, respectively, as shown in Eq. (7-9a) and (7-9b):

$$\sigma_{au} = \frac{\bar{E}_e \varepsilon_{au}}{1 + \frac{A_c \bar{E}_e}{A_I E_I}} \tag{7-9a}$$

$$\sigma_T = \frac{\bar{E}_e \alpha \Delta T}{1 + \frac{A_c \bar{E}_e}{A_I E_I}} \tag{7-9b}$$

The newly proposed analytical model from Eq. (7-9a) and Eq. (7-9b) can separate the autogenous shrinkage induced stress and thermal stress. In this model, autogenous shrinkage of concrete can be simply measured on a prism test, elastic modulus can also be measured using a straightforward experimental test on concrete cylinders, and the temperature variation can be determined through the software ConcreteWorks. The other required parameters such as coefficient of thermal expansion and tensile creep coefficient will be explained in Section 7.4.2 and Section 7.4.3, respectively.

7.4.2 Evaluation of coefficient of thermal expansion (CTE)

As mentioned above, the CTE of concrete is one of the most important parameters for evaluating thermally induced strain and stress. Concrete with a high CTE is generally leading to a higher risk of cracking. According to Eq. (7-7), CTE can be rewritten using the thermal strain divided by the temperature change, as shown in Eq. (7-10):

$$\alpha = \frac{\varepsilon_T}{\Delta T} \quad (7\text{-}10)$$

In Eq. (7-10), ε_T can be determined using the absolute free deformation from FSF minus the measured autogenous shrinkage from the prism, ΔT can be evaluated by calculating the temperature difference between two adjacent temperatures.

Li et al. [61] conducted a precise measurement of CTE of concrete at an early age using a newly-built temperature stress testing machine (TSTM), stepped temperature profiles and temperature cycles ranging between 18 and 25 °C. They observed that the measured CTE showed a rising trend. The measured CTE increased from 7.2 to 12.3 × 10^{-6}/°C for concrete with a w/b of 0.42. However, in the current research, the CTE values are quite fluctuated over time within the range between 5.8 to 12.0 × 10^{-6}/°C. This may be due to the difference between the TSTM test and the RCF test. Moreover, this study considered continuous temperature profiles based on the heat of hydration instead of stepped temperature profiles, which may affect the measured CTE values. As such, the CTE was calculated according to Eq. (7-10) and the average values were adopted, which were approximately equal to 8.5, 7.1 and 8.4 × 10^{-6}/°C for OPC, fly ash and GGBFS concrete, respectively. Similar results can be found in [276, 277]. Shui et al. [276] illustrated that replacing the cement with fly ash and GGBFS lowers the CTE of the hardened cement paste. The reduction in CTE of fly ash and GGBFS systems is mainly due to the change in the porosity and portlandite (CH) [276]. Gao et al. [277] also showed that the CTE of fly ash concrete is lower than reference concrete. Thus, the results that CTE of concrete decreased with an increasing proportion of fly ash or GGBFS in this research seems to be reasonable.

7.4.3 Basic tensile creep coefficient

It is critical to take into account the tensile creep of concrete into tensile stress development as it leads to stress relaxation. Most models such as ACI 209R-92 [206] and AS3600-2018 [192] predominately apply compressive creep, and the drying and basic creep are not distinguished in these models. Instead, FIB 2010 model [207] is a commonly used code for predicting basic creep. It considers the effects of curing temperature and hydration degree on the creep coefficients by calculating the temperature-adjusted concrete age. However, according to Dabarera et al. [84], the basic tensile creep coefficient was underestimated by FIB 2010 model. They also proposed a modified tensile creep model based on FIB 2010 model and this model has been successfully validated by the results in Ref. [278, 279]. Therefore, the modified tensile creep model proposed by Dabarera et al. [84] is adopted for predicting the basic tensile creep coefficient $\varphi_{bc}(t, t_0)$ in this chapter. The modified model is shown as follows [84]:

$$\varphi_{bc}(t, t_0) = \beta_{bc}(f_{cm})\beta_{bc}(t, t_0) \tag{7-11}$$

where $\beta_{bc}(f_{cm})$ is the strength-dependent factor which is shown in Eq. (7-12a); $\beta_{bc}(t, t_0)$ is the time-development function which is shown in Eq. (7-12b):

$$\beta_{bc}(f_{cm}) = \frac{7}{(f_{cm28})^{0.7}} \tag{7-12a}$$

$$\beta_{bc}(t, t_0) = \ln\left\{\left(\frac{55}{t_{0,adj}} + 0.05\right)^2 \times (t - t_0) + 1\right\} \tag{7-12b}$$

where $t_{0,adj}$ is the modifying factor considering the effects of cement type and curing temperature to convert the age at loading t_0 to $t_{0,adj}$, which is equal to 8.03, 6.94 and 6.85 days for control, fly ash and GGBFS concrete, respectively, as shown in Eq. (7-12c):

$$t_{0,adj} = t_{0,T}[\frac{9}{2 + t_{0,T}^{1.2}} + 1]^{\alpha} \quad (7\text{-}12c)$$

where α represents the coefficient ranging from -1 to 1, depending on the type of cement, for example, -1for strength class 32.5 N, 0 for strength class 42.5 N and 1 for strength class 52.5 N, respectively [207]. Moreover, Dabarera et al. [84] proved their model can work for different types of concrete (fly ash, silica fume concrete) without any adjustment. As a result, in this chapter, the value of α is taken as 0 because the cement strength class of 42.5 is used. $t_{0,T}$ is the modified age at loading based on the curing history to take account into elevated or reduced temperatures on maturity of concrete, as shown in Eq. (7-12d):

$$t_{0,T} = \sum_{i=1}^{n} \Delta t_i \exp\left[13.65 - \frac{4000}{273 + T(\Delta t_i)}\right] \quad (7\text{-}12d)$$

where Δt_i is the number of days where a temperature T occurs; $T(\Delta t_i)$ is the temperature in °C during the time period of Δt_i.

Figure 7-10 presents the predicted basic tensile creep coefficient of all the concrete mixes. The start of calculation is assumed to be the same as autogenous shrinkage measurement (at 24 hours after demoulding) due to the modelling purpose. The results stopped at the cracking when experimentally observed, i.e., 62, 104 and 92 hours for control, fly ash and GGBFS concrete, respectively. It can be seen that the prediction results for fly ash concrete and GGBFS concrete were similar because of the similar temperature profile. While the reference concrete exhibited slightly lower results compared to that of SCMs based concrete. This is attributed to a greater temperature profile due to a higher early age hydration degree, resulting in increased stiffness properties, leading to a decrease in creep [280]. It indicated that the modified model suggested by Dabarera et al. [84] captured the evolution of the temperature profile and the basic tensile creep coefficient of concrete. In

addition, a slightly lower tensile creep coefficient of control concrete contributed to a less stress relaxation to compensate for the tensile stress development, explaining a reduced cracking time of control concrete compared to that of fly ash and GGBFS concrete.

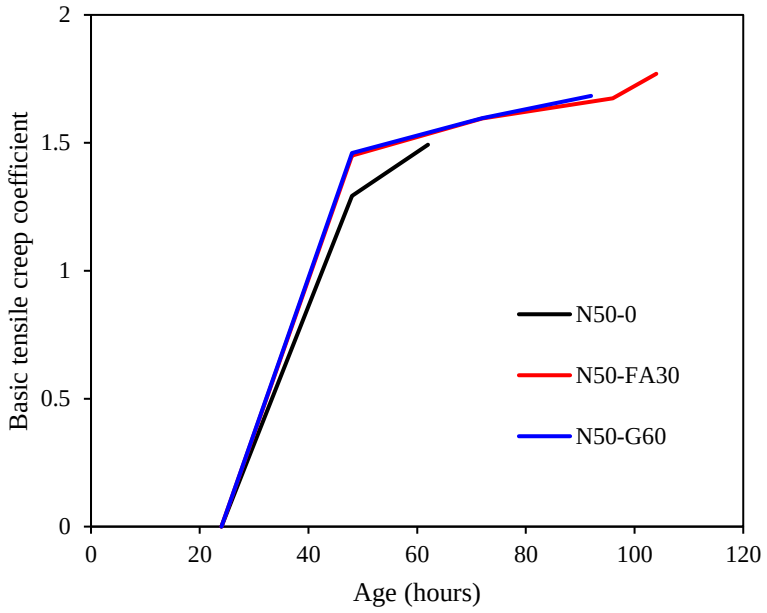

Figure 7 - 10: Predictions of basic tensile creep coefficient using modified FIB 2010 model.

7.4.4 Comparison of measured and calculated tensile stress

Figure 7-11 shows the comparison of concrete tensile stress measured experimentally and tensile stress calculated analytically using Eq. (7-4). The experimental tensile stress can be computed using the measured Invar strain from strain gauges multiplied by the elastic modulus of Invar. The age-adjust effective modulus $\bar{E}_e$ can be calculated using the predicted values from the tensile creep coefficient model (see Figure 7-10) and time-dependent elastic modulus of concrete (Table 7-3). As such, D_R can be calculated using Eq. (7-5). The autogenous shrinkage induced stress and thermally induced stress were calculated utilising Eqs. (7-9a) and (7-9b) are included for sensitivity analysis. It can be

observed that the analytically calculated tensile stress as per Eq. (7-4) agrees well with experimentally measured tensile stress for all mixes, indicating the accurate prediction of the time-dependent tensile creep. The analytical maximum stress was also calculated using Eq. (7-1) to reveal the importance of tensile creep. The analytical maximum stress using Eq. (7-1) was greatly higher than experimental stress for all mixes, showing that the tensile creep can relax the concrete tensile stress and thus cannot be neglected. In addition, the thermal stress of reference concrete is much higher than that of fly ash and GGBFS concrete, leading to an accelerating cracking time.

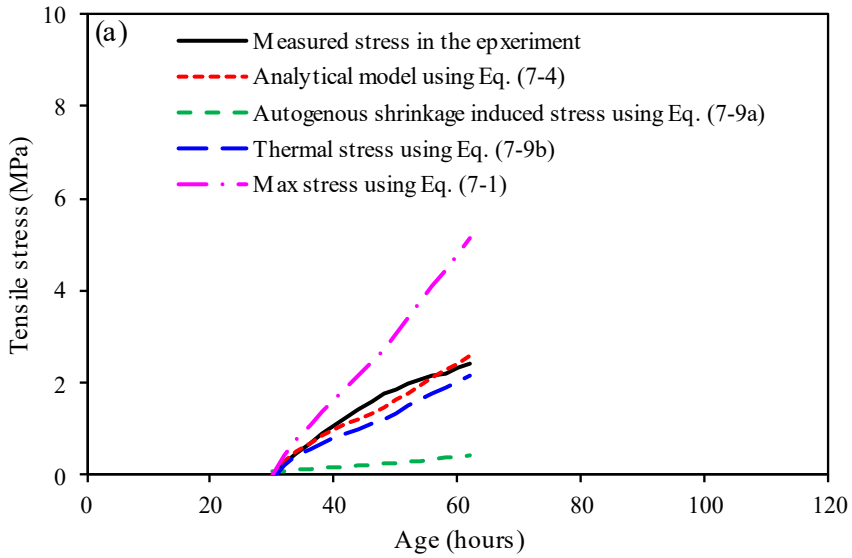

Figure 7 - 11: Time-dependent stress development: (a) N50-0; (b) N50-FA30; (c) N50-G60.

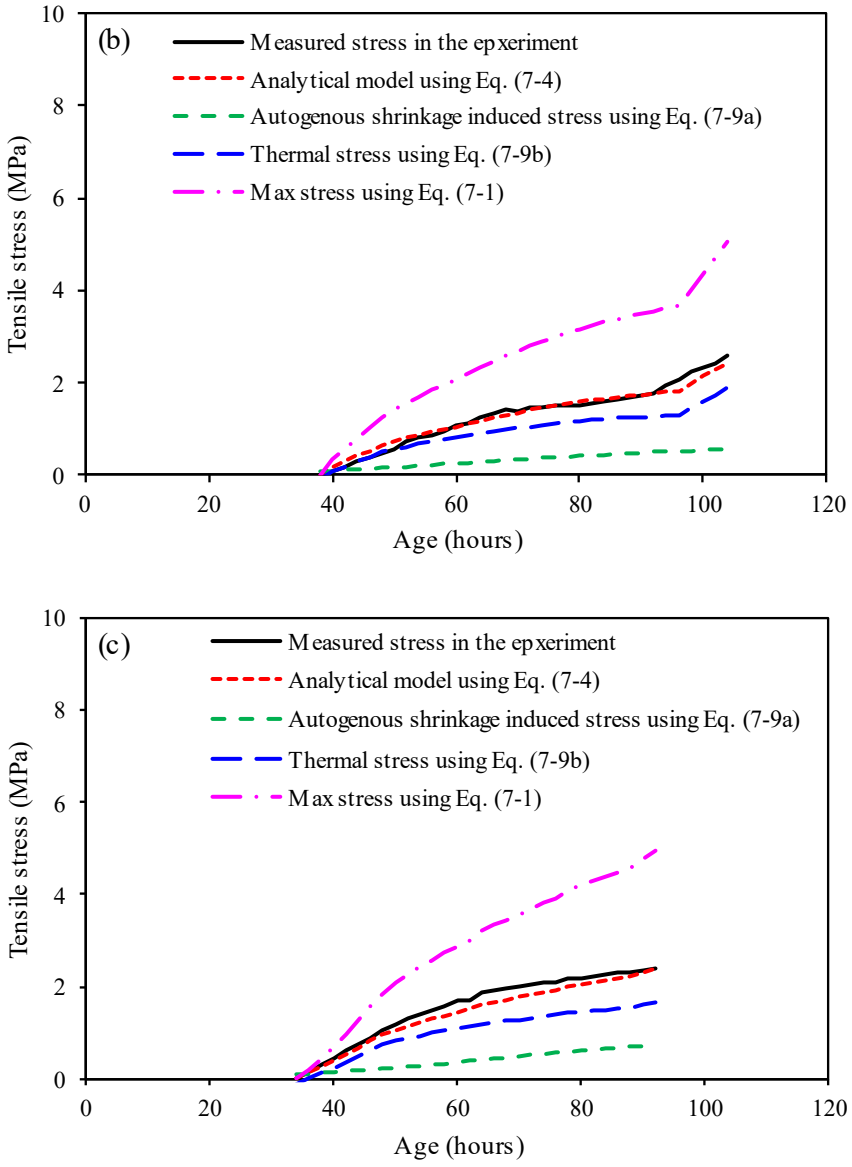

Figure 7 – 11: (continued)

7.4.5 Risk of early age cracking

The risk coefficient is commonly used to assess the risk of early age concrete cracking [87, 205, 51]. It is defined as the ratio between the concrete tensile stress calculated using Eq. (7-4) and the tensile strength of concrete, both being time-dependent, as shown in Eq. (7-13):

$$R(t) = \frac{\sigma_t(t)}{f_{ct}(t)} \quad (7\text{-}13)$$

When the risk coefficient equals 0, there is no tensile stress developed in concrete, and the cracking does not occur. When the risk coefficient increases as tensile stress is generated gradually, the cracking risk becomes higher. Figure 7-12 shows the calculated cracking risk coefficient for the tested specimens until cracking occurs. It can be observed that at the same time, the $R(t)$ of N50-0 is the highest, followed by N50-G60, then N50-FA30. The calculated tensile stress of concrete at cracking is 72%, 70% and 65% of the splitting tensile strength for N50-0, N50-FA30 and N50-G60, respectively, which agrees with the results in [257, 66]. Altoubat and Lange [257] reported that the cracking stress is taken to be 80% of direct tensile strength, and the direct tensile strength can be approximated as ~80% of the splitting tensile strength for concrete at an age greater than 100 h. As such, the ratio of cracking stress to splitting tensile strength can be about 64%. Khan et al. [66] demonstrated that the cracking stress is equivalent to 65% of splitting tensile strength. Thus, these previous works supported the results that the calculated cracking risk coefficient of concrete in this research.

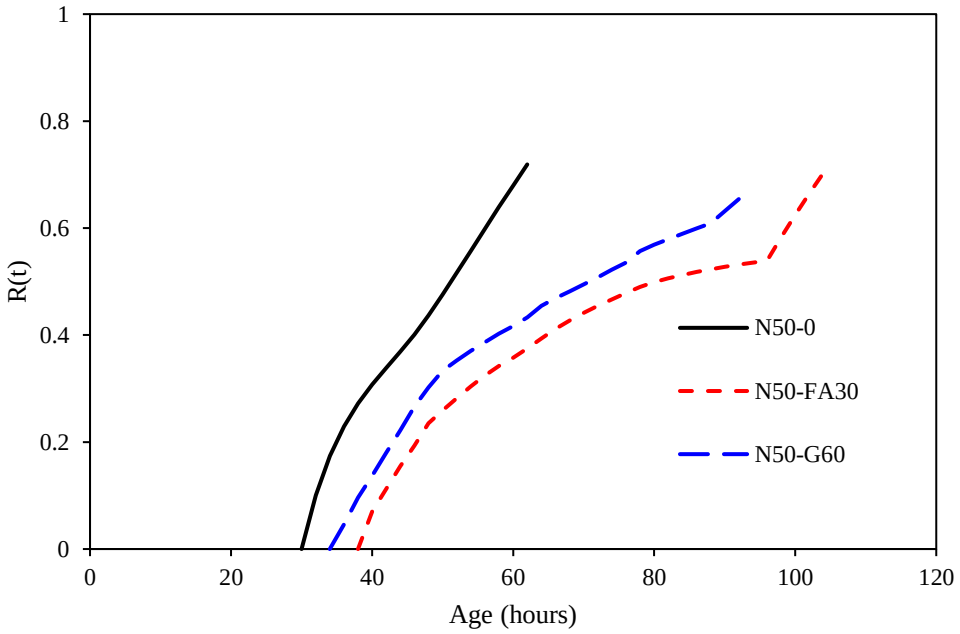

Figure 7 - 12: Cracking risk coefficient R(t).

7.5 Conclusions

In this chapter, the early age cracking of concrete mixes with fly ash and GGBFS is experimentally investigated using the RCF. The free total deformation, including thermal strain and autogenous shrinkage, is measured by FSF. Mechanical properties are evaluated under match-curing conditions using an oven delivering the same temperature profile. The temperature profile was simulated using the software ConcreteWorks and applied to all relevant tests. The main observations are outlined below:

1. Partially replacing the cement content with fly ash and GGBFS in concrete mix design significantly decreases the maximum temperature rise, leading to less thermal strain development and lowering the risk of early age cracking.
2. The free total deformation of control and SCMs mixtures exhibits an early age swelling. The control mixture shows higher swelling than SCMs concretes, which is attributed to the higher thermal dilatation. After the zero-stress time, the absolute free total

deformation of the control concrete was higher than SCMs concrete, contributing to reduce the cracking time.

3. The time-dependent tensile strength and elastic modulus of fly ash and GGBFS concretes were lower than that of the control mixture under match-curing conditions. The trends were similar to that of under standard curing or ambient curing conditions.
4. The predicted basic tensile creep coefficient of concrete mixes without SCMs was lower than with SCMs, leading to a lower early age stress relaxation. This was due to a greater temperature profile caused by a higher early age hydration degree, resulting in the increase of the stiffness properties, which led to a decrease in creep.
5. The risk of early age cracking of the reference concrete was the highest. This was mainly attributed to the higher free deformation due to a higher temperature rise. GGBFS concrete exhibited a higher autogenous shrinkage, leading to a shorter cracking time compared to fly ash concrete despite being exposed to a similar temperature profile. The cracking stress occurred at about 70% of the splitting tensile strength.

CHAPTER 8: CONCLUDING REMARKS AND RECOMMENDATIONS

8.1 Concluding remarks

This dissertation reports experimental investigations and proposes analytical models for concrete mixes with a high volume of fly ash and GGBFS relating to shrinkage, tensile creep and thermal effects.

Chapter 3 presents an experimental study investigating the shrinkage of concrete with a high volume of SCMs including fly ash and GGBFS. In modern concrete, SCMs are widely used to reduce the cement content to achieve economic and environmental objectives. As a result, understanding the shrinkage of blended cement-based concrete is essential. In total, 21 concrete mixes were produced with GP cement and with cement replacements of 30% by fly ash, 40% and 60% by GGBFS. The concrete compressive strength ranged from 25 MPa to 100 MPa. Experimental results were also compared to the predictions by Australian Standard AS3600 (2009 and 2018 versions) and Eurocode 2.

Additional tests on pastes with the same SCM content were conducted to investigate both autogenous and chemical shrinkage in relation to their time-dependent pore structure refinement assessed using the nitrogen adsorption isotherm technique. For concrete with a characteristic compressive strength lower than 50 MPa, the autogenous shrinkage of concretes with 40-60% GGBFS was significantly higher than that of reference concretes mostly due to a later increase in the autogenous shrinkage between 28 and 100 days. No clear difference was observed for GGBFS concretes with a compressive strength greater than 50 MPa. Autogenous shrinkage of fly ash concretes was overall equivalent to that of the reference concretes. However, the drying shrinkage of concrete mixes with SCMs was

significantly lower than that of reference concretes, leading to an overall reduction in total shrinkage for most of the concretes with SCMs. Some amendments to the shrinkage model in AS3600 were proposed to improve the estimation of both autogenous shrinkage and drying shrinkage of high-volume fly ash or GGBFS concretes.

Chapter 4 proposes an analytical model for stress analysis of the restrained ring test by capturing the effect of both restrained shrinkage and tensile creep based on the age-adjusted effective modulus theory. The analytical model allows for accurately predicting the tensile stress of the restrained concrete ring based on the experimental measurements of the time-dependent development of elastic modulus, total free shrinkage, and tensile creep of concrete. A numerical finite element simulation was also successfully carried out to validate the new analytical model. Importantly, the model was validated considering a total of 21 concretes consisting of 6 strength grades ranging from 25 MPa to 100 MPa. For each grade, one fly ash blend (30%), two GGBFS blends (40% and 60%) and a reference mix without supplementary cementitious materials were tested.

Chapter 5 investigates the tensile creep behaviour of the same fly ash and GGBFS concrete mixes described in previous chapters. Tensile creep can relax the strain caused by restrained shrinkage and thermal effects, leading to a decrease in the restrained induced stress at an early age. Meanwhile, SCMs have been widely used in concrete to achieve economic and environmental goals. Therefore, an understanding of the tensile creep behaviour of SCMs based concrete is vital. In this chapter, tensile creep tests have been carried out using dog-bone specimens under uniaxial tensile loading. The test series was conducted from the age of 2 days until 28 days. It was observed that the tensile creep of fly ash concretes was slightly lower than that of the reference mixtures without SCM. For

GGBFS concrete, the higher the GGBFS content, the higher the tensile creep. The experimental results could not be predicted existing models developed for creep in compression. A tensile creep model was proposed to improve the prediction for concretes with fly ash and GGBFS. The new model was calibrated only for controlled environmental conditions (23 °C and 50% RH and loading at 2 days after casting) and has been validated to analyse the development of concrete tensile stress in the restrained ring test.

Chapter 6 assesses the nonlinear tensile creep behaviour of UHPC subjected to three tensile stress levels (40%, 60% and 75%). UHPC is an excellent material due to its good workability, high strength, high toughness, and low porosity. It can be used in reinforced concrete (RC) structures by fully or partially replacing the traditional concrete to avoid concrete cracking and enhance the service life of concrete structures. In a continuous system, the concrete in the negative bending moment zone is often under tension which has a significant impact on the long-term deflection including the tensile creep deformation. UHPC may put the RC structures to exceed the linear limit due to its high tensile capacity. Therefore, understanding the nonlinear tensile creep behaviour of UHPC is vital. The tensile creep test series were loaded at the age of 2 and 28 days after curing. The experimental results were compared with the values calculated based on the various prediction models (ACI-209R-92, GL 2000, AS3600-2018, and Eurocode 2). In addition, some simple analytical models from the literature for calculating nonlinear creep coefficient were also compared with the experimental values. A nonlinear tensile creep model was proposed for UHPC and verified using experimental results.

Chapter 7 examines the risk of early age thermal cracking of concrete mixes with a high volume of supplementary cementitious materials (SCMs) such as fly ash and ground

granulated blast furnace slag (GGBFS). SCMs are found to control the maximum temperature and the accompanying thermal gradients effectively. However, it has been reported that SCMs also lead to low early age strength development. As a result, it is crucial to understand the cracking behaviour of SCMs based concrete and how they are affected by the mix design parameters, especially at an early age. In this chapter, the thermal cracking resistance was evaluated using a rigid cracking frame (RCF) with a computer-controlled temperature profile. The temperature profile was determined using the software ConcreteWorks by assuming the centre point of the mass concrete. The free shrinkage frame (FSF) and match-curing oven follow the same temperature profile as RCF to measure the free total deformation and time-dependent mechanical properties of concrete, respectively. Autogenous shrinkage was measured using concrete prisms. Basic tensile creep was computed according to the modified FIB 2010 model. An analytical model was proposed to calculate the autogenous shrinkage and the thermal stress separately. A time-dependent cracking risk coefficient allowing to estimate the risk of early-age cracking of concrete was also proposed.

8.2 Recommendations for future work

The current research focused on experimental investigations and analytical models for concrete mixes with a high volume of fly ash and GGBFS with consideration of shrinkage, tensile creep, and thermal effects. Since the application of advanced materials is becoming diverse and more complex, further works is required to fill the insufficient areas of this study.

- With the development of sustainable concrete materials such as UHPC, geopolymer concrete, limestone calcined clay cement (LC3) concrete, engineering cement-based

composite (ECC), etc., the mechanical properties and time-dependent behaviour such as shrinkage and creep should be further investigated and can be extended to the early age restrained shrinkage induced cracking analysis.

- The reactivity and hydration reaction of fly ash and GGBFS concrete needs to be further investigated to understand the mechanism of shrinkage, tensile creep and thermal effect related to early age cracking. The properties of fly ash and GGBFS significantly vary depending on their sources and this variation needs to be considered.
- Although a tensile creep model has been established in this dissertation, the model was developed in a limited condition (23°C, RH of 50%). The tensile creep of SCMs based concrete remains a topic of interest for future research. A more general tensile creep model for fly ash and GGBFS concrete needs to be established.
- A theory of structural analysis considering the shrinkage, tensile creep and thermal effects needs to be established for UHPC. In the engineering field, high performance concrete exhibits higher shrinkage and greater thermal effects. Furthermore, in a crack resistance analysis, UHPC experiences high tensile stress levels before reaching its tensile strength. As a result, a nonlinear tensile creep analysis should be considered. Therefore, it is necessary to propose a high-precision structural analysis method for UHPC relating to shrinkage, nonlinear tensile creep and thermal effects.

REFERENCES

[1] C. Meyer, "The greening of the concrete industry," *Cement and Concrete Composite,* vol. 31, pp. 199-206, 2009.

[2] V. Malhotra, "Role of supplementary cementing materials in reducing greenhouse gas emissions," in *Concrete technology for a Sustainable Development in the 21st Century, E&FN Spon,*, London, 2000.

[3] RILEM-TC281-CCC, "Understanding the carbonation of concrete with supplementary cementitious materials: a critical review," *Materials and Structures,* vol. 53, p. 136, 2020.

[4] M. Elahi, C. Shearer, A. Reza, A. Saha, M. Khan, M. Hossain and P. Sarker, "Improving the sulfate attack resistance of concrete by using supplementary cementitious materials (SCMs): A review," *Construction and Building Materials,* vol. 281, p. 122628, 2021.

[5] A. Beglarigale and H. Yazici, "Mitigation of detrimental effects of alkali-silica reaction in cement-based composites by combination of steel microfibers and ground-granulated blast-furnace slag," *Journal of Materials in Civil Engineering,* vol. 26, no. 12, p. 04014091, 2014.

[6] H. Moon, S. Ramanathan, P. Suraneni, C. Shon, C. Lee and C. Chung, "Revisiting the effect of slag in reducing heat of hydration in concrete in comparison to other supplementary cementitious materials," *Materials,* vol. 11, no. 10, p. 1847, 2018.

[7] AS1012.13-2015, Methods of testing concrete – Determination of the drying

shrinkage of concrete for samples prepared in the field or in the laboratory, Sydney: Standards Australia, 2015.

[8] R. Blissett and N. Rowson, “A review of the multi-component utilisation of coal fly ash,” *Fuel,* vol. 97, pp. 1-23, 2012.

[9] Z. Yu and G. Ye, “New perspective of service life prediction of fly ash concrete,” *Construction and Building Materials,* vol. 48, pp. 764-771, 2013.

[10] W. Khaliq and V. Kodur, “Behavior of high strength fly ash concrete columns under fire conditions,” *Materials and Structures,* vol. 46, pp. 857-867, 2013.

[11] S. Wang, E. Llamazos, L. Baxter and F. Fonseca, “Durability of biomass fly ash concrete: Freezing and thawing and rapid chloride permeability tests,” *Fuel,* vol. 87, pp. 359-364, 2008.

[12] J. Zhang, S. Zhang and B. Liu, “Degradation technologies and mechanisms of dioxins in municipal solid waste incineration fly ash: A review,” *Journal of Cleaner Production,* vol. 250, p. 119507, 2020.

[13] I. De la Varga, J. Castro, D. Bentz, F. Zunino and J. Weiss, “Evaluating the hydration of high volume fly ash mixtures using chemically inert fillers,” *Construction and Building Materials,* vol. 161, pp. 221-228, 2018.

[14] W. Wongkeo, P. Thongsanitgarn, C. Poon and A. Chaipanich, “Heat of hydration of cement pastes containing high-volume fly ash and silica fume,” *Journal of Thermal Analysis and Calorimetry,* vol. 138, pp. 2065-2075, 2019.

[15] B. Dockter, “Using class C fly ash to mitigate alkali-silica reactions in concrete,” in *3rd World of Coal Ash, WOCA Conference - Proceedings*, Lexington, 2009.

[16] X. Ling, S. Setunge and I. Patnaikuni, “Effect of different concentrations of lime water on mechanical properties of high volume fly ash concrete,” in *From Materials to Structures: Advancement Through Innovation - Proceedings of the 22nd Australasian Conference on the Mechanics of Structures and Materials, ACMSM 2012*, Sydney, 2013.

[17] T. Naik, S. Singh and M. Hossain, “Permeability of concrete containing large amounts of fly ash,” *Cement and Concrete Research,* vol. 24, no. 5, pp. 913-922, 1994.

[18] Q. Niu, N. Feng, J. Yang and X. Zheng, “Effect of superfine slag powder on cement properties,” *Cement and Concrete Research,* vol. 32, no. 4, pp. 615-621, 2002.

[19] S. Liu and L. Li, “Influence of fineness on the cementitious properties of steel slag,” *Journal of Thermal Analysis and Calorimetry,* vol. 117, no. 2, pp. 629-634, 2014.

[20] S. Tavasoli, M. Nili and B. Serpoosh, “Effect of GGBS on the frost resistance of self-consolidating concrete,” *Construction and Building Materials,* vol. 165, pp. 717-722, 2018.

[21] J. Gao, C. Qian, H. Liu, B. Wang and L. Li, “ITZ microstructure of concrete containing GGBS,” *Cement and Concrete Research,* vol. 35, no. 7, pp. 1299-1304, 2005.

[22] Z. Li and Z. Ding, “Property improvement of Portland cement by incorporating with metakaolin and slag,” *Cement and Concrete Research,* vol. 33, no. 4, pp. 579-584, 2003.

[23] J. Khatib and J. Hibbert, “Selected engineering properties of concrete incorporating

slag and metakaolin," *Construction and Building Materials,* vol. 19, no. 6, pp. 460-472, 2005.

[24] A. Oner and S. Akyuz, "An experimental study on optimum usage of GGBS for the compressive strength of concrete," *Cement and Concrete Composites,* vol. 29, no. 6, pp. 505-514, 2007.

[25] C. Cheah, L. Tan and M. Ramli, "The engineering properties and microstructure of sodium carbonate activated fly ash/ slag blended mortars with silica fume," *Composites Part B,* vol. 160, pp. 558-572, 2019.

[26] P. Richard and M. Cheyrezy, "Reactive powder concretes with high ductility and 200-800 mpa compressive strength," *American Concrete Institute, ACI Special Publication,* Vols. SP-144, pp. 507-518, 1994.

[27] Y. Li, T. Mi, W. Liu, Z. Dong, B. Dong, L. Tang and F. Xing, "Chemical and mineralogical characteristics of carbonated and uncarbonated cement pastes subjected to high temperatures," *Composites Part B: Engineering,* vol. 216, p. 108861, 2021.

[28] K. Wille, A. Naaman and G. Parra-Montesinos, "Ultra-high performance Concrete with compressive strength exceeding 150 MPa (22 ksi): A simpler way," *ACI Materials Journal,* vol. 108, no. 1, pp. 46-54, 2011.

[29] S. Granger, A. Loukili, G. Pijaudier-Cabot and G. Chanvillard, "Experimental characterization of the self-healing of cracks in an ultra high performance cementitious material: Mechanical tests and acoustic emission analysis," *Cement and Concrete Research,* vol. 37, no. 4, pp. 519-527, 2007.

[30] R. Yu, P. Spiesz and H. Brouwers, "Effect of nano-silica on the hydration and

microstructure development of Ultra-High Performance Concrete (UHPC) with a low binder amount," *Construction and Building Materials,* vol. 65, pp. 140-150, 2014.

[31] K. Kovler and S. Zhutovsky, "Overview and future trends of shrinkage research," *Materials and Structures,* vol. 39, no. 9, pp. 827-847, 2006.

[32] A. Neville, W. Dilger and J. Brooks, Creep of Plain and Structural Concrete, London and New York: Construction Press, 1983.

[33] G. Kim, E. Lee, J. Nam and K. Koo, "Analysis of hydration heat and autogenous shrinkage of high-strength mass concrete," *Magazine of Concrete Research,* vol. 63, no. 5, pp. 377-389, 2011.

[34] H. Lee, K. Lee and B. Kim, "Autogenous shrinkage of high-performance concrete containing fly ash," *Magazine of Concrete Research,* vol. 55, no. 6, pp. 507-515, 2003.

[35] P. Termkhajornkit, T. Nawa, M. Nakai and T. Saito, "Effect of fly ash on autogenous shrinkage," *Cement and Concrete Research,* vol. 35, pp. 473-482, 2005.

[36] Y. Zhao, J. Gong and S. Zhao, "Experimental study on shrinkage of HPC containing fly ash and ground granulated blast-furnace slag," *Construction and Building Materials,* vol. 155, pp. 145-153, 2017.

[37] S. Lim and T. Wee, "Autogenous shrinkage of ground-granulated B last-furnace slag concrete," *ACI Structural Journal,* vol. 97, no. 5, pp. 587-593, 2000.

[38] Y. Wei, W. Hansen, J. Biernacki and E. Schlangen, "Unified Shrinkage Model for Concrete from Autogenous Shrinkage Test on Paste with and without Ground-Granulated Blast-Furnace Slag," *ACI Materials Journal,* vol. 108, no. 1, pp. 13-20,

2011.

[39] T. Xie, C. Fang, M. Ali and P. Visintin, “Characterizations of autogenous and drying shrinkage of ultra-high performance concrete (UHPC): An experimental study,” *Cement and Concrete Composites,* vol. 91, pp. 156-173, 2018.

[40] P. Nath and P. Sarker, “Effect of Mixture Proportions on the Drying Shrinkage and Permeation Properties of High Strength Concrete Containing Class F Fly Ash,” *KSCE Journal of Civil Engineering,* vol. 17, no. 6, pp. 1437-1445, 2013.

[41] T. Seo, M. Lee, C. Choi and Y. Ohno, “Properties of drying shrinkage cracking of concrete containing fly ash as partial replacement of fine aggregate,” *Magazine of Concrete Research,* vol. 62, no. 6, pp. 427-433, 2010.

[42] J. Yuan, W. Lindquist, D. Darwin and J. Browning, “Effect of slag cement on drying shrinkage of concrete,” *ACI Materials Journal,* vol. 112, no. 2, pp. 267-276, 2015.

[43] M. Shariq, J. Prasad and H. Abbas, “Creep and drying shrinkage of concrete containing GGBFS,” *Cement and Concrete Composites,* vol. 68, pp. 35-45, 2016.

[44] S. Saluja, K. Kaur, S. Goyal and B. Bhattacharjee, “Long-Term Drying Shrinkage of GGBFS-Incorporated RCC under Various Temperature Exposures,” *Journal of Materials in Civil Engineering,* vol. 33, no. 6, p. 04021122, 2021.

[45] B. Han, H. Xie, L. Zhu and P. Jiang, “Nonlinear model for early age creep of concrete under compression strains,” *Construction and Building Materials,* vol. 147, pp. 203-211, 2017.

[46] N. Ranaivomanana, S. Multon and A. Turatsinze, “Basic creep of concrete under compression, tension and bending,” *Construction and Building Materials,* vol. 38, pp.

173-180, 2013.

[47] A. Klausen, T. Kanstad, Ø. Bjøntegaard and E. Sellevold, “Comparison of tensile and compressive creep of fly ash concretes in the hardening phase,” *Cement and Concrete Research,* vol. 95, pp. 188-194, 2017.

[48] Q. Zhao, X. Liu and J. Jiang, “Effect of curing temperature on creep behavior of fly ash concrete,” *Construction and Building Materials,* vol. 96, pp. 326-333, 2015.

[49] J. Wang, Z. Fang and Z. Tang, “The Experimental Study on Creep and Shrinkage of High Strength Concrete with Fly Ash,” *Advanced Materials Research,* Vols. 639-640, pp. 423-426, 2013.

[50] Y. Wei and W. Hansen, “Tensile Creep Behavior of Concrete Subject to Constant Restraint at Very Early Ages,” *Journal of Materials in Civil Engineering,* vol. 25, pp. 1277-1284, 2013.

[51] I. Khan, T. Xu, M. Khan, A. Castel and R. Gilbert, “Effect of Various Supplementary Cementitious Materials on Early-Age Concrete Cracking,” *Journal of Materials in Civil Engineering,* vol. 32, no. 4, p. 04020049, 2020.

[52] Y. Zhu, Y. Zhang, H. Hussein, J. Liu and G. Chen, “Experimental study and theoretical prediction on shrinkage-induced restrained stresses in UHPC-RC composites under normal curing and steam curing,” *Cement and Concrete Composites* , vol. 110, p. 103602, 2020.

[53] Y. Xu, J. Liu, J. Liu, P. Zhang, Q. Zhang and L. Jiang, “Experimental studies and modeling of creep of UHPC,” *Construction and Building Materials,* vol. 175, pp. 643-652, 2018.

[54] V. Garas, K. Kurtis and L. Kahn, “Creep of UHPC in tension and compression: Effect of thermal treatment,” *Cement & Concrete Composites,* vol. 34, pp. 493-502, 2012.

[55] ACI207.1R-05, Guide to mass concrete, Farmington Hills: American Concrete Institute, 2012.

[56] J. Ha, Y. Jung and Y. Cho, “Thermal crack control in mass concrete structure using an automated curing system,” *Automation in Construction,* vol. 45, pp. 16-24, 2014.

[57] B. Zhu, Thermal Stresses & Temperature Control of Mass Concrete, Tsinghua University Press, 2014.

[58] P. Bamforth and S. Oenton, “Early-age Thermal Crack Control in Concrete - Changes in UK design resulting from the introduction of EN1992,” in *11th Annual International fib Symposium - Concrete: 21st Century Superhero: Building a Sustainable Future,* London, 2009.

[59] J. Emanuel and L. Hulsey, “Prediction of the Thermal Coefficient of Expansion of Concrete,” *Journal of the American Concrete Institute,* vol. 74, no. 4, pp. 149-155, 1977.

[60] H. Kada, M. Lachemi, N. Petrov, O. Bonneau and P.-C. Aitcin, “Determination of the coefficient of thermal expansion of high performance concrete from initial setting,” *Materials and Structures,* vol. 35, no. 1, pp. 35-41, 2002.

[61] L. Li, V. Dao and P. Lura, “Autogenous deformation and coefficient of thermal expansion of early-age concrete: Initial outcomes of a study using a newly-developed Temperature Stress Testing Machine,” *Cement and Concrete Composites ,* vol. 119,

p. 103997, 2021.

[62] R. Springenschmid and R. Breitenbücher, “Influence of Constituents, Mix Proportions and Temperature on Cracking Sensitivity of Concrete,” In RILEM Report 15, Prevention of Thermal Cracking in Concrete, London, 1998.

[63] G. De Schutter and L. Taerwe, “Degree of Hydration-Based Description of Mechanical Properties of Early Age Concrete,” *Materials and Structures,* vol. 29, no. 190, pp. 335-344, 1996.

[64] A. Gutsch, “Properties of early age concrete - Experiments and modelling,” *Materials and Structures,* vol. 34, no. 246, pp. 76-79, 2002.

[65] S. Igarashi, A. Bentur and K. Kovler, “Autogenous shrinkage and induced restraining stresses in high-strength concretes,” *Cement and Concrete Research,* vol. 30, no. 11, pp. 1701-1707, 2000.

[66] I. Khan, A. Castel and R. Gilbert, “Tensile creep and early-age concrete cracking due to restrained shrinkage,” *Construction and Building Materials,* vol. 149, pp. 705-715, 2017.

[67] Y. Zhang, S. Afroz, Q. Nguyen, T. Kim, J. Eisentrager, A. Castel and T. Xu, “Analytical model predicting the concrete tensile stress development in the restrained shrinkage ring test,” *Construction and Building Materials,* vol. 307, p. 124930, 2021.

[68] Y. Kawabata, N. Ueda, T. Miura and S. Multon, “The influence of restraint on the expansion of concrete due to delayed ettringite formation,” *Cement and Concrete Composites*, p. 104062, 2021.

[69] M. Zych, “Degree of external restraint of wall segments in semi-massive reinforced

concrete tanks: Part I rectangular segments," *Structural Concrete*, vol. 19, no. 3, pp. 820-828, 2018.

[70] A. Knoppik-Wróbel and B. Klemczak, "Degree of restraint concept in analysis of early-age stresses in concrete walls," *Engineering Structures*, vol. 102, pp. 369-386, 2015.

[71] S. Altoubat, M. Junaid, M. Leblouba and D. Badran, "Effectiveness of fly ash on the restrained shrinkage cracking resistance of self-compacting concrete," *Cement and Concrete Composites*, vol. 79, pp. 9-20, 2017.

[72] Z. Zhao, K. Wang, D. Lange, H. Zhou, W. Wang and D. Zhu, "Creep and thermal cracking of ultra-high volume fly ash mass concrete at early age," *Cement and Concrete Composites*, vol. 99, pp. 191-202, 2019.

[73] D. Shen, Y. Jiao, J. Kang, Z. Feng and Y. Shen, "Influence of ground granulated blast furnace slag on early-age cracking potential of internally cured high performance concrete," *Construction and Building Materials*, vol. 233, p. 117083, 2020.

[74] P. Mehta and J. Monteiro, Concrete: Microstructure, Properties and Materials, New York: McGraw-Hill, 2014.

[75] Y. Ballim and P. Graham, "The effects of supplementary cementing materials in modifying the heat of hydration of concrete," *Materials and Structures*, vol. 42, no. 6, pp. 803-811, 2009.

[76] M. Batog and Z. Giergiczny, "Influence of mass concrete constituents on its properties," *Construction and Building Materials*, vol. 146, pp. 221-230, 2017.

[77] A. Markandeya, N. Shanahan, D. Gunatilake, K. Riding and A. Zayed, "Influence of

slag composition on cracking potential of slag-portland cement concrete," *Construction and Building Materials,* vol. 164, pp. 820-829, 2018.

[78] AS1012.13-2015, Methods of testing concrete – Determination of the drying shrinkage of concrete for samples prepared in the field or in the laboratory, Sydney: Standards Australia, 2015.

[79] Q. Nguyen, S. Afroz, Y. Zhang, T. Kim, W. Li and A. Castel, "Autogenous and total shrinkage of limestone calcined clay cement (LC3) concretes," *Construction and Building Materials,* vol. 314, p. 125720, 2022.

[80] R. Gibert, A. Castel, I. Khan, J. Mohammadi, W. South and T. Thomas, "Characterisation of autogenous shrinkage in Australian concrete," in *28th Biennial Conference of the Concrete Institute of Australia*, Adelaide, 2017.

[81] R. Gilbert, A. Castel, I. Khan, W. South and J. Mohammadi, "An Experimental Study of Autogenous and Drying Shrinkage," in *High Tech Concrete: Where Technology and Engineering Meet*, 2018.

[82] S. Liang and Y. Weo, "Biaxial creep of high-strength concrete at early ages assessed from restrained ring test," *Cement and Concrete Composites,* vol. 104, p. 103421, 2019.

[83] M. Ozawa, T. Tanibe, R. Kamata, Y. Uchida, K. Rokugo and S. Parajuli, "Behavior of ring-restrained high-performance concrete under extreme heating and development of screening test," *Construction and Building Materials,* vol. 162, pp. 215-228, 2018.

[84] A. Dabarera, L. Li and V. Dao, "Experimental evaluation and modelling of early-age basic tensile creep in high-performance concrete," *Materials and Structures,* vol. 54,

no. 3, p. 130, 2021.

[85] Z. Cheng, R. Zhao, Y. Yuan, F. Li, A. Castel and T. Xu, "Ageing coefficient for early age tensile creep of blended slag and low calcium fly ash geopolymer concrete," *Construction and Building Materials,* vol. 262, p. 119855, 2020.

[86] T. Ni, Y. Yang, C. Gu, J. Liu, J. Chen and X. Lou, "Early-Age Tensile Basic Creep Behavioral Characteristics of High-Strength Concrete Containing Admixtures," *Advances in Civil Engineering,* vol. 2019, p. 9495231, 2019.

[87] I. Khan, T. Xu, A. Castel and R. Gilbert, "Early-age tensile creep and shrinkage induced cracking in internally restrained concrete members," *Magazine of Concrete Research,* vol. 71, no. 22, pp. 1167-1179, 2019.

[88] R. Breitenbücher, "Investigation of Thermal Cracking with the Cracking-Frame," *Materials & Structures,* vol. 23, pp. 172-177, 1990.

[89] A. Neville, Properties of concrete, Harlow, England: Pearson, 2011.

[90] N. De Belie, M. Soutsos and E. Gruyaert, Properties of Fresh and Hardened Concrete Containing Supplementary Cementitious Materials: State-of-the-Art Report of the RILEM Technical Committee 238-SCM, Working Group 4, Cham, Switzerland: Springer International Publishing, 2018.

[91] Y. Li, J. Bao and Y. Guo, "The relationship between autogenous shrinkage and pore structure of cement paste with mineral admixtures," *Construction and Building Materials,* no. 24, p. 1855–1860, 2010.

[92] D. Mokarem, R. Weyers and D. Lane, "Development of a shrinkage performance specifications and prediction model analysis for supplemental cementitious material

concrete mixtures. Cement and Concrete Research," *Cement and Concrete Research,* no. 35(5), pp. 458-925, 2005.

[93] M. Shariq, J. Prasad and H. Abbas, "Creep and drying shrinkage of concrete containing GGBFS," *Cement and Concrete Composites,* vol. 68, pp. 35-45, 2016.

[94] H. Zhao, W. Sun, X. Wu and B. Gao, "The properties of the self-compacting concrete with fly ash and ground granulated blast furnace slag mineral admixtures," *Journal of Cleaner Production,* vol. 95, pp. 66-74, 2015.

[95] J. Yuan, W. Lindquist, D. Darwin and J. Browning, "Effect of slag cement on drying shrinkage of concrete," *ACI Materials Journal,* vol. 112, no. 2, pp. 267-276, 2015.

[96] J. Li and Y. Yao, "A study on creep and drying shrinkage of high performance concrete," *Cement and Concrete Research,* vol. 31, no. 8, pp. 1203-1206, 2001.

[97] AS3600-2009, Australian standard for concrete structures, Sydney: Standards Australia, 2009.

[98] AS3600-2018, Australian standard for concrete structures, Sydney: Standards Australia, 2018.

[99] EN 1992-1-1, Design of concrete structures Part 1-1: General rules and rules for buildings., Brussels: European Committee for Standardisation, 2004.

[100] AS3972-2010, General purpose and blended cements, Sydney: Standards Australia, 2010.

[101] AS3582.1-2016, Supplementary cementitious materials - Fly ash, Sydney: Standards Australia, 2016.

[102] AS3582.2-2016, Supplementary cementitious materials - Slag - Ground granulated

blast-furance, Sydney: Standards Australia, 2016.

[103] AS1012.9-2014, Methods of testing concrete - Compressive strength tests - Concrete, mortar and grout specimens, Australia, 2014.

[104] AS1012.8.4-2015, Methods of testing concrete - Method for making and curing concrete - Drying shrinkage specimens prepared in the field or in the laboratory, Sydney: Standards Australia, 2015.

[105] AS1379-2007, Specification and supply of concrete, Sydney: Standards Australia, 2007.

[106] AS1012.3.1-2014, Methods of testing concrete - Determination of properties related to the consistency of concrete - Slump test, Sydney: Standards Australia, 2014.

[107] AS1012.4.2-2014, Methods of testing concrete - Determination of air content of freshly mixes concrete - Measuring reduction in air pressure in chamber above concrete, Sydney: Standards Australia, 2014.

[108] AS1012.5-2014, Methods of testing concrete - Determination of mass per unit volume of freshly mixed concrete, Sydney: Standard Australia, 2014.

[109] T. Xie, C. Fang, M. M. Ali and P. Visintin, "Characterizations of autogenous and drying shrinkage of ultra-high," *Cement and Concrete Composites*, pp. 156-173, 2018.

[110] H. Huang and G. Ye, "Examining the "time-zero" of autogenous shrinkage in high/ultra-high performance cement pastes," *Cement and Concrete Research,* vol. 97, pp. 107-114, 2017.

[111] G. Fang, H. Bahrami and M. Zhang, "Mechanisms of autogenous shrinkage of alkali-

activated fly ash-slag pastes cured at ambient temperature within 24 h," *Construction and Building Materials,* vol. 171, pp. 377-387, 2018.

[112] AS2350.4-2006, Methods of testing portland, blended and masonry cements - Setting time, Sydney: Standards Australia, 2006.

[113] A. Darquennes, S. Staquet and B. Espion, "Determination of time-zero and its effect on autogenous shrinkage deformation evolution," *European Journal of Environmental and Civil Engineering,* vol. 15, no. 7, pp. 1017-1029, 2011.

[114] V. Mechtcherine, M. Gorges, C. Schroefl, A. Assmann, W. Brameshuber and A. Ribeiro, "Effect of internal curing by using superabsorbent polymers (SAP) on autogenous shrinkage and other properties of a high-performance fine-grained concrete: results of a RILEM round-robin test," *Materials and Structures,* vol. 47, no. 3, pp. 541-562, 2014.

[115] R. Si, S. Guo, Q. Dai and J. Wang, "Atomic-structure, microstructure and mechanical properties of glass powder modified metakaolin-based geopolymer," *Construction and Building Materials,* vol. 254, p. 119303, 2020.

[116] Z. Giergiczny, "Fly ash and slag," *Cement and Concrete Research,* vol. 124, p. 105826, 2019.

[117] ASTMC1698-19, Test Method for Autogenous Strain of Cement Paste and Mortar, West Conshohocken: ASTM International, 2019.

[118] ASTMC1608-17, Standard test method for chemical shrinkage of hydraulic cement paste, West Conshohocken: ASTM International, 2017.

[119] T. Zhang, P. Gao, R. Luo, Y. Guo, J. Wei and Q. Yu, "Measurement of chemical

shrinkage of cement paste: Comparison study of ASTM C 1608 and an improved method," *Construction and building materials,* vol. 48, pp. 662-669, 2013.

[120] R. Snellings, J. Chwast, Ö. Cizer, N. De Belie, Y. Dhandapani, P. Durdzinski, J. Elsen, J. Haufe, D. Hooton, C. Patapy and M. Santhanam, "RILEM TC-238 SCM recommendation on hydration stoppage by solvent exchange for the study of hydrate assemblages," *Materials and Structures,* vol. 6, no. 51, pp. 1-4, 2018.

[121] K. Scrivener, R. Snellings and B. e. Lothenbach, A practical guide to microstructural analysis of cementitious materials, Crc, 2018.

[122] E. Barrett, L. Joyner and P. Halenda, "The Determination of Pore Volume and Area Distributions in Porous Substances. I. Computations from Nitrogen Isotherms," *Journal of the American Chemical Society,* vol. 73, no. 1, pp. 373-380, 1951.

[123] P. Lura, K. Breugel and I. Marayama, "Effect of curing temperature and type of cement on early-age shrinkage of high-performance concrete," *Cement Concrete Research,* vol. 31, pp. 1867-1872, 2001.

[124] E. Tazawa, Y. Matsuoka, S. Miyazawa and S. Okamoto, "Effect of autogenous shrinkage on self stress in hardening concrete," in *Proc. Int. RILEM Symp. Thermal Cracking in Concrete at early Ages,* London, 1995.

[125] B. Miao, "A new method to measure the early-age deformation of cement based materials," in *Int. RILEM Workshop on Shrinkage of Concrete,* Paris, 2000.

[126] Ø. Bjøntegaard, T. Hammer and E. Sellevold, "On the measurement of free deformation of early age cement paste and concrete," *Cement and Concrete Composites,* vol. 26, no. 5, pp. 427-435, 2004.

[127] B. Craeye, G. De Schutter, B. Desmet, J. Vantomme, G. Heirman, L. Vandewalle, Ö. Cizer, S. Aggoun and E. Kadri, "Effect of mineral filler type on autogenous shrinkage of self-compacting concrete," *Cement and Concrete Research,* vol. 40, no. 6, pp. 908-913, 2010.

[128] P. Mehta, "Mechanism of expansion associated with ettringite formation," *Cement and Concrete Research,* vol. 3, no. 1, pp. 1-6, 1973.

[129] A. Darquennes, B. Espion and S. Staquet, "How to assess the hydration of slag cement concretes?," *Construction and Building Materials,* pp. 1012-1020, 2013.

[130] S. Lim and T. Wee, "Autogenous shrinkage of ground-granulated blastfurnace slag concrete," *ACI Materials Journal,* vol. 97, pp. 587-593, 2000.

[131] E. Tazawa and S. Miyazawa, "Influence of cement and admixture on autogenous shrinkage of cement paste," *Cement Concrete Research,* vol. 25, pp. 281-287, 1995.

[132] D. Roy and G. Idorn, "Hydration, structure and properties of blast-furnace slag cements, mortars, and concrete," *ACI Journal,* vol. 79, no. 6, pp. 444-457, 1982.

[133] H. Chen, M. Wyrzykowski, K. Scrivener and P. Lura, "Prediction of self-desiccation in low water-to-cement ratio pastes based on pore structure evolution," *Cement and Concrete Research,* vol. 49, pp. 38-47, 2013.

[134] K. Lee, H. Lee, S. Lee and G. Kim, "Autogenous shrinkage of concrete containing granulated blast-furnace slag," *Cement and Concrete Research,* vol. 36, pp. 1279-1285, 2006.

[135] J. Brooks, M. Megat Johari and M. Mazloom, "Effect of admixtures on the setting times of high-strength concrete," *Cement & Concrete Composites,* vol. 22, pp. 293-

301, 2000.

[136] P. Mounanga, M. Khokhar, R. Hachem and A. Loukili, “Improvement of the early-age reactivity of fly ash and blast furnace slag cementitious systems using limestone filler,” *Materials and structures,* vol. 44, pp. 437-453, 2011.

[137] G. De Schutter and L. Taerwe, “General hydration model for Portland cement and blast furnace slag cement,” *Cement and Concrete Research,* vol. 25, no. 3, pp. 593-604, 1995.

[138] E. Güneyisi , M. Gesoğlua and E. Özbay, “Strength and drying shrinkage properties of self-compacting concretes incorporating multi-system blended mineral admixtures,” *Construction and Building Materials,* vol. 24, no. 10, pp. 1878-1887, 2010.

[139] D. Bentz and O. Jensen, “Mitigation strategies for autogenous shrinkage cracking,” *Cement and Concrete Composites,* vol. 26, no. 6, pp. 677-685, 2004.

[140] K. Li, Q. Zeng, M. Luo and X. Pang, “Effect of self-desiccation on the pore structure of paste and mortar incorporating 70% GGBS,” *Construction and Building Materials,* vol. 51, pp. 329-337, 2014.

[141] C. Yalcinkaya and H. Yazici, “Early-age shrinkage properties of eco-friendly reactive powder concrete with reduced cement content,” *European Journal of Environmental and Civil Engineering,* vol. 12, pp. 1-17, 2019.

[142] T. Merzouki, M. Bouasker, N. Khalifa and P. Mounanga, “Contribution to the modeling of hydration and chemical shrinkage of slag-blended cement at early age,” *Construction and Building Materials,* vol. 44, pp. 368-380, 2013.

[143] P. Lura, O. Jensen and K. Breugel, “Autogenous shrinkage in high-performance cement paste: An evaluation of basic mechanisms,” *Cement and Concrete Research,* vol. 33, no. 2, pp. 223-232, 2003.

[144] S. Mindess, J. Young and D. Darwin, Concrete, Upper Saddle River: Prentice-Hall, 2003.

[145] R. Cortas, E. Rozière, S. Staquet, A. Hamami, A. Loukili and M. Delplancke-Ogletree, “Effect of the water saturation of aggregates on the shrinkage induced cracking risk of concrete at early age,” *Cement & Concrete Composites,* vol. 50, pp. 1-9, 2014.

[146] B. Klemczak, M. Batog, M. Pilch and A. Zmij, “Analysis of Cracking Risk in Early Age Mass Concrete with Different Aggregate Types,” *Procedia Engineering,* vol. 193, pp. 234-241, 2017.

[147] A. Schindler, B. Byard and A. Tankasala, “Mitigation of early-age cracking in concrete structures,” in *MATEC Web of Conferences,* 2019.

[148] B. Klemczak and A. Zmij, “Insight into Thermal Stress Distribution and Required Reinforcement Reducing Early-Age Cracking in Mass Foundation Slabs,” *Materials,* vol. 14, no. 3, p. 477, 2021.

[149] I. Khan, T. Xu, A. Castel and R. Gilbert, “Early-age tensile creep and shrinkage-induced cracking in internally restrained concrete members,” *Magazine of Concrete Research,* pp. 1167-1179, 2019.

[150] M. Sule and K. Van Breugel, “Cracking behaviour of reinforced concrete subjected to early-age shrinkage,” *Materials and Structures,* vol. 34, pp. 284-292, 2001.

[151] H. Zhu, Y. Hu, Q. Li. and R. Ma, “Restrained cracking failure behavior of concrete due to temperature and shrinkage,” *Construction and Building Materials,* vol. 244, p. 118318, 2020.

[152] A. Hossain and J. Weiss, “Assessing residual stress development and stress relaxation in restrained concrete ring specimens,” *Cement and Concrete Composite,* vol. 26, no. 5, pp. 531-540, 2004.

[153] S. Shh, M. Krguller and M. Sarigaphuti, “Effects of shrinkage reducing admixtures on restrained shrinkage cracking of concrete,” *Journal of Materials,* vol. 89, no. 3, pp. 289-295, 1992.

[154] W. J. Weiss, W. Yang and S. Shah, “Influence of specimen size/geometry on shrinkage cracking of rings,” *Journal of Engineering Mechanics,* vol. 126, no. 1, pp. 93-101, 2000.

[155] R. Bloom and A. Bentur, “Free and restrained shrinkage of normal and high-strength concretes,” *ACI Materials Journal,* vol. 92, pp. 211-217, 1995.

[156] S. Altoubat and D. Lange, “A New Look at Tensile Creep of Fiber Reinforced Concrete,” in *ACI Special Publication on Fiber Reinforced Concrete,* 2003.

[157] N. Banthia, C. Yan and S. Mindess, “Restrained shrinkage cracking in fiber reinforced concrete — a novel test technique,” *Cement and Concrete Research,* vol. 26, no. 1, pp. 9-14, 1996.

[158] J. Weiss, W. Yang and S. Shah, “Shrinkage cracking of restrained concrete slabs,” *Journal of Engineering Mechanics,* vol. 124, pp. 756-764, 1998.

[159] R. Carlson and T. Reading, “Model of studying shrinkage cracking in concrete

building walls," *ACI Structures Journal,* vol. 85, pp. 395-404, 1988.

[160] R. Swamy and H. Stavrides, "Influence of fiber reinforcement on restraint shrinkage and cracking," *ACI Materials Journal,* vol. 76, no. 3, pp. 443-460, 1979.

[161] D. Shen, H. Shi, X. Tang, Y. Ji and G. Jiang, "Effect of internal curing with super absorbent polymers on residual stress development and stress relaxation in restrained concrete ring specimens," *Construction and Building Materials,* vol. 120, pp. 309-320, 2016.

[162] H. See, E. Attiogbe and M. Miltenberger, "Shrinkage cracking characteristics of concrete using ring specimens," *ACI Materials Journal,* vol. 100, no. 3, pp. 239-245, 2003.

[163] S. Uthaman, V. Vishwakarma, R. George, D. Ramachandran, K. Kumari, R. Preetha, M. Premila, R. Rajaraman, U. Mudali and G. Amarendra, "Enhancement of strength and durability of fly ash concrete in seawater environments: Synergistic effect of nanoparticles," *Construction and Building Materials,* vol. 187, pp. 448-459, 2018.

[164] M. Chi, J. Chi and C. Wu, "Effect of GGBFS on Compressive Strength and Durability of Concrete," *Advanced Materials Research,* vol. 1145, pp. 22-26, 2018.

[165] E. Allen and J. Iano, Fundamentals of building construction: materials and methods, Hoboken, New Jersey: John Wiley & Sons, 2019.

[166] S. Ghahari, L. Assi, A. Alsalman and K. Alyamac, "Fracture properties evaluation of cellulose nanocrystals cement paste," *Materials,* vol. 13, no. 11, p. 2507, 2020.

[167] S. Kang, Z. Lloyd, T. Kim and M. Lay, "Predicting the compressive strength of fly ash concrete with the Particle Model," *Cement and Concrete Research,* vol. 137, p.

106218, 2020.

[168] T. Kim, M. Ley, S. Kang, J. Davis and S. Kim, “Using particle composition of fly ash to predict concrete strength and electrical resistivity,” *Cement and Concrete Composites,* vol. 107, p. 103493, 2020.

[169] L. Wang, H. Yang, S. Zhou, E. Chen and S. Tang, “Mechanical properties, long-term hydration heat, shinkage behavior and crack resistance of dam concrete designed with low heat Portland (LHP) cement and fly ash,” *Construction and Building Materials,* vol. 187, pp. 1073-1091, 2018.

[170] I. Khan, A. Castel and R. Gilbert, “Effects of Fly Ash on Early-Age Properties and Cracking of Concrete,” *ACI Materials Journal,* vol. 114, no. 4, pp. 673-681, 2017.

[171] Q. Nguyen, M. Khan, T. Xu and A. Castel, “Mitigating the risk of early age cracking in fly ash blended cement-based concrete using ferronickel slag sand,” *Journal of advanced concrete technology,* vol. 17, pp. 295-308, 2019.

[172] A. Manaseer and R. Zayed, “Tensile Creep of Concrete at Early Age,” *ACI Materials Journal,* vol. 115, pp. 769-772, 2018.

[173] D. Shen, J. Jiang, Y. Jiao, J. Shen and G. Jiang, “Early-age tensile creep and cracking potential of concrete internally cured with pre-wetted lightweight aggregate,” *Construction and Building Materials,* vol. 135, pp. 420-429, 2017.

[174] R. Gilbert and G. Ranzi, Time-Dependent Behaviour of Concrete Structures, London: Spon Press, 2011.

[175] H. Torst, “Auswirkungen des Superpositionsprinzips auf Kriech- und Relaxations Probleme bei Beton und Spannbeton,” *Beton-und stahlbetonbau,* vol. 10, pp. 230-

238, 1967.

[176] W. Dilger and A. Neville, “Method of creep analysis of structural members,” *Special Publication,* vol. 27, pp. 349-372, 1971.

[177] Z. Bazant, “Prediction of concrete creep effects using age-adjusted effective method,” *ACI Materials Journal,* vol. 69, no. 4, pp. 212-217, 1972.

[178] A. 207.2R95, Effect of Restraint, Volume Change, and Reinforcement on Cracking of Mass Concrete, Farmington Hills, MI: American Concrete Institute, 1995.

[179] A. A. Ramezanianpour, V. Sivasundaram and V. M. Malhotra, “Superplasticizers: Their effect on the strength properties of concrete.,” *Concrete International,* no. 17, pp. 30-35, 1995.

[180] D. Sathyan, K. B. Anand, K. M. Mini and S. Aparna, “Optimization of superplasticizer in portland pozzolana cement,” in *International Conference on Advances in Materials and Manufacturing Application*, Bengaluru, 2017.

[181] J. Sun, X. Shen, G. Tan and J. Tanner, “Compressive strength and hydration characteristics of high-volume fly ash concrete prepared from fly ash,” *Journal of Thermal Analysis and Calorimetry,* vol. 136, pp. 565-580, 2019.

[182] M. Shariq, J. Prasad and A. Masood, “Effect of GGBFS on time dependent compressive strength of concrete,” *Construction and Building Materials,* vol. 24, pp. 1469-1478, 2010.

[183] AS1012.9-2014, Methods of Testing Concrete Compressive Strength Tests - Concrete, Mortar and Grout Specimens, Sydney: Standard Australia, 2014.

[184] AS1012.10-2000, Method of testing concrete - Determination of indirect tensile

strength of concrete cylinders (Brasil or splitting test), Sydney: Standard Australia, 2000.

[185] AS1012.17-1997, Method of testing concrete - Determination of the static chord modulus of elasticity and Poisson's ratio of concrete specimens, Sydney: Standard Australia, 1997.

[186] ASTMC1581/C1581M, Standard Test Method for Determining Age at Cracking and Induced Tensile Stress Characteristics of Mortar and Concrete under Restrained Shrinkage, West Conshohocken, PA: ASTM International, 2018.

[187] R. Swamy, A. Bandyopadhyay and H. Stavrides, "The ring method of measuring restrained shrinkage in mortar and concrete," *Cement, Concrete and Aggregates,* vol. 1, no. 1, pp. 13-20, 1979.

[188] F. Kanavaris, M. Azenha, M. Soutsos and K. Kovler, "Assessment of behaviour and cracking susceptibility of cementitious systems under restrained conditions through ring tests: A critical review," *Cement and Concrete Composites,* vol. 95, pp. 137-153, 2019.

[189] D. Romildo, G. Khosrow, A. Miguel and L. George, "Free, restrained and drying shrinkage of cement mortar composites reinforced with vegetable fibres," *Cement and Concrete Composite,* vol. 27, pp. 537-546, 2005.

[190] H. Rong, W. Dong, X. Zhao and X. Zhou, "Investigation on multi-cracks initiation and propagation of fiber reinforced concrete in restrained shrinkage ring tests," *Theoretical and Applied Fracture Mechanics,* vol. 111, p. 102856, 2021.

[191] W. Dong, X. Zhou and Z. Wu, "Influence of Specimen Thicknesson Cracking

Behavior in Restrained Shrinkage Ring Test," *IACSIT International Journal of Engineering and Technology*, vol. 5, no. 6, pp. 698-702, 2013.

[192] AS3600-2018, Australian standard for concrete structures, Sydney: Standards Australia, 2018.

[193] Y. Wang, Y. Ma and L. Zhou, "Creep of FRP-wrapped concrete columns with or without fly ash under axial load," *Construction and Building Materials,* vol. 25, pp. 697-704, 2011.

[194] R. Khatri, V. Sirivivatnanon and W. Gross, "Effect of different supplementary cementitious materials on mechanical properties of high performance concrete," *Cement and Concrete Research,* vol. 25, no. 1, pp. 209-220, 1995.

[195] W. Dong, X. Zhou, Z. Wu, H. Luo and G. Kastiukas, "Quantifying the influence of elliptical ring geometry on the degree of restraint in a ring test," *Computers and Structures,* vol. 207, pp. 111-120, 2018.

[196] J. Xin, G. Zhang, Y. Liu, Z. Wang and Z. Wu, "Effect of temperature history and restraint degree on cracking behavior of early-age concrete," *Construction and Building Materials,* vol. 192, pp. 381-390, 2018.

[197] S. Cha and S. Jin, "Prediction of thermal stresses in mass concrete structures with experimental and analytical results," *Construction and Building Materials,* vol. 258, p. 120367, 2020.

[198] Z. Bazant, Mathematical Modeling of Creep and Shrinkage of Concrete, New York, USA: Wiley, 1988.

[199] Z. Bazant and A. Asghari, "Constitutive law for nonlinear creep of concrete," *Journal*

of the Engineering Mechanics, vol. 103, no. 1, pp. 113-124, 1977.

[200] Z. Bazant and J. Kim, "Improved prediction model for time-dependent deformations of concrete: Part 2 – Basic creep," *Materials and Structures,* vol. 24, no. 6, pp. 409-421, 1991.

[201] A. Hilaire, F. Benboudjema, A. Darquennes, Y. Berthaud and G. Nahas, "Modeling basic creep in concrete at early-age under compressive and tensile loading," *Nuclear Engineering and Design,* vol. 269, pp. 222-230, 2014.

[202] N. Reviron, G. Nahas, J. Tailhan, F. Le Maou, F. Benboudjema and A. Millard, "Experimental study of uniaxial tensile creep of concrete," in *Creep, Shrinkage and Durability Mechanics of Concrete and Concrete Structures,* Japan, Proceedings of the 8th International Conference on Creep, Shrinkage and Durability of Concrete and Concrete Structures, 2009, pp. 453-457.

[203] N. Ranaivomanana, S. Multon and A. Turatsinze, "Tensile, compressive and flexural basic creep of concrete at different stress levels," *Cement and Concrete Research,* vol. 52, pp. 1-10, 2013.

[204] P. Rossi, J. Tailhan and F. Maou, "Comparison of concrete creep in tension and in compression: Influence of concrete age at loading and drying conditions," *Cement and Concrete Research,* vol. 51, pp. 78-84, 2013.

[205] I. Khan, T. Xu, A. Castel, R. Gilbert and M. Babaee, "Risk of early age cracking in geopolymer concrete due to restrained shrinkage," *Construction and Building Materials,* vol. 229, p. 116840, 2019.

[206] ACI209R, Prediction of creep, shrinkage, and temperature effects in concrete

structures, Farmington Hills, Michigan: American Concrete Institute Committee 209, 2008.

[207] FIB, fib Model Code for Concrete Structures, Weinheim: Wiley-VCH Verlag GmbH & Co. KGaA, 2010.

[208] N. Gardner and M. Lockman, "Design provisions for drying shrinkage and creep of normal strength concrete," *ACI Materials Journal,* vol. 98, no. 2, pp. 159-167, 2001.

[209] Eurocode 2 and EN 19920101, Design of concrete structures. General rules and rules for buildings, Belgium: European Committee for Standardization, 2004.

[210] Y. Wei, W. Guo and S. Liang, "Microprestress-solidification theory-based tensile creep modeling of early-age concrete: Considering temperature and relative humidity effects," *Construction and Building Materials,* vol. 127, pp. 618-626, 2016.

[211] Z. Zhao, H. Zhang, B. Fang, Y. Sun, Y. Zhong and T. Shi, "Tensile creep model of slab concrete based on microprestress-solidification theory," *Materials,* vol. 13, no. 14, p. 3157, 2020.

[212] J. Forth, "Predicting the tensile creep of concrete," *Cement & Concrete Composites,* vol. 55, pp. 70-80, 2015.

[213] A. Brugger, P. Gamnitzer and G. Hofstetter, "Multiphase modeling of the effect of external loading on the shrinkage of concrete and its consequences for modeling tensile creep," *Cement and Concrete Composites,* vol. 130, p. 104499, 2022.

[214] I. Pane and W. Hansen, "Investigation on key properties controlling early-age stress development of blended cement concrete," *Cement and Concrete Research,* vol. 38, pp. 1325-1335, 2008.

[215] Q. Nguyen, M. Khan, A. Castel and T. Kim, “Durability and Microstructure Properties of Low-Carbon Concrete Incorporating Ferronickel Slag Sand and Fly Ash,” *Journal of Materials in Civil Engineering,* vol. 31, no. 8, p. 04019152, 2019.

[216] S. Afroz, Y. Zhang, Q. Nguyen, T. Kim and A. Castel, “Effect of limestone in General Purpose cement on autogenous shrinkage of high strength GGBFS concrete and pastes,” *Construction and Building Materials,* vol. 327, p. 126949, 2022.

[217] G. Liu, G. Zhang, Y. Zhang and L. Lu, “Study on Tensile Creep Characteristics of High Strength Concrete,” *Applied Mechanics and Materials,* vol. 835, pp. 535-541, 2015.

[218] S. Hwang and K. Khayat, “Effect of mix design on restrained shrinkage of self-consolidating concrete,” *Materials and Structures,* vol. 43, pp. 367-380, 2010.

[219] B. Bissonnette, M. Pigeon and A. Vaysburd, “Tensile creep of concrete: study of its sensitivity to basic parameters,” *ACI Materials Journal,* vol. 104, no. 4, p. 360, 2007.

[220] H. Hashida and N. Yamazaki, “A Calculation Method of Autogenous Shrinkage Stress in High-strength Concrete Structures Subjected to Elevated Temperature at Early Age,” *Journal of Structural and Construction Engineering,* vol. 65, pp. 7-12, 2000.

[221] D. Shen, J. Jiang, W. Wang, J. Shen and G. Jiang, “Tensile creep and cracking resistance of concrete with different water-to-cement ratios at early age,” *Construction and Building Materials,* vol. 146, pp. 410-418, 2017.

[222] Y. Wei, Z. Wu, J. Huang and S. Liang, “Comparison of Compressive, Tensile, and Flexural Creep of Early-Age Concretes under Sealed and Drying Conditions,”

Journal of Materials in Civil Engineering, vol. 30, no. 11, p. 04018289, 2018.

[223] R. Goel, R. Kumar and D. Paul, "Comparative study of various creep and shrinkage prediction models for concrete," *Journal of Materials in Civil Engineering,* vol. 19, no. 3, pp. 249-260, 2007.

[224] A. Al-Manaseer and A. Prado, "Statistical comparisons of creep and shrinkage prediction models using RILEM and NU-ITI databases," *ACI Materials Journal,* vol. 112, no. 1, pp. 125-136, 2015.

[225] A. Neville, "Creep of concrete as a function of its cement paste content," *Magazine of Concrete Research,* vol. 16, no. 46, pp. 21-30, 1964.

[226] Z. Bazant, A. Hauggaard, S. Baweja and F. Ulm, "Microprestress-solidification theory for concrete creep. I: Aging and drying effects," *Journal of Engineering Mechanics,* vol. 123, no. 11, pp. 1188-1194, 1997.

[227] A. Neville, Properties of concrete, Harlow, England: Pearson, 2011.

[228] T. Powers, "Mechanisms of shrinkage and reversible creep of hardened portland cement paste," in *Proceedings of International Conference On the Structure of Concrete, Cement and Concrete Association*, London, England, 1968.

[229] B. Tamtsia and J. Beaudoin, "Basic creep of hardened cement paste. A re-examination of the role of water," *Cement and Concrete Research,* vol. 30, no. 9, pp. 1465-1475, 2000.

[230] A. Neville, Creep of concrete: plain, reinforced and prestressed, Amsterdam: Noth-Holland Publishing Company, 1970.

[231] T. Powers, "Structure and Physical Properties of Hardened Portland Cement Paste,"

Journal of the American Ceramic Society, vol. 41, no. 1, pp. 1-6, 1958.

[232] Z. Bazant, "RILEM draft recommendation: TC-242-MDC multi-decade creep and shrinkage of concrete: material model and structural analysis* Model B4 for creep, drying shrinkage and autogenous shrinkage of normal and high-strength concretes with multi-decade applicabilit," *Materials and Structures,* vol. 48, no. 4, pp. 753-770, 2015.

[233] M. Berndt, "Properties of sustainable concrete containing fly ash, slag and recycled concrete aggregate," *Construction and Building Materials,* vol. 23, no. 7, pp. 2606-2613, 2009.

[234] C. Shi, D. Wang, L. Wu and Z. Wu, "The hydration and microstructure of ultra high-strength concrete with cement-silica fume-slag binder," *Cement and Concrete Composites,* vol. 61, pp. 44-52, 2015.

[235] S. Park, D. Kim, G. Ryu and K. Koh, "Tensile behavior of Ultra High Performance Hybrid Fiber Reinforced Concrete," *Cement and Concrete Composites,* vol. 34, no. 2, pp. 172-184, 2012.

[236] S. Kang, J. Choi, G. Koh, K. Lee and B. Lee, "Hybrid effects of steel fiber and microfiber on the tensile behavior of ultra-high performance concrete," *Composite Structures,* vol. 145, pp. 37-42, 2016.

[237] J. Nie, Y. Wang and C. Cai, "Elastic rigidity of composite beams with full width slab openings," *Journal of Constructional Steel Research,* vol. 73, pp. 43-54, 2012.

[238] K. Voit and J. Kirnbauer, "Tensile characteristics and fracture energy of fiber reinforced and non-reinforced ultra high performance concrete (UHPC),"

International Journal of Fracture, vol. 188, no. 2, pp. 147-157, 2014.

[239] Z. Bazant and M. Jirasek, Creep and hygrothermal effects in concrete structures, Netherlands: Springer, 2018.

[240] V. Garas, L. Kahn and K. Kurtis, "Short-term tensile creep and shrinkage of ultra-high performance concrete," *Cement & Concrete Composites,* vol. 31, pp. 147-152, 2009.

[241] Y. Wei, S. Liang and W. Guo, "Decoupling of Autogenous Shrinkage and Tensile Creep Strain in High Strength Concrete at Early Ages," *Experimental Mechanics,* vol. 57, pp. 475-485, 2017.

[242] F. Ruiz, A. Muttoni and P. Gambarova, "Relationship between nonlinear creep and cracking of concrete under uniaxial compression," *Journal of Advanced Concrete Technology*, vol. 5, no. 3, pp. 383-393, 2007.

[243] GB175-2020, Common Portland Cement, China: Quality Supervision Inspection and Quarantine of the People's Republic of China and Standardization Administration of the People's Republic China, 2020.

[244] GB/T27690-2011, Silica fume for cement, mortar and concrete, China: Quality Supervision Inspection and Quarantine of the People's Republic of China and Standardization Administration of the People's Republic China, 2011.

[245] GB/T18046-2017, Ground granulated blast furnace slag used for cement, mortar and concrete, China: Quality Supervision Inspection and Quarantine of the People's Republic of China and Standardization Administration of the People's Republic China, 2017.

[246] GB/T50081-2019, Standard for test methods of concrete physical and mechanical properties, China: Quality Supervision Inspection and Quarantine of the People's Republic of China and Standardization Administration of the People's Republic China, 2019.

[247] N. Banthia, "Load Relaxation in Steel Fibers Embedded in Cementitious Matrices," *International Journal of Cement Composites and Lightweight Concrete,* vol. 11, no. 4, pp. 1-6, 1989.

[248] E. Hamed, "Relaxation Behavior of Concrete under Sustained Uniaxial Compressive Deformation," *Journal of Materials in Civil Engineering,* vol. 28, no. 6, p. 06016007, 2016.

[249] P. Cruz, A. Mari and P. Roca, "Nonlinear Time-Dependent Analysis of Segmentally Constructed Structures," *Journal of Structural Engineering,* vol. 124, no. 3, pp. 278-287, 1998.

[250] C. Mazzotti and M. Savoia, "Nonlinear Creep Damage Model for Concrete under Uniaxial Compression," *Journal of Engineering Mechanics,* vol. 129, no. 9, pp. 1065-1075, 2003.

[251] E. Hamed, "Non-linear creep effects in concrete under uniaxial compression," *Magazine of Concrete Research,* vol. 67, no. 16, pp. 876-884, 2015.

[252] A. Neville and P. Aitcin, "High performance concrete—an overview," *Materials and Structures,* vol. 31, no. 2, pp. 111-117, 1998.

[253] K. Truman, D. Petruska and C. Norman, "Creep, shrinkage, and thermal effects on mass concrete structure," *Journal of Engineering Mechanics,* vol. 117, no. 6, pp.

1274-1288, 1991.

[254] W. Hansen and J. Almndaiheem, “Ultimate drying shrinkage of concrete — influence of major parameters,” *ACI Materials Journal,* vol. 84, no. 3, pp. 217-223, 1987.

[255] B. Bissonnette, P. Pierre and M. Pigeon, “Influence of key parameters on drying shrinkage of cementitious materials,” *Cement and Concrete Research*, vol. 29, no. 10, pp. 1655-1662, 1999.

[256] Z. Tao and Q. Weizu, “Tensile creep due to restraining stresses in high-strength concrete at early ages,” *Cement and Concrete Research,* vol. 36, no. 3, pp. 584-591, 2006.

[257] S. Altoubat and D. Lange, “Creep, shrinkage, and cracking of restrained concrete at early age,” *ACI Materials Journal,* vol. 98, no. 4, pp. 323-331, 2001.

[258] K. Mehta and P. Monteiro, Concrete: Microstructure, Properties, and Materials, United States of America: McGraw-Hill Companies, 2006.

[259] ACI207.2R-07, Report on Thermal and Volume Change Effects on Cracking of Mass Concrete, Farmington Hills: American Concrete Institute, 2007.

[260] R. Breitenbucher, “Investigation of thermal cracking with the cracking-frame,” *Materials and Structures,* vol. 23, pp. 172-177, 1990.

[261] R. Springenschmid, E. Gierlinger and W. Kiernozycki, “Thermal stresses in mass concrete: A new testing method and the influence of different cements,” in *15th International Congress on Large Dams (ICOLD),* Paris, 1985.

[262] M. Mangold, “Prevention of Thermal Cracking in Concrete at Early Ages,” Methods for Experimental Determination of Thermal Stresses and Crack Sensitivity in the

Laboratory. In RILEM Report 15, London, 1998.

[263] J. Whigham, “Evaluation of Restraint Stresses and Cracking in Early-Age Concrete with the Rigid Cracking Frame,” Master Thesis, Auburn University, 2005.

[264] B. Byard, A. Schindler, R. Barnes and A. Rao, “Cracking tendency of bridge deck concrete,” *Transportation Research Record,* vol. 2164, pp. 122-131, 2010.

[265] A. Tankasala, A. Schindler and K. Riding, “Risk of thermal cracking from use of lightweight aggregate in mass concrete,” *Transportation Research Record,* vol. 2629, no. 1, pp. 42-50, 2017.

[266] Y. Sargam, M. Faytarouni, K. Riding, K. Wang, C. Jahren and J. Shen, “Predicting thermal performance of a mass concrete foundation – A field monitoring case study,” *Case Studies in Construction Materials,* vol. 11, p. e00289, 2019.

[267] R. Breitenbücher and M. Mangold, “Minimization of Thermal Cracking in Concrete at Early Ages,” in *RILEM Proceedings 25,* London, 1994.

[268] X. Wang, Q. Xia and P. Zhu, “Experimental Research on the Effect of Ground Slag on Basic Tensile Creep of Early-age Concrete,” *The Open Construction and Building Technology Journal,* vol. 9, no. 1, pp. 68-72, 2015.

[269] J. Carette, S. Joseph, O. Cizer and S. Staquet, “Decoupling the autogenous swelling from the self-desiccation deformation in early age concrete with mineral additions: Micromacro observations and unified modelling,” *Cement and Concrete Composites,* vol. 85, pp. 122-132, 2018.

[270] Y. Gao, H. Zhang, S. Tang and H. Liu, “Study on early autogenous shrinkage and crack resistance of fly ash high-strength lightweight aggregate concrete,” *Magazine*

of Concrete Research, vol. 65, no. 15, pp. 906-913, 2013.

[271] K. Riding, J. Poole, A. Schindler, M. Juenger and K. Folliard, "Quantification of Effects of Fly Ash Type on Concrete Early-Age Cracking," *ACI Materials Journal,* vol. 105, no. 2, pp. 149-155, 2008.

[272] JCI, "Guidelines for control of cracking of mass concrete," in *Japan Concrete Istitute,* Tokyo, 2016.

[273] I. Maruyama and P. Lura, "Properties of early-age concrete relevant to cracking in massive concrete," *Cement and Concrete Research,* vol. 105770, p. 123, 2019.

[274] K. Kovler, "Testing system for determining the mechanical behaviour of early age concrete under restrained and free uniaxial shrinkage," *Materials and Structures,* vol. 27, pp. 324-330, 1994.

[275] R. Gilbert and G. Ranzi, Time-dependent behaviour of concrete structures, London: Spon Press, 2011.

[276] Z. Shui, R. Zhang, W. Chen and D. Xuan, "Effects of mineral admixtures on the thermal expansion properties of hardened cement paste," *Construction and Building Materials,* vol. 24, pp. 1761-1767, 2010.

[277] G. Gao, C. Qian and Y. Wang, "Effect of Fly Ash and Slag Powder on Coefficient of Thermal Expansion of Concrete," *Advanced Materials Research,* Vols. 374-377, pp. 1230-1234, 2011.

[278] G. Ji, T. Kanstad, O. Bjøntegaard and E. Sellevold, "Tensile and compressive creep deformations of hardening concrete containing mineral additives," *Materials and Structures,* vol. 46, no. 7, pp. 1167-1182, 2013.

[279] D. Atrushi, Tensile and compressive creep of early age concrete: Testing and modelling, The Norwegian University of Science and Technology, Norway: PhD Thesis, 2003.

[280] M. Briffaut, F. Benboudjema, J. Torrenti and G. Nahas, "Concrete early age basic creep: Experiments and test of rheological modelling approaches," *Construction and Building Materials,* vol. 36, pp. 373-380, 2012.